Mathematisch-Naturwissenschaftliche Fakultät
der Universität Augsburg

Possible Influences of Low Dose Ionising Radiation on Living Cells – A Static and a Dynamic Approach

Dissertation
zur Erlangung des akademischen Grades
eines Doktors der Naturwissenschaften (Dr. rer.nat.)

von
Teresa Maria Neumaier
Juli 2010

1. Korrektor: Prof. Dr. Achim Wixforth
2. Korrektor: Prof. Dr. Herwig Paretzke

Termin der Mündlichen Prüfung: 22.11.2010

Für meinen Vater

In memoriam

Acknowledgement

Diese Doktorarbeit wäre nicht zustande gekommen ohne die Unterstützung, die ich von vielen Seiten erfahren habe und für die ich mich herzlich bedanken möchte.

Allen voran möchte ich meinem Doktorvater Prof. Dr. Achim Wixforth danken für sein Interesse am Fortschritt meiner Arbeit, seine uneingeschränkte Unterstützung und das außerordentliche Vertrauen, das er mir entgegengebracht hat. An all das werde ich mich in Zukunft dankbar zurück erinnern, ebenso wie an seine besondere Art Menschen zu führen und anzuleiten.

Des Weiteren möchte ich mich bei Prof. Dr. Herwig Paretzke bedanken. Er hat mich während meiner Zeit am Helmholtz Zentrum gefördert und unterstützt. Bei strahlenbiophysikalischen Fragen konnte ich mich stets an ihn wenden und ich erhielt durch ihn die Möglichkeit mich auf Tagungen mit führenden Forschern der Strahlenwissenschaften auszutauschen.

Danken möchte ich ebenfalls meinem Betreuer am Helmholtz Zentrum München PD Dr. Stefan Thalhammer. Seine Unterstützung wie auch seine Hilfestellungen weiß ich sehr zu schätzen. Durch seine kritischen Denkanstöße lernte ich, manche Problemstellungen aus einem anderen Blickwinkel zu betrachten. Auch hat er mir einen Auslandsaufenthalt am Lawrence Berkeley National Laboratory ermöglicht, wovon ich wissenschaftlich sehr profitierte.

Je souhaite remercier le Dr. Sylvain Costes pour son encadrement lors de mon stage effectué au sein du LBNL. Son expertise dans le domaine, sa qualité d'interprétation des résultats, l'excellence de ses nombreuses idées méritent mon plus profond respect.

Furthermore, I want to thank Prof. Mary Helen Barcellos-Hoff for the possibility to work in her lab in Berkeley. The time at the Lawrence Berkeley National Laboratory, enabled me to experience a scientific and personal development.

Gerolf Lieckfeld möchte ich dafür danken, dass er während meiner Doktorarbeit meine Proben bestrahlte und mir bei strahlungstechnischen Fragen nützliche Hinweise gab.

Ebenso weiß ich seine Umsetzung meiner Ideen und Skizzen in CAD Konstruktionen sehr zu schätzen.

Dr. Klaus Wittmaack, Norbert Menzel und Prof. Dr. Wolfgang Heidenreich möchte ich für ihre Unterstützung und Zusammenarbeit danken. Nicht zuletzt fand ich unsere zahlreichen interessanten Diskussionen im Gebäude 36 im Hinblick auf mein Forschungsprojekt äußerst fruchtbar.

Auch möchte ich mich bei Helmut Niedermayer bedanken, der mir half, wenn es darum ging experimentelle Aufbauten zusammenzubauen, zu fräsen oder zuzuschneiden.

Bei Dr. Guido Drexler an der LMU München möchte ich mich ebenfalls bedanken. Seine fachliche Kompetenz und Unterstützung bei Fragen zur Biologie waren für meine Arbeit von unschätzbarem Wert.

Bei Anna-Lena Idzko möchte ich mich für ihre nun schon seit dem 1. Semester andauernde Freundschaft bedanken. Ebenso dafür, dass sie auch in schwierigen Zeiten zu mir gestanden hat.

Dr. Helmut Schlattl vom Helmholtz Zentrum München möchte ich für seine Unterstützung bei der Berechnung der Röntgenemissionsspektren danken.

Bei Dr. Ulrich Rothbauer und Dr. Kourosh Zolghadr möchte ich mich für ihre Hilfestellungen bei benötigten Zellkulturen und zellkulturtechnischen Fragen bedanken.

Meiner Mutter Ulrike Neumaier möchte ich für ihr grenzenloses Vertrauen in mich danken: Für ihre immerwährende Unterstützung, für ihr offenes Ohr wenn ich ihr von Problemen bei den Experimenten erzählt habe... einfach für alles. Danke!

Meinen Geschwistern Dr. Christopher Neumaier und Katharina Neumaier möchte ich ebenfalls für ihre Unterstützung danken. In schwierigen Zeiten sind sie ein wichtiger Rückhalt für mich gewesen. Auch möchte ich mich bei Christopher für das Korrekturlesen bedanken.

Ebenfalls möchte ich mich auch bei meinem Freund Michael Graser für seine Geduld und Unterstützung bedanken. In schwierigen Zeiten konnte ich mich stets auf ihn verlassen, er hat mir immer den Rücken gestärkt.

Zuletzt möchte ich mich bei meinem Vater Albert Neumaier bedanken. Auch wenn er den Abschluss meiner Arbeit nicht mehr miterleben konnte, bin ich ihm einfach nur dankbar dafür, dass er immer für mich da war und meine Wissbegierigkeit und mein Interesse für Neues unterstützt und gefördert hat. Ich werde mich immer gerne an die schöne Zeit erinnern, die wir als Familie erlebt haben.

Abstract

Ionising radiation can produce a number of effects in living cells and organisms. One way to investigate its influence on cells is the analysis of microscopically visible nuclear domains, so-called radiation-induced foci (RIF). These foci are protein accumulations, eventually responding to and indicating the presence of DNA double strand breaks (DSBs). RIF have raised much interest as a way to measure DNA damage on a cell-by-cell basis. This work presents a novel experimental approach for RIF quantification in cells by using different chemically modified glass slides. On these slides, cells were cultivated in a volume of $V = 5\,\mu l$ and it was possible to optimise and to accelerate immunostaining of DNA damage markers. Combined with an automated image analysis and biophysical model, this led to a dose response screening of several human cell lines over a wide range of irradiation doses as well as repair times. By including the biophysical kinetic model of foci formation and resolution, the absolute RIF yield at various doses could be evaluated unambiguously. Instead of being constant as it had been assumed previously, we find that 53BP1 and γH2AX RIF yield per unit of radiation decreased with irradiation dose. A two- to threefold drop in the number of RIF/mGy/cell from the lowest dose (50 mGy, 150 mGy) to the highest irradiation dose (1000 mGy, 2000 mGy) was deducted from our data. In addition, kinetic constants were also found to be dose dependent, suggesting a faster formation (e.g. 3,5 - 2,2 min for 150 - 2000 mGy) but slower loss of RIF (e.g. 40 min - 2 h for 150 - 2000 mGy) as the dose increased. Overall, these results challenge the concept that one DSB leads to one RIF but suggests instead that multiple DSB in close proximity are likely to cluster into one common repair location. The more DSB per cluster, the faster was the RIF induction but the slower the RIF resolution. More generally, the multi-sample microculture array platform allows for a more detailed but still rapid screening of DNA damage markers and turns out to be a perfect tool for the study of radiosensitivity, DNA repair and the heterogeneity of DNA damage response among populations.

Another way to investigate the influence of ionising radiation presented in this work is the evaluation of cell growth experiments under different growth conditions. Experiments with complete and partial irradiation of cells revealed that cells were more affected by the partial irradiation as e.g. observed for the co-cultures of human fibroblasts and HeLa cells. Furthermore, differences in the reaction of cells were observed for different states of confluence in the cell culture. These findings might shed

some light on tumor development inside a cellular system and on possible bystander effects that affect neighbouring cells of directly irradiated cells in irradiation tumor therapy.

Zusammenfassung

Ionisierende Strahlung kann eine Vielzahl von Effekten bei Zellen und Organismen hervorrufen. Eine Möglichkeit, diese zu untersuchen, ist die Analyse von mikroskopisch sichtbaren kleinen Bereichen, den so genannten strahlungsinduzierten Foci (engl. RIF). Diese Foci sind Proteinanlagerungen, welche möglicherweise auf einen DNS-Doppelstrangbruch (engl. DSB) reagieren bzw. diesen anzeigen. RIF ermöglichen eine Abschätzung von DNS-Schäden auf zellulärer Ebene. Im Rahmen dieser Arbeit wird ein neuartiger experimenteller Ansatz vorgestellt, welcher die Quantifizierung von RIF unter Verwendung von chemisch modifizierten Glasobjektträgern erlaubt. Auf diesen chemisch vorbehandelten Oberflächen wurden Zellen in einem Volumen von $V = 5\,\mu l$ kultiviert, und es war möglich, die Immunofluoreszenzfärbung von DNS-Schäden-Markern zu optimieren und zu beschleunigen. Kombiniert mit einer automatischen Bildanalyse sowie einem biophysikalischen Modell war es dadurch möglich, die Reaktion von mehreren menschlichen Zelllinien über eine Vielzahl von Bestrahlungsdosen und Reparaturzeiten zu klassifizieren. Durch das biophysikalisch kinetische Modell zur Focusbildung und -auflösung konnte die absolute Ausbeute von RIF eindeutig bestimmt werden. Im Gegensatz zu der bisherigen Annahme, dass diese Ausbeute ein konstanter Wert sei, nahmen die Werte sowohl für 53BP1 als auch γH2AX RIF mit steigender Dosis ab. Eine zwei- bis dreifache Reduktion in den Werten für RIF/mGy/Zelle wurde von der niedrigsten Dosis (50 mGy, 150 mGy) zu höchsten Dosis (1000 mGy, 2000 mGy) berechnet. Des Weiteren wurde auch eine Dosisabhängigkeit der kinetischen Konstanten bestimmt, welche eine schnellere Bildung (z.B. 3,5 - 2,2 min für 150 - 2000 mGy), jedoch zugleich langsameres Verschwinden von RIF (z.B. 40 min - 2 h für 150 - 2000 mGy) mit steigender Dosis aufzeigten. Allgemein kann festgehalten werden, dass die Ergebnisse aus den verschiedenen Experiment die bisherige Annahme, ein DSB entspricht immer einem RIF in Frage stellen. Vielmehr weisen die Ergebnisse darauf hin, dass mehrere DSB in näherer Umgebung zueinander, sich in einem gemeinsamen Reparaturzentrum anlagern. Je mehr DSB pro Cluster zu finden sind, desto schneller kommt es zur RIF-Bildung und desto langsamer zur RIF-Auflösung. Letztlich zeigen die Forschungsergebnisse, dass die Mikrokultur-Arrayplatformen eine genauere und schnellere Analyse von DNS-Schäden-Markern ermöglichen und dass sie somit ein optimales Instrument für die Untersuchung von Strahlungsempfindlichkeit, DNS-

Reparatur und Heterogenität der Antwort auf DNS-Schäden innerhalb einer Population darstellen.

Eine andere in dieser Arbeit vorgestellte Möglichkeit für die Analyse von strahlungsinduzierten Effekten wird durch Zellwachstumsexperimente für verschiedene Bedingungen aufgezeigt. Experimente mit Komplett- bzw. Teilbestrahlung von Zellen zeigten, dass die teilbestrahlten Zellen zum Teil mehr durch die Strahlung beeinflusst wurden als die komplettbestrahlten Zellen, wie z.B. im Fall von Co-Kulturen bestehend aus menschlichen Fibroblasten und HeLa-Zellen. Des Weiteren wurden Unterschiede im Zellverhalten für verschiedene Konfluenzstadien beobachtet. Durch diese Art von Experimenten wäre es möglich, mehr Erkenntnisse über die Tumorentwicklung zu erhalten sowie mögliche Bystandereffekte in Nachbarzellen von direkt bestrahlten Zellen in der Tumortherapie durch Bestrahlung zu erforschen.

Contents

1 Introduction and Aim of this Work

Humans are permanently exposed to low doses of radiation from natural and artificial sources. In Germany, the average effective dose of exposure is around 4,5 mSv per year, of which 2,0 mSv are due to medical applications (1). Possible adverse health effects due to such irradiations are of ongoing public interest, notably in the low dose regime (2). Experimental studies revealed a rather complex picture, which showed, for example, that irradiation can affect neighbouring cells in the same or similar way as targeted cells. A phenomenon referred to as the 'bystander effect' (3-6). DNA double strand breaks are often considered to present a relevant early damage for final detrimental effects of ionising radiation with respect to cancer development (7). A common *in vitro* technique to investigate this kind of damage in cultured cells is the immunofluorescence staining of DNA double strand breaks (DSB) (8-10). The approach is based on the observation that certain proteins settle at the site of DNA double strand breaks within seconds to minutes following irradiation exposure. In favourable cases this labelling of double strand breaks can be visualised microscopically in the form of nuclear domains referred to as radiation-induced foci (RIF) (8). In mammalian cells, Rad51 was the first protein identified as being capable of forming radiation-induced foci in mitotic and meiotic cells (8, 11). Since then, the technique has been developed further, allowing a distinction between proteins recruited to damage sites such as 53BP1 (12), modifications of pre-existing proteins near the damage site, like the phosphorylation of H2AX (γH2AX) (13), or proteins involved in both recruitment and protein modifications, such as phosphorylation of *Ataxia telangiectasia mutated* (ATM) (14).

Two groups have reported a linear relationship from mGy to Gy of exposures between frequency of RIF and the dose delivered (9, 15). In both of these studies, the authors had to deal with the problem of spontaneous foci present before irradiation (IR) in order to identify "real" RIF at low doses (i.e. 10 mGy would lead to about 0.3 DSB/cell). This was achieved either by using cells with very low γH2AX background foci (i.e. 0.05 foci/cell in primary human lung MRC-5 fibroblasts) (9) or by using an *in vivo* detectable DNA damage marker (i.e. 53BP1-GFP), which can track foci that were present in the cells before exposure to ionising radiation (15). Even though both groups obtained linear dose responses, their results show discrepancies. The first study reported a maximum of 35 γH2AX RIF/Gy at 3 min post irradiation (9), whereas the latter study reported maximum yield much later in time (i.e. 30 to 60 min post irradiation), with

16 - 20 53BP1 RIF/Gy for human HT1080 cells as well as 60 53BP1 RIF/Gy for immortalised human bronchial epithelial cells (15). Furthermore, background corrected γH2AX RIF yields measured on fixed cells in the latter study matched the 53BP1 GFP RIF yields, indicating that differences were not due to the different types of foci markers. These large numerical discrepancies for human cells in G1 are contradicting the 1 to 1 correspondence between DSB and RIF, as all these cells should have similar genome sizes and, thus, similar number of DSB/Gy. Many of the discrepancies between DSB and RIF are outlined in a recent published review (16). For example, reported RIF kinetics have a 15 to 30 min delay before reaching a maximum number of RIF, which is typically lower than the expected 25 - 35 DSB/Gy. In contrast, DSB measurements decay exponentially with time after exposure, as measured in pulse field gel electrophoresis (PFGE) (17).

One experimental approach presented in this work challenges the concept of linearity between RIF yield and dose, since the data presented in some other works suggest saturation of RIF yields with increasing dose: e.g. maximum yields of 18 - 24 γH2AX RIF/Gy for doses of X-rays less than 1 Gy (10) when compared to 13 - 15 γH2AX RIF/Gy for doses between 1 - 4 Gy in normal human fibroblasts 1 h post irradiation or in the hamster V79 cell line 30 min post irradiation (18). Lower RIF yields detected at higher doses could be due in part to a resolution problem as there might be more overlapping RIF. However, the total intensity of γH2AX in each V79 cell, a measurement that should not depend on RIF overlapping, also showed saturation at higher doses (17). Furthermore, at doses where RIF overlap was unlikely (i.e. from 50 to 250 mGy), it was also observed that RIF yield decreased as the irradiation dose increased (19).

The discrepancies in quantification of RIF may be traced back to the lack of harmonisation in measurement methodology (i.e. imaging, immunostaining, analysis). This work presents a reproducible RIF analysis after resolving many confounding factors. Since visual scoring of relatively small numbers of nuclei adds statistical uncertainty (9), automatic computer analysis allows the evaluation of larger sample sizes. Miniaturisation of cell cultures using microwell slide technology was also adopted to further simplify and normalise sample treatment and processing. Furthermore, a mathematical model of RIF kinetics was included in the analysis to observe the irradiation time response. The obtained results confirmed that the absolute yield of

RIF/Gy and the rates of RIF formation and resolution changed significantly with the irradiation dose.

Aspects of a possible bystander effect were explored in the second part of this work through living cell experiments. It was necessary to differentiate between irradiated and non-irradiated cells. This was achieved by using the green fluorescent protein as live cell reporter e.g. of irradiated cells (20). Then, it was possible to track green fluorescent irradiated cells in cellular co-culture with non-irradiated non-painted cells, and to analyse their influence on growth and survival of the non-irradiated cells. Furthermore, these experiments can shed light on the possibility of tumor development through irradiated, and, thus possibly mutated cells, inside a cellular system.

2 Effects of Ionising Radiation on Cells

The effects of ionising radiation on living organisms can be divided into four phases, which are characterised by distinctly different time scales. The first, physical phase, involves the transfer of energy from the photon or swift particle (electrons, protons, alpha particles) to the biological tissue, predominantly to the electrons in the material. The transferred energy is consumed in excitation, ionisation and dissociation processes that are completed within only about 10^{-12} s after impact. The second, chemical phase, takes place from 10^{-12} to 1 s. Processes occurring during these two phases might lead to instability and damage in complex biological molecules like the 'deoxyribonucleic acid' (DNA). The third, biological phase, can last many years, ending up in the fourth and final medical health phase, which includes long-term alterations in living organisms like cancer development.

2.1 Dosimetry

Exposure to ionising radiation in tissue is quantified by the so-called 'absorbed dose', which is defined as the energy absorbed per unit mass (Jkg^{-1}) from any kind of ionising radiation in any target material (21). The unit of absorbed dose is called 'gray' ($1\,Gy = 1\,Jkg^{-1}$). The efficiency of different types of ionising radiation in transferring energy to a biological target is described by the concept of 'linear energy transfer' (LET), which is defined as the energy transferred to a target per unit length along a charged-particle track (usually specified in units of $keV/\mu m$). Radiation with 'high' LET (~ 100 - 200 keV/µm), like α-particles, low-energy protons or heavy ions, is in general more damaging to a biological system than radiation with a 'low' LET (~ 1keV/µm), like X-rays or γ-rays (22).

In order to account for the differences in the biological effectiveness for different kinds of radiation, the International Commission on Radiological Protection (ICRP), the National Council on Radiation Protection and Measurement (NCRP) and the International Commission on Radiation Units and Measurements (ICRU) introduced the concept of the 'dose equivalent' H, which is defined as the product of the absorbed dose D and a dimensionless quality factor Q, i.e. $H = Q \cdot D$. The parameter Q depends on the LET, which describes the radiation quality, see Table 2.1. The unit of the dose equivalent is called 'sievert' (Sv). The dose equivalent has been used extensively in radiation

protection programs for the quantification of radiation limits. These limits are specified for the exposure of individuals (22).

Table 2.1: Dependence of quality factor Q on LET of radiation as currently recommended by ICRP, NCRP, and ICRU (21)

LET [keV μm^{-1}] in water	Q
< 10	1
10 - 100	$0,32LET - 2,2$
> 100	$300/\sqrt{LET}$

2.2 DNA Damage induced by Ionising Radiation

Biological matter such as living cells, may be damaged by direct energy absorption as well as by interaction with radicals formed in their environment. Since mammalian cells typically consist of 70 – 80% water, knowledge of the radiation chemistry of water is essential for a complete understanding of radiobiological phenomena.

Ionising radiation can either excite or ionise water molecules, generating H_2O^*, H_2O^+ and free electrons respectively. Within ~10^{-15} to ~10^{-12} s after impact, the water begins to adjust to the change in its physical state (21), as described by the following reactions.

$$H_2O^+ + H_2O \rightarrow H_3O^+ + OH \tag{2.1}$$

$$H_2O^* \rightarrow \begin{cases} H_2O + e^- \\ H + OH \end{cases} \tag{2.2}$$

$$e^- \rightarrow e^-_{aq} \tag{2.3}$$

First, ionised water molecules react with neighbouring molecules and form a hydronium ion, H_3O^+, and a hydroxyl radical, OH (reaction 2.1). Second, the excited water molecules loose their energy either by losing an electron and becoming an ion, which then proceeds as indicated in reaction 2.1, or by molecular dissociation (reaction 2.2). Third, the free electrons migrate, losing energy through excitation of water molecules and become thermalised. Thermalised electrons orient the permanent dipole moments of the neighbouring water molecules, thus forming clusters called hydrated electrons (reaction 2.3).

The four chemical active species H_2O^+, $OH^\bullet$, $H^\bullet$, and e^-_{aq} are residing close to the original molecules triggering their formation. Three of the new reactants, $OH^\bullet$, $H^\bullet$, and e^-_{aq}, possess unpaired electrons and are, thus, highly reactive radicals. They migrate randomly due to thermal motion, thus being able to react with other molecules, including DNA molecules, with the possibility of creating DNA damage (21).

A DNA double strand is formed through two complementary DNA single strands twisted around each other, thus forming a double helix (Figure 2.1A). Each DNA single strand consists of two parts, a sugar-phosphate backbone and a sequence of four different bases[1], encoding the genetic information. Each human cell contains around 2 m of DNA if stretched, which has to be packed closely to fit in a cell nucleus with a diameter of around 6 µm. This compression is achieved through special proteins, so-called histones and nonhistones, which coil and fold the DNA into higher and higher levels of organisation, thus, forming chromatin.

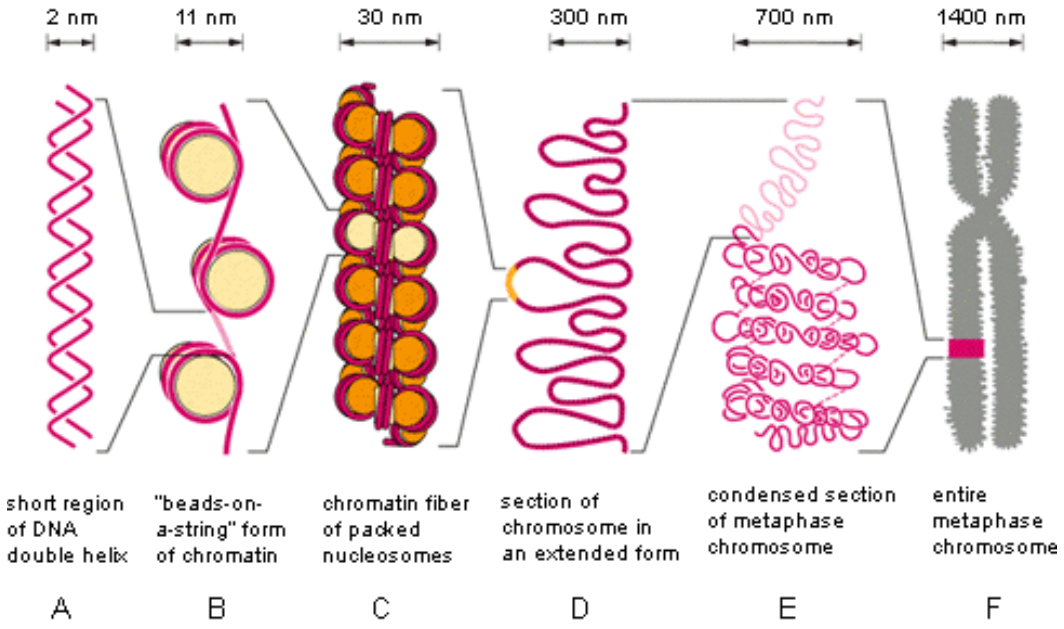

Figure 2.1: Schematic diagram of different stages of chromosome packing. The DNA double helix (A) is packed into higher stages of organisation resulting in the condensed mitotic chromosome. The DNA double helix is first wound around histones, thus, forming nucleosomes (B), which are then packed on top of each other resulting in condensed chromatin (C). In the further process, this leads to the organisation in metaphase chromosomes (D-F) (adapted from (23)).

First, the DNA double helix is wound around a protein core formed from histones. This results in the formation of so-called nucleosomes (Figure 2.1B) (23). Subsequently, the nucleosomes are packed on top of each other generating more highly condensed chromatin fibers (Figure 2.1C). The chromatin fibers then fold into large looped

[1] Adenin, Thymine, Guanine and Cytosine

domains, which are organised into distinct structures called chromosomes during mitotic phase (Figure 2.1D-F). Carl Rabl published in 1885 a theory describing an internal structure of the chromosomes in cell nuclei during the interphase where the chromatin is generally decondensed and located in distinct territories in the whole nucleus (23).

Depending on the dose and type of irradiation, the ionisation occurring in cells can have very different biological effects. Low LET radiation causes randomly scattered ionisations separated by fairly large distances. Hence, the probability that a single photon will induce damage in the DNA is low (Figure 2.2A). Nevertheless, secondary electrons produced from the water molecules inside the cell can cause clusters of ionisations in the close vicinity of the DNA. This leads to more complex damages, even for low LET irradiation (24, 25). In contrast, high LET radiation deposits its energy densely along its passage through the nucleus. Hence, the probability is much higher for this radiation type to produce several lesions in the DNA within a small range (Figure 2.2B). However, for the same irradiation dose, the total number of ionisations within a cell nucleus is similar for both radiation types (high and low LET).

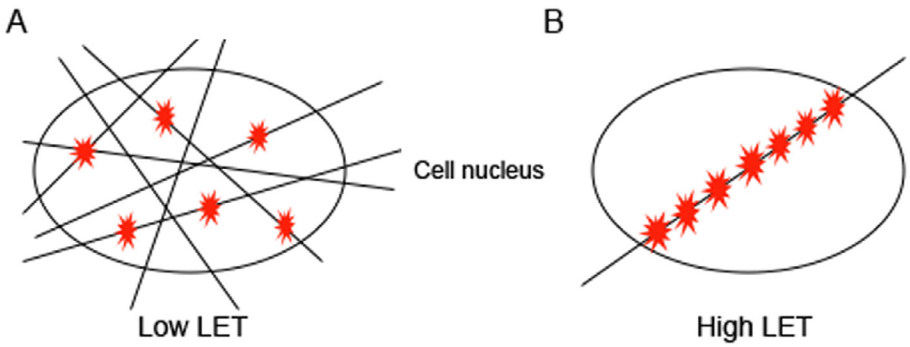

Figure 2.2: Schematic illustration of the ionisation patterns induced by low and high LET radiations inside a cell nucleus. The number of ionisations is similar for both radiation types for the same irradiation dose. However, their interactions with matter are quite different. Low LET radiation causes randomly scattered ionisations, usually well separated. High LET particles deposit the energy densely along their track through the nucleus, causing several ionisations close to their paths.

2.3 DNA Damage Repair

Accidental lesions of the DNA occur continuously. They can occure naturally or are induced by DNA damaging agents, like terrestrial radiation, X-rays or chemicals. The survival of individuals is guaranteed through the genomic stability in cells. This means that damaged DNA has to be repaired accurately to ensure survival.

Damages to the DNA double strand (Figure 2.3A) can be base modifications and alterations of the sugar-phosphate backbone. This includes breakage of phosphodiester

bonds resulting in a single strand break (SSB) as indicated in Figure 2.3B. If two SSBs are less than 14 base pairs apart, the base pairing is generally not strong enough to keep both strands attached to each other, which results in the formation of a double strand break (DSB) (26). However, DSBs can also arise directly after irradiation. They are a 'severe' damage and, thus, a threat to cell survival (27). They can lead to loss or damage of base pairs and leave no intact template strand for repair (Figure 2.3C) (28).

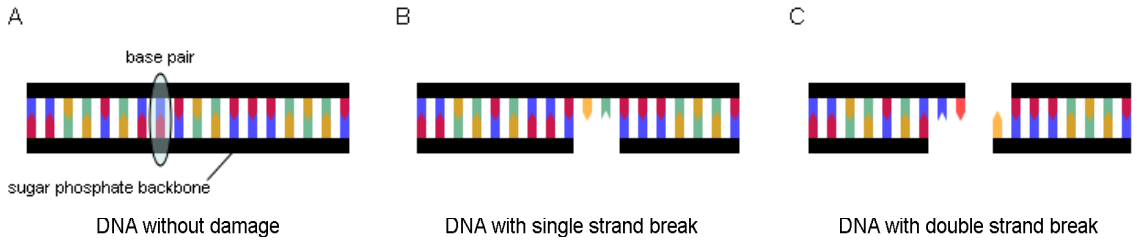

Figure 2.3: Schematic illustration of a DNA double strand before and after induced damage. Image A shows the DNA double strand before damage induction. Image B illustrates a DNA double strand with a single strand break and image C a DNA double strand with double strand break.

Two distinct mechanisms for double strand break repair are known in mammalian cells. Both, the 'non-homologous end-joining' (NHEJ) and the 'homologous recombination' (HR) demonstrate the importance of reliable and effective DSB repair (29). For the cell it is the easier way to repair damaged DNA double strands via non-homologous end-joining.

The two ends of the DNA are juxtaposed and then rejoined by DNA ligation[2], thus, taking a possible base loss into account. NHEJ might benefit from existing complementary base pairs in the length range from 1 to 4 bases. This is called 'micro-homology' (30). However, the NHEJ repair process also connects the ends of incompatible DNA strands, leading to translocations. NHEJ is triggered by the Ku-proteins and DNA PK_{CS} protein kinase, which bind to both ends of the DNA double strand as indicated in Figure 2.4. The possibility of an accurate repair is only given when the right DSB ends are joined, when no resections of the end takes place for microhomology usage and when no nucleotides[3] are lost through the induced damage. If one or more nucleotides are lost, the two ends of the DNA double strand are no longer compatible at the site of damage since the two DNA ends have not any longer the complementary base sequences, which can be connected with each other. Therefore, both

[2] Ligation is the process of joining two pieces of DNA to a single piece through the use of the DNA enzyme ligase.
[3] Nucleotides are the elements of the DNA double strand, consisting of the encoding base, sugar, and phosphate.

DNA ends are altered by adding or removing further nucleotides to at least achieve complementary base pairs at the ends. This process is executed by the protein complex Artemis-DNA-PK_{CS} or DNA polymerase (30). Both now complementary DNA double strand ends are then bound to each other and the single stranded gaps are closed by DNA ligase. The errors in the genetic information induced through such a repair have generally not much influence on the survival of cells. Eucaryotic genes are broken up into small pieces of protein coding sequences, called 'exons', interspersed with much longer non-coding sequences called 'introns'. Thus, the protein coding portions of an eukaryotic gene is often only a small fraction of the length of the gene (23). Both intron and exon sequences are transcribed into RNA, whereat the intron sequences are removed from the synthesised RNA through the process of 'RNA splicing'. However, an assembly of DNA ends of different chromosomes, which might occur, has an enormous effect on the cell.

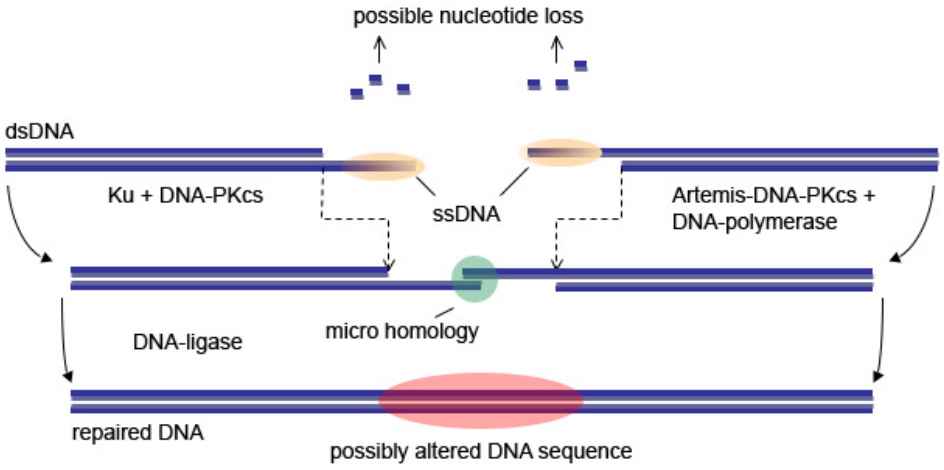

Figure 2.4: Schematic illustrations of the NHEJ repair process. The DSB is repaired correctly if no nucleotides of the double stranded DNA (dsDNA) get lost through damage induction. If one or more nucleotides are lost, the repair might lead to base pair loss in the repaired DNA sequence. The single stranded DNA (ssDNA) ends of the damaged DNA are not compatible if nucleotides are lost at the site of damage. Thus, the DNA ends are altered by removing or adding further nucleotides to achieve complementary base pairs at the ends. The protein complex Artemis-DNA-PK_{CS} or DNA polymerase attains the alterations of the DNA ends. Both now complementary DNA ends are then bound to each other and the single stranded gaps are closed by DNA ligase (adapted from (23)).

The other repair mechanism, HR, makes use of the homologous base sequence of the identical sister chromatid as a template (Figure 2.5A). General recombination mechanisms transfer nucleotide sequence information from the intact DNA double helix to the site of the double-strand break in the broken helix. Therefore, nucleotides at both ends of the broken DNA strand are removed, which results in overlapping single stranded DNA ends. Then, the protein Rad52 binds to these single stranded DNA ends similar to the Ku protein in the NHEJ repair process. This means that the annealing repair proteins

determine the repair mechanism of the cellular DNA (31). In the further process of the HR the homologous DNA is split partially into single strands. Both ends of the damaged DNA are brought to the intact homologous chromosome with the help of the protein Rad51 and bound to its bases over hydrogen bonds (Figure 2.5B). The damaged DNA is then reconstructed along the template (Figure 2.5C).

The reconstruction of the damaged DNA strand can be executed in two ways. In the first process, two cross points, so-called holiday junctions, arise as soon as the damaged DNA molecule is completed (Figure 2.5D). The DNA molecules can be separated after the DNA molecules are cut at the holiday junctions (Figure 2.5E). This way of repair results in an exchange of bases also in the template DNA as indicated by the green DNA strand in Figure 2.5E.

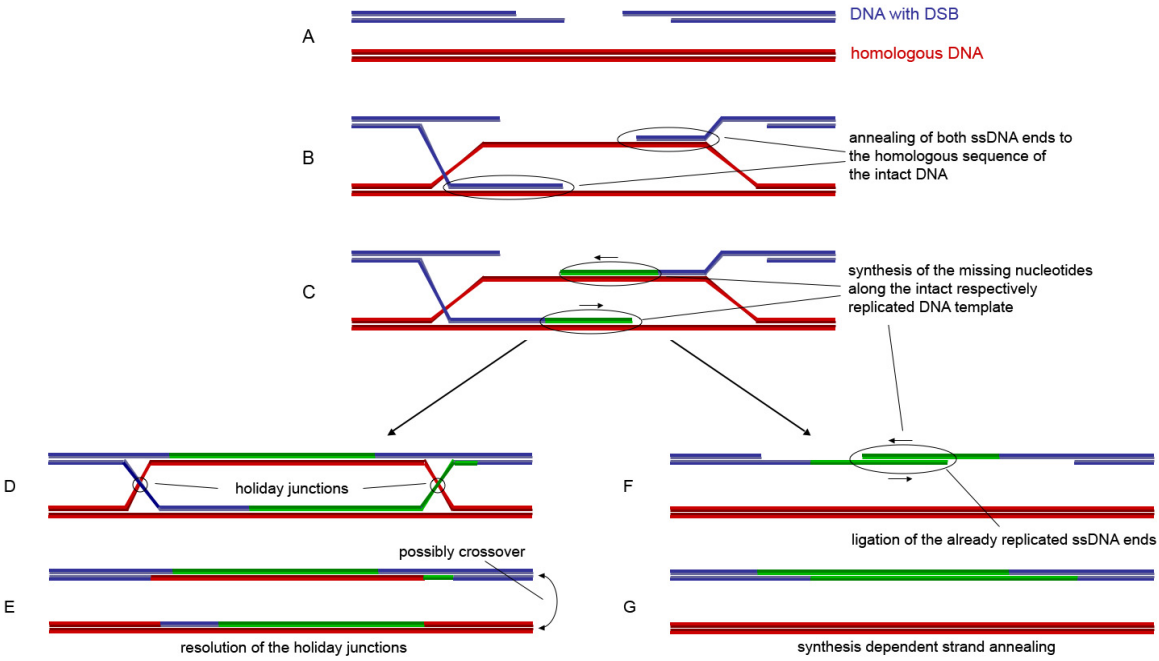

Figure 2.5: Schematic illustrations of the HR repair mechanism. Both ends of the damaged DNA molecule are bound to the homologous sister chromatid, which is used as template. In the next step, the damaged DNA is reconstructed along the intact respectively replicated DNA template. The reconstruction can either occur via the holiday junction resolution or via the synthesis-dependent strand-annealing. There is an exchange of bases also in the template DNA molecule (green DNA molecules) for the holiday junction resolution in contrast to the synthesis-dependent strand-annealing where the template stays intact (adapted from (23)).

Alternatively, it is also possible that the damaged DNA separates from the homologous chromosome at an earlier stage. The further reconstruction can be executed without template as soon as the reconstructed single strands have overlapping complementary base sequences (Figure 2.5F). The homologous chromosome stays intact for this reconstruction via the so-called synthesis-dependent strand-annealing (Figure 2.5G). The

repair mechanism of the HR is generally error-free. However, double-strand breaks induced in human cells are mostly repaired via the NHEJ. The HR is present in human cells but is predominating in bacteria and yeast (23). Both specialised and overlapping roles of the two repair pathways have been demonstrated in cell systems (32-34).

It is not fully understood how the contributions of NHEJ and HR in DSB repair are exactly regulated. However, the cell cycle phase is one of the factors involved in the pathway choice (Figure 2.6). The cell cycle is the essential mechanism by which all living cells reproduce. It is classified in mitosis, the actual cell division and the interphase. The interphase is subdivided in the G1 phase, in which the cell gains double the size by growing, the S phase, where the DNA is replicated and the G2 phase, which primes the cell for mitosis. In the repair pathway of the HR, an undamaged sequence on the homologous chromosome or sister chromatid is used as template. Using the homologous chromosome in the G1 cell cycle phase might lead to homozygosity[4], which is not desirable in regard to genomic instability. Furthermore, the homologous chromosomes could be too far apart, making it difficult and slow to find the correct template (35, 36). These considerations could be two reasons for the down regulation of the HR in the G1 phase when only the homologous chromosome is present. However, HR repair is present when the sister chromatid is present during the S and G2 phase of the cell cycle. DSB are then repaired with the HR repair in addition to NHEJ repair (37, 38).

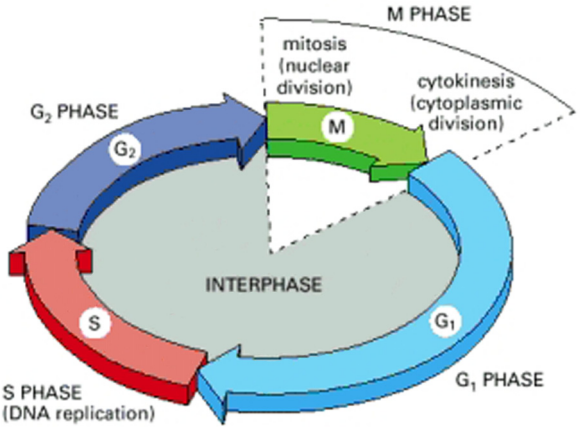

Figure 2.6: Illustration of the cell cycle phases. The replication of cells is controlled via the cell cycle, which consists of the mitosis, the actual cell division, and the interphase. The interphase consists of three parts, the G1 phase, in which the cells gain the double size by growing, the S phase, where the DNA is replicated and the G2 phase, which primes the cell for the mitosis (23).

[4] Homozygosity describes the state of a cell where the two alleles of a trait, an inherited characteristic, are the same.

A complex cell-cycle control system has been evolved in eukaryotic cells, which governs the progression through the cell cycle over different checkpoints. The cell has the possibility to gain time for repair by retarding the cell cycle after damage induction, e.g. by ionising radiation. If the damage in the cellular DNA is too drastic, the cell falls into apoptosis, the programmed cell death (23, 39). All signalling processes inside a cell are controlled via different protein cascades. However, it is far from being completely understood how the DSB response is initiated and sustained although some key proteins have been identified.

One of these identified proteins is the protein kinase *Ataxia-telangiectasia mutated* (ATM), which is essential for the cellular response to DSBs. ATM is rapidly activated after irradiation by autophosphorylation (14) and, by phosphorylating further proteins like for example p53, leading to a cell cycle arrest in the G1, S or G2 phase (40). Furthermore, ATM is also the major kinase responsible for the phosphorylation of a histone variant called H2AX after DSB induction (41). H2AX histones situated within several kilobases up to a megabase region next to a DSB will be rapidly phosphorylated after DSB induction (13). The phosphorylated histone H2AX (γH2AX) can be detected via immunofluorescence staining in a fluorescence microscope as dots, so-called radiation-induced foci (RIF). The number of γH2AX foci reaches its maximum after 15-30 min post irradiation (9). Although observations indicate H2AX phosphorylation is not essential for DSB repair, it was shown that cells lacking H2AX have increased genomic instability. This indicated that H2AX and its phosphorylation is needed for maximal efficiency in DSB repair (42, 43).

A rapid relocalisation of various proteins involved in the DSB response is detected after DSB induction. Although the recruitment of these proteins to DSBs is independent of H2AX, the accumulation of these proteins into visible foci requires phosphorylated H2AX (43). One of these proteins is the p53 Binding Protein 1 (53BP1), which has been found to colocalise with γH2AX along the entire region of modified chromatin (12, 44, 45). 53BP1 might be connected to ATM recruitment and phosphorylation after irradiation. A clear definition of the function of this protein after DSB induction is not yet possible. However, it is known that 53BP1 is jointly responsible for the G2 arrest after DNA damage induction (46).

2.4 Targeted and Non-Targeted Effects

A central paradigm in radiation research was that the energy of ionising radiation must be deposited directly into the cell nucleus to elicit a biological effect. This leads to the conclusion that only cells hit directly by ionising radiation are damaged (5). However, in recent years responses of cells to radiation in the absence of direct irradiation have been reported. These so-called non-targeted effects, like for example genomic instability in not directly irradiated cells and the bystander effect, challenge the 'classical' idea of targeted DNA damage (3-6).

'Genomic instability' describes the increased rate of acquisition of alterations in the genome (5). It is measured in terms of chromosomal alterations, changes in ploidy, micronucleus formation, gene mutations and amplifications (47, 48). Radiation-induced instabilities can be observed in cells at delayed times after irradiation and appear in the progeny of direct irradiated cells several generations after the initial event (Figure 2.7A).

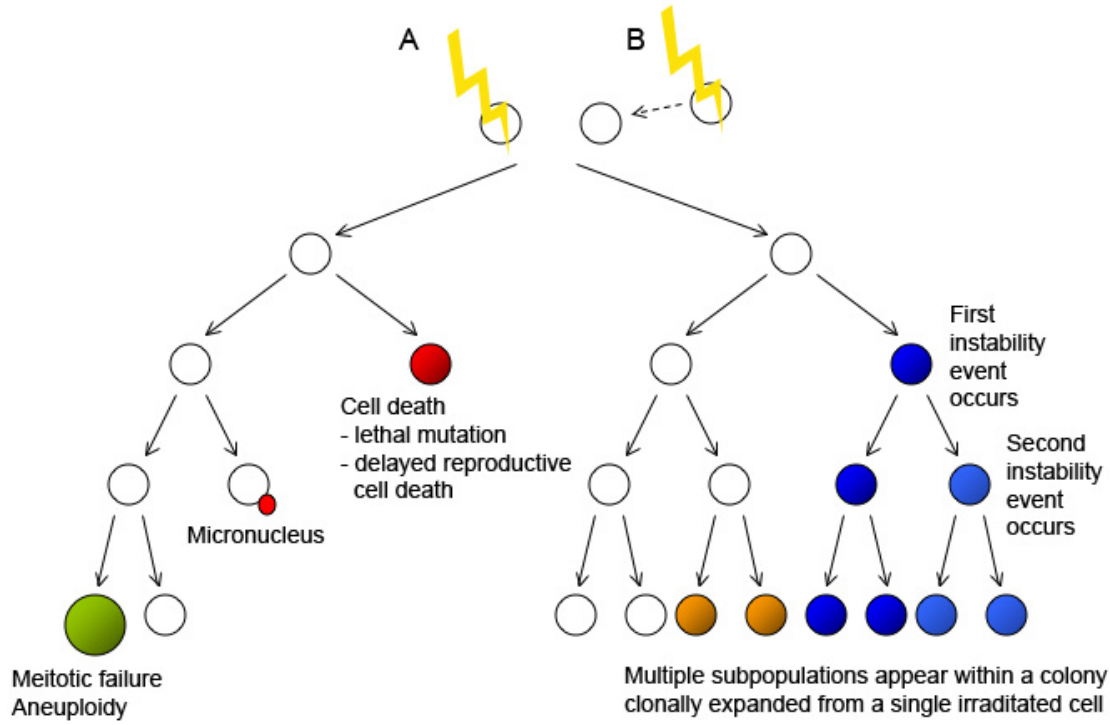

Figure 2.7: Schematic illustration of radiation-induced genomic instability in the progeny of a directly irradiated cell (A) or an indirectly irradiated cell, which is affected by the signal sent from an irradiated cell (B). In both ways it is assumed that cells survive the irradiation process and are clonally expanded. During the process of clonal expansion a number of progeny are dying due to lethal mutations or delayed reproductive cell death. This results in a reduced plating efficiency in this clone. Furthermore, it is possible that instability events occur in the progeny of the irradiated cell like chromosomal rearrangements, aberration, micronuclei, mutations or aneuploidy[5] (adapted from (49)).

[5] Aneuploidy is an abnormal number of chromosomes inside a cell nucleus.

Kadhim and colleagues (50) were the first to demonstrate that induced genomic instability could also manifest in the progeny of not directly irradiated cells. They showed with their experiments that chromosomal instability occurred in a significantly greater number of clonogenic survivors than, could have been directly hit by radiation. Furthermore, Lorrimore et al. (51) described chromosomal instability in cells protected from radiation exposure by a metal grid, while cells around them had been lethally irradiated.

These findings indicate that an irradiated cell may communicate with its neighbours, non-irradiated cells, and pass on the damaging signals induced by radiation. Furthermore, these observations have an effect on the fate of cells surviving radiation exposure and also indicate that even cells outside the radiation field can display phenotypes similar to irradiated cells (Figure 2.7B).

Every non-irradiated cell can evolve radiation effects through secreted or shed factors by irradiated cells. This is referred to as the 'bystander effect'. Bystander effects can be evoked by either soluble factors secreted from the directly irradiated cell into the media or via gap-junction communication between irradiated and non-irradiated cell (Figure 2.8).

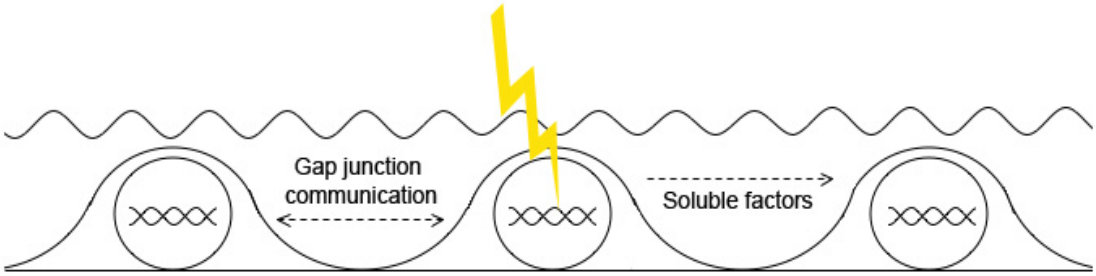

Figure 2.8: Schematic illustration of the bystander cell-cell communication after the irradiation of a single cell. The irradiated cell communicates after the irradiation a signal to non-irradiated cells by either intercellular gap junction communication or the transmission of soluble factors via the cell medium (adapted from (49)).

Communication between cells of a multi-cellular organism takes place in many different ways (52, 53). Hence, it is necessary to understand the transmitted signal of an irradiated cell and how the signal triggers a response in non-irradiated cells in order to understand bystander effects. Several *in vitro* and *in vivo* experiments were performed to shed light on the bystander process. Medium transfer experiments from irradiated cells to non-irradiated cells proof the cell-cell communication via soluble factors in the media (54, 55). The gap junction communication between irradiated and non-irradiated cells was shown in experiments with low fluences of α-particles and appropriate cell lines (56, 57).

These in vitro studies indicate two possible ways of cell-cell communication between a direct irradiated cell and its non-irradiated neighbours. These two-dimensional *in vitro* studies, however, do not provide a realistic multicellular morphology and can, thus, only display the influence of the bystander effect in three-dimensional tissues to a certain way (5). Belyakov at al. (58) performed irradiation experiments with microbeams in three-dimensional normal human tissue systems. These experiments can be not understood as a real *in vivo* assay. However, they do provide the three-dimensional architecture and, thus, the possibility to understand the bystander effect in the three-dimensionality of living tissues. *In vivo* studies in context of the bystander effect in living tissue show that the effect probably involves a genetic component *in vivo*. Experiments with murine bladder epithelium after low dose irradiation showed for example the genotypic difference in calcium signalling and signalling pathways (59).

The majority of bystander responses described above are also observed after direct exposure to ionising radiation (60). DSB have been considered to be the crucial lesion induced by ionising radiation after targeted irradiation. However, Sokolov et al. (61) reported the formation of γH2AX foci also in bystander cells after irradiation with low and high LET ionising radiation. This finding suggests that H2AX phosphorylation is not only an early step after targeted irradiation but also in the bystander response. A similar result was reported by Yang et al. (62). Mothershill et al. (63) analysed a number of DSB repair deficient cell lines according to bystander induced cell killing after medium transfer from irradiated cells. The result was a significant increase in cytotoxity in the repair deficient cell lines as well as in mismatch repair deficient cell lines. These results indicate that bystander induced DNA interaction, which hinders or damages replication ways, may also contribute to DSB formation.

Another experimental approach is the analysis of the relationship between adaptive response and bystander effects. ‘Adaptive response’ is the effect of a priming dose of irradiation on cells, which then respond differently to a subsequent irradiation. Iyer et al. (64) transferred medium from with 10 mGy irradiated cells to cells which were subsequently irradiated with 2 or 4 Gy γ-rays. They observed an increased clonogenic survival. A similar response was observed for α-particle irradiation (65).

2.4 Systemic Dose Response Curves

It is a matter of common knowledge that intermediate and high doses of ionising radiation (e.g. > 100 mSv) have deleterious effects in humans (66). However, the effects are less clear at lower doses. Non-targeted effects, including genomic instability, low-dose hypersensitivity, adaptive response and gene expression, appear to predominate at low doses of low LET radiation. Hence, it is necessary to consider their role *in vivo* and, thus, their relevance in radiation risk and low dose therapy approaches such as fractionated radiotherapy (67). Several models are described here, which outline possible low dose radiation oncogenesis (Figure 2.9). Different endpoints may exhibit different dose-response relations.

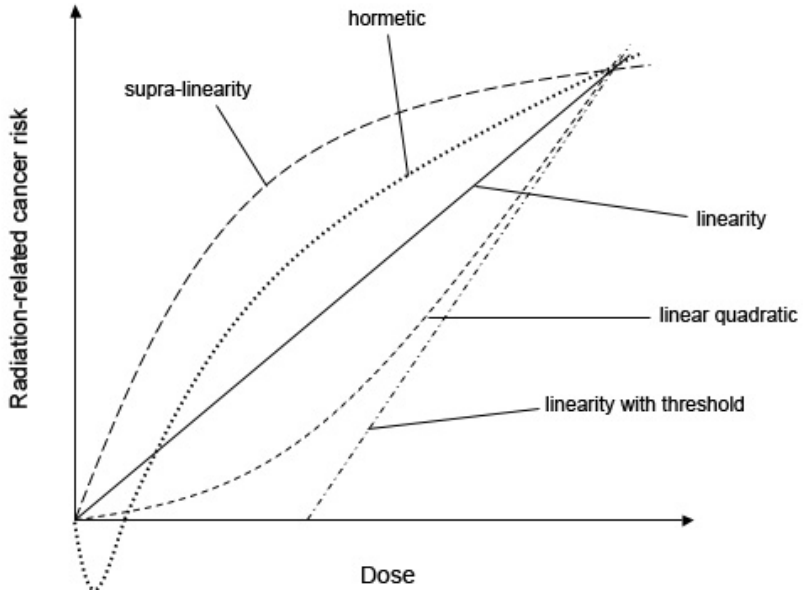

Figure 2.9: Alternative assumptions for the extrapolation of cancer risk in dependence on dose. The linearity assumption describes the estimation of cancer risk at low doses extrapolated from observations at high doses. The supra-linearity curve displays a greater risk than implied by linearity and the linear quadratic curve. The linear quadratic curve shows the assumption in which the low dose risk is depressed. Hormesis describes the beneficial effect at low doses pointed out by the negative region at very low doses. There might also be a threshold, below which there is no appreciable cancer induction (adapted from (66)).

The linearity hypothesis (linear no-threshold model (LNT model)), describes the estimation of the rate of cancer induction at low doses by extrapolation from observations at high doses. This means that the increased risk is proportional to the excess radiation dose without threshold of exposure below which the response ceases to be linear. This hypothesis bases on a large number of epidemiological and laboratory studies (68). Linearity assumptions for lower doses are assumed from the stochastic nature of ionising radiation energy deposition (66). However, there are uncertainties at low doses.

On the one hand, the effect of low doses could be underestimated resulting in a supra-linearity curve. Such a curve progression, however, has been shown in epidemiological and laboratory studies and was interpreted in several ways. First, the existence of small subpopulations within a population was assumed that showed a hypersensitivity to radiation (69). Second, the occurrence of induced radioresistance, where a small priming radiation dose decreases the radiosensitivity to subsequent larger radiation exposure, in terms of adaptive response (70). Third, bystander effects are predominating at low doses (71).

On the other hand the low dose effect could also be overestimated as indicated in the threshold and hormetic curves. Hormesis describes the reduced background incidences of a deleterious endpoint for a given radiation dose. The threshold indicates that below some dose the risk of a particular radiation-induced endpoint is zero (72). It has been reported in some animal experiments that low and intermediate dose of radiation can enhance the lifespan, which can be understood as potential hormesis (73). Further experiments showed that the increased lifespan, if real, is most likely to be associated with a radiation-induced enhancement in the immune system (74) and not with a radiation-related stimulation of DNA repair mechanisms (75). The linear quadratic curve is a good description of acute dose-effect relations for radiation-induced leukaemia (76) and chromosome aberration induction (77). Both have been extensively analysed by using mechanistically motivated models such as linear-quadratic and related approaches (78) as well as modelling competition between different recombinational processes (79).

All these studies show effects that challenge the prevailing model of linearity between radiation effects and dose in cellular systems. They also show that cells, which were not directly hit, respond to irradiation in the same way as directly hit cells in the low dose regime (67). Thus, it is necessary to include bystander effects in the risk assumptions at low doses.

3 Materials and Methods

3.1 Experimental Set-Up

The discrepancies in the analysis of RIF after irradiation necessitate a common approach in data acquisition and analysis. A novel approach outlined in the following chapters demonstrates a possible common approach by using chemically modified multiwell glass slides in RIF experiments. Multiwell slides enable the quantification over a large number of samples in one go, thus, leading to more reproducible and statistical robust results. Furthermore, the experimental process could be accelerated due to the smaller volumes, and the analysis could be performed automatically due to the regular spacing of the multiwells.

3.4.1 Chemically Modified Glass Slides

Two different chemically modified glass slides were used for RIF experiments. For separate irradiations without absorber, chemically modified glass slides with only one hydrophilic spot were used (Munich RIF experiments). These samples were analysed as reference samples for the step-filter irradiation experiments. For the Berkeley RIF experiments (matrix experiments), and the step-filter and fractionated dose experiments of the Munich RIF experiments a chemically modified glass slide with 48 independent hydrophilic spots was used (AmpliGrid, Beckman Coulter GmbH, Krefeld, Germany) (Figure 3.1). The AmpliGrid glass slide is called in the following chapters ‘multiwell slide’.

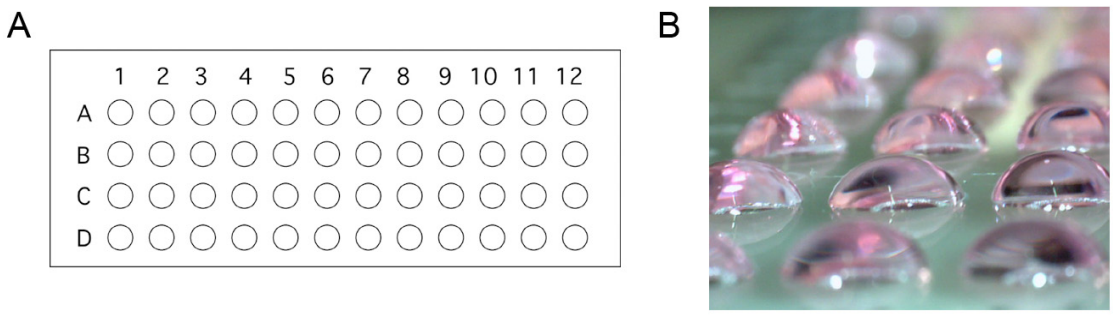

Figure 3.1: Image A is a schematic illustration of the AmpliGrid design with the 48 hydrophilic spots. Image B shows the droplet formation of cell culture media on the surface of the multiwell slide with 48 hydrophilic spots.

Each hydrophilic spot is equivalent to a microwell in which cells can be cultivated under a droplet of $V = 5 - 10\,\mu l$ cell culture medium. The chemical structure on both glass slides consists of Fluor and Epoxysilan. Fluor is known to be very hydrophobic and oleophobic and is used as substrate around the hydrophilic spots to keep the reagents as little droplets on the surfaces. Epoxysilan is hydrophilic and, thus, forms the substrate of the hydrophilic areas. The structuring of the surface is achieved via lithography. The positions of the 48 hydrophilic spots on the AmpliGrid are illustrated in Figure 3.1A and the droplet formation on the surface of the chemically modified glass slide in Figure 3.1B.

3.1.2 BioSpot® Pipetting Robot for Automatic Immunostaining

In the process of experiment optimisation and automation the BioSpot® device (BioFluidix, Freiburg, Germany) was included in the experimental cycle. It is a device for automatic non-contact dispensing of liquids in the range of a few nanoliter up to several microliter.

An automation of the immunostaining process, which is necessary for a visualisation of RIF, requires the ability to dispense all staining reagents at any spot of the multiwell slides. Therefore, a set-up was designed for the staining process of two multiwell slides. It consists of a Teflon block with an implemented resistor controlled heating device. By applying a voltage of around $V = 5\,V$ to the resistors a temperature of $T = 37°C$ can be reached. On top of the heating device is a metal block in contact with the resistor heating device over heat conductive paste. The metal block has two notches for the multiwell slides (Figure 3.2 A). The set-up is mounted on the slide rail of the BioSpot® to be able to reach all spots on the two glass slides automatically. The x-position of the set-up can be adjusted with an accuracy of $\Delta x = \pm 50\,\mu m$ (Figure 3.2 B). The y-position of the set-up is changed by hand over a guide rail included in the set-up. The z-position of the PipeJets is changed over the z-axis to which the PipeJets are attached.

Each PipeJet has a polymeric tube reservoir, which can hold a volume of $V = 50\,\mu l$ for PipeJet 2 and 3 and a volume of $V = 1\,ml$ for PipeJet 1. PipeJet tips and tube reservoirs can be changed easily to ensure a clean staining process. All reagents of the immunostaining process were in Eppendorf tubes in a carrier attached to the Teflon

block right beneath the PipeJets. Each PipeJet can reach five of these 13 Eppendorf tubes.

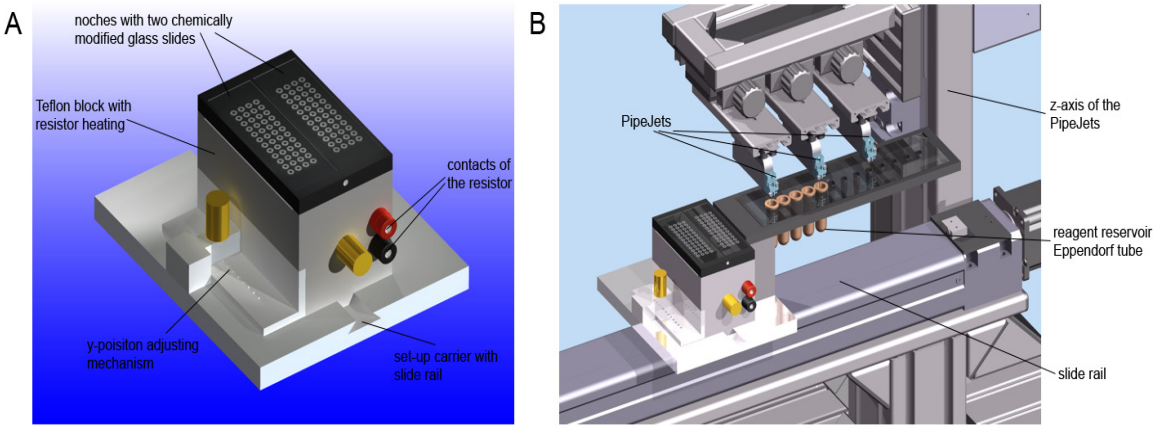

Figure 3.2: CAD images of the enlarged staining set-up for two AmpliGrids (A) and the staining set-up mounted on the slide rail of the Biospot® (B). These CAD images were designed and kindly provided by Gerolf Lieckfeld of the Helmholtz Zentrum München.

Liquids in the polymeric tube of each PipeJet are dispensed by squeezing the tube reservoir via a piston, which results in a fast displacement of the liquid to both sides of the tube. The amplitude of the piezo actuator can control the volume dispensed (Figure 3.3). The description of the BioSpot® and the laboratory intern protocol (LIP) for its use in the immunostaining process are attached in Appendix A.

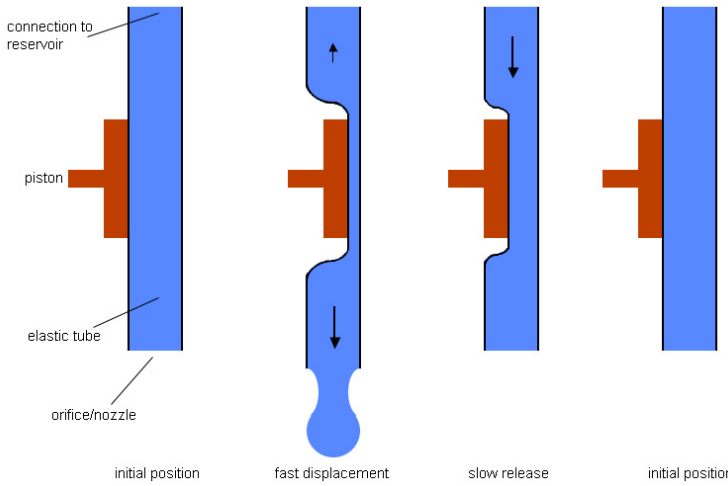

Figure 3.3: BioSpot® dosage principle. Squeezing the polymeric reservoir tube with a piston dispenses the liquid inside the tube. The movement of the piston results in a fast displacement of the liquid to both sides of the tube. The dispensed volume is controlled via a piezo actuator (adapted from (80)).

Due to the provided software, the BioSpot® can be fully computer controlled. The "Batch Mode" allows the programming of a complete sequence, which is processed successively

by the BioSpot®. The batch program written for the immunostaining automation relates to the optimised immunostaining protocol (see chapter 3.6.1) and is attached in Appendix B.

3.2 X-Ray Irradiation

3.2.1 Irradiation Sources

For RIF experiment optimisation and analysis, cells were irradiated with low LET X-ray radiation to induce DNA DSBs and, thus, foci in the cell nuclei.

Cells for immunostaining optimisation and the Berkeley RIF experiments performed at Lawrence Berkeley National Laboratory were irradiated with a CP160 (FAxitron, Lincolnshire, Il, USA) X-ray source running with 160 kV and 6,3 mA. Dose rates measured during irradiation were 22,02 mGy/s (1000 and 2000 mGy), 10,13 mGy/s (150 and 400 mGy), and 1,5 mGy/s (0 and 50 mGy). Dosimetry was performed using ion chamber dosimeters (Victoreen, Moedling, Austria).

Samples of the Munich RIF experiments as well as the living cell experiments were irradiated with a TR 300f X-ray machine (Siemens-Reiniger-Werke AG, Erlangen, Germany) at the Helmholtz Zentrum München. The distance between the samples and the X-ray machine was 14 cm in all experiments. The X-ray machine was operated at 155 kV and 20 mA, and had a pre-filtration of 4 mm Aluminium, thus, leading to a relative does rate of 11,9 mGy/s at a distance of 14 cm. Dose measurements were performed with a dose area product meter type Diamentor (PTW, Freiburg, Germany) and a Diamentor II (PTW, Freiburg, Germany).

3.2.2 Radiation Absorbing Experimental Chamber

Variations in irradiation dose are usually achieved by changes in the irradiation time as e.g. for the separate dose irradiation experiment samples. An experimental set-up with step-filter absorption was designed for the multiwell slides for the irradiation of multiple samples with different doses in one irradiation step (Figure 3.4A). It is possible to perform a wide range of experiments in one go with this kind of irradiation set-up. It leads to a faster processing and analysis of irradiation experiments, thus, resulting in better statistics.

For the irradiation of samples with varying doses at the same time a successive absorption of the ionising radiation is necessary. Thus, a Pb stair was mounted on top of the lid of a Petri dish ($d = 10\,cm$). Pb is known to absorb X-ray radiation effectively. Thus, only thin layers of Pb were necessary to achieve an observable change in the X-ray dose transmitted. With Pb it is also possible to easily achieve a total blocking of the radiation for sham irradiated samples.

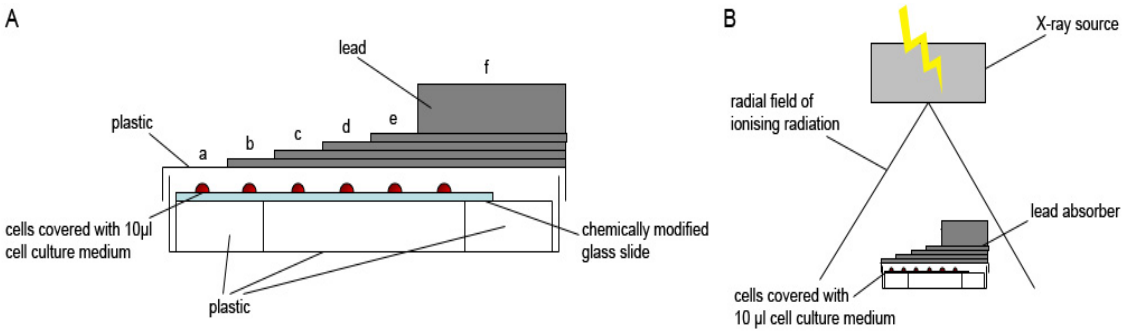

Figure 3.4: Image A is the schematic illustration of the experimental set-up for the step-filter and fractionated irradiation experiments. A Pb stair with increasing Pb thickness ensures a variation in the doses applied to the cells in one irradiation step. The whole set-up with the Pb absorber and the cells cultivated on the multiwell slide was placed right underneath the radiation source as illustrated in B. The illustrations are not to scale.

Table 3.1 shows the dimensions of the lead stair in context of the through absorption induced dose attenuation coefficient and which row of the multiwell slide was shielded by the single steps. To avoid scattering effects and to ensure a clear difference between the different irradiation doses, cells were only cultivated on every second row. Furthermore, the multiwell slide was placed on top of the lids of small Petri dishes resulting in a relative distance of $d_{SL} = 5\,mm$ between the sample surface and the bottom of the lead stair. The centre of the irradiation source was right above row 7 of the multiwell slide as indicated in Figure 3.4 B.

Table 3.1: Dimensions of the lead stair in context of dose attenuation coefficient. It is also indicated which row is shielded by which lead step.

Row	*Attenuation Coefficient*	*Step-filter*	*Pb Thickness [mm]*	*Pb Length [cm]*	*Pb Width [cm]*
1	*0*	*a*	*-*	*-*	*-*
3	*4,1*	*b*	*0,25*	*7,3*	*5,5*
5	*9,9*	*c*	*0,4*	*6,4*	*5,5*
7	*18,2*	*d*	*0,6*	*5,5*	*5,5*
9	*87,3*	*e*	*1,1*	*4,6*	*5,5*
12	*100*	*f*	*7,1*	*3,7*	*5,5*

3.2.3 Theoretical X-ray Photon Spectra Calculations

For X-ray radiation passing matter an exponential decrease in radiation intensity is observed proportionally to the absorbing material thickness. Furthermore, the decrease in intensity strongly depends on the absorbing material and bases on the three interaction effects, photoelectric effect, Compton scattering, and pair production (Figure 3.5A). More radiation with lower energy is absorbed with increasing Pb thickness, while photons with higher energies can still pass the Pb shielding (Figure 3.5B). This results in different radiation qualities behind the Pb stair and possibly different induced effects in the cells. Thus, the use of a Pb stair to partially block the X-ray radiation requires an understanding and knowledge of the effect of the Pb on the emission spectra.

Therefore, the emission spectra for each Pb filtration were calculated and kindly provided by Helmut Schlattl of the Helmholtz Zentrum München with the program SpekCalc (81). This software program was designed primarily for use in a medical physics context. It is possible to model with SpekCalc a wide range of tube potentials and anode angles. Before spectra calculation, the tube potential in kV, the take-off/anode angle and the amount of filtration are specified. After the calculation a central-axis spectrum is presented. Several beam qualifiers are provided, like the 1st and 2nd half value layer. Furthermore, also the mean energy of the spectrum E_{mean}, and the effective energy E_{eff} in keV are shown, as well as the estimated bremsstrahlung and characteristic radiation contributions to the tube output. It is also possible to select the filtration before emission spectrum calculation.

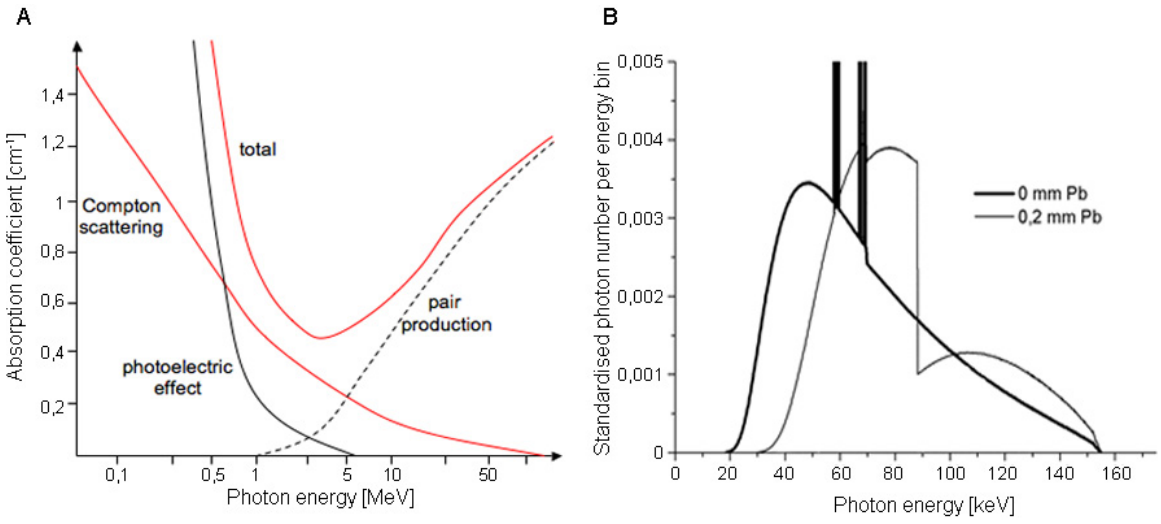

Figure 3.5: Illustration of the absorption coefficient of Pb in dependence of the photon energy (A). The total absorption consists of the occurring photoelectric effect, Compton scattering as well as the pair production (adapted from (82)). Partial shielding of the X-ray radiation via Pb leads to a shift to higher photon energies with increasing Pb thickness (B).

X-ray emission spectra for the TR 300f X-ray machine (Siemens-Reiniger-Werke AG, Erlangen, Germany) used in the step-filter dose and fractionated irradiation experiments were calculated with this program. The material of the anode of the X-ray machine was Wolfram, the applied anode voltage was 155 kV and a current of 20 mA. The angle of the anode was estimated to be 45° and there was a 4 mm Aluminium prefiltration. From these values, it was possible to calculate the emission spectra without Pb filtration. In order to be able to calculate the emission spectra with an additional, Pb filtration the attenuation of Pb had to be included in the calculation.

The attenuation of each energy-bin was calculated with an IDL program written by Helmut Schlattl of the Helmholtz Zentrum München. This program calculates the attenuation coefficient from the NIST database (83). Thus, it was possible to calculate the emission spectra for each Pb step depending on the thickness of the Pb and the distance from the X-ray anode.

3.3 Microscopy

The past decade has witnessed an enormous growth in the application of optical microscopy for micron and submicron level investigations in a wide variety of disciplines (84). Advances in sectors like fluorescent labels, digital imaging and analysis have enabled researchers to acquire quantitative measurements quickly and efficiently.

The resolution of a microscope is limited by diffraction effects. The numerical aperture (NA) is the most important parameter for the optical resolution of a microscope. It can be calculated from the aperture angel α, which is half the angle of the objective lense aperture, and the refraction index n of the media between object and lense (85).

$$NA = n \cdot \sin\alpha \tag{3.1}$$

The optical resolution D of an objective can be calculated as indicated in equation 3.2 from the numerical aperture NA and the wavelength λ of the emission light.

$$D = \frac{\lambda_{em}}{NA} \tag{3.2}$$

D can be understood as the distance between two structures, which can just be separated in the microscopic image.

3.3.1 Phase Contrast and Fluorescence Microscopy

The imaging of three-dimensional objects like cells via microscopy can be achieved in several ways depending on the pre-treatment of the cells.

Phase contrast microscopy is used for unstained cells, which have no absorbing structure but different indices of refraction. The refracted rays of light are usually retarded at ¼ wavelength compared to the direct light passing through or around the specimen unaffectedly. This shift in wavelength is not visible for the eye. By inserting a phase plane into the optical path the shifted wavelength is accelerated at another ¼ wavelength, which results in a total shift of ½ wavelength (Figure 3.6A). Thus, the direct and diffracted rays of light arriving at the eyepiece produce destructive interference. Thus, the details of an image appear darker against a lighter background (84).

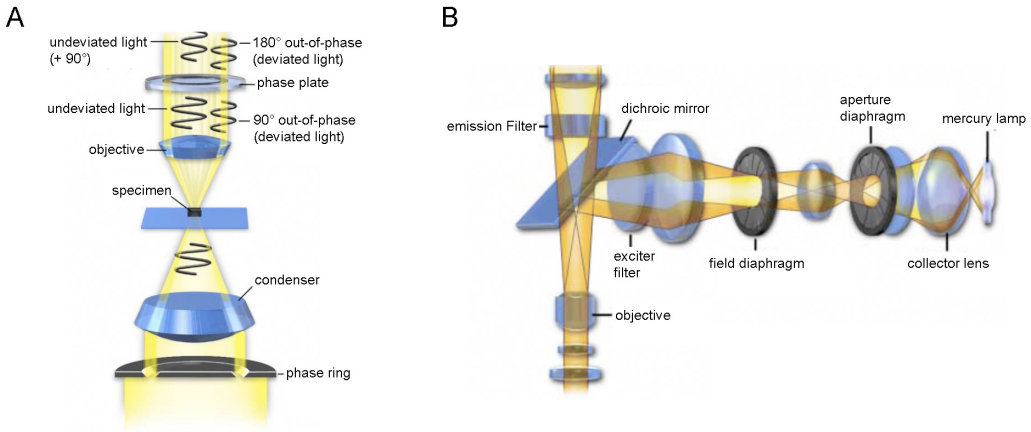

Figure 3.6: Schematic illustration of the phase contrast microscopy (A) and reflected light fluorescence microscopy (B) principle. Light passing through the condenser is in phase contrast microscopy, first concentrated on the specimen. In the further process, the undeviated light is accelerated by the phase plate resulting in a total shift of 180° between deviated and undeviated light and, thus, destructive interference. The light emitted from a mercury lamp in fluorescence microscopy is first concentrated from the collector lens before passing the aperture and field diaphragm. Only the desired excitation wavelength passes the exciter filter, which then illuminates the specimen. The light emitted from the specimen passes back through the objective and dichroic mirror before being filtered by the emission filter since it has a longer wavelength (84).

Fluorescent cell samples on the other hand are imaged via fluorescence microscopy. The fluorescing light emitted from the sample has a longer wavelength compared to the excitation light. This shift is called Stokes shift. The basic rule for fluorescence microscopy is to permit excitation light to irradiate the specimen and to separate the weaker emitted fluorescent light from the brighter excitation light over appropriate filters inserted in the optical path (84). This procedure ensures that only the emission light reaches the eye or the detector. As a result, fluorescing areas shine against a darker

background. Figure 3.6B shows the schematic diagram of reflected light fluorescence microscopy.

3.3.2 Confocal Microscopy

The microscopic analysis of fluorescently labelled cell samples has to deal with several optical side effects interfering with the image quality. A broadening of small point-like structures induced by light diffraction makes it difficult to determine the actual size of the object and to distinguish between different structures. Furthermore, cell samples are thicker than the focal plane and by using a mercury lamp and, thus, illuminating the whole sample in light a lot of background fluorescence as well as out-of-focus fluorescence are detected apart from the actual object fluorescence, resulting in blurred images. The confocal microscopy is one technical approach to optimise the acquisition of three-dimensional samples.

Confocal microscopy comprises the serial point-wise analysis of samples compared to conventional fluorescence microscopy where the object-to-image transformation takes place simultaneously. One or more lasers are used as light sources, which enable point-wise illumination and detection. The focused laser beam is scanned across the specimen by deflection in x and y direction by means of two galvanometric scanners. The crucial feature of a confocal microscope is the confocal aperture, the so-called pinhole. The pinhole diameter is variable and it is added in a plane conjugate to the plane of the intermediate image and hence the object plane of the microscope. Thus, only light passing the pinhole can be detected.

If both the point illuminated and the point observed are located in conjugate planes, the result is called a confocal beam path (Figure 3.7). For samples thicker than the focal plane, it is then possible to get rid of fluorescence from above or below the focal plane, resulting in focused images.

The resolution in the case of a large pinhole diameter describes the separate visibility of points during the scanning process, both laterally and axially. Figure 3.8 illustrates the important components necessary for the analysis of a point-like structure in a cell nucleus via confocal microscopy. Structures in the object plane are displayed in the image plane. A point-like isotropically shining object generates a three-dimensional intensity distribution in the image plane, the so-called point-spread function due to geometrical optics and diffraction effects. The dashed line of the object in the image plane marks the area where the intensity reaches only half of the maximal intensity value.

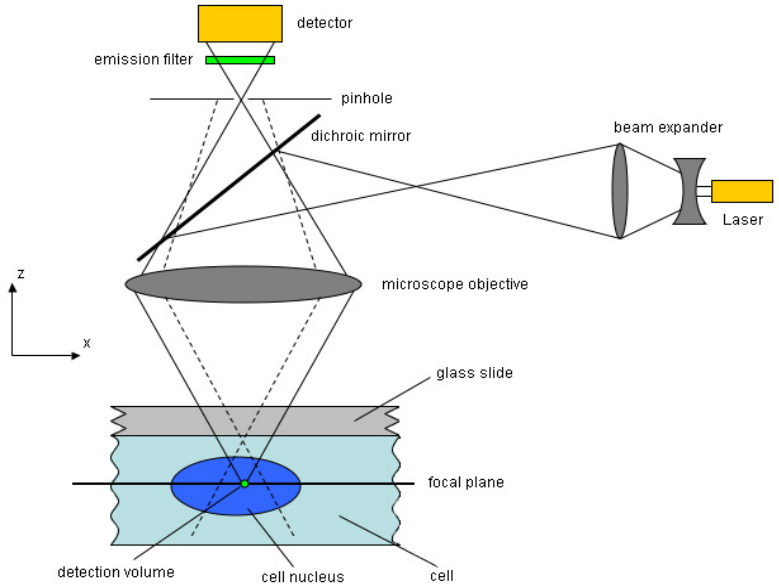

Figure 3.7: Beam path of a confocal microscope. The microscope objective is used to focus a laser beam onto the specimen for fluorescence excitation. The radiated fluorescence is then collected by the objective and directed onto the detector via a dichroic beamsplitter. An emission filter inserted into the beam path filters the wavelength of interest from the rest. A pinhole is located in front of the detector on a plane conjugate to the focal plane of the objective. Thus, light coming from planes above or below the focal plane is out of focus and cannot pass the pinhole and therefore does not contribute to the final image (adapted from (86)).

The image, which is blurred due to diffraction effects, has to be calculated back into the object area in order to be able to make predictions about the optical resolution of the analysed object. These calculations result in an object with following lateral and axial dimension in terms of the full width at half maximum (FWHM) (86)

$$FWHM_{lateral} = \frac{0{,}51 \cdot \lambda_{exc}}{NA} \quad bzw. \quad FWHM_{axial} = \frac{1{,}77 \cdot n \cdot \lambda_{exc}}{NA^2} \tag{3.3}$$

The only difference between these two equations and the equations for conventional imaging is the wavelength (87). The optical resolution of a confocal microscope depends on the wavelength of the illuminating light compared to the conventional case where the resolution exclusively depends on the emission wavelength.

These features of confocal microscopy reduce image degrading out-of-focus information, thus, resulting in defined images. Furthermore, it is possible to produce serial sections of three-dimensional objects with a confocal microscope, so-called z-stacks. This enables the acquisition of information from the whole sample by sectioning of the sample over incremental changes in the z-position of the focus. The image information acquired for all sections is restricted to a well-defined plane due to the reduction of fluorescence bleed through from other planes. Once a z-stack of a specimen

is acquired it can be processed into a three-dimensional representation of the object (86, 88).

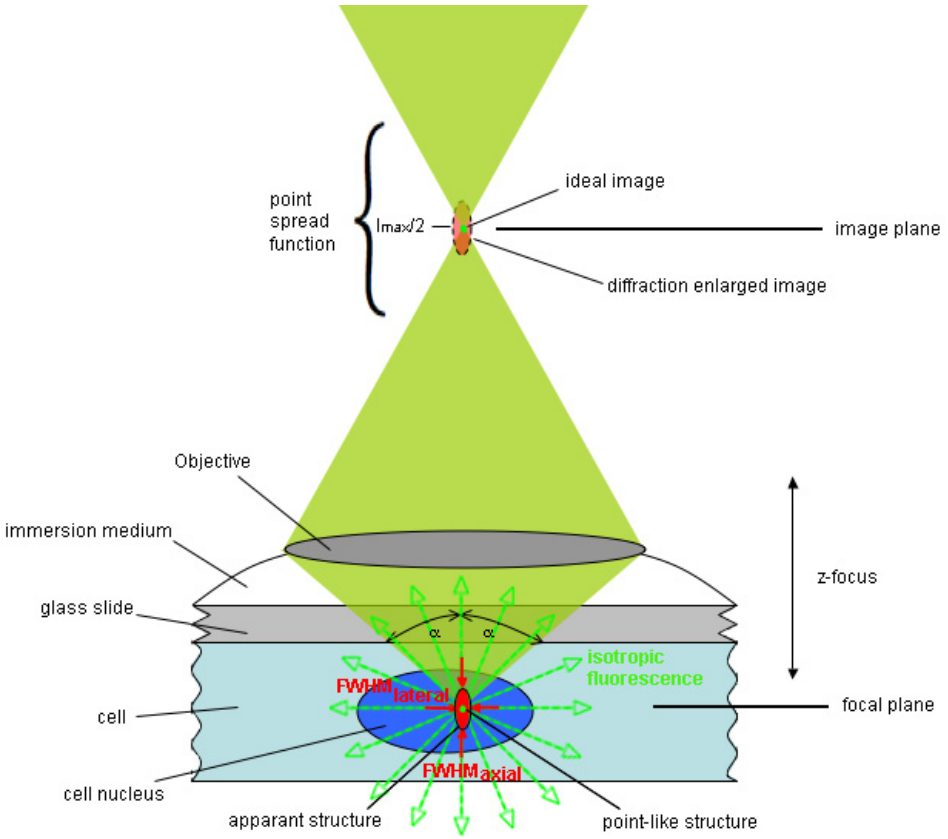

Figure 3.8: Illustration of the lateral and axial resolution of a fluorescence microscope when imaging a point-like structure inside a cell nucleus. The imaging of a point-like structure with a fluorescence microscope results in a three-dimensional intensity distribution due geometrical optics and diffraction effects. The intensity distribution is called point-spread function, which is only shown schematically in the drawing (adapted from (89)).

3.3.3 ApoTome®

The imaging of three-dimensional samples is not only possible with confocal microscopes but also with the ApoTome mode included in fluorescence microscopes (Carl Zeiss Jena, Germany).

For the ApoTome® mode a grid structure is inserted into the light path, which is then visible in the object plane. The grid structure is included in the imaging process to reduce the stray light information in the focal plane. Therefore, the grid is moved across the sample plane and at each grid position images are acquired (Figure 3.9A-C, the grid shift is indicated by the blue line). These images (interference structures) are then combined via a mathematical algorithm, thus, resulting in a background reduced image

of the specimen (Figure 3.9D). Out of focus information only shows blurred grid lines (Figure 3.9A, see arrow) and, hence, is subtracted from the final image.

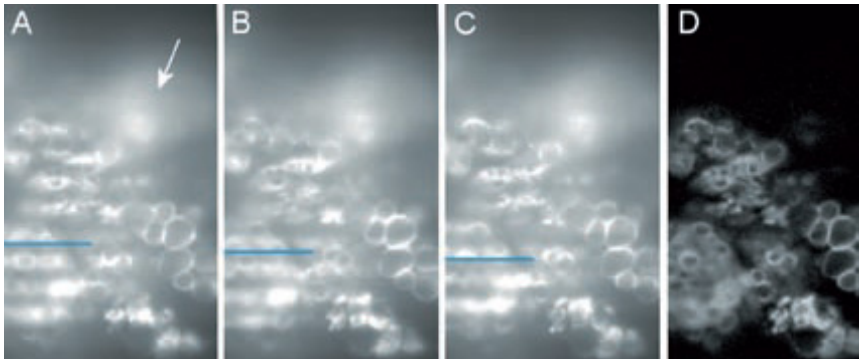

Figure 3.9: Schematic depiction of the grid projection in a fluorescence specimen. Images A-C are raw images with different grid positions indicated through the blue line. Image D is the calculated optical section through the specimen (90).

The calculated image of the focal plane is an optical section of the specimen with no blurring in the structures and elevated contrast. Thus, it is possible to acquire z-stacks of the sample by including a z-step motor in the fluorescence microscope.

3.4 Tissue Culture

In the context of natural science, it was of general interest to cultivate living cells and tissue outside of an organism for further investigations. In 1885, Wilhelm Roux was able to cultivate embryonic chicken cells in salt solution for several days. In 1913, Alexis Carrel showed that cells could also be cultivated for a longer time span when they were feeded and treated asceptic (91). In the following years, cell culture media, growth factors and conditions were developed further and it was possible to cultivate more and more different cell lines.

Today, cell culture is mostly used in science to investigate metabolism, division and other cell processes within the scope of fundamental research. Cell cultures can be understood as *in vitro* test systems for living organisms. Thus, cell culture is a valuable tool for the investigation of DNA damage induced in cells by ionising radiation on a two-dimensional basis.

3.4.1 Handling of Cells

Table 3.2 is an overview of the different cell experiments, the cell cultures and cell culture medium used as well as medium additives.

Table 3.2: Overview of the different cell culture experiments

Experiment/Aim	Cell Type	Source/Supplier	Culture Medium	Medium Additives	Cell Cultivation
Optimisation of the Immunostaining Process	MCF10A, human mammary epithelial cells	Bought from ATCC the global bioresource center	MEMB medium (Invitrogen Inc., Carlsbad, CA)	2 ml of Bovine Pituitatry hormone (13mg/ml) 0,5 ml hydrocortisone (0,5 mg/ml) 0,5 ml hEGF (10 µg/ml) 0,5 ml insulin (5 mg/ml) 10 µl cholera toxin (100 ng/ml) (Invitrogen Inc., Carlsbad, CA)	Cell were cultivated in Permanox plastic 8-well Lab-Tek chamber slides (Nalge Nunc International Corp., Rochester, NY)
Berkeley RIF Experiments	HCA2, human foreskin diploid fibroblasts MCF10A, human mammary epithelial cells	HCA2 cells were kindly provided by Dr. Judith Campisi, LBNL, Berkeley, CA MCF10A cells were bought from ATCC the global bioresource center	Minimum essential medium (MEM) alpha (Invitrogen Inc., Carlsbad, CA) MEMB medium (Invitrogen Inc., Carlsbad, CA)	10 % fetal bovine serum (Invitrogen Inc., Carlsbad, CA) 2 ml of Bovine Pituitatry hormone (13mg/ml) 0,5 ml hydrocortisone (0,5 mg/ml) 0,5 ml hEGF (10 µg/ml) 0,5 ml insulin (5 mg/ml) 10 µl cholera toxin (100 ng/ml) (Invitrogen Inc., Carlsbad, CA)	Cultivation on the 48 hydrophilic spots of the multiwell slide (AmpliGrid, Beckman Coulter GmbH, Krefeld, Germany)

Munich RIF Experiments	BJ1-hTERT, human foreskin fibroblasts HeLa cells derived from human cervical cancer	Both cell lines were kindly provided by Dr. Guido Drexler, LMU, München, Germany	Both cell lines were cultivated in Dulbecco's MEM Medium (Biochrom AG, Berlin, Germany)	10% fetal bovine serum (Biochrom AG, Berlin, Germany)	Cultivation on chemically modified glass slides with a single hydrophilic spot and slides with 48 hydrophilic spots (AmpliGrid, Beckman Coulter GmbH, Krefeld, Germany)
Living Cell and Live Cell Imaging	L929, mouse connective tissue fibroblasts L929, mouse connective tissue fibroblasts transfected with green fluorescent protein plasmid	Cell culture stock brought form the LMU Munich by PD Stefan Thalhammer	Both L929 cell lines were cultivated in RPMI medium (Biochrom AG, Berlin, Germany)	10% fetal bovine serum (Biochrom AG, Berlin, Germany)	Cultivation of the cells in 12-well-dishes (NUNC, Roskilde, Denmark)
	BJ1-hTERT, human foreskin fibroblasts HeLa H2B cells derived from human cervical cancer and transfected with green fluorescent protein plasmid	Kindly provided by Dr. Guido Drexler, LMU, München, Germany Kindly provided by Dr. Kourosh Zolghadr, LMU, München, Germany	BJ1 hTERT and HeLa H2B cells were cultivated in Dulbecco's MEM Medium (Biochrom AG, Berlin, Germany)	10% fetal bovine serum (Biochrom AG, Berlin, Germany)	Cultivation of the cells in 12-well-dishes (NUNC, Roskilde, Denmark)
Recultivation	L929, mouse connective tissue fibroblasts L929, mouse connective tissue fibroblasts transfected with green fluorescent protein plasmid	Cell culture stock brought from the LMU Munich by PD Dr. Stefan Thalhammer	Both L929 cell lines were cultivated in RPMI medium (Biochrom AG, Berlin, Germany)	10% fetal bovine serum (Biochrom AG, Berlin, Germany)	Cells were cultivated in DuplexDish 35 (D) (Carl Zeiss, Jena, Germany) or in and µ-slides (Ibidi GmbH, Martinsried, Germany)

General precautions were undertaken to maintain sterile conditions in tissue culture. All experiments were prepared under a flow hood, which was sterilised with UV light for 20 min before and after its use. The bench under the hood was cleaned with 70% ethanol before working with cells, and again after finishing the preparations. The chemically modified glass slides were also rinsed with ethanol before use and sterilised for 20 min under UV light. All cell cultures were cultivated at 37°C with 95% humidity and 5% CO_2 in a cell incubator. The lab intern protocol for cell splitting is attached in Appendix C.

Cells used for the immunostaining optimisation, the Berkeley and Munich RIF experiments were always cultivated to a confluent layer in the corresponding cell culture well. To determine cell growth rates and to see cellular behaviour in cell layers, different cell lines were plated with a certain number of cells in 12-well-dishes. Thereafter, the average number of cells was determined every day over a triple determination until the cell layer reached a total confluence in the wells. Furthermore, optical images of the cells were taken every day to follow their growth with a 10x magnification. Changes in the cell growth rate for cellular co-cultures with and without irradiation were analysed by plating different cell lines in the same wells in different cellular concentrations.

3.4.2 Irradiation of the Cellular Samples

Cells were not synchronised for both experimental approaches, the static and dynamic. Cycling cells represent living organisms better than synchronised cell, since cells in an organism have all their own rhythms of cell division and replication. Thus, the effects evoked by ionising radiation, in this case X-rays, in cells can be better analysed and compared to cells in organisms, for cycling cells.

Irradiation of Cells for Immunostaining Optimisation and Berkeley RIF experiments

To optimise the immunostaining protocol of radiation-induced foci, identical dose- and time-response experiments were performed with cells exposed to 1 Gy of X-rays. Cells were fixed after 30 min repair time post irradiation in order to get a maximum of radiation-induced foci as previously shown (10).

For the Berkeley RIF experiments, where cells were cultivated on all hydrophilic spots of a single multiwell slide, one slide was irradiated with two doses. Therefore, half of the multiwell slide was shielded with a Pb block with a thickness of $h = 1\,cm$ and the other half was irradiated with a certain dose. Following the first irradiation, the Pb shielding was removed and the multiwell slide was irradiated a second time with another

dose resulting in the following radiation dose pairings on one slide: 0 mGy and 50 mGy, 150 mGy and 400 mGy, 1000 mGy and 2000 mGy. To minimise backscattering, the samples were placed on top of a Pb block with a thickness of $h = 1\,cm$. After the second irradiation cells were fixed at different repair time-points post irradiation for each dose (1 min, 5 min, 10 min, 20 min, 40 min, 80 min). The composition of the Berkeley RIF experiment with different dose- and time-responses is indicated in Figure 3.10.

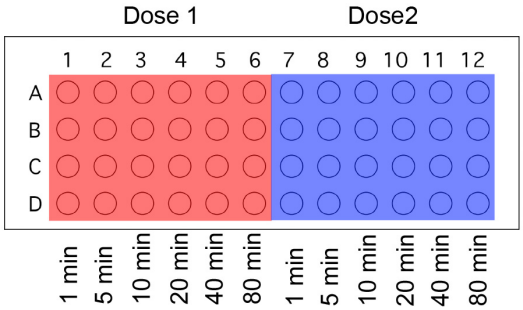

Figure 3.10: Schematic illustration of the multiwell slide used in the Berkeley RIF experiments with the division in two dose areas each with six fixation time-points.

Fixation of the cells took place on a thermal pack with a temperature of $T = 37°C$. During fixation and between the fixation of the different repair time-points the samples were returned to the incubator at a temperature of $T = 37°C$. After all samples had been fixed the RIF were stained following the optimised immunostaining protocol and the samples were analysed.

Irradiation of cells used in the Munich RIF experiments

A Pb stair was mounted on top of a multiwell side to further improve and accelerate dose- and time-response experiments, i.e. the Berkeley RIF experiments. Thus, it was possible to irradiate one single slide with six different doses in one go. A Pb block with a thickness of $h = 0{,}5\,cm$ was placed underneath the samples during irradiation of all Munich RIF experiments to avoid backscattering.

For the investigation on the question whether the partial Pb shielding has an influence on the effects evoked in cells, separate dose irradiation experiments were performed with the chemically modified glass slide with one single hydrophilic spot. The difference in irradiation dose was achieved over variations in the irradiation time. Following irradiation, the samples were fixed after certain repair time-points as indicated in Table 3.3.

For the step-filter irradiation experiments, each multiwell slide with the Pb stair on top (see chapter 3.2.2) was irradiated once with a dose of 1000 mGy, which resulted

in six different irradiation doses through the successive absorption of the lead. Samples of each dose were fixed after certain repair time-points resulting in 24 different samples (see Table 3.3).

Table 3.3: Irradiation dose and repair time-points for the Munich RIF experiments

Experiment	**Exposures**	**Time-Points post IR**
Separate Irradiation	0 mGy, 10 mGy, 50 mGy, 100 mGy, 250 mGy, 1000 mGy	5 min, 30 min, 2 h, 6 h, 24 h
Step-Filter Irradiation	0 mGy, 10 mGy, 50 mGy, 100 mGy, 250 mGy, 1000 mGy	5 min, 30 min, 1 h, 2 h, 4 h, 6 h, 24 h
Fractionated Irradiation	0 mGy + 1000 mGy, 10 mGy + 1000 mGy, 50 mGy + 1000 mGy, 100 mGy + 1000 mGy, 250 mGy + 1000 mGy, 1000 mGy + 1000 mGy	5 min, 30 min, 1 h, 2 h

For the fractionated irradiation experiments, cells were first irradiated like the samples in the step-filter irradiation experiments resulting in varying doses, and then irradiated a second time with an over all dose of 1000 mGy. The second irradiation of the multiwell slide was performed after different time intervals following the first irradiation to trigger different repair settings (0 min, 30 min, 1 h and 2 h). Table 3.3 indicates the sum of doses for the first and second irradiation as well as the repair time-points at which the cells were fixed.

All samples of the Munich RIF experiments were immunostained after fixation and the RIF were analysed.

Irradiation of the Living Cell Experiments

Irradiation of the living cell experiments was performed in different approaches. Either the whole 12 well plates were irradiated or only one cell line of the co-cultures was irradiated and added to the other non-irradiated cells.

The homogenous cell cultures were irradiated completely and returned to the incubator after the irradiation. For the co-cultures, two sets of experiments were performed. In one approach the GFP transfected cells, HeLa H2B and L929 EGFP mouse fibroblasts, were added to the wells to the non-transfected BJ1-HTERT human and L929 mouse fibroblasts and the whole 12 well plates were irradiated. In the other approach, the GFP transfected cells were first irradiated and then added to the not-irradiated and non-transfected cells in a certain number. Therefore, the transfected cells were trypsinised[6] and the cell number per ml was determined before irradiation. All co-cultures were returned to the incubator after irradiation at a temperature of $T = 37°C$ and were left to grow.

Furthermore, the growth of cells was analysed when the BJ1-HTERT human fibroblasts and the non-transfected L929 mouse fibroblasts were left to reach a confluence of around 80%. A certain number of not-irradiated or irradiated GFP transfected cells was added into the wells. The whole 12-well-plates were irradiated for not-irradiated GFP cells, which were added to the non-transfected cells. All samples were returned to the incubator and left to grow.

The irradiation of all living cell experiments included irradiations with 0 Gy (Sham irradiation), 10 mGy, 50 mGy, 100 mGy, 250 mGy and 1000 mGy.

3.4.3 Recultivation of Living Cells

Recultivation of living cells is used as a tool for the analysis of certain cells of a cell culture via isolation of the cells of interest. It bases upon the laser based microdissection principle, where a UV-A laser, here a Palm nitrogen laser ($\lambda = 337\ nm$) (Carl Zeiss, Jena, Germany), is focused through the objective lense of a microscope and is used for cutting the carrier membrane on which cells are growing. For the transfer of the isolated cells into new wells, two different experimental approaches were performed: the transfer of the isolated cells via pressure catapulting (92) (Figure 3.11) or via low pressure adsorption (93) (Figure 3.12).

For cell culture, special wells with PEN foil as bottom were used. The PEN foil was the carrier membrane for the cells during the isolation process. The pressure catapulting required the use of DuplexDish (Carl Zeiss, Jena, Germany) for cell culture. Its bottom consists of two foils, a 2 µm PEN foil, which is the carrier membrane and a

[6] Dissolution of adherent growing cells from the cell culture flask bottom via Trypsin, a serine protease.

20 µm Teflon membrane, which avoids loss of liquid during the isolation process. For the low-pressure adsorption approach a µ-Slide I slide (Ibidi GmbH, Martinsried, Germany) was used. This slide has only a 2 µm PEN foil as bottom, which is the carrier for the cells. The medium was removed from the cell culture devices before the isolation processes. Thus, only a thin liquid layer remained on top of the cells. The laser beam was controlled during the isolation process via joystick movement.

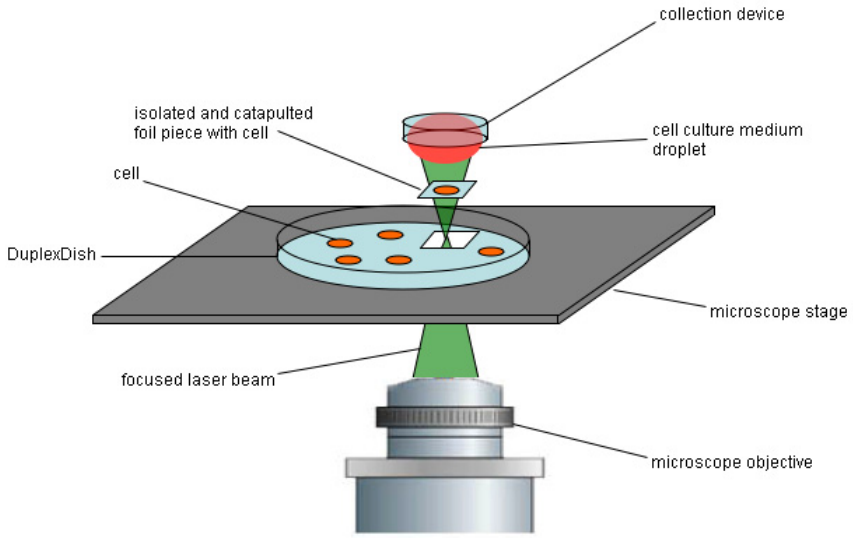

Figure 3.11: Schematic illustration of the laser microdissection and catapulting principle. Adherent growing cells cultivated in a DuplexDish are isolated with a laser beam focused through the microscope objective. Isolated foil pieces with cells are catapulted over a single laser impulse into the air and captured in a collection device filled with fresh cell culture medium.

For the pressure catapulting approach it was necessary to install a collection device with a medium droplet right above the objective and the isolated piece (Figure 3.11). After isolation of the cells of interest, the isolated piece was catapulted with a single laser impulse into the collection device by increasing the laser energy to its maximum. The collection device with the isolated piece was then rinsed with fresh medium over a new cell culture well and the isolated cells were left to grow.

To minimise the stress on the cells for the low-pressure adsorption approach, the µ-slides were turned upside down. Thus, the adsorption head was only in contact with the carrier membrane and not the cells (Figure 3.12). Right before the complete isolation, the low-pressure was turned on, and the isolated piece was adsorbed to the adsorption head. After adsorption the isolated piece was immediately released into a new culture well by turning of the low-pressure of the system. This was done to minimise the stress on the isolated living cells. The culture well with the isolated cells was then filled with fresh cell

culture medium and the cells were left to grow. A LIP for the isolation of single particles via a UVA laser and the low-pressure transfer system are attached in Appendix D.

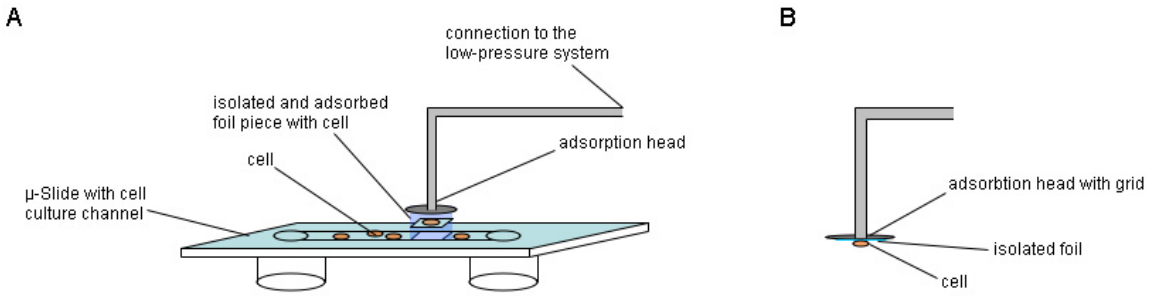

Figure 3.12: Schematic illustration of the isolation and adsorption process (A) and the enlarged schematic illustration of the adsorption head with an adsorbed foil piece with a cell (B). Cells were cultivated in the channel of a µ-Slide, which was turned upside down before the isolation process. While cutting the last connection between the isolated foil piece and the slide the low-pressure in the adsorbing system was turned on and the isolated piece was adsorbed at the grid of the adsorption head.

3.5 Green Fluorescent Protein Transfection

3.5.1 Green Fluorescent Protein Plasmid

In the margin of its umbrella the jellyfish *Aequorea victoria* possesses a green fluorescent protein (GFP, 27 kDa), which serves as light emitter in the bioluminescence reaction of the animal. The GFP consists of 238 amino acid residues in a single polypeptide chain. It produces a green fluorescence with λ_{max} = 508 nm when excited with long ultraviolet light pulses. GFP is one of the best-known proteins in biochemistry and cell biology and is used widely as a reporter protein for monitoring gene expression (94). On 10th October 2008 Martin Chalfie, Osamu Shimomura and Roger Y. Tsien were awarded the Nobel Prize in chemistry for their discovery and development of the green fluorescent protein.

For the use as a reporter protein, the GFP has to be first brought inside the cell via plasmids, so-called vectors. Plasmids are circular extra chromosomal DNA molecules and have the ability to replicate independently from the chromosomal DNA. These small circular double stranded DNA structures occur naturally in bacterial cells. These plasmids can be genetically engineered, so that they harbour a gene of interest under the control of an appropriate regulatory element (promotor), for the expression in a certain species, here mammalian cells.

Plasmid vectors used here for transfection were the pEGFP-N1 (clontech) vector and the pMC-16 EGFP vector (95, 96). Both are vectors encoding a red-shifted variant of wild-type GFP, which has been optimised for brighter fluorescence and higher

expression in mammalian cells. Furthermore, HeLa cells transfected with H2B-GFP were also used in experiments. H2B is a histone, which leads to a green fluorescene of the cell nucleus when combined with GFP.

3.5.2 Transfection of Adherent Cells

GFP is a well known live cell reporter in cell biology as mentioned above. In context of cell growth and recultivation experiments, it was necessary to be able to distinguish between different cells. Thus, cells had to be transfected with the GFP plasmid.

One day before transfection, cells were split and seeded in 6-well-dishes (NUNC, Roskilde, Denmark) in 2 ml appropriate growth medium. The cells had a confluence of 60 - 80% on the day of transfection[7]. Prior to the transfection 18 µg of plasmid DNA (GFP-plasmid) were diluted with cell growth medium containing no serum or antibiotics to a total volume of 90 µl[8]. The dilution was briefly vortexed for optimal mixing. Subsequently 120 µl SuperFect Transfection Reagent (Qiagen, Hilden, Germany) were added to the DNA solution and the solution was mixed by pipetting five times up and down. Following a 5 - 10 min incubation step at room temperature, to allow transfection-complex formation, 6 ml fresh growth medium were added to the transfection solution.

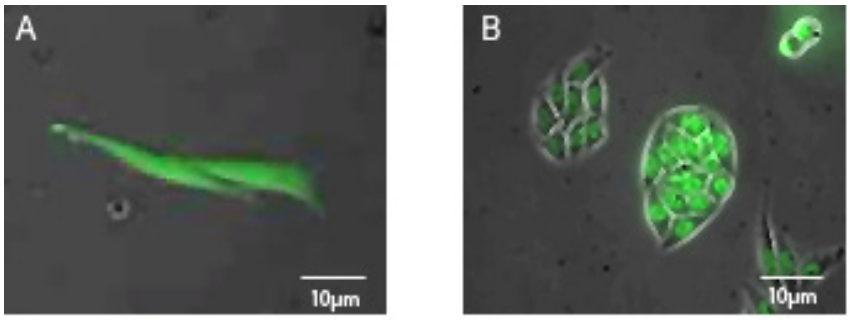

Figure 3.13: Merged phase contrast and fluorescence microscopic images of A) BJ1-hTERT cells expressing EGFP Plasmid, leading to a green fluorescence in the whole cell and B) HeLa H2B cells only expressing EGFP in the cell nuclei.

Then, the medium of the cells in the wells of the 6-well-dish was removed, the cells were washed with PBS and 1150 µl of the transfection solution were added to each well. After 2 - 3 h of incubation under normal growth conditions, the medium containing the remaining complexes was removed from the cells. Subsequently, the cells were washed

[7] This state of confluence is given by the company as optimum for a successful transfection.
[8] Serum and antibiotics present during this step will interfere with complex formation and will significantly decrease transfection efficiency.

three times with PBS and fresh growth medium was added into each well (97). A green fluorescence in the cells was visible after about 24 - 48 h post transfection (Figure 3.13).

3.5.3 Antibiotic Cell Kill Curve

For a clear differentiation between transfected and non-transfected cells, it was necessary to create stable transfected cell lines expressing GFP. Therefore, an extinction of non-transfected cells in the transfected cell culture was required.

Some plasmids contain a resistance against certain antibiotics and, hence, also the cells expressing this plasmid. This resistance can be used for the selection of the cells by adding the specific antibiotic to the cell culture. However, it is necessary to determine the minimum amount of antibiotic in the cell culture medium, which kills all non-transfected cells. This minimum concentration is not toxic for transfected cells.

The same number of cells was seeded in each well of a multiple-well dish and after 5 h different concentrations of the specific antibiotic were added to the wells. After 2 – 3 days, the medium containing the antibiotic was replaced. Each day the cell viability was checked under the microscope. After 5 days, the cells in the wells were trypsinised and their number was determined by counting the cells with a Neubauer cell counting chamber. The minimum concentration of selective antibiotic, which killed all of the non-transfected cells in a well was the required antibiotic concentration for the generation of a stable transfected cell line (98).

For a transfection with the pEGFP-N1 vector, Geneticin (Gibco, Invitrogen, Karlsruhe, Germany) was used as selective antibiotic. Cells transfected with pMC-16 EGFP were selected with the antibiotic Puromycin (Gibco, Invitrogen, Karlsruhe, Germany).

3.6 Immunocytochemistry

As mentioned above, the irradiation of cells with ionising radiation results in the formation of microscopically visible nuclear domains so called ‘radiation-induced foci’. These can either be protein accumulations sensing double strand breaks or changes in the DNA double strand like phosphorylations at certain sites. It is possible to visualise these foci via immunofluorescence staining. The staining process usually implies the use of two sets of antibodies. The primary antibody binds to the antigen of interest, in this case the protein accumulation of 53BP1 and the phosphorylated histone H2AX (γH2AX). A

subsequent added secondary antibody with a fluorescent tag binds then to the primary antibody and makes a fluorescent microscopic detection possible (Figure 3.14).

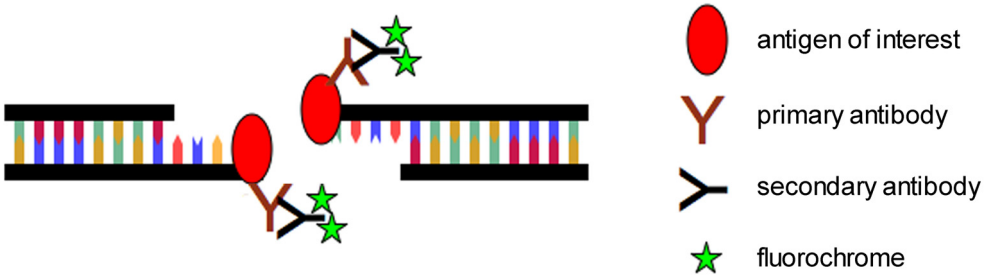

Figure 3.14: Schematic illustration of the immunostaining principle. Ionising radiation causes double strand breaks in cellular DNA and, thus, leading to the formation of radiation-induced foci. Radiation-induced foci can either be proteins sensing double strands breaks or phosphorylations at components of the DNA double strand. These foci can be visualised via immunofluorescence staining. A primary antibody is used against the antigen of interest. A secondary antibody with a fluorescent tag binds to the primary antibody enabling the detection via fluorescence microscopy.

3.6.1 Optimisation of the Immunostaining Process

Immuonstaining of samples is a process, which requires several hours until it is possible to analyse the samples via fluorescence microscopy. Generally, larger amounts of antibody solutions (several tens of µl) are necessary for the staining of cells cultivated on glass slides or in Petri dish. The use of the multiwell slides made it possible to reduce the volume of the reagents to only some µl. Furthermore, the smaller volume made it possible to reduce the incubation times of the staining reagents, resulting in a shorter immunostaining process.

The primary antibodies were either a rabbit polyclonal anti 53BP1 antibody (Bethyl Laboratories, San Francisco, CA) or a mouse monoclonal phospho-histone H2AX antibody (clone JBW301; Upstate Cell Signalling Solutions Inc. Charlottesville, VA). The corresponding secondary antibody was either a FITC labelled anti-rabbit IgG or, a FITC or Texas-Red labelled anti-mouse IgG (Molecular Probes Invitrogen, Carlsbad, CA).

Immunostaining was optimised using cells exposed to 1 Gy of X-rays and fixed 30 min after irradiation with 2% Paraformaldehyde in PBS for 15 min at room temperature followed by permeabilisation with 100% ice-cold Methanol for 15 min at a temperature of $T = -20°C$. Subsequently, the blocking, primary antibody incubation and secondary antibody incubation were optimised. Titration times were 1, 2, 4, 8, 16, 32 or 64 min as well as additional 128 min for the primary antibody. After three washing steps

with PBS at room temperature, cells were either blocked with 0,1% BSA for 1 h for the antibody titers or the blocking titer was performed with 0,1%, 0,2% and 1% BSA at room temperature. The samples of the blocking titer were incubated with the primary antibody for 2 h and then, after extensive washing with PBS, incubated with the secondary antibody for 1 h. The other samples were either incubated with the primary antibody for 2 h and, subsequently, used for the secondary antibody titer, or the primary titer with the dilutions 1:10, 1:100, 1:200 was performed at room temperature. The primary titer samples were washed extensively with PBS after the titration and then incubated with the secondary antibody for 1 h. The secondary antibody titer samples were also washed with PBS before the secondary antibody titration was performed. Dilutions used for the secondary antibody incubation optimisation were 1:10, 1:100, 1:200. All samples were washed with PBS prior to counterstaining with DAPI.

Samples of the Berkeley RIF experiments were immunostained following the optimised protocol implying a blocking step with 0,2% BSA for 15 min, incubation with the primary antibody (dilution 1:100) for 15 min and incubation with the secondary antibody (dilution 1:100) for 15 min. Cells on the functionalised glass slides were covered with Vectashield (Vector Laboratories Inc., Burlingame, CA) to avoid bleaching after counterstaining with DAPI and sealed with a coverslip.

3.6.2 Immunostaining of the Munich RIF Experiments

In all three Munich RIF experiments cells were fixed with 2% Paraformaldhyde for 15 min at room temperature post-irradiation. After the fixation step, cells were washed three times with PBS, permeabilised three times with 0,15% Triton X 100 for 5 min at room temperature, and blocked three times with 0,1% BSA for 10 min at room temperature. Then, the slides were incubated with mouse monoclonal anti γH2AX mouse primary antibody (clone JBW301; Millipore, Billerica, MA, USA) and rabbit polyclonal anti 53BP1 primary antibody (Acris Antibodies, Herford, Germany) for 1 h at room temperature. Dilutions used were 1:100 for the anti γH2AX antibody and 1:500 for the anti 53BP1 antibody. Subsequently, the slides were washed 5 min with PBS, 10 min with 0,15% Triton X 100, 5 min with PBS, 7 min with 0,1% BSA. Then, the samples were incubated with the corresponding secondary antibodies in a dilution of 1:100 for 1 h at room temperature. Secondary antibodies used were an Alexa Fluor 488 conjugated anti-rabbit IgG (Invitrogen, Karlsruhe, Germany) and a Cy3 conjugated anti-mouse IgG (Invitrogen, Karlsruhe, Germany). After the incubation with the secondary antibodies,

the cells were washed extensively with PBS and incubated with the Hoechst 33342 intercalating dye for 10 min at room temperature. Finally, the cells were washed with PBS, mounted with 10 µl of Vectashield mounting medium (Vector Laboratories Inc., Burlingame, CA, USA) and covered with a coverslip.

3.7 Image Acquisition and Analysis

The analysis of RIF in cell nuclei via fluorescence microscopy requires a three-dimensional recording, since the RIF are distributed in the whole nucleus. Furthermore, confocal microscopes and similar set-ups provide a better resolution of small structures. Thus, it is possible to better distinguish between RIF close to each other, and to make an improved prediction about real foci size and dimensions.

Immunostaining Optimisation and Berkeley RIF Experiments

Cells were viewed and imaged by using a Zeiss Axiovert 200M automated microscope with Ludl position-encoded scanning stage (Carl Zeiss Jena, Germany). Images were acquired by using a Zeiss plan-apochromat 40X dry objective with a NA of 0.95 and a sensitive scientific-grade EM-CCD camera (Hamamatsu C9100-02). All images were captured with the same exposure time and, hence, could be compared between specimens. A CSU-10 spinning disk confocal scanner was used to acquire optical slices of 0,5 µm thickness and 4 solid-state lasers provided illumination at 405, 491, 561, and 638 nm under AOTF control.

Titration intensity measurements were done with Metamorph imaging software (Molecular Devices, Sunnyvale, CA). All image manipulations and foci analysis were done with Matlab (MathWorks, Inc., Natick, MA) and DIPimage (image processing toolbox for Matlab, Delft University of Technology, The Netherlands). Foci detection and foci size were obtained using a modified version of a wavelet algorithm made available online (99). With this method a focus is detected when its size is larger than 4 pixels (2x2). This corresponds to a minimum detectable focus size of 0,08 mm^3. A focus is selected if the intensity of its wavelet transform is above a threshold. The threshold, which is determined to minimize the number of foci in non-irradiated specimens, is kept constant for the analysis of all irradiated specimens. ANOVA and non-linear least square fits were performed with Matlab software as well. For both cell matrix experiments (HCA2 and MCF10A), about 700 nuclei were isolated per well with duplicate well and two independent treatments (i.e. blocking and no blocking). As described previously

(13), foci counts were scaled to represent the number of foci for the same size nucleus, using the G1 cell area as the reference nuclear area. This permits to correct for high foci count from G2 cells present in these cycling populations (i.e. G2 cells would have double amount of DNA and thus of damages).

Munich RIF Experiments

Due to technical problems, the confocal microscope could not be used for the analysis of the Munich RIF experiments. Thus, the irradiation experiments in Germany were imaged with a Zeiss Axiovert 200M microscope with included ApoTome® (Carl Zeiss, Jena, Germany). Images were acquired by using a Zeiss c-apochromat 40X water objective with a NA of 1,2 and a sensitive CCD camera (AxioCam HRm, Carl Zeiss Jena, Germany). All images of each irradiation experiment were acquired with the same exposure time. Thus, the images of the specimen could be compared for each experiment. Z-stacks of the three-dimensional samples were acquired with a step-size of 0,3 µm. Illumination was provided by a mercury lamp epq 100 (Carl Zeiss Jena, Germany).

The Microscope and the CCD camera were both controlled via the AxioVision software provided from Zeiss. Further image analysis was performed with the imageJ software. ImageJ is a Java-based free download image processing program. It was developed at the National Institutes of Health (NIH, USA). In the first step of the image analysis, the zvi data sets acquired with the AxioVision software were exported as multicolour jpg files for each slice. These jpg files were imported in imageJ again as stacks with the command “import image sequence”. In the next step, the z-stack was projected into one plane via the command “maximum z-projection”. Subsequently, the colour channels of these z-projections were separated and each channel was analysed independently.

First, the background was subtracted from the images with the software (command: sliding paraboloid, rolling ball radius 50 pixels). Then, the foci images, the red and green channel, were compared with the blue channel, the cell nuclei. This process was performed to find and remove background particles from outside the cell nuclei and focus particles from cells at the edge of the image. Also, particles inside of a cell nucleus larger than normal, possibly indicating the presence of G2-phase, were not considered for evaluation and removed from the image. Thus, only particles inside the cell nuclei with normal size were left for the analysis. In the next step, the particles of the green and red channel were counted automatically by the software with the command “analyse

particles", which gave the number of 53BP1 and γH2AX foci for the experiment. Furthermore, the cell nuclei were counted automatically with the software, but leaving out the nuclei of cells, which were only partly present in the image. All channel images were handled with an individual threshold, before the automatic analysis of the particles. This threshold was kept constant for each experiment. For all irradiation experiments between 200 and 400 cells per sample were analysed.

3.8 Biophysical Model

In order to interpret RIF kinetic in an unbiased manner, a simple kinetic model describing RIF formation was used. A detailed model of repair kinetic was recently introduced where the different proteins involved in the repair pathway were considered (100). The simplified model introduced here only considers radiation-induced foci, independently from the other repair factors. This model emphasises the biological detection of one DSB into a RIF and the resolution of RIF at later time-points. The following equation represents the principle of the model, assuming each process is irreversible.

$$DSB \xrightarrow{k_1} RIF \xrightarrow{k_2} RIF_{resolved} \tag{3.4}$$

C_0 and C_1 are assumed to be the amount of DSB and RIF per average nucleus at time t. The parameters k_1 and k_2 are the rates at which DSB are detected and RIF are resolved (in min^{-1}), respectively. They are only related to repair kinetic, but do not describe necessarily the repair itself since the formation of RIF does not imply the repair of DSB. It just implies that the site of damage was recognized. Similarly, a RIF being resolved does not necessarily mean that a DSB was repaired since it may take time for a RIF with a repaired DSB to be resolved. As soon as a cell is irradiated, DSBs are induced and RIF start to form at the sights of damage. It is assumed that the number of RIF is equal to the number of the induced DNA DSBs minus the number of the already resolved RIF. This kinetic model translates into the following set of differential equations:

$$\begin{cases} \dfrac{dC_0}{dt} = -k_1 C_0 \\ \dfrac{dC_1}{dt} = k_1 C_0 - k_2 C_1 \end{cases} \Rightarrow \begin{cases} C_0(t) = C_0(0).e^{-k_1 t} \\ \dfrac{dC_1}{dt} = k_1 C_0(0).e^{-k_1 t} - k_2 C_1 \end{cases} \overset{C_1(0)=0}{\Rightarrow} \begin{cases} C_0(t) = \alpha D.e^{-k_1 t} \\ C_1(t) = \dfrac{\alpha D k_1}{k_2 - k_1}\left(e^{-k_1 t} - e^{-k_2 t}\right) \end{cases} \tag{3.5}$$

α is theoretically the number of DSB/Gy and should be constant for all irradiation doses. But the factor analysed in the foci experiments is the number of RIF as a function of time (i.e. $C_1(t)$) and, thus, α is really the number of RIF/Gy. Nevertheless, it is assumed one DSB leads to one RIF, thus, also the number of RIF/Gy has to be independent from the irradiation dose and should be constant. The same should be valid for the kinetic constants of RIF induction, k_1, and RIF resolution, k_2. Thus, fitting of the time response for different irradiation doses using C_1 of equation 3.5 should result in similar curve progressions as indicated in Figure 3.15. The only difference between the four curves is the value, which was assumed for the irradiation dose (1000, 500, 250 mGy). The three fitting parameters α, k_1, and k_2 had constant values for all graphs, thus, were dose independent.

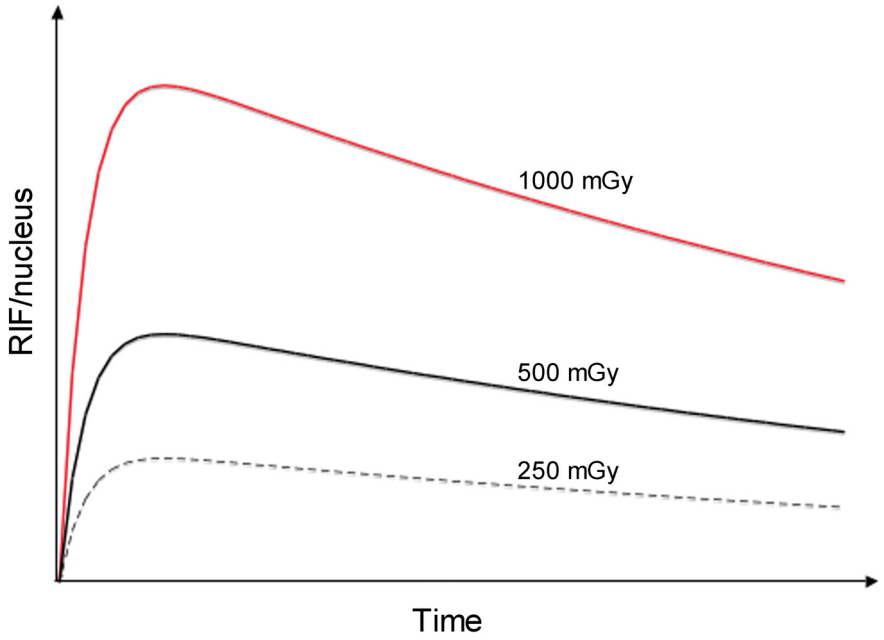

Figure 3.15: Fitting curves for constant values for α, k_1 and k_2 but different irradiation doses. For the irradiation doses values of 1000, 500, and 250 mGy were assumed.

To test the dose dependence of the three parameters α, k_1, and k_2, they were fitted individually for each time response at a given dose. As it will be shown in the results section, it was impossible to fit the time responses of all doses with the same values for α, k_1, and k_2. The time responses appear to be dose dependent (see chapter 4.1.2). Thus, the time response was fitted individually for each dose (i.e. $k_1(D)$, $k_2(D)$ and $\alpha(D)$). $\alpha(D)$ is the parameter that determines the maximum of the fit curve. Its dose dependent behaviour entails a non-linear relation between the time response maxima reached for the different irradiation doses. RIF induction is described by the parameter $k_1(D)$, which

defines the slope in the beginning of the fit curve until the maximum is reached. While higher values imply a faster RIF induction, thus, a steeper curve progression, lower values, which are a factor for slower RIF induction, result in flatter curve progressions. The same curve progression behaviour is valid for lower or higher values of the RIF resolution parameter $k_2(D)$. This parameter influences the curve progression after the maximal RIF number was reached. Figure 3.16 shows the three graphs for changes in the values of either α, k_1, or k_2. The other two parameters were kept constant.

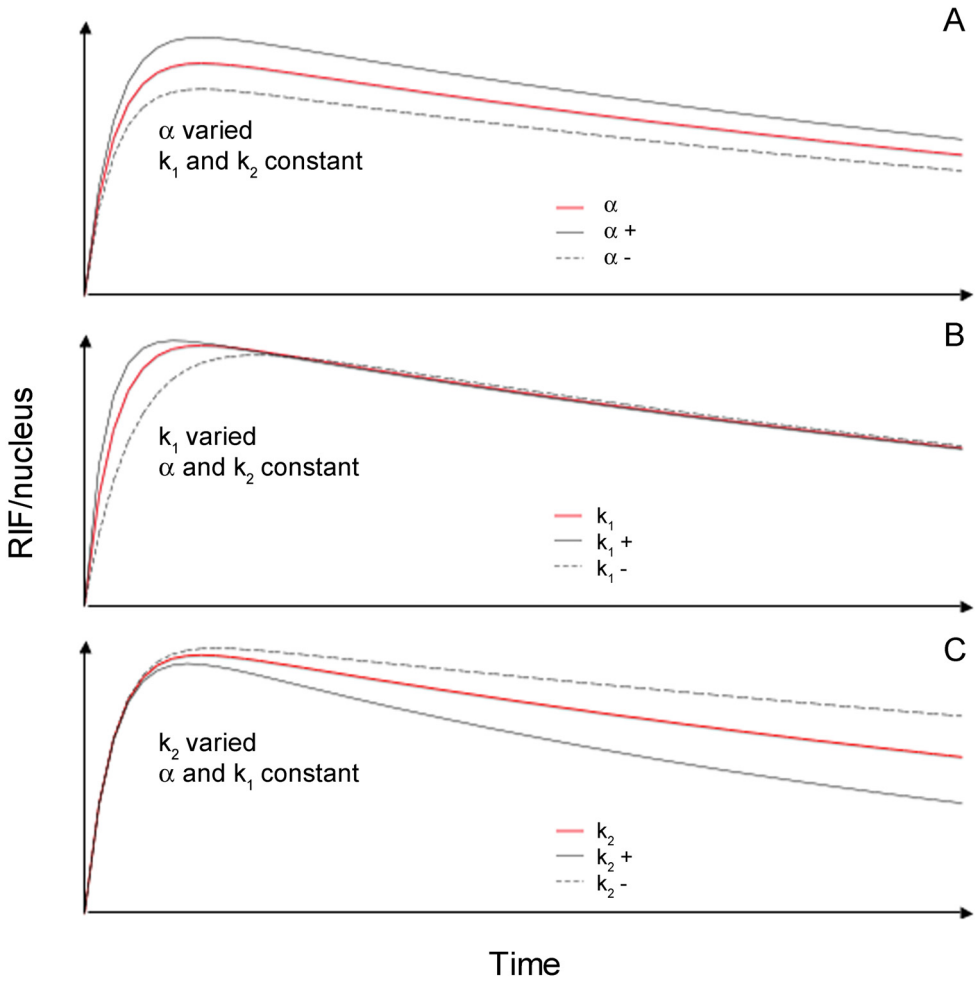

Figure 3.16: Graph A) shows the changes in the curve progression for different values of α. B) is the graph for changes in the RIF induction parameter k_1 and C) the graph for different values of the RIF resolution parameter k_2. The other two parameters were kept constant.

The determined dose dependence of the parameters implies that the model assumption that one DSB leads to one RIF is not true at all doses. This suggests the following process for the model:

$$\beta \times DSB \xrightarrow{k_1(\beta)} RIF \xrightarrow{k_2(\beta)} RIF_{resolved} \tag{3.6}$$

$\beta(D)$ is the average number of DSB within one RIF ($\beta > 1$ and increases with dose). The corresponding half-life for k_1 and k_2 are reported as the time span until half of all DSB to be detected as RIF (i.e. $ln(2)/k_1$) or the time span until half of fully formed RIF to be resolved (i.e. $ln(2)/k_2$).

A mathematical description of the foci size is required to discriminate foci being present in the cells before exposure to radiation (Background foci, BF) and radiation-induced foci (RIF). Therefore, different parameters describing the number and size of BF, RIF and total foci are defined. Let n_{BF}, n_{RIF} and n be the number of BF, RIF and total foci identified by the developed analysis algorithm at a given time-point. The parameter n is measured during the analysis and represents the sum of the number of BF and RIF (i.e. $n = n_{BF} + n_{RIF}$). It is a function of time post-IR (t) and dose received (D). Higher irradiation doses result in higher focus numbers and different repair times in a focus number distribution as indicated in Figure 3.15 with an increase in the beginning, and a maximum followed by a decrease in focus number. Let s_{BF}, s_{RIF} and s be the average BF, RIF and overall focus size reported at a given (t,D). Again it is only possible to measure the overall focus size, which is the sum of BF size and RIF size. Both BF size and RIF size can be understood as size distributions over all analysed foci. Due to statistical reasons, the average focus size reported over all un-irradiated (0 Gy) time controls was used for the average size of BF. No significant differences in focus size were observed for these samples. Figure 3.17 is an outline of these considerations for a possible focus size distribution over focus number.

Thus, the measured overall foci size can be corrected so that it only reflects the size of RIF as demonstrated in the set of equations (3.7):

$$s(t,D) = \frac{n_{BF}(t,D)}{n(t,D)}\langle s_{BF}\rangle + \frac{n_{RIF}(t,D)}{n(t,D)} s_{RIF}(\mathrm{t,D}), \text{ where } \langle s_{BF}\rangle = \frac{\sum_{\text{all t}} n(t,0) s_{BF}(t,0)}{\sum_{\text{all t}} n(t,0)}$$
$$\Rightarrow s_{RIF}(t,D) = \frac{s(t,D).n(t,D) - \langle s_{BF}\rangle.n_{BF}(t,D)}{n_{RIF}(t,D)} \quad (3.7)$$

A correction was employed for the fact that all RIF are formed at various time-points after exposure, after taking the background RIF contribution into account. Thus, the reported RIF size at a given time-point is the convolved average of the theoretical RIF size increase over time with the DSB detection kinetic modelled in equation (3.5). Let s_m be the theoretical size of RIF, which is proposed to be modelled. As previously published

by Costes et al. (10), RIF size increases over time reflecting recruitment of proteins (e.g. 53BP1) or protein phosphorylation (e.g. gH2AX). Thus, an early kinetic of the observed foci size can be modeled by neglecting RIF decays once a DSB is repaired. This implies that the mathematical model described here is only valid within a short time after foci formation (within ~20 min post-IR).

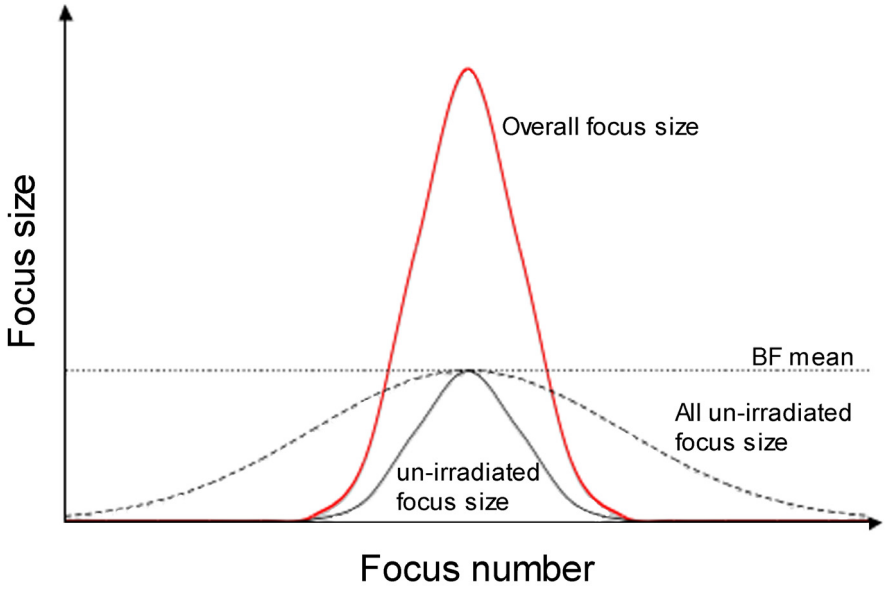

Figure 3.17: Outline of a possible focus size distribution over focus number for one time point. The distribution of the overall focus size reaches the highest maximal value (red curve). The mean of the BF size distribution is indicated by the dotted black line. It is the mean of both, the foci size distribution over all un-irradiated samples (black dashed line) as well as of un-irradiated samples at the investigated time-point (black line) since no significant differences in focus size were observed for these samples.

Let A and A' be the amount of protein non-recruited (or non-phosphorylated) and recruited (or phosphorylated) respectively. The parameter k_3 is the rate at which protein is either recruited or phosphorylated. Assuming there is a finite amount of proteins involved in focus formation (101), described by A_∞, and focus size is assumed to be proportional to the amount of protein recruited or phosphorylated, then a model can be derived for size kinetic as follows:

$$A \xrightarrow{k_3} A' \text{ and } \mathrm{A} + \mathrm{A}' = \mathrm{A}_\infty \Rightarrow \frac{dA'}{\mathrm{dt}} = k_3 A = k_3(\mathrm{A}_\infty - A'), \text{ where } \mathrm{A}_\infty \text{ is a constant}$$
$$A'(t) = \mathrm{A}_\infty(1 - e^{-k_3 t}) \text{ and thus } s_m(t) = \mathrm{s}_\infty(1 - e^{-k_3 t}) \qquad (3.8)$$

$s_m(t)$ is the measured focus size due to the recruited or phosphorylated protein and s_∞ the maximum size, which can be reached by a focus since only a finite amount of protein is

involved in focus formation. It is then possible to derive the size $s_{RIF}(t)$ at a given time t from these considerations.

The focus size distribution that we see is the result of all the foci, which have been formed between the time of exposure (0) and t. Equation (3.5) can be used to compute the number of RIF being formed at time t' during the infinitely small time interval dt' where t' is within [0,t]. Foci formed during this short period will lead to a focus at time t of size $s_m(t-t')$. Having described these conditions, it is now possible to solve for $s_{RIF}(t)$ as follows:

$$s_{RIF}(t) = \frac{\int_0^t s_m(t-t')\frac{dC_1}{dt'}dt'}{\int_0^t dC_1} \tag{3.9}$$

$$\Rightarrow s_{RIF}(t) = s_\infty\left(1 - \frac{k_1}{k_1-k_3}\cdot\frac{e^{-k_1 t}-e^{-k_3 t}}{e^{-k_1 t}-e^{-k_2 t}} + \frac{k_2}{k_2-k_3}\cdot\frac{e^{-k_2 t}-e^{-k_3 t}}{e^{-k_1 t}-e^{-k_2 t}}\right)$$

Figure 3.18 is the illustration of possible curve progressions that describes the increase in focus size over time following irradiation in dependence of dose. Estimates for k_1, k_2 from equation (3.5), are then substituted into equation (3.9) in order to estimate k_3. $k_3(D)$ is obtained by fitting the corrected RIF sizes equation (3.7) with equation (3.9) using non-linear least square-fits for all time-points of a given dose, repeated for each dose.

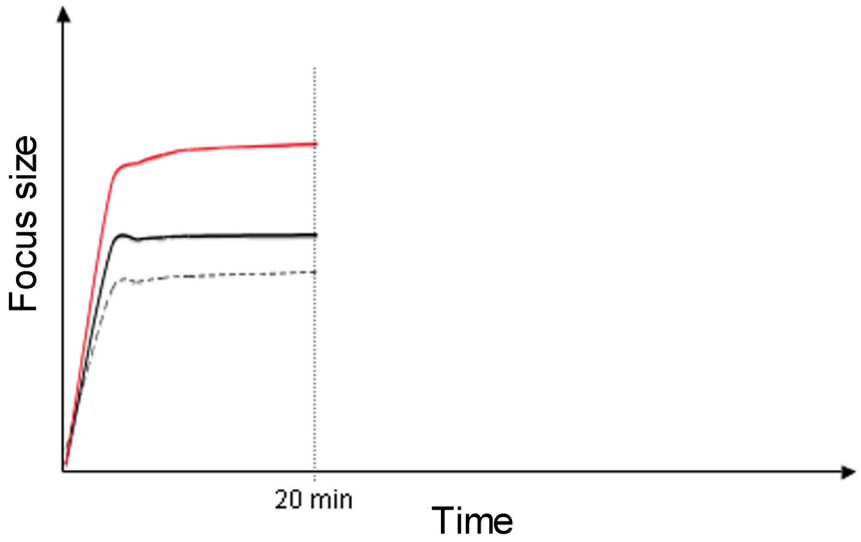

Figure 3.18: Possible curve progressions for the RIF size increase over time of samples irradiated with different doses. The introduced model is only valid within a short time after focus formation (~ 20 min).

4 Static and Retrospective Experiments

4.1 Results

Foci statistic experiments with fixed cells give only snapshots of the cell repair status at certain time-points. However, the immunostaining of DNA DSB in irradiated cells is a valuable tool for studying repair dynamics of cells after irradiation. It reveals the occurrence of different repair proteins by using specific antibodies and it gives an idea about co-localisation of different proteins or the occurrence of certain posttranslational protein modifications (e.g. phosphorylation) in cell nuclei. Nevertheless, it is necessary in the context of the comparison of experiments to work with a common methodology. Different groups report varying results due to diversities in staining and acquisition approaches. Automated image analysis over a large number of cell nuclei leads to more reproducible and statistically more robust results. Furthermore, a common approach for RIF experiments would lead to results, which could be compared between the different groups.

4.1.1 Optimisation of Immunostaining

By using the multiwell slides it was possible to reduce the volume of the reagents of the immunostaining process. In context of immunostaining optimisation with these low volumes, titration curves were performed for three different reagent concentrations and doubling incubation times, for the blocking step, the primary antibody and secondary antibody incubation.

After irradiation of the cells with 1000 mGy of X-ray, the samples were treated as described in chapter 3.3.1. The focus intensity as well as the background of the microscopic images were measured with the Metamorph software for all three titrations and the relative focus intensities were calculated. Figure 4.1A shows the three relative focus intensities of the different primary antibody dilutions over incubation time. The relative focus intensity reached for all dilutions saturation after around 16 min (see dashed line in Figure 4.1A). This led to the conclusion that longer incubation with the primary antibody did not result in better microscopic images, which refers to the focus intensity. Furthermore, an increase in the relative focus intensity was observed with increasing antibody concentration (Figure 4.1B, C, D). The highest antibody concentration led to the brightest images.

However, the standard deviation was also increasing with rising antibody concentration. Its values were almost twice as high for the lowest dilution as for the medium dilution. This implied that the higher the concentration of the antibody the bigger were the fluctuations of the relative focus intensities referring to the background of the microscopic images.

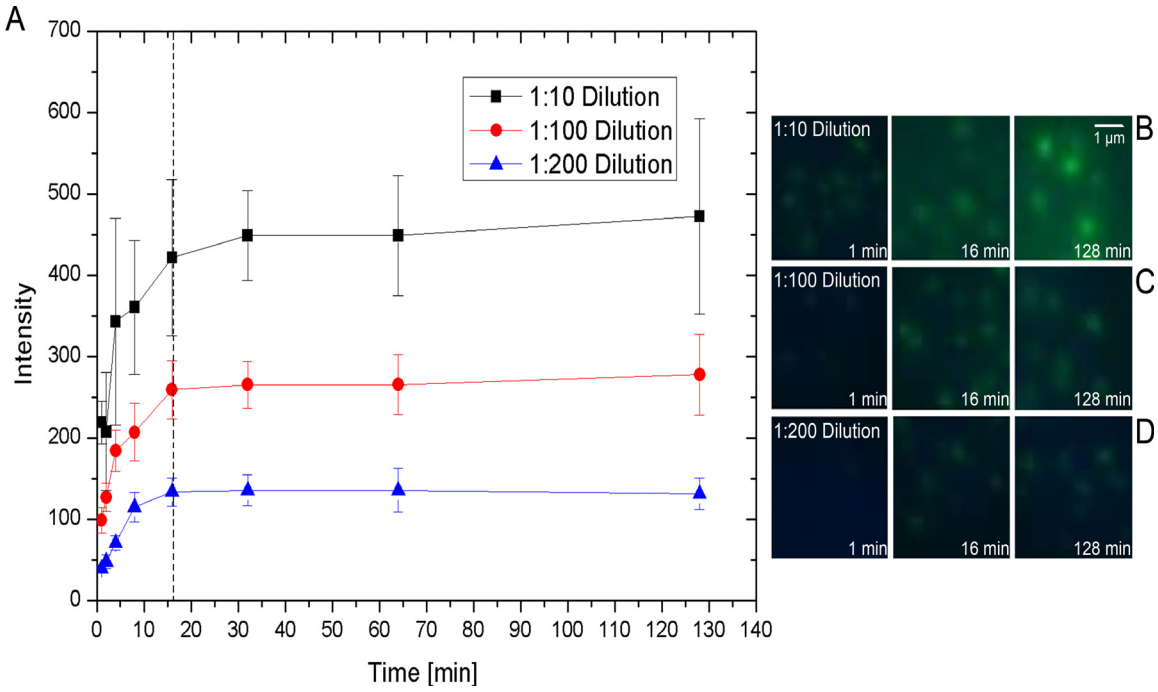

Figure 4.1: Graph of the primary antibody titration for the three different primary antibody dilutions used (A). All curves show saturations in the relative focus intensities after around 16 min (see dashed line). Thus, a longer incubation with the primary antibody did not lead to a higher focus intensity. Furthermore, a difference in the relative focus intensities for the three concentrations is observable in the enlarged confocal microscopic images of 53BP1 foci (B, C, D). The highest antibody concentration results in the brightest foci (B). However, the standard deviation increases with the antibody concentration and is almost twice as high as for the medium antibody dilution. This implies, that the higher the concentration of the antibody is, the bigger is the fluctuation of the relative focus intensity referring to the background of the microscopic image (B).

Table 4.1 shows the concentrations and dilutions tested, the time-points when intensity saturation was reached, and the signal to background ratio for the three reagents.

Saturation was reached for the blocking titration between 8 – 16 min in dependence on the BSA concentration. For the primary antibody the saturation was always reached after 16 min independent from the antibody concentration as mentioned above. The secondary antibody plot showed more variations in the saturation time-points in dependence on the antibody concentration. Saturation was obtained after 32 min for the 1:200 antibody dilutions, after 16 min for the 1:100 dilution and after 8 min for the 1:10 dilution.

Table 4.1: Immunostaining optimisation results

Blocking step	Concentration tested	0.1%	0.2%	1%
	Incubation time to reach saturation	8 min	8 min	16 min
	Signal to Background ratio	0.9	1.0	1.4
Primary Antibody	Dilution tested	1:200	1:100	1:10
	Incubation time to reach saturation	16 min	16 min	16 min
	Signal to Background ratio	0.5	0.8	0.7
Secondary Antibody	Dilution tested	1:200	1:100	1:10
	Incubation time to reach saturation	32 min	16 min	8 min
	Signal to Background ratio	1.1	1.2	2

Figure 4.2A shows the progression of the relative focus intensities for the 1:100 dilutions for both antibodies and the curve for the 1% BSA blocking solution. The relative focus intensities increased for both antibodies until their saturation. The curve of the relative focus intensities of the blocking titer decreased instead over time till saturation was reached after 16 min.

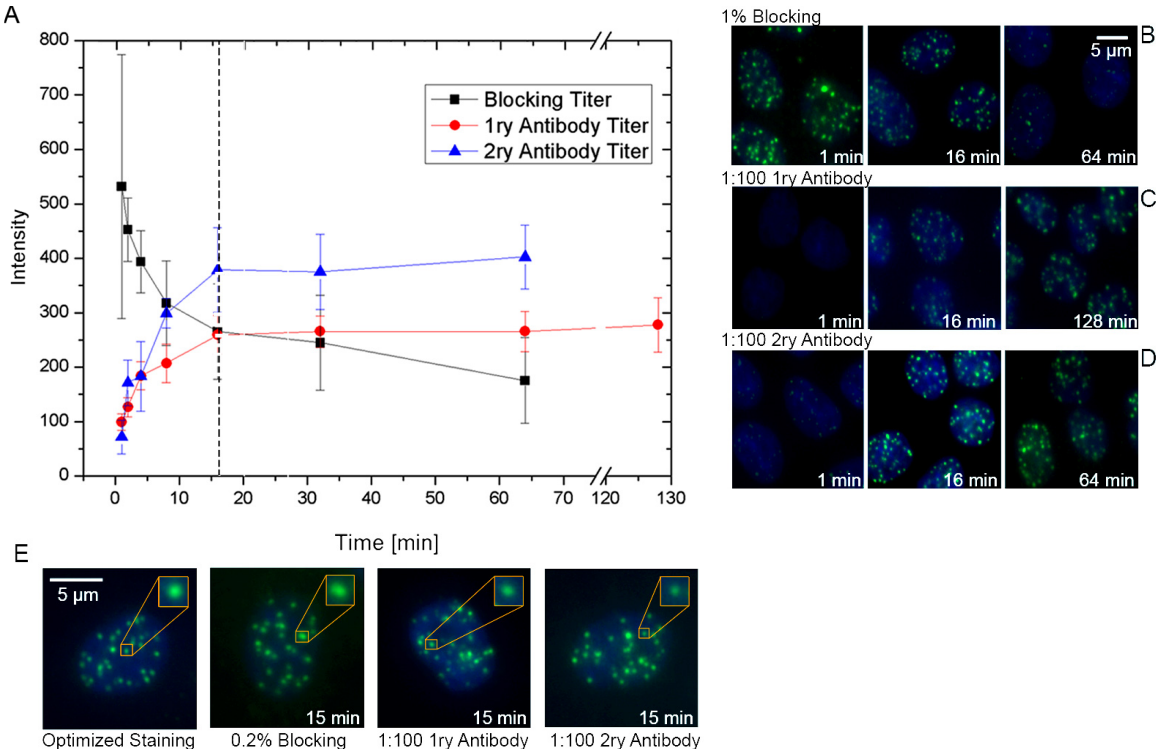

Figure 4.2: The graph (A) shows the relative focus intensities for the blocking titer (black curve), primary (red curve) and secondary (blue curve) antibody titer. The relative focus intensities saturated for the three titers after about 16 min (dashed line). This indicates that a shorter incubation of the sample is sufficient for good immunostaining results. This conclusion is supported by the visual analysis of the confocal microscopic images showing 53BP1 foci in HCA2 cells (B, C, D). A longer blocking step leads to a fluorescent image with lower intensity. And a longer incubation with the primary or secondary antibody did not result in a brighter image. Panel E shows images of the optimised incubation times as well as an image of the optimised immunostaining.

Not only the observance of saturation in the relative focus intensity for the three reagents but also the intensity of the microscopic images led to the conclusion that longer incubation did not improve the quality of the images. Indeed, longer blocking resulted in lower foci intensities (Figure 4.2B). For both antibodies the saturation of the relative focus intensity was reached after 16 min (dashed line), which can also be seen in the microscopic images (Figure 4.2C, D).

The saturation of the titration curves observed as well as the quality of the images led to the decision to reduce the incubation time for the three staining steps from 1 or 2 h to 15 min. Furthermore, a 0,2% concentration of BSA and the 1:100 dilution for both antibodies were used in further experiments. Corresponding images for these incubation times and dilutions as well as an optimised staining are shown in Figure 4.3E. They clearly show the improvement in image quality compared to other conditions (Figure 4.3B, C, D). Primary antibody and secondary antibody titration were also performed for the mouse monoclonal phospho-histone H2AX antibody and the corresponding FITC and Texas-Red labelled anti-mouse IgG. They led to the same results.

The next step in the immunostaining optimisation and achievement of a faster processing time was the automated staining process. Therefore, the BioSpot® was used as described in chapter 3.1.2. The BioSpot® has the ability to either shoot the liquid from the tube reservoirs of the PipeJets or to dispense a certain amount of µl. Water was used during the staining tests as reagent alternative and the whole staining process was programmed for both, shooting and dispensing. However, PBS and thus, all the other reagents have less surface tension in comparison to water and it was not possible to shoot the reagents. As soon as the valves, the PipeJets, were connected to air, which is necessary for the shooting mode, the reagents started to drip from the PipeJet tips. Thus, the automated staining was conducted with the dispensing mode of the reagents.

The evaporation of the reagent droplets was also problematic. Only a volume of $V = 10\,\mu l$ of each reagent were dispensed on the sample spots. Thus, by implying a step-motor in the y-axis, the speed of the staining process would be improved and reagent evaporation could be prevented. A test staining was performed with HeLa cells grown on the multiwell slides and irradiated with 250 mGy of X-rays. The cells were fixed 30 min post-irradiation to reach a maximum for both, γH2AX and 53BP1 foci. Following fixation the multiwell slides were placed on top of the staining set-up and the optimised staining was performed automatically. No difference in the quality of the images was

observed in the fluorescence microscopic images for samples on different spots as indicated in Figure 4.3.

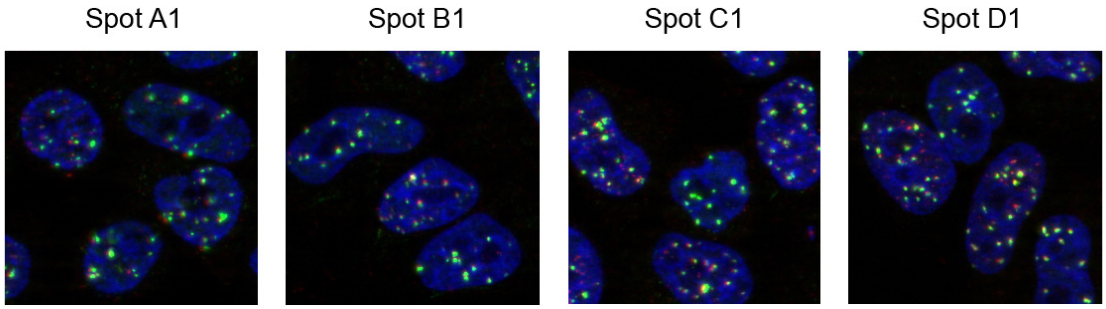

Figure 4.3: Fluorescence microscopic images of HeLa cells grown on each spot of a multiwell slide and irradiated with 250 mGy of X-ray. The cells were fixed 30 min post-irradiation. Following fixation the cells were stained automatically with the BioSpot® according to the optimised immunostaining protocol. The images show cell nuclei (blue) with γH2AX foci (red) and 53BP1 foci (green). No differences in the image quality of the diverse spots are visible. This indicates that all spots were stained in the same way and the staining result is independent from the location of the sample on the multiwell slide.

Images of each spot of the first row on a multiwell slide are shown. The fluorescence microscopic images show cell nuclei (blue) with both kinds of foci, γH2AX (red) and 53BP1 (green) from each spot. The quality of the fluorescence microscopic images suggests that the reagents did not dry up on any spot and all samples were stained in the same way. Thus, the staining result is independent from the location of the sample on the multiwell slide.

4.1.2 RIF Background Subtraction

The human cells used in the Berkeley RIF experiments have significant amounts of spontaneous foci. Thus, a correction for spontaneous foci was performed in all foci experiments for the further analysis by Sylvain Costes at the Lawrence Berkeley National Laboratory. DNA damages occur randomly in the cell nuclei with an average frequency Φ after irradiation (RIF/nucleus). Hence, the probability of having N radiation-induced damages in a given cell is defined by the following Poisson distribution P(N,Φ). By measuring the number of cells with N RIF/nucleus it is possible to construct a histogram H(N,D) for a given dose D as indicated in the following equation:

$$H(N,D) = H(N,0) \otimes Pois(N,\Phi) \tag{4.1}$$

H(N,0) is the histogram of the number of foci in cell nuclei without radiation. Thus, the distribution of RIF observed in a specimen can be assumed as Poisson distribution whose means is the average number of RIF/nucleus convolved with the distribution of spontaneous foci present before exposure to ionising radiation. The best fit with a certain value of Φ was determined by incremental changes of Φ. It was searched for each measured distribution H(N,D). Figure 4.4 illustrates this kind of fit for two time-points of the 150 mGy and 2000 mGy samples from the Berkeley RIF experiments.

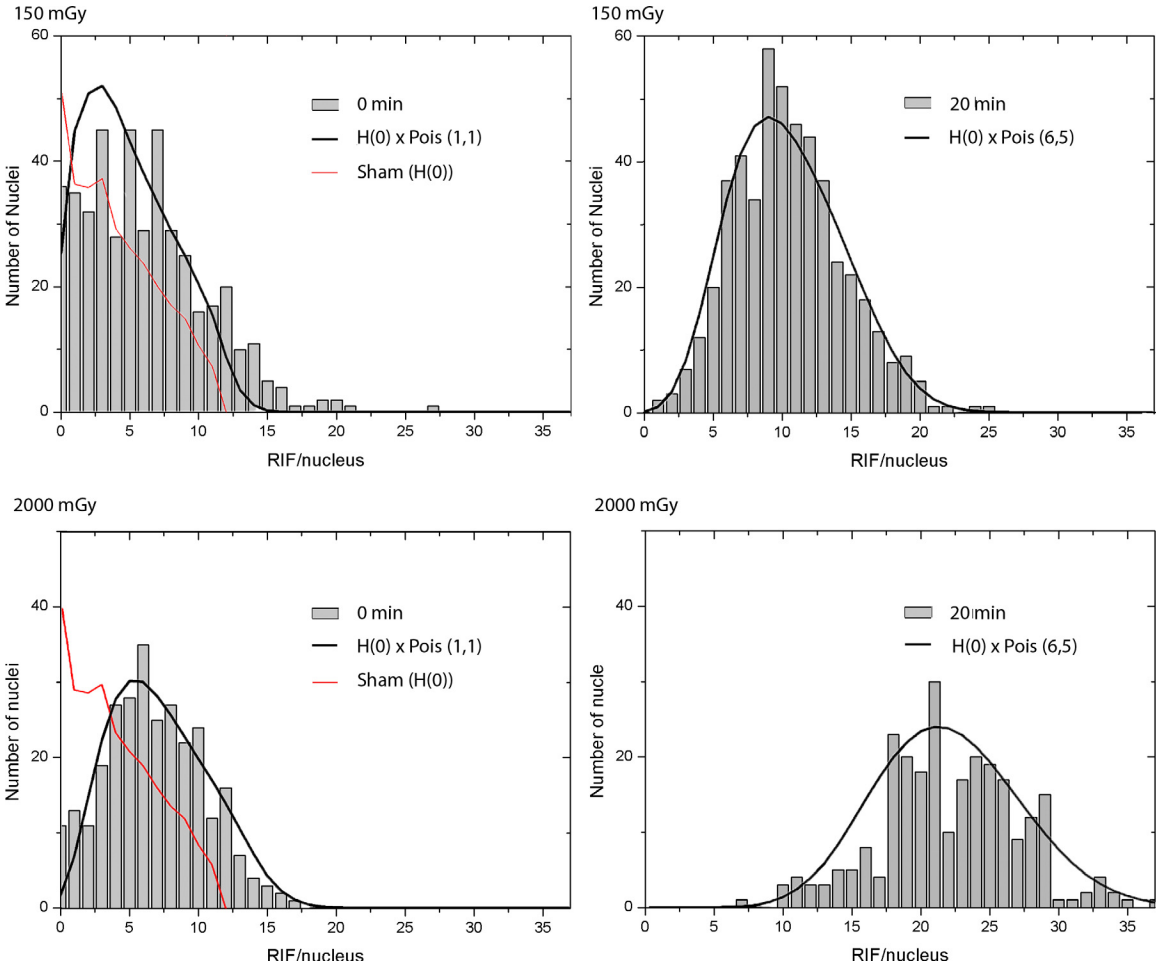

Figure 4.4: Illustration of the determination of the number of RIF/nuc for two time-points 0 min and 20 min post IR for the doses 150 and 2000 mGy in MCF10A labelled with 53BP1. Counts distribution are shown for RIF/nuc as histogram (H(Dose)) and fitted by a Poisson distribution of mean M (POIS(M)) convolved with the RIF/nuc distribution of un-irradiated specimen (red curve in both 0 min panels, H(0 Gy)). The mean M that led to the best fit, which is displayed over each histogram as a black solid line, corresponds to the reported real RIF yield for a given time-point corrected for spontaneous foci.

Analysis of the Munich RIF experiments did not provide the number of RIF per individual cell but the average RIF number over all cells analysed. However, for several samples the cell number distribution over RIF was analysed to confirm the Poisson distribution in these experiments in order to be able to use the standard error of the mean

as part of the statistical error. Background RIF numbers were for the cells used in the Munich RIF experiments not as high as in the matrix experiments. Thus, background subtraction for the Munich RIF experiments was not performed over the convolution of H(N,0) and Pois(N,Φ) but over the direct subtraction of the background foci distribution from the average RIF number detected in each experiment.

4.1.3 Berkeley RIF Experiments

4.1.3.1 RIF yield and formation-resolution kinetics

The array format of the multiwell slide was used to simultaneously expose cells to doses of ionizing radiation from 50 to 2000 mGy, which were fixed at 1 min to 80 min post-irradiation (Figure 3.9 in chapter 3.1.2 illustrates the setup). Figure 4.5A, B show the DNA damage response of human mammary epithelial cells, MCF10A, which was fully characterised for this approach for both DNA damage markers γH2AX and 53BP1. The foci kinetics reached for both markers a maximum around 20 min post irradiation.

Time responses led to statistically significant least square fits for all doses at 150 mGy and above, using equation 3.5 (see Materials and Methods). On the other hand, 50 mGy responses were more sporadic leading to fits that were not statistically significant, suggesting a detection threshold with the approach used in these experiments. As already mentioned in chapter 3.8 a dose dependence of the fitted parameters, i.e. the absolute RIF yield normalised to dose (α in RIF/mGy/nucleus), the kinetic constant of RIF formation (k_1 in min^{-1}) and the kinetic constant of RIF resolution (k_2 in min^{-1}), was observed. Repetitions of these irradiation experiments also led under different conditions, i.e. cultivation in 8 well chamber slides, to the dose dependent behaviours of the fit parameters (102). Furthermore, no significant difference was observed in the kinetic curves obtained from all experimental approaches, thus the results were averaged for more robust statistics.

Figure 4.6A-C displays the dose dependent behaviour of the fit parameters for both foci markers for the MCF10A cells derived from the average time response from all experimental approaches. Figure 4.6A shows that the RIF yield normalised to dose decreased between 150 and 2000 mGy. A threefold decrease was observed for the 53BP1 marker and a twofold decrease for the γH2AX marker. This decreasing trend was statistically significant, which was tested over a one way ANOVA and a Tukey-Kramer test between doses (indicated by asterisks in Figure 4.6).

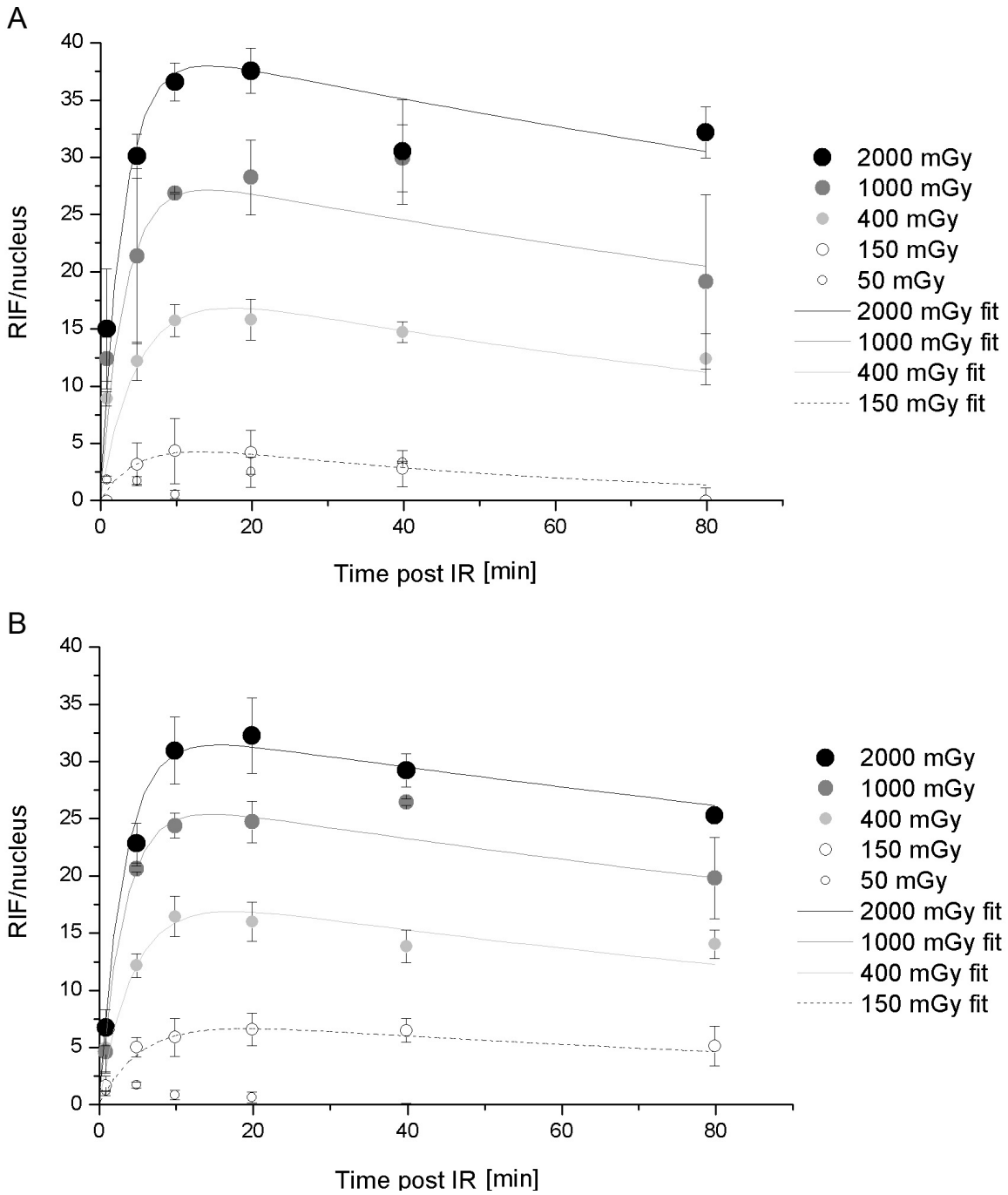

Figure 4.5: Time response of background corrected RIF per nucleus in human mammary epithelial cells (MCF10A) exposed to various doses of X-rays and immunostained for γH2AX (A) and 53BP1 (B). Experimental data points (circles) get larger with dose and they correspond to the averages between N independent experimental approaches with their corresponding error bars. The lines indicate the best fits for each time response obtained from equation 3.5 in Materials and Methods.

These results confirm a saturation of the number of RIF at higher doses, contradicting the hypothesis that 1 DSB always leads to 1 RIF (9). Furthermore, the RIF formation kinetics was also dose dependent with a faster RIF formation for higher doses. The induction half-life decreased from 3,5 min (~0,18 min^{-1} k_1) to 2,2 min (~0,32 min^{-1} k_1) from 150 to 2000 mGy respectively. It was also observed that both foci markers, γH2AX and 53BP1, had similar dose dependences for either α or k_1, thus suggesting that both proteins have

similar roles in the detection of DNA damage. Also the RIF resolution kinetic was comparable for both markers. The resolution half-life increased with increasing dose. More specifically it increased from 2 to 4 h for 53BP1 and from 40 min to 3 h for γH2AX. RIF yield normalised to dose, induction half-lives and resolution half-lives of the MCF10A cells are displayed in Table 4.2.

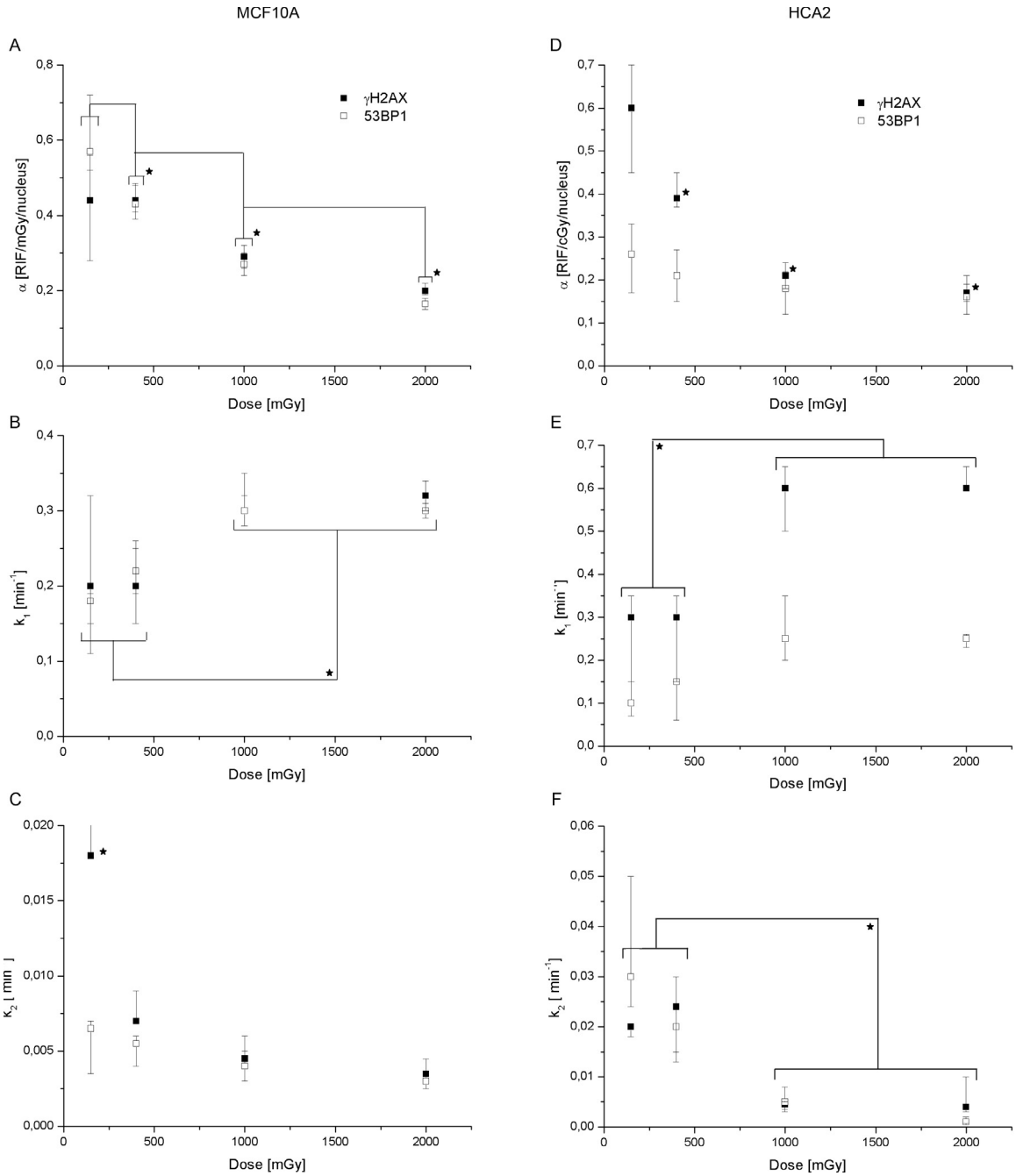

Figure 4.6: Corresponding fit parameter for both cell lines, MCF10A and HCA2, are displayed against dose for γH2AX and 53BP1. All statistically significant trends between dose points are indicated by asterisks and were tested over a one way ANOVA and a Tukey-Kramer test. (A, D) Absolute RIF yield α [RIF/mGy/nucleus], which shows a decrease with dose for both cell lines. (B, E) RIF induction kinetic constant k_1, which shows a faster induction with dose. (C, F) RIF resolution kinetic constant k_2, which shows a slower RIF resolution with dose. The error bars of each parameter display the values reached by the maximum and minimum fit of the data points with equation (3.5).

To investigate whether the dose dependent behaviour of the fit parameters was only specific to MCF10A cells a matrix experiment was also performed with human foreskin fibroblasts, HCA2. For these cells, the matrix experiment was only performed once, using a confocal microscope for analysis and the multiwell slides. Again a dose dependent behaviour of the fit parameters was observed (Figure 4.6D-F).

The HCA2 cells also showed a systematic decrease of RIF yield per Gy between 150 and 2000 mGy for γH2AX. The 53BP1 yield per Gy also appeared to decrease with dose but the changes were too low to be statistically significant. However, the kinetics of both markers showed the same statistically significant kinetic trends characterised by a faster RIF induction and a slower resolution as the dose increased (Table 4.3). However, the dose dependence had a different shape than for MCF10A cells, as both k_1 and k_2 dose responses looked more like step functions with a sudden change of value occurring between 400 and 1000 mGy (Figure 4.6E, F), instead of monotonic functions observed in MCF10A cells.

Table 4.2: Fitted coefficients for MCF10A cells

	Dose [mGy]	RIF yield [RIF/mGy/nucleus]	$T_{1/2}$ [min] (induction)	$T_{1/2}$ [min] (resolution)
γH2AX	150	0,044	3,5	39
	400	0,044	3,5	99
	1000	0,029	2,3	154
	2000	0,02	2,2	198
53BP1	150	0,057	3,9	107
	400	0,043	3,2	126
	1000	0,027	2,3	173
	2000	0,017	2,3	231

Table 4.3: Fitted coefficients for HCA2 cells

	Dose [mGy]	RIF yield [RIF/mGy/nucleus]	$T_{1/2}$ [min] (induction)	$T_{1/2}$ [min] (resolution)
γH2AX	150	0,06	2	35
	400	0,039	2	29
	1000	0,021	1	154
	2000	0,017	1	173
53BP1	150	0,026	7	23
	400	0,021	5	35
	1000	0,018	3	139
	2000	0,016	3	693

The lack of linearity in the RIF yield is displayed for all time-points in Figure 4.7A. One could question the accuracy of the RIF detection. To illustrate the precision of detection, images at 20 min post irradiation are depicted, with red dots at the centre of each detected

focus (Figures 4.7B-E). Enlarged nuclei of each sample demonstrate the image quality as well as the full shape identification of RIF and the ability of the algorithm to separate touching RIF. Each RIF is labelled with a different colour.

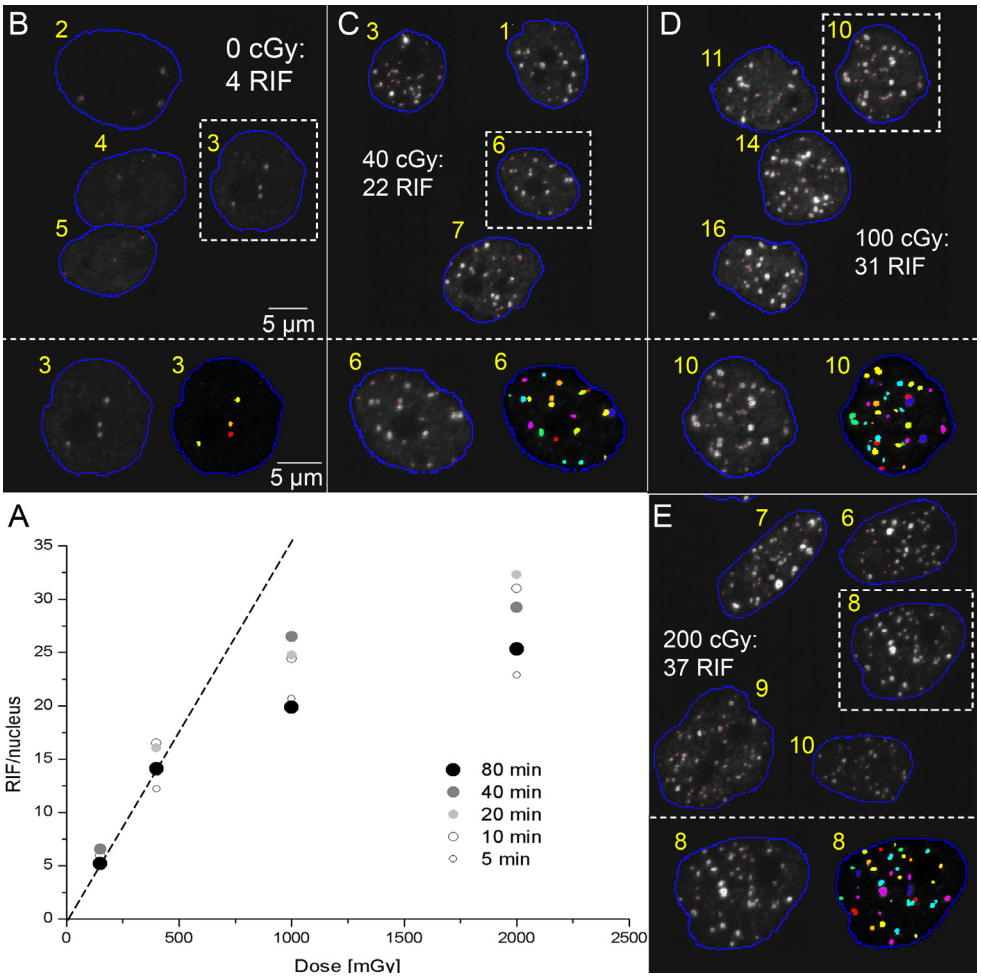

Figure 4.7: Foci yield is dose dependent as illustrated in the MCF10A cell line for the 53BP1 marker. Panel A shows the averaged dose response for various time-points (circle size increases with time) over all samples. The dashed line is shown as a reference for the linear response at 20 min post IR indicating departure from linearity at 1000 and 2000 mGy. Panel B through E show exemplary images at 20 min post IR for various doses. Blue lines delimit each nucleus obtained automatically from DAPI stain and red dots indicate, which foci were detected. Enlarged nuclei of each image display how well the algorithm separates RIF. Different RIF are labelled with different colours in the images.

4.1.3.2 Foci size

As previously reported, foci size is another important parameter that characterises different DNA damage markers (10). A simple theoretical model, representing the recruitment of proteins at the damage site, is described here by assuming that only a finite amount of proteins is available for recruitment at each DSB site (see equation 3.7 Materials and Methods). This is probably a valid assumption for the early response of the cell (i.e. < 20 min), as the production of more proteins is not likely within such a short

period of time. For simplification, the removal of the proteins forming the foci is also neglected in this model, making the model accurate only for early time-points.

Furthermore, it is important to note that the original foci size kinetic responses had to be corrected since not all RIF formations were triggered instantaneously after having been exposed to IR. This is suggested by equation 3.5 suggest (see equation 3.9 Materials and Methods). As an example, results for γH2AX foci in MCF10A cells are plotted in Figure 4.8A, showing the kinetic of histone H2AX phosphorylation at a focus site.

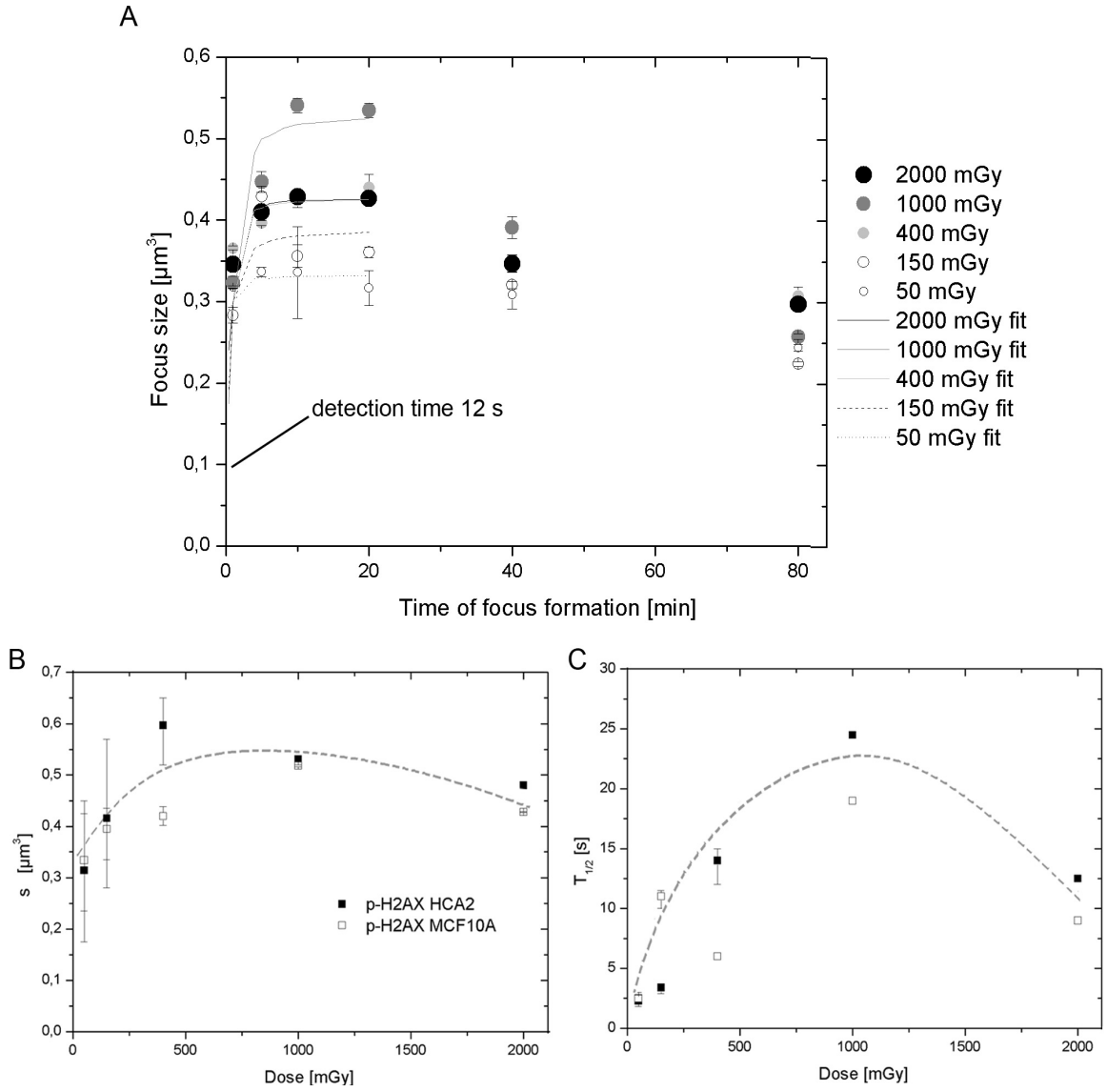

Figure 4.8: Foci size kinetics of γH2AX foci. Foci sizes in MCF10A cells plotted over time post-IR for various doses (A). Experimental data points are shown as circles, with increasing diameters with doses. Non-linear least square fits from equation 3.9 are shown as curves only for the early kinetic (< 20 min). Foci sizes were corrected for the spontaneous foci size, so that they only reflect sizes of RIF. Intersection of fit with the minimally detectable foci size (0,08 μm^3) is indicated, corresponding to a 12 s delay. (B) shows the dose dependence of the fitted maximum foci size (s_∞) for MCF10A and HCA2 cell lines. The dashed line indicates the common trend for the γH2AX marker in both cell lines. (C) shows the dose dependence of the fitted half-life for protein recruitment at damaged sites for MCF10A and HCA2 cell lines. Again the dashed line indicates the common trend for both markers.

This kind of analysis could only be performed on confocal images, since RIF volumes were necessary for the complete quantification of RIF signal.

It was possible to infer two important properties of H2AX phosphorylation at damage sites from the measurements. First, a focus was formed rapidly reaching 95% of its maximum size within 5 min (Figure 4.8A). This corresponded to a 15 s half-life (Figure 4.8C) and led to the detection of a focus by the applied imaging technique within 12 s, which is the time span it takes a focus to reach the detection threshold size of 0,08 μm^3.

Values for s_∞ and kinetic constants were similar for both cell lines, MCF10A and HCA2, which suggests a conserved chemical process for H2AX phophorylation. Second, the dose response for both fitted parameters looked parabolic with a maximum around 1000 mGy. This suggests competing events in the low and high dose range for the phosphorylation of H2AX (Figure 4.8B, C).

More specifically, the maximum size (s_∞) was largest between 400 and 1000 mGy (~0,5 μm^3) with a twofold range, and half-life for protein phophorylation was slowest at 100 mGy (~22 s recruitment) with a tenfold range between 150 and 2000 mGy.

4.1.4 Munich RIF Experiments

The algorithm used in the Berkeley RIF experiments could not be used for the experiments performed in the context of the Munich RIF experiments. Thus, a different analysis method was developed for an automatic focus detection with a set threshold.

The analysis of the foci statistic experiments was performed as mentioned in chapter 3.7 over the maximum projection of a z-stack acquired with an ApoTome®. After splitting the channels the background was subtracted from the different images and a specific threshold for optimal foci detection was applied before counting the particles (Figure 4.9).

Before setting the threshold, the images of each colour channel were compared to the corresponding images with subtracted background. Thus, it was possible to find the optimal threshold for the image analysis and particle count. If the threshold was to low, it was not possible to distinguish between foci close to each other since the outlines of these foci merged with each other. If the threshold was to high, foci with a lower intensity were not detected with the software. The chosen threshold should ensure a differentiation between foci close to each other and a distinction between background information and foci (Figure 4.10).

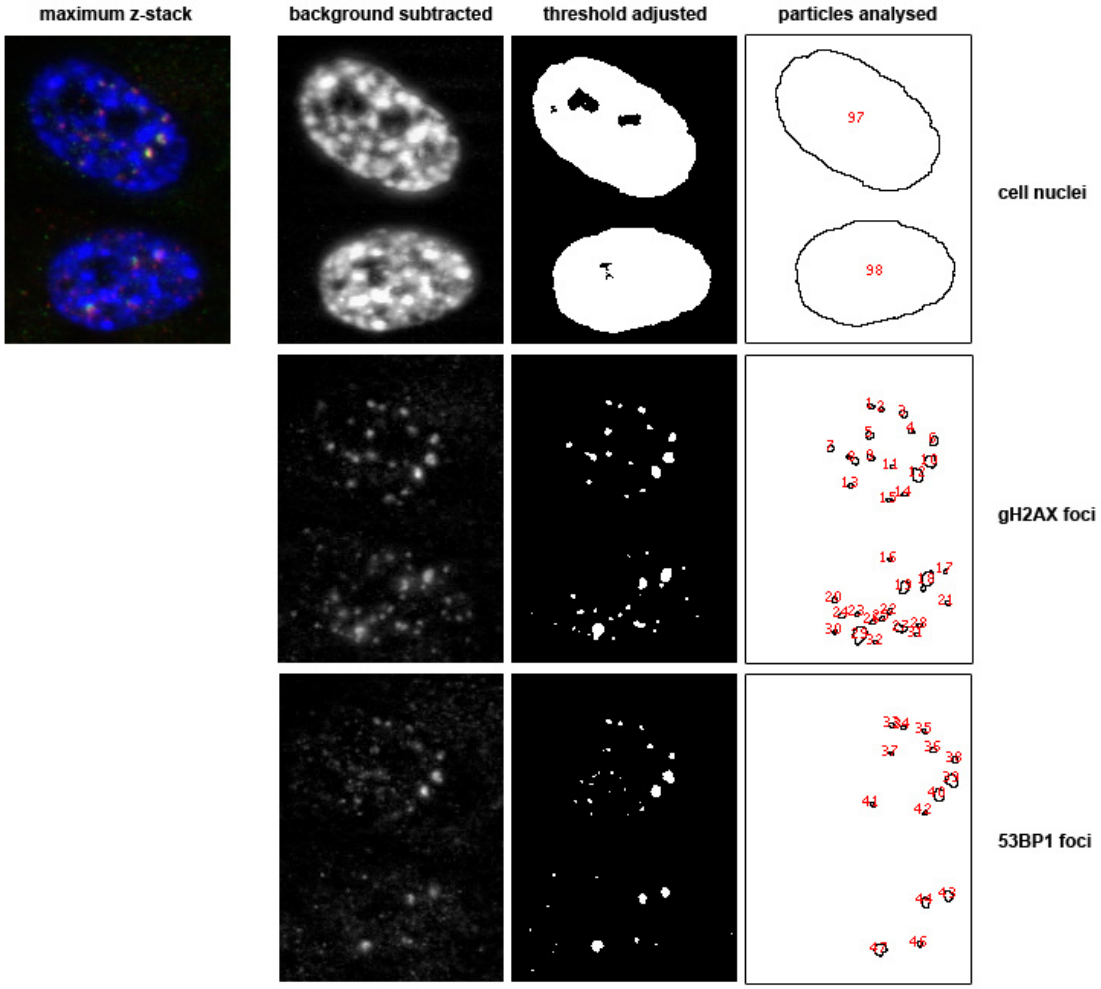

Figure 4.9: Image analysis was performed of the Munich RIF experiments via the program ImageJ. After acquiring a maximum z-projection of the z-stack, the channels of the image were split and analysed independently. First the background was subtracted from the image and then a threshold was applied, which was adjusted before. After applying the threshold the particles on the images could be counted automatically.

The adjustment of the optimal threshold was one problem in the foci analysis. Slight changes in the threshold resulted in variations in the foci counts. Thus, the threshold had to be kept constant over the whole analysis of one experiment to ensure comparability of the results. The minimum foci size detected was 4 pixel, which corresponds to a minimum detectable foci size of 0,09 μm^2.

Furthermore, a statistical error was included in the count results since a z-projection might lead to foci loss for overlapping foci especially for higher doses. Therefore, 100 nuclei were analysed manually by scrolling through the three-dimensional z-stack for each dose and the foci counts were compared with the computer data. The manual counts revealed an around 5% higher foci count than for the automatic acquired data.

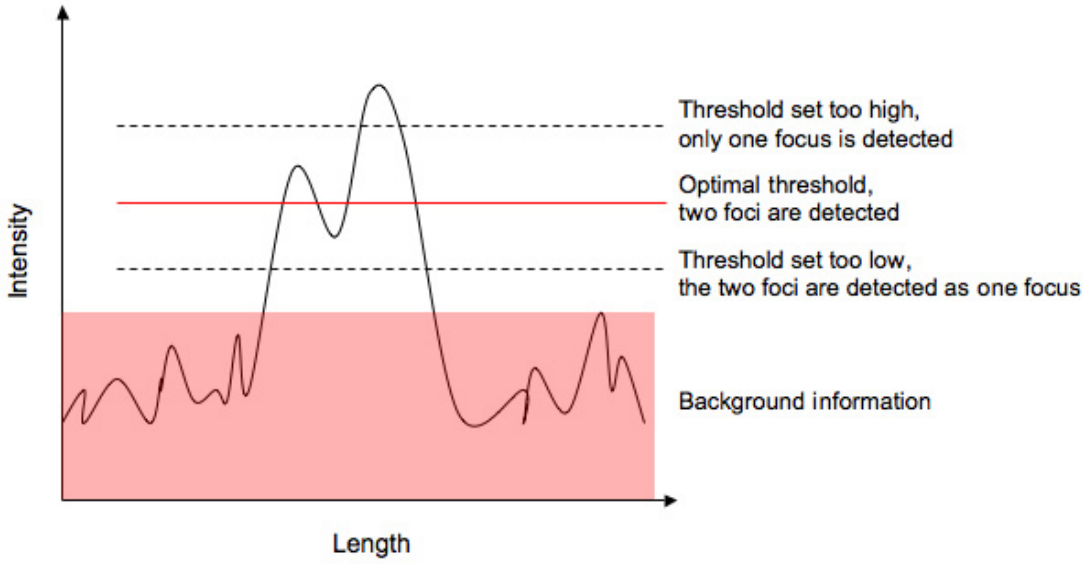

Figure 4.10: Illustration of the problems when searching the optimal threshold. The threshold has to be high enough to be able to distinguish between background information and foci. When setting the threshold to high it is not possible to detect foci with lower intensities. For a threshold set too low two foci close to each other are detected as one focus.

4.1.4.1 Separate Dose Experiments

In the process of a further development in RIF experiments with the multiwell slide, the use of a Pb stair made it possible to irradiate one slide with six different doses. Therefore, it was necessary to perform reference experiments with separate sample irradiation, due to the possible influence of Pb on the irradiation quality and, thus, the effects evoked inside the cells. It could be that the Pb absorption has an influence on the RIF formation and, thus, it would not be possible to directly compare the samples irradiated with the "same" dose for both experiments with each other. Therefore, samples cultivated on the chemically modified glass slide with a single hydrophilic spot were irradiated with different doses by changing the irradiation time but not the radiation quality.

Following irradiation the samples were fixed from 5 min to 24 h post irradiation. Both cell lines, the BJ1-hTERT and HeLa cells were analysed individually and the time response data were fitted with equation 3.5 (see Materials and Methods). A maximum in RIF/nucleus could be observed for each time response curve around 30 min post irradiation (IR).

One could argue that fitting the parameter k_1 with only one data point between the irradiation time-point and the maximum might lead to insufficient fits and values. However, as indicated in Figure 4.11 with a double logarithmic diagram of the fitted time response of γH2AX RIF in BJ1-hTERT cells, the curves pass all data points.

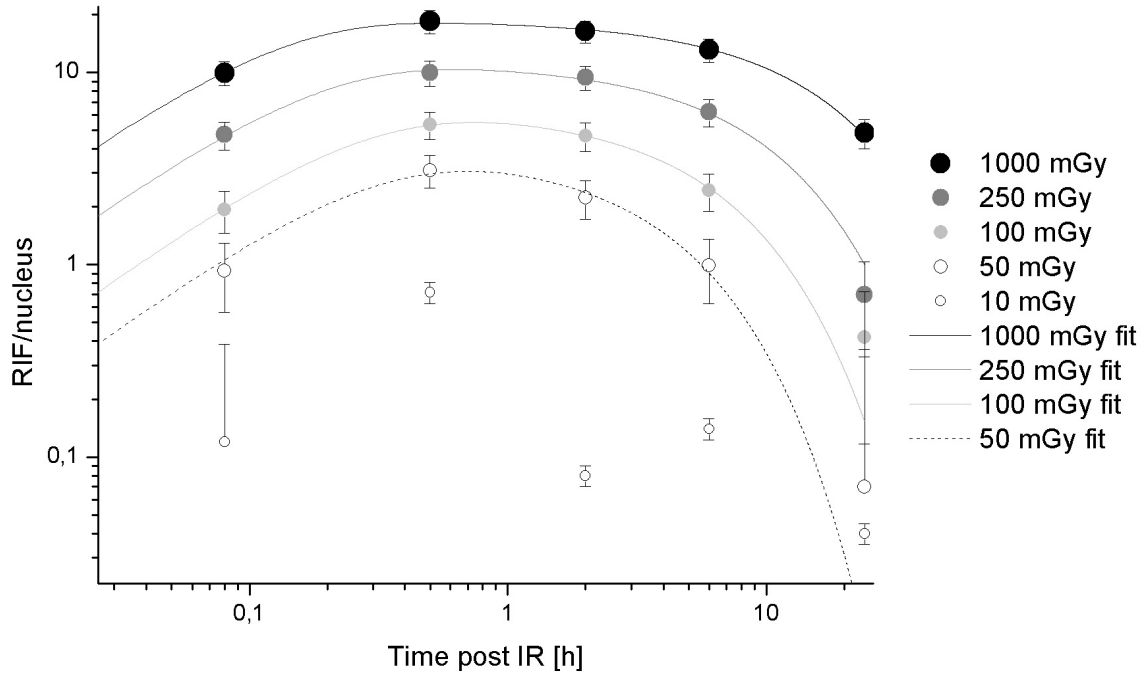

Figure 4.11: Time response of γH2AX in BJ1-hTERT cells in a double logarithmic diagram. It is possible to see, that the fitted curves do always pass the corresponding data points. Thus, fitting the evaluated data points with equation 3.5 (see Materials and Methods) leads to adequate fits and, thus, fit parameters.

For all doses exceeding 10 mGy it was possible to fit the data points with least square fits using equation 3.5 (see Materials and Methods). Some 10 mGy time responses showed a maximum like the time responses of the other irradiation doses (Figure 4.12). However, most 10 mGy samples had inconsistent values and it was not possible to fit the data (Figure 4.11). Possible slight variations between data points and fits could be prevented through more data points and more independent experiments. Nevertheless, the fits of the analysed data give a good insight in RIF yield, induction and resolution in dependence on dose.

Figure 4.12 shows the time response curves of 53BP1 RIF in BJ1-hTERT cells. These data were acquired from the same experiments as the γH2AX RIF time responses. The data of the HeLa cell reference experiments are not presented here. However, both γH2AX and 53BP1 RIF did show similar behaviour as observed for the BJ1-hTERT cells. It was also possible to fit the data of both RIF markers for doses exceeding 10 mGy. This resulted in estimates for the three fit parameter α, k_1 and k_2.

Again a decrease in foci yield normalised to dose could be observed for the data sets of both cell lines, as in the Berkeley RIF experiments and in contrast to the previously published data (9). The foci yield decreased for both foci kind in the BJ1-hTERT cell line around 3,5 fold between 50 mGy and 1000 mGy (Table 4.4). For HeLa cells a threefold decrease was observed in the foci yield for both markers (Table 4.5).

Thus, the non-linear behaviour of the RIF number in dependence on dose, which was observed in the Berkeley RIF experiments, was confirmed in these separate dose irradiation experiments (Figure 4.13A, C).

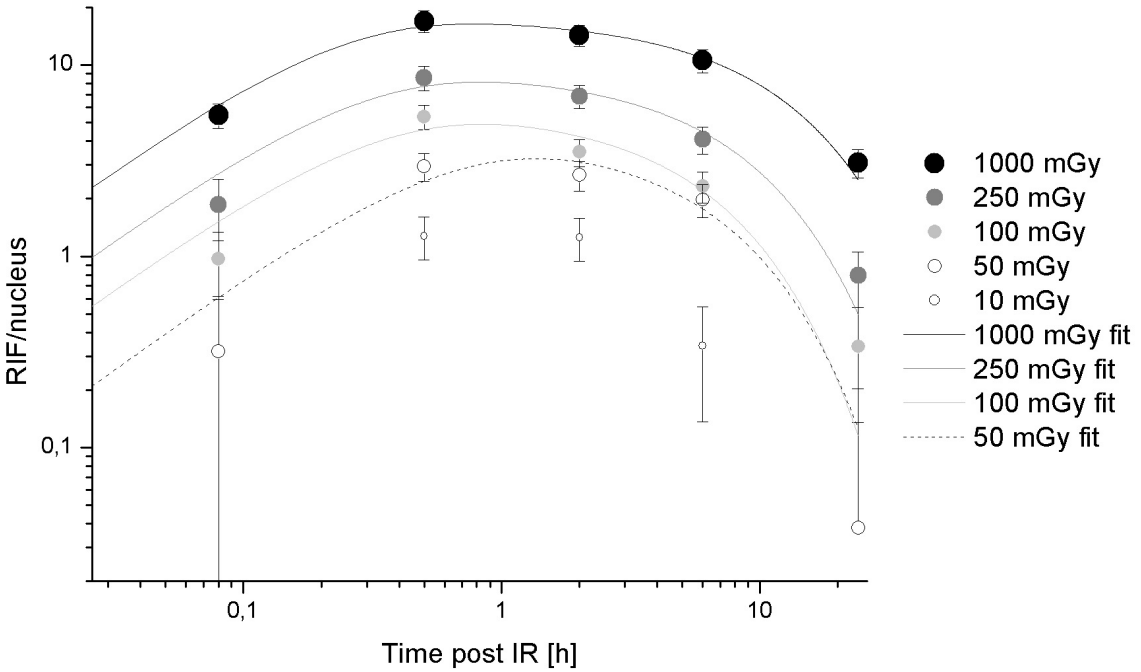

Figure 4.12: Time response curves of 53BP1 RIF in BJ1-hTERT cells fitted with equation 3.5 (see Materials and Methods). The double logarithmic diagram shows that again the fitted curves pass the data points and, thus, give good insight in RIF formation and resolution.

Also the half-lives calculated from the fit parameters k_1 and k_2 show the same behaviour as in the Berkeley RIF experiments. Foci induction was for both markers fast with half-lives below 10 min. Only the 53BP1 marker had a more than ten minute longer half-life for both cell lines for the 50 mGy sample. Foci resolution lasted again longer for higher irradiation doses for both foci in both cell lines as in the Berkeley RIF experiments (Figure 4.13B). But when comparing the determined values of both experiments, it could be observed that the foci resolution lasted considerably longer in the separate dose irradiation experiments. Going from 3 h for the 50 mGy up to 12 h for the 1000 mGy sample for the γH2AX foci in irradiated BJ1-hTERT cells. For 53BP1 an increase from 4 to 9 h was observed between 50 and 1000 mGy respectively.

For the HeLa cells the trend in the resolution half-lives was not statistically significant for γH2AX since the 50 mGy and 100 mGy samples had longer half-lives when compared to the 250 mGy sample. For the 53BP1 foci again the increase in resolution time span with dose could be observed with a statistically significant trend. It increased from 1,5 h for the 50 mGy sample up to 10 h for the 1000 mGy sample. The

resolution for 53BP1 RIF occurred faster than for γH2AX in both cell lines for doses exceeding 50 mGy (Figure 4.13D). Statistical significant trends in the development of the three parameters over dose are indicated by asterisks in Figure 4.13.

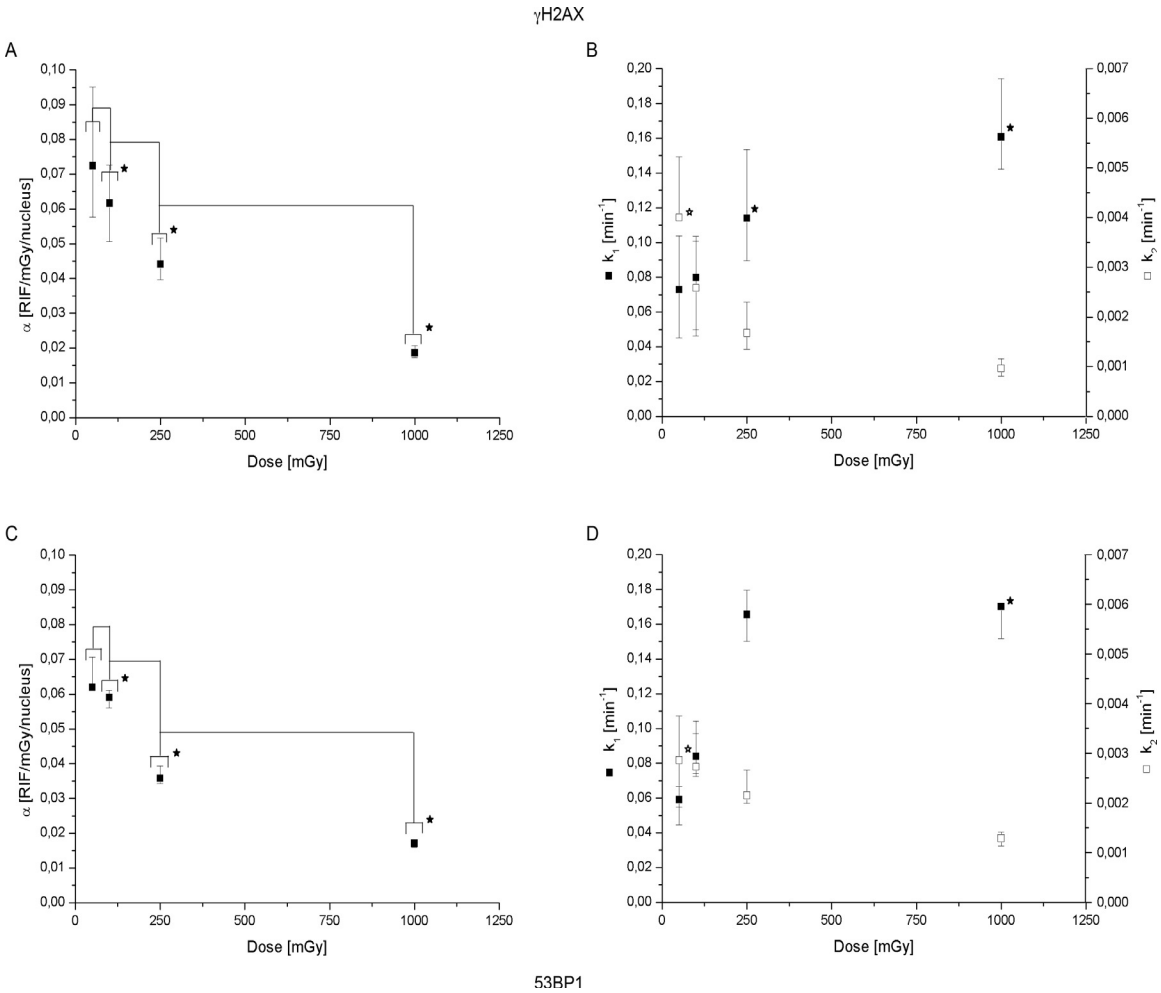

Figure 4.13: Fitted parameters for 53BP1 and γH2AX obtained from Figure 4.11 and 4.12 the time response curves of BJ1-hTERT cells. The absolute RIF yield α [RIF/mGy/nucleus] are shown for γH2AX (A) and 53BP1 (C), for both makers a faster RIF induction and slower RIF resolution was observed with increasing dose (B, D). All statistically significant trends between dose points are indicated by asterisks and were tested over a one way ANOVA and a Tukey-Kramer test.

Table 4.4: Fitted coefficients for BJ1-hTERT cells

	Dose [mGy]	RIF yield [RIF/mGy/nucleus]	$T_{1/2}$ [min] (induction)	$T_{1/2}$ [min] (resolution)
γH2AX	50	0,072	9	173
	100	0,062	9	268
	250	0,044	6	413
	1000	0,019	4	718
53BP1	50	0,07	12	242
	100	0,057	8	253
	250	0,039	5	321
	1000	0,017	4	536

Table 4.5: Fitted coefficients for HeLa cells

	Dose [mGy]	RIF yield [RIF/mGy/nucleus]	$T_{1/2}$ [min] (induction)	$T_{1/2}$ [min] (resolution)
γH2AX	50	0,035	9	787
	100	0,028	7	710
	250	0,028	7	559
	1000	0,014	5	764
53BP1	50	0,058	14	93
	100	0,052	8	235
	250	0,029	6	280
	1000	0,014	4	583

4.1.4.2 Step-Filter Irradiation Experiments

As mentioned in chapter 3.2.3 the Pb stair induced in the radiation path for successive radiation absorption might lead to alterations in the emission spectra. This change in radiation quality could also influence the radiation effects evoked in the irradiated cells. Thus, the emission spectra were calculated theoretically to better understand possible changes in the RIF formation in the step-filter experiments. The step-filter experiments can be understood as further optimisation of RIF experiments resulting in a higher throughput of more samples in shorter time.

The X-ray emission spectra after Pb absorption were calculated for the different Pb thicknesses of each step in the experimental set-up used for the step-filter experiments (Figure 4.14). All emission spectra were standardised to guarantee a direct comparison of the different spectra. The calculations revealed that the emission spectra changed indeed with increasing Pb thickness. A shift to higher photon energies could be observed as expected as well as additional fluorescence lines from Pb between 80 and 90 keV.

Thus, the spectra are getting harder through the Pb filtration, since the photons with lesser energy are absorbed more easily from the Pb than the photons with higher energies. Furthermore, less photons are reaching the sample with increasing Pb thickness. As a consequence, the average energy reaching the sample increases with the thickness, which is in correlation with higher energies reached by the photons, but lower number of photons reaching the samples.

An overview of the different spectra and the percentage of the energy in each emission spectrum under the absorption edge of Pb at 88 keV are given in Table 4.6.

When analysing the average RIF numbers per nucleus for all samples, a similar time response progression as in the separate dose irradiation experiments could be observed for γH2AX and 53BP1 in both cell lines, BJ1-hTERT and HeLa cells. Foci

maxima were reached in this experiment again around 30 min post irradiation but the average RIF numbers for both foci markers reached in each cell line always lower values than the corresponding values in the separate dose irradiation experiments.

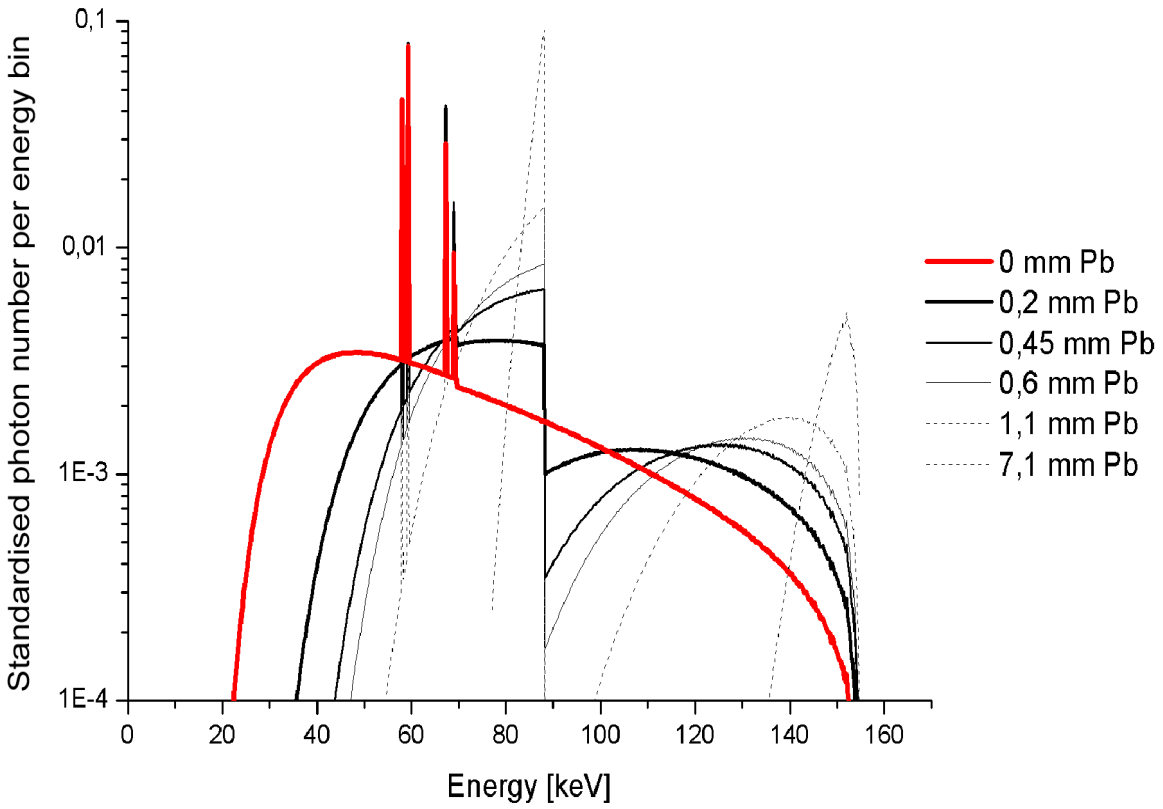

Figure 4.14: Standardised X-ray emission spectra with and without Pb absorption. For thicker Pb layers a shift to higher photon energies can be observed. Indicating the emission spectra becomes harder with increasing Pb thickness.

Table 4.6: Overview of the emission spectra without and with Pb absorption

Pb thickness [mm]	**0,00**	**0,20**	**0,45**	**0,60**	**1,10**	**7,10**
Kerma[9]/charge [µGy/mAs]	840,57	229,08	76,91	43,58	8,38	3,0e-6
Photons per area [1/(mAs µm^2)]	22,79	6,78	2,24	1,25	0,24	8,3e-8
Average energy [keV]	68,5	79,4	84,7	86,9	91,2	95,1
Kerma-percentage for E ≤88 keV [%]	76,0	66,6	65,2	65,1	66,3	76,2

Figure 4.15 shows the maximal RIF numbers reached 30 min post irradiation for both markers in BJ1-hTERT cells from both experiments. The numbers obtained for the HeLa cells showed a similar behaviour but are not shown here. A comparison of the maximal

[9] Kerma is the abbreviation for kinetic energy released in matter. It is different from absorbed dose, according to the energies involved. The Kerma is much higher than absorbed dose at higher energies, since some of the energy escapes from the absorbing volume in the form of bremsstrahlung X-rays or fast moving electrons.

values reached in both experiments revealed no difference in the values of the 1000 mGy samples. However, a difference was determined in the numbers reached by the samples irradiated with 10 mGy to 250 mGy.

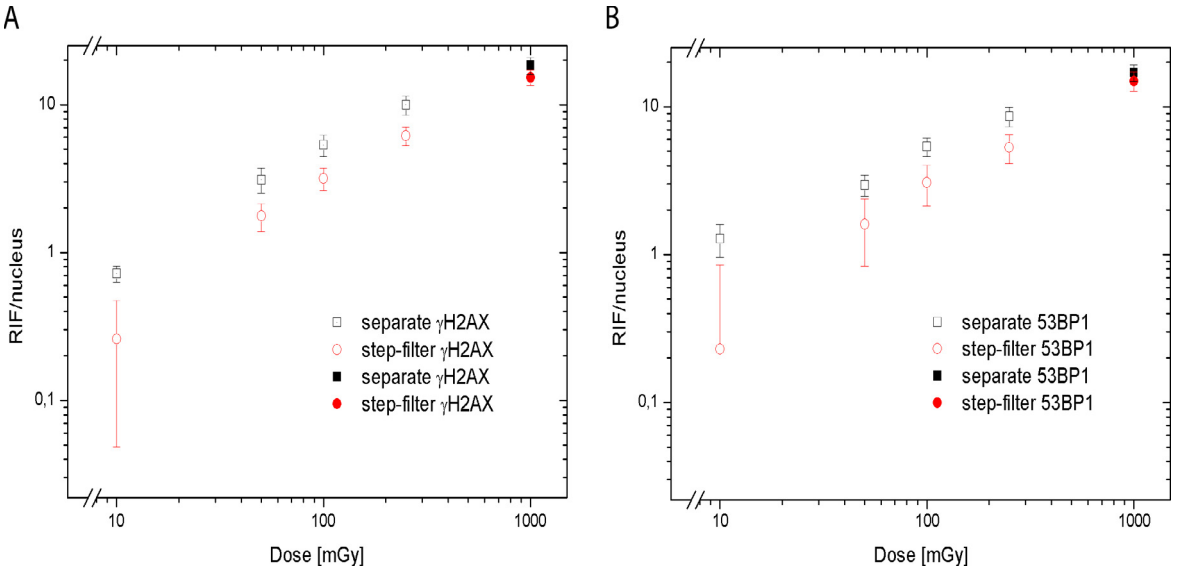

Figure 4.15: Average RIF number/nucleus 30 min post irradiation for both foci marker, γH2AX (A) and 53BP1 (B) in BJ1-hTERT cells in separate dose and step-filter irradiation experiments. No statistical difference between the RIF numbers was determined for the 1000 mGy samples for both markers (filled symbols). Thus, it was possible to directly compare the RIF numbers of both experiments with each other and to average the values in the further progress for better statistics. The RIF numbers obtained for the other irradiation samples were for both experiments statistically not comparable and could thus not be averaged.

Thus, it was not possible to compare the samples irradiated with doses under 1000 mGy of both irradiation experiments with each other. It was necessary to analyse them as samples irradiated with different irradiation doses. Thus, fitting with the same values for the parameters α, k_1 and k_2 was not possible. The 1000 mGy samples of both experiments were averaged and fitted with equation 3.5 (see Materials and Methods). To manifest the observation of the negative influence of the Pb on the radiation quality, more independent experiments with both set-ups, the separate and step-filter irradiation, are necessary to create a better statistic and to verify the differences in irradiation doses due to the Pb induced X-ray emission spectra changes.

Again it was not possible to fit the 10 mGy samples due to the inconsistent behaviour of the data. But also the 50 mGy samples implied some problems during the fitting process here. The responses were too variable to yield statistically significant fits for either marker for both cell lines (Figure 4.16). When comparing the fit parameters obtained for the other samples the same behaviour as before was observed for α, k_1 and k_2.

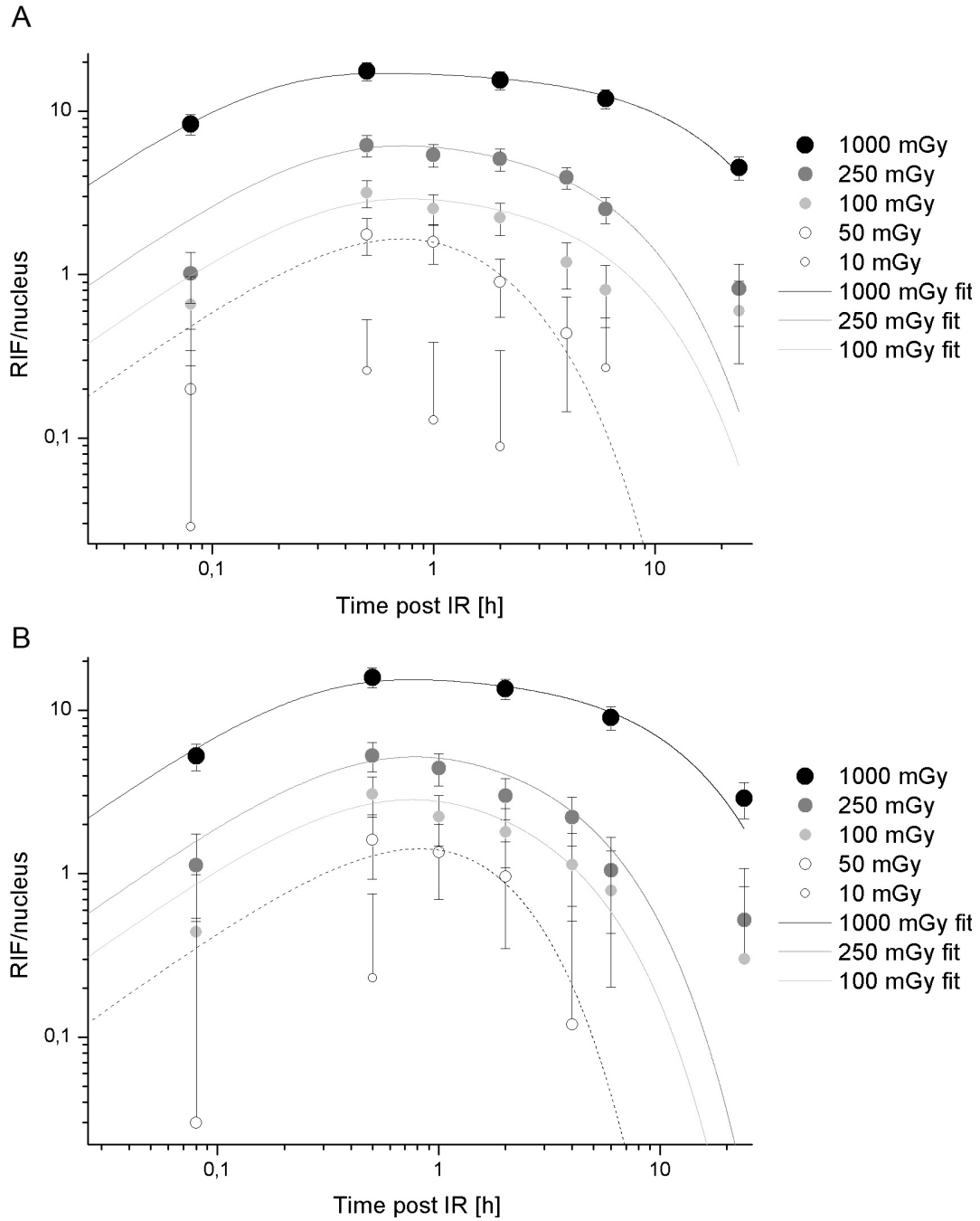

Figure 4.16: Time response of the average number of RIF/nucleus in the step-filter irradiation experiments. Background is subtracted for spontaneous foci. Panels A and B are the response for the BJ1-hTERT cells for γH2AX and 53BP1 foci respectively. Experimental data points are shown as circles, with increasing diameter with dose. Non-linear least square fits from equation 3.5 are shown as solid curves. Data points of the 1000 mGy samples are the averaged values from the separate dose and step-filter irradiation experiments since no statistical difference was observed between the maximal values reached in both experiments. The values of the other samples could not be averaged from both experiments since the Pb absorption caused a shift to higher energies in the emission spectra and, thus, had an influence on the damages caused inside the cell nuclei.

The foci yield α normalised to dose had decreasing values with increasing dose. A twofold decrease was observed for γH2AX and 53BP1 from the 100 to the 1000 mGy sample in both cell lines (Table 4.7 and 4.8).

Table 4.7: Fitted coefficients for BJ1-hTERT cells

	Dose [mGy]	RIF yield [RIF/mGy/nucleus]	$T_{1/2}$ [min] (induction)	$T_{1/2}$ [min] (resolution)
γH2AX	100	0,032	9	254
	250	0,027	8	256
	1000	0,018	5	681
53BP1	100	0,032	12	130
	250	0,024	11	158
	1000	0,017	8	456

Table 4.8: Fitted coefficients for HeLa cells

	Dose [mGy]	RIF yield [RIF/mGy/nucleus]	$T_{1/2}$ [min] (induction)	$T_{1/2}$ [min] (resolution)
	100	0,029	11	155
	250	0,017	8	307
	1000	0,014	7	624
	100	0,028	11	168
	250	0,018	9	198
	1000	0,014	7	433

Foci induction was slightly slower than in the separate dose irradiation experiments for both markers. But again a faster induction was observed with increasing irradiation dose for both markers in both cell lines, e.g. for 53BP1 in BJ1-hTERT cells a decrease from 9 min (~0,07 min^{-1}) for the 100 mGy sample to 5 min (~0,13 min^{-1}) for the 1000 mGy sample was determined. For the RIF resolution slightly shorter time spans were determined in these experiments when compared to the separate dose irradiation experiments but still the durations were increasing with irradiation dose. For 53BP1 in BJ1-hTERT cells an increase in RIF resolution from 4 to 11 h for the 100 to 1000 mGy was observed respectively. In both cell lines the resolution of the 53BP1 RIF occurred faster than for the γH2AX RIF.

4.1.4.3 Fractionated Irradiation Experiments

Apart from the changes induced by the successive X-ray absorption through Pb in cells the step-filter set-up is still a valuable tool for RIF experiments. It provides the possibility to irradiate samples with e.g. different doses and radiation qualities, followed by a second irradiation of the whole sample with the same dose. Thus, differences in RIF formation and resolution can be observed for different radiation doses and qualities in connection with a fractionated irradiation in a simple way through the multiwell slides.

Consequently, it is also possible to investigate the cellular response in context of occurring adaptive response due to fractionated irradiation.

When analysing the fractionated irradiated samples no trends in the time responses of both cell lines were observed. More independent experiments must be performed with this experimental approach, in order to clearly understand cellular behaviour after fractionated irradiation. After the analysis of only one experiment in the context of this experimental approach it is not possible to make a definite prediction about the time responses and possible trends since the time responses cannot be compared to the responses of the experiments with a one-time irradiation. Thus, only the γH2AX data of the fractionated irradiation with BJ1-hTERT cells are presented here without fitting the data with equation 3.5 (see Materials and Methods). Comparable time responses were observed for 53BP1 in BJ1-hTERT cells. HeLa cells showed for both markers time responses with slight divergence from the response curves of the BJ1-hTERT cells but did not look completely different.

Both cell lines had time responses as expected for the fractionated irradiation where first and second irradiation were carried through right after another. A maximum was reached in this experiment for all samples 30 min post IR (Figure 4.17).

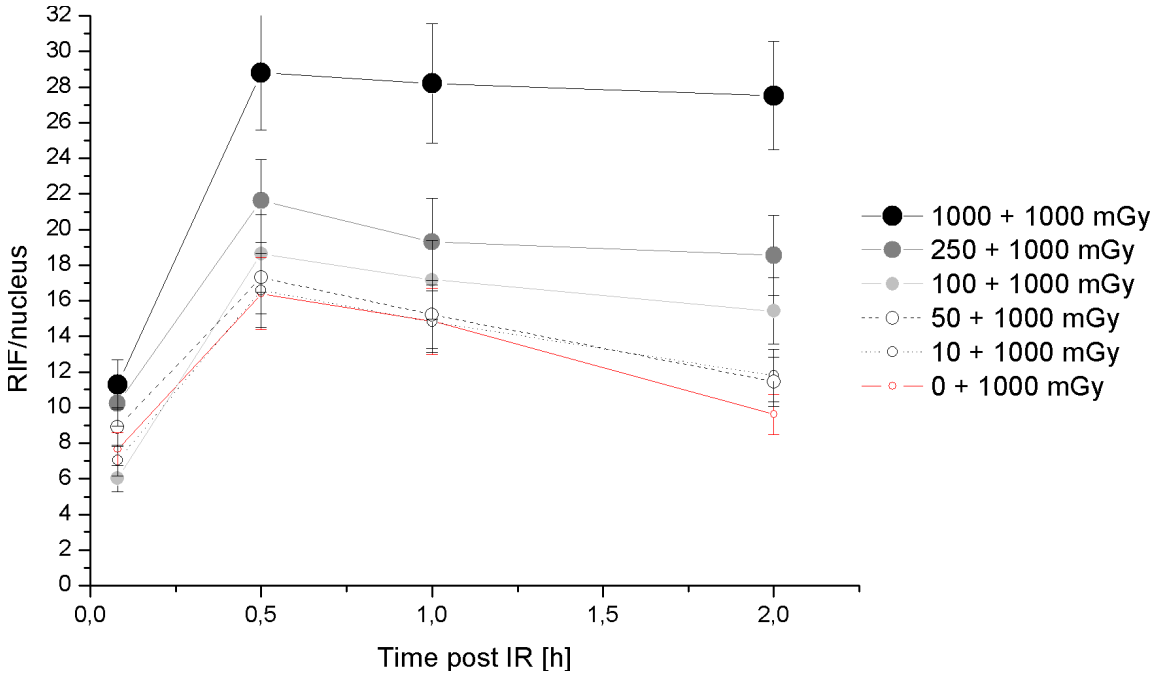

Figure 4.17: Time response of the average number of RIF/nucleus in the fractionated irradiation experiment where first and second irradiation were carried through right after another for γH2AX RIF in BJ1-hTERT cells. All time responses did show a maximum after around 30 min following the second irradiation. The differentiation between the maxima of the lower irradiation doses was not possible when including the statistical errors in the analysis. The values were overlapping.

The maximal values reached enabled a differentiation among the different irradiation doses applied to the samples in both cell lines for both markers. They were increasing with increasing irradiation dose. However, the difference in the number of RIF/nucleus was insignificantly small between the 1000 and 10 + 1000 mGy samples for the γH2AX marker in BJ1-hTERT cells. Furthermore, also the differentiation between these samples and the 50 + 1000 mGy and 100 + 1000 mGy samples was not exactly possible when including the statistical errors in the analysis.

A change in the time response behaviour of the different samples was observed for the fractionated irradiation with 30 min between first and second irradiation. The maximal values were observed for all samples under the RIF numbers per nucleus in the reference irradiation experiment. Furthermore, all samples showed an increase in the beginning of the time post IR and a decrease after the reached maximal value around 30 min after the second irradiation apart from the 250 + 1000 mGy sample (Figure 4.18).

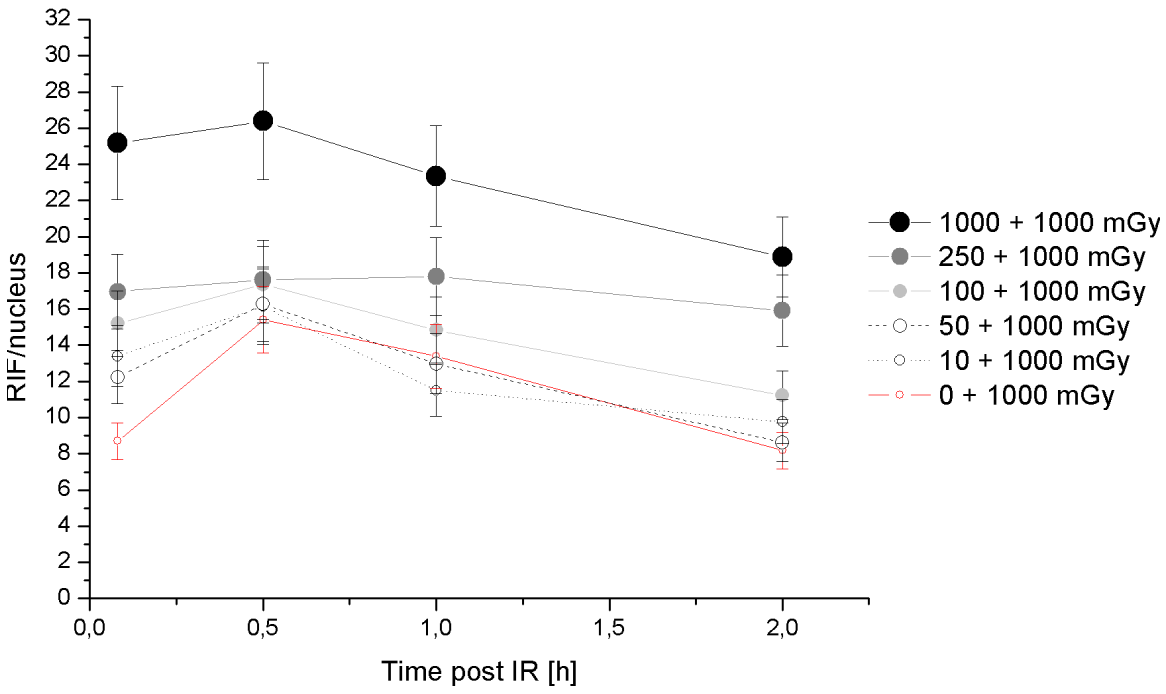

Figure 4.18: Time response of the average number of RIF/nucleus in the fractionated irradiation experiment where first and second irradiation were carried through 30 min apart for γH2AX RIF in BJ1-hTERT cells. Again all time responses did show maximal values around 30 min following the second irradiation. However, the values were lower when compared to the reference experiment and the increase in RIF number was also not so big since the cell nuclei had already higher number of RIF due to the first irradiation. It was difficult to differentiate between the maxima of the samples irradiated with doses less than 2000 mGy in total. Furthermore, the 1000, the 10 + 1000 mGy, and the 50 + 1000 mGy samples had also in the further curve progression very similar RIF numbers.

However, the increase in RIF number per nucleus was not as big as for the reference samples since the samples were irradiated again when they had reached their foci

maxima from the first irradiation. Thus, the number of "background" RIF was higher than in the reference fractionated irradiation experiment. The 250 + 1000 mGy sample had over the whole time response almost constant values with only a slight increase and decrease in the values. In this experiment the maximal values of all samples irradiated with less than 2000 mGy in total were again close to each other making a differentiation difficult. Furthermore, the RIF numbers reached at later time-points were in the same range for the 1000, the 10 + 1000 and the 50 + 1000 mGy samples.

The time response curve of the 250 + 1000 mGy sample had also more or less constant values for the fist three time-points for the fractionated irradiation experiment where the second irradiation took place 1 h after the first (Figure 4.19). But the RIF number per nucleus showed a slight decrease at the last time-point.

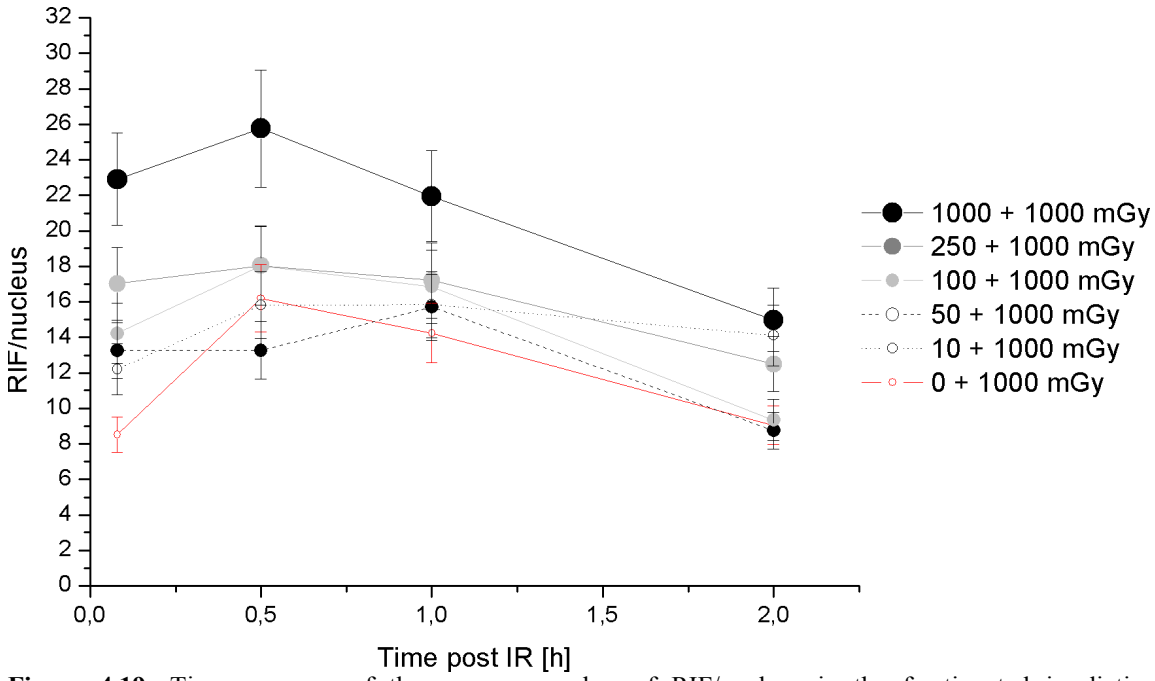

Figure 4.19: Time response of the average number of RIF/nucleus in the fractionated irradiation experiment where first and second irradiation were carried through 1h apart for γH2AX RIF in BJ1-hTERT cells. The increase in RIF number was again steeper in this experiment until maxima were reached. But still flatter than the increase in the reference samples. Whereas all samples did reach their maximum around 30 min post the second irradiation the 50 + 1000 mGy sample had its maximum 1h after the second irradiation. It had constant values at the first two time-points, and then a maximum followed by a fast decrease in RIF number. Again it was difficult to differentiate between the values reached by the different samples irradiated with doses under 2000 mGy in total.

The 1000 mGy sample again showed a similar curve progression as for the reference experiment. Also the 10 + 1000 mGy, the 100 + 1000 mGy, and the 1000 + 1000 mGy sample showed an increase in RIF number until a maximum was reached at 30 min post the second irradiation and then a decrease. The increase in RIF numbers was for this experiment steeper in the beginning of the experiment as for the experiment where the

second irradiation took place only 30 min after the first irradiation. Nevertheless, it was still flatter when compared to the reference samples. The decrease in RIF number per nucleus was noticeable slower for the 10 + 1000 mGy sample than for the others. The time response of the 50 + 1000 mGy sample did first show constant RIF numbers for the first two time-points than a maximum at the third time-point followed by a fast decrease. It was not possible to distinguish between the maximal values reached by the 1000 mGy and the 10 + 1000 mGy samples as well as the numbers reached by the 100 + 1000 and 250 + 1000 mGy samples.

All time response curves showed a maximum followed by a decrease in RIF number per nucleus for the fractionated irradiation experiment, where the second irradiation took place 2 h after the first irradiation (Figure 4.20).

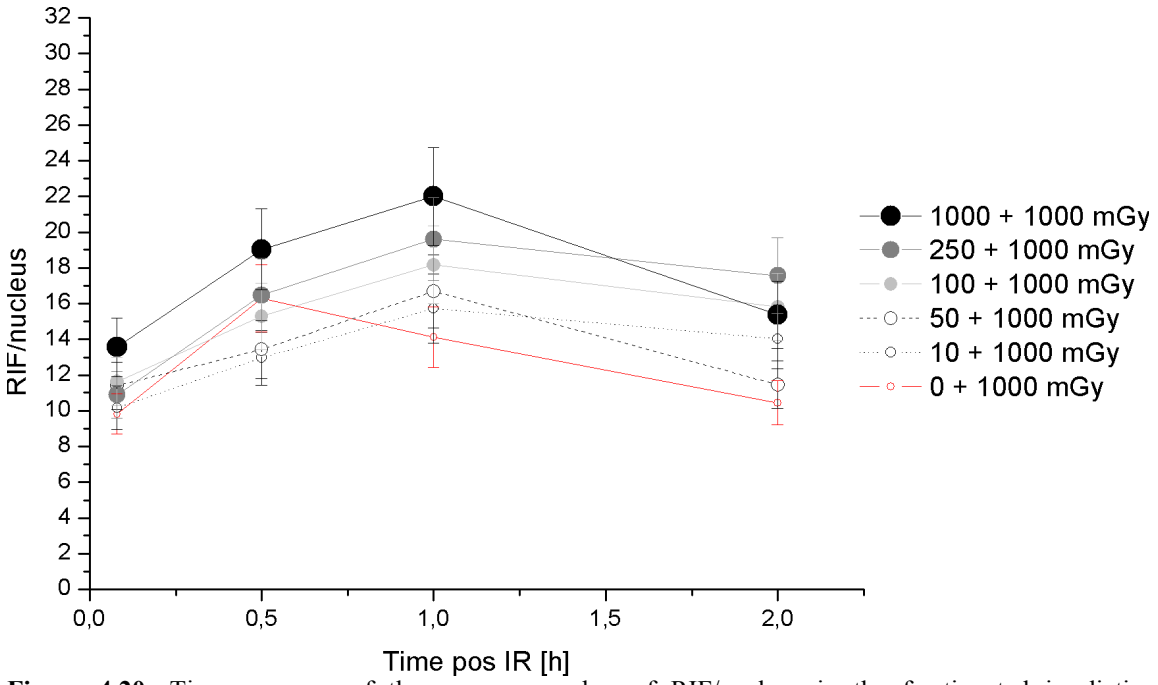

Figure 4.20: Time response of the average number of RIF/nucleus in the fractionated irradiation experiment where first and second irradiation were carried through 2 h apart for γH2AX RIF in BJ1-hTERT cells. The 1000 mGy sample had again a similar curve progression as in the other experiments. However, the other samples did show a shift in the time-point when the RIF maxima were reached 1 h after the second irradiation. Furthermore, the 1000 + 1000 mGy and the 50 + 1000 mGy samples did show a faster decrease in their RIF numbers when compared to the other samples.

Whereas the maximum for the 1000 mGy sample was reached 30 min post the second irradiation, the maxima of the other samples were reached without exception 1 h post the second irradiation. The whole time response of the 1000 mGy sample was comparable to the corresponding reference sample. The other samples did show some difference in their further curve progressions after the reached maximum. A faster reduction in RIF number per nucleus was observed for the 50 + 1000 mGy and 1000 + 1000 mGy samples, while

the 10 + 1000 mGy sample, the 100 + 1000 mGy and the 250 + 1000 mGy samples all showed a slower RIF resolution. The 1000 + 1000 mGy sample had even a RIF value under the 250 + 1000 mGy sample.

Table 4.9 gives an overview of the maximal RIF numbers reached in each experiment by the different samples as well as the time-points when the maxima were reached for γH2AX in BJ1-hTERT cells.

Table 4.9: RIF maxima and time-points when maxima were reached for γH2AX in BJ1-hTERT cells.

	2. irradiation 0 min		**2. irradiation 30 min**		**2. irradiation 1 h**		**2. irradiation 2 h**	
	RIF	**T_{max} [h]**	**RIF**	**T_{max} [h]**	**RIF**	**T_{max} [h]**	**RIF**	**T_{max} [h]**
1000 mGy	16,39	0,5	15,41	0,5	16,2	0,5	16,29	0,5
10 mGy+	16,59	0,5	16,14	0,5	15,84	0,5	15,72	1
50 mGy+	17,29	0,5	16,27	0,5	15,7	1	16,69	1
100 mGy+	18,65	0,5	17,36	0,5	18,03	0,5	18,18	1
250 mGy+	21,61	0,5	17,79	1	18,03	0,5	19,61	1
1000 mGy+	28,81	0,5	26,39	0,5	25,75	0,5	22	1

4.2 Discussion

4.2.1 The next Step in Radiation-induced Foci Experiments

Single time or dose points are snapshots and might not capture the necessary complexity of the response of DNA damage sensing proteins. In contrast, the methodology and the mathematical kinetic model presented here can characterise the DNA damage response simultaneously over both time and across dose levels. Several modifications to cell culture and foci analysis methods, which started with the experiments performed in Berkeley, allowed to achieve time vs. dose matrix experiments (irradiation with two different doses Figure 3.10) and in the further process also time vs. step-filter irradiation experiments (irradiation with six different doses Figure 3.4).

The use of microwells created an array of independent cell cultures, which allowed the analysis of various treatments on a single slide. This led to lower volumes of higher antibody concentrations during immunostaining, which enabled a fast (1 h) and low cost immunostaining. At the Helmholtz Zentrum München the automation of the immunostaining with the BioSpot® pipetting robot was performed successfully, which

improved even more the immunostaining optimisation (chapter 4.1.1). Furthermore, the regular spacing between the cell cultures on the multiwell slide enabled an automated microscopic imaging of the samples.

In addition, the automatic image analysis performed in Berkeley enabled the quantification in an unbiased manner of thousands of nuclei over several cell types. It combined different imaging modalities across time and dose. This provided strong statistical significance, which indicated a DNA damage response that was altered across increasing doses of ionising radiation (chapter 4.1.3.1). The analysis performed at the Helmholtz Zentrum was only semi-automatic since the threshold was set manually after visual analysis of the images. However, the inclusion of a threshold in the image analysis as well as its constant value over the analysis enabled a stable quantification of the images and, thus, led to better statistics. The results did confirm the observed alteration in DNA damage response with dose, observed in the Berkeley RIF experiments (chapter 4.1.4.1 and chapter 4.1.4.2).

The introduced system combining multiwell slides, automatic image analysis as well as a biophysical model revealed a systematic dose dependence of RIF formation-disappearance, which was validated across cell lines and DNA damage markers. Further improvements in microwell, cell array and lab on a chip techniques, will further benefit this approach and, thus, possibly lead to a common approach in RIF experiments.

4.2.1.1 Radiation-induced Foci Frequencies saturate with Dose

As recently reviewed (103), most studies in the literature report RIF yield well below the expected 25-35 DSB/Gy measured by PFGE in G1 cells (9, 104). These findings probably reflect that the measured values at any time-point are the numbers of RIF, which were formed since the irradiation minus the number of RIF, which were already resolved. Furthermore, these numbers also do not account for RIF, which have not yet appeared. The biophysical model introduced in this work can fit the kinetic curves observed for the number of RIF per nucleus and accounts for these missing RIF.

The fits obtained from the model suggest that the absolute RIF yield normalised to dose (α) is not constant over radiation dose but varies. A two- and threefold decrease between 150 mGy and 2000 mGy was observed in the matrix experiments with MCF10A and HCA2 cells (Table 4.2, 4.3). Furthermore, a 3,5 and threefold decrease, and a three and 2,5 fold decrease were observed in the separate dose (Table 4.4, 4.5) and step-filter irradiation experiments (Table 4.7, 4.8) with BJ1-hTERT and HeLa cells respectively.

This determined dose dependence of α indicates that there cannot be a 1 to 1 equivalence between DSB and RIF, as first assumed with a constant yield of DSB/Gy/nucleus for cells in the G1 phase and as previously published (9).

The lower RIF yield per Gy observed with increasing dose for both RIF markers 53BP1 and γH2AX in all cell lines might indicate saturation of the kinase, which phosphorylates H2AX or a depletion of the stores of 53BP1. Even in flow cytometry data a saturation had been suggested for the total amount of γH2AX per cell with increasing dose (105). Whereas, the observed change in RIF yield per Gy was less dramatic in this study for doses between 1 - 8 Gy, it was significant for doses between 0 - 1 Gy. This saturation effect may also reflect the quantised nature of H2AX into spatially confined clusters, as suggested by high resolution 4Pi microscopy (101).

While the determined RIF yields were below the expected 25 - 35 DSB/Gy for higher doses (1000 and 2000 mGy), the introduced analysis method led to RIF yields in good agreement with the expected values of DSB/Gy for the lower dose range (100 to 400 mGy) for both markers. However, the RIF yields were above the maximal expected 35 RIF/Gy for the lowest irradiation doses in the Berkeley and Munich RIF experiments (150 mGy, 50 mGy). It would be interesting to confirm this trend statistically for low dose irradiation by increasing the sample size at lower doses.

One could argue that the observed non-linearity of RIF yields depends on the substrate on which cells are growing or the cell line used for RIF experiments. However, cells were not only cultivated on the multiwell slides but also in 8 well chamber slides, which did show the same DNA damage response. Furthermore, four different cell lines were used in the different RIF experiments, all leading to the same results. Thus, neither the substrate nor the cell line used could be the reason for the observed non-linearity in foci yield.

4.2.1.2 Kinetic Constants are Dose Dependent

The same trends were observed over both DNA damage markers and cell types studied in the different experiments: i.e. as the IR dose increased RIF formation was faster and RIF remained longer in the nucleus.

It has previously been shown that DSB repair kinetic correlates with RIF resolution (106, 107). Before the discovery of RIF, the DNA repair could only be monitored by electrophoresis or neutral filter-elution using very high doses (> 10 Gy).

These methods have shown that repair kinetic typically has two phases: a rapid repair (5-30 min half-life) and a slower one (4 to 10 h half-life) (108). In comparison, the kinetic constants reported here are in good agreement with these repair kinetics, with half-lives for foci resolution as 45 to 65 min for low doses (50 mGy and 150 mGy) and as slow as 10 to 12 h for 1000 and 2000 mGy (Tables 4.2 and 4.3, Tables 4.4 and 4.5, Tables 4.7 and 4.8).

Assuming that resolution kinetics reflect the ability to repair DNA, these results give new insights as to what kind different factors, e.g. LET might result in either slow or fast repair (102). The complexity of a lesion has been associated with the repair time. Thus, higher doses or higher LET would lead to more complex lesions and, consequently to slower repair rates. For example, low LET IR (X-rays) only induces 30% of complex DNA damage, whereas high LET (1 GeV/amu Fe) elicits 70% of complex DNA damage (109, 110). Thus, when assuming a Poisson distribution for the numbers of complex DSB with decreasing X-ray dose, one will start to observe subpopulations of cells without any complex DSB. In detail, at 400 mGy 98,5% of the cells will have at least one complex DSB, while at 150 mGy only 80% will have at least one complex DSB. Nevertheless 99% of the cells irradiated with 150 mGy will have some kind of DSB. The lack of a complex DSB in this 20% subpopulation for 150 mGy irradiation may elicit a different response, misrepresenting the overall dose response. As a consequence, the dose dependent change in the half-lives for DSB detection is in agreement with this concept. For higher irradiation doses faster DSB detection was observed, e.g. 1,6 times faster at 2000 mGy than at 150 mGy (Berkeley) as well as 2,3 faster at 1000 mGy than at 50 mGy (Munich).

4.2.1.3 Protein Recruitment at DNA Damage Sites

Fitting the RIF size response from the mathematical model also provided some insights into the study of protein recruitment at DNA damage sites. Figure 4.8 illustrates such response acquired by confocal microscopy for both human mammary epithelial cells and human skin fibroblasts. The model introduced in this work shows that the assumption of a finite amount of H2AX proteins being phosphorylated at the DNA damage site as well as a limited amount of kinase is adequate to account for the early foci size kinetic.

However, this was only clearly apparent at doses exceeding 400 mGy. The maximum RIF size for γH2AX (S_∞) was dose dependent indicating two competing events between high and low doses (Figure 4.8B). At low doses, S_∞ was smaller, probably

reflecting the fact that the cell elicited a different response. It was maximal between 400 and 1000 mGy (S_∞ = 0.55 μm^3). At 2000 mGy S_∞ again got smaller, adding the evidence of kinase saturation. The RIF γH2AX size saturation is a circumstance, which was reported previously in studies without correction for DSB detection kinetic (10, 105).

Furthermore, also insight into another aspect of RIF formation is provided in Figure 4.8. One could question the result that RIF yields were always lower than the expected number of DSB due to the possibility that some DSB got repaired before they could elicit a focus large enough to be detected by microscopy (111). However, the foci size analysis suggests that half of the H2AX histone proteins are phosphorylated near the site of damage within 5 - 25 s (Figure 4.8C). Furthermore, taking into account that a focus of size 0,08 μm^3 can be resolved unambiguously by microscopy, a 12 s delay was estimated between RIF formation and its possible detection. This means, all DSB eliciting the formation of a RIF should be detected by immunostaining within less than one minute. In addition, the fact that corrected RIF sizes decreased after 20 min may reflect a second phase where less H2AX must stay phosphorylated in order to recruit other repair proteins to the damage site.

4.2.2 What Kind of Cellular Reaction can be evoked through Fractionated Irradiation

Fractionated irradiation experiments did not show a consistent trend and are not shown completely in this work. For robust results and better statistics more independent experiments have to be performed to be sure that the observed cellular reactions in RIF formation and resolution are consistent over the experiments.

However, since all of the 1000 mGy samples did show a similar behaviour for the four different irradiations, it can be assumed that the observed results were not completely wrong (Table 4.9). Furthermore, the time responses of the reference fractionated irradiation experiment all showed the expected progression with a maximum 30 min post irradiation (Figure 4.16). In further experiments, maxima of RIF number per nucleus were always reached by each sample. No consistent trend was observed for the maximal values reached in the different experiments by the corresponding samples.

The decrease in the maximal values reached by the 10 + 1000 mGy and 1000 + 1000 mGy samples in the different experiments could be some kind of process in context of adaptive response (Table 4.9). The effect of adaptive response is the alteration in the response to an external stress, which results in a lower than expected biological response

(112). Therefore, cells are for example irradiated with a very low trigger dose followed by an irradiation with a higher dose and, thus, resulting in different radiation responses.

However, experiments with fractionated irradiation, thus, pre-exposure of lymphocytes to doses as low as 10 mGy of X-rays showed that the cells became adapted (113) and that adaptive response required a certain minimal dose before it became active. Thus, adaptive response occurs only within a relatively small window of dose, it is dose-rate dependent and depends on the genetic constitution of the irradiated subject. Furthermore, it did not occur instantaneously but took approximately 4 – 6 h to become fully active (114). Consequently, one can argue that it is most likely that the reduced RIF number of the 1000 + 1000 mGy sample is not due to adaptive response but due to some other effect induced through the pre-exposure to ionising radiation since the priming dose of 1000 mGy is not within the small window of adaptive response inducing priming doses. However, the 10 mGy priming dose could have evoked an adaptive response in the cells.

Another explanation for the reduced RIF numbers could be that the fractionated irradiation resulted in the accumulation of DNA damage and, thus, RIF clusters (115). A RIF cluster formation, which was already reasoned from the dose dependent behaviour of the fit parameters, could also occur in fractionated irradiation experiments. Thus, it would not be possible to conclude from the number of RIF to the number of DSB induced in a cell through the irradiation. However, by combining the fractionated RIF experiments performed on multiwell slides with PGFE analysis it would be then feasible to determine the relation between DSB and RIF number for these experiments.

Apart from the uncertainties in the cellular behaviour due to the not observed trend, the results from the reference fractionated irradiation (Figure 4.16) showed that the cellular reaction was not affected by further external stress factors, e.g. repeated in and out of the incubator during the experiment. Thus, the use of the multiwell slides and the step-filter irradiation set-up would enable a fast and low-cost analysis over a wide range of fractionated irradiated samples. By performing more experiments with this set-up including alterations in the dose rate, the priming doses, time intervals between first and second irradiation as well as different cell types would lead to a good insight into the response of cells to fractionated irradiation and, thus, might give insights into the optimisation of tumor irradiation.

4.2.3 Lead Absorption changes the X-ray Emission Spectra

By calculating the X-ray emission spectra for the different Pb thicknesses it was possible to observe a shift to higher energies (Figure 4.14). This shift to higher energies can be explained through the exponential decrease in X-ray radiation intensity when passing matter (chapter 3.2.3). Photons with lower energies are absorbed earlier and, thus, a successive reduction in photons numbers at lower energies is observed.

However, the ability of great attenuation and absorption decreases fast with increasing photon energies. Thus, it is possible to describe the increase in the emission spectrum generated by the thickest Pb step at higher keV. However, since the number of photons is strongly decreasing for higher keV the decreasing absorption is generally not observed. If the spectra were flat before the Pb filter this behaviour could be observed all the time. Only for increasing Pb thickness the spectra are getting flatter for higher keV and the observed increase in the spectrum is becoming visible.

To understand up to which point the altered emission spectra have an influence on the irradiated samples, one has to analyse the principle mechanisms of energy deposition by photons in matter. Photons are not charged and, thus, have the ability to travel some distances in matter before interacting with an atom. The probability of photon interaction in matter is described statistically by the linear attenuation coefficient μ (21). μ depends on photon energy as well as on the material being traversed. The linear attenuation coefficient for photons of a certain energy in a material includes the individual contributions from the different physical processes that can occur between photons and matter. This includes the interaction through the photoelectric effect, Compton scattering as well as pair production (83). Figure 4.21 shows the mass attenuation coefficient μ/ρ of water since cells consist of a considerable amount of water. Furthermore, the attenuation coefficients of the photoelectric effect, Compton scattering, pair production and for comparison the Rayleigh scattering are displayed as well.

At photon energies < 15 keV the photoelectric effect is the predominating effect and accounts for practically all of the interactions since the binding of the atomic electrons is important in this energy range. With rising photon energy the contribution of the photo electric effect drops rapidly and goes below the percentage of Compton scattering. At around 30 keV the contribution of photoelectric effect and Compton effect are equal. For photon energies equal or greater than hundred keV the dominant interaction is the Compton scattering since the binding of atomic electrons becomes

relatively unimportant. Above 1,022 MeV pair production is the most probable effect (21). The relevant energy range in the Munich RIF experiments was between 20 and 157 keV (light red area in Figure 4.21).

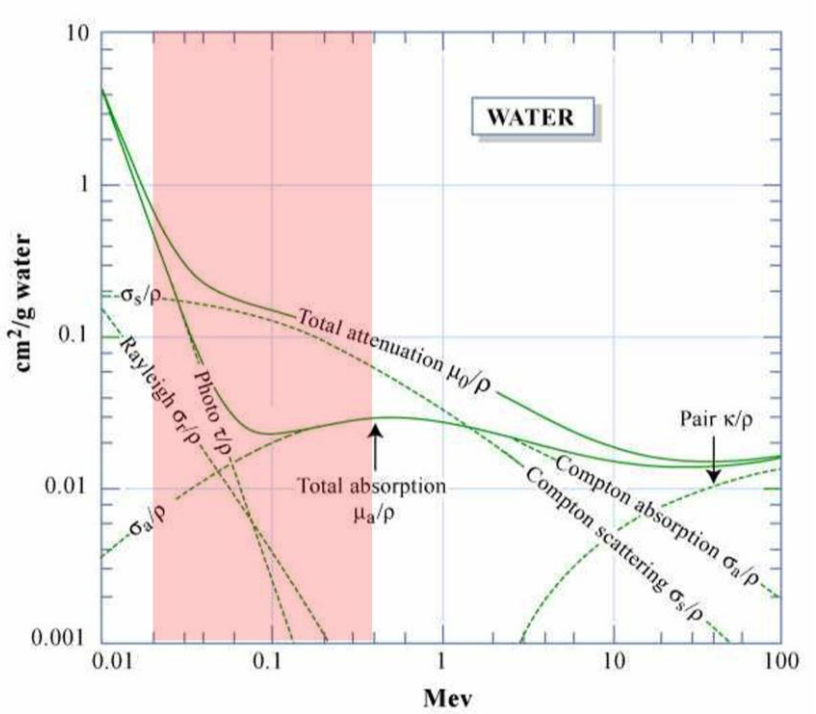

Figure 4.21: Mass attenuation and energy-absorption coefficients as functions of energy for photons in water. At the lowest energies, the photoelectric effects accounts for more or less all of the interactions. As the photon energy rises this contribution drops and goes below the Compton scattering, which is then for energies equal or higher 100 keV the dominating effect. The Compton coefficient decreases with further increasing energy, and pair production becomes the dominant process (116).

Since the photoelectric effect is predominating at lower keV a successive absorption of these energy ranges through the insertion of Pb decreases the probability of occurring photoelectric effects in the samples. This possibly reduces the number of induced double strand breaks and, thus, RIF (Figure 4.15). The photoelectric effect is compared to the Compton effect more local and, hence, induces more damage. However, the differences observed in the maximum RIF numbers reached is not as obvious and to preclude the possibility that this effect was not only evoked due to an artefact, more independent experiments should be performed with this set-up. If the observance was only an artefact, it is possible to compare the results of both experiments, the separate dose and step-filter irradiation experiments and average them to get more robust statistics and an optimal prediction of the fit parameter. Furthermore, the step-filter irradiation can be used as further optimisation in RIF experiments, with multiple samples on one slide.

5 Dynamic and Real Time Experiments

5.1 Results

While RIF experiments give only snapshots of the cellular response after irradiation, it is possible to observe the long-term effects evoked in cells via cytokinetic experiments. Thus, the arising changes induced by ionising radiation, i.e. in cell growth behaviour, can be analysed. Combined with the microscopic analysis of a certain area in the cell culture over the same time span, cell growth experiments are a valuable tool to investigate the influences of ionising radiation on cellular growth and behaviour.

5.1.1 GFP Plasmid Transfection

GFP Transfection of Human Fibroblasts

For the analysis of the influences induced by ionising radiation on cycling cells growing in co-cultures, it was necessary to distinguish between different cell cultures as well as irradiated and not-irradiated cells. Thus, cells were transfected with EGFP plasmid before the cell growth experiments, and it was possible to track the then green fluorescent cells.

Before transfection of the EGFP plasmid into BJ1-hTERT human fibroblasts the necessary selective antibiotic concentration had to be determined for the creation of a stable transfected cell line. Since the human fibroblasts were transfected with two vectors, the pEGFP-N1 vector and the pMC16 EGFP vector, the deadly concentrations of Geneticin and Puromycin, the particular selective antibiotics, for non-transfected cells were analysed. Varying concentrations of both antibiotics were added to different cell culture wells and after five days the cell numbers were determined. A decrease in cell viability was observed in correlation with an increase in the concentrations of both antibiotics (Table 5.1).

Table 5.1: Selective antibiotic concentrations and the corresponding numbers of BJ1-hTERT cells

Geneticin [µg/µl]	0	0,1	0,2	0,3	0,4	0,5	0,6	0,7	0,8
Cell number/ml	187500	72500	17500	12500	5000	2500	0	0	0
Puromycin [µg/ml]	0	0,06	0,1	0,14	0,16	0,18	2,0	2,2	2,4
Cell number/ml	242500	110000	675000	52500	30000	15000	0	0	0

As indicated in Table 5.1 a concentration of 0,6 µg/µl for Geneticin and a concentration of 0,2 µg/ml Puromycin were required for a selection of non-transfected human fibroblast since the cell number could not be determined for these and higher antibiotic concentrations.

The transfection of the BJ1-hTERT cells was successful for both kinds of vectors. A green fluorescence was visible in around 30% of the cells for the pEGFP-N1 vector and in circa 15% for the pmc16 EGFP vector, 48 h post transfection. However, a decrease in cell growth and survival was observed for both transfections. The cell density decreased from 70% before transfection to 40% after transfection and even more the following days after adding the cell culture medium and the appropriate selective antibiotic (Figure 5.1).

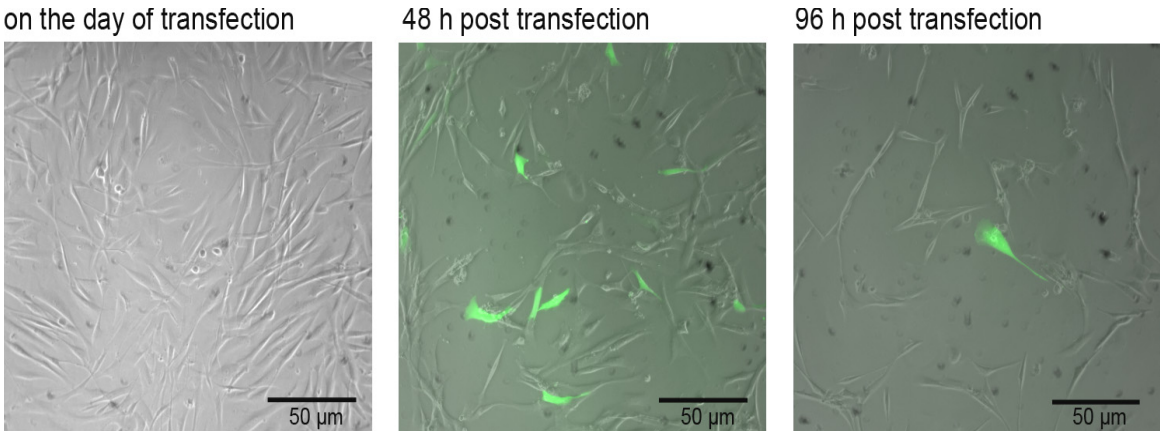

Figure 5.1: Merged phase contrast and fluorescence microscopic images of BJ1-hTERT cells in the process of GFP transfection. The cells had a confluence of around 70% on the day of transfection. 48 h post transfection while checking the green fluorescence also a decrease in cell density was observed. A further reduction in cell density and vitality could be seen the following days until all cells were dead.

Further transfections with differing incubation times during the transfection process as well as a decrease in the selective antibiotic concentration, and an increase in the FCS concentration did not result in the survival of transfected BJ1-hTERT cells. These findings suggest a possible toxicity of the EGFP plasmids for BJ1-hTERT human fibroblasts. Furthermore, it is possible that the plasmid was not build into the genome of the BJ1-hTERT cells, which is necessary for a stable transfection. Thus, the cells had no resistance against the selective antibiotic and died.

As a consequence L929 mouse fibroblasts were transfected with EGFP plasmid to be able to perform the reference cell growth experiments, with co-cultures of transfected and non-transfected cells of the same cell line.

GFP Transfection of Mouse Fibroblasts

A stable transfection of L929 mouse fibroblasts with EGFP plasmid also required the determination of the necessary selective antibiotic concentration before transfection. This time only different concentrations of Geneticin were added to cultures of non-transfected cells, since only the pEGFP-N1 vector was used. Again the cell number count revealed a decrease in the cell number dependent on the increasing Geneticin concentration. For an antibiotic concentration of 0,3 µg/µl and higher concentrations the cell number could not be determined and no cell growth was observed (Figure 5.2A). Thus a Geneticin concentration of 0,3 µg/µl was required for an effective cell killing of non-transfected cells.

After the necessary antibiotic concentration was determined, the transfection of L929 mouse fibroblasts with the pEGFP-N1 vector was performed. 48 h post transfection a green fluorescence in about 40% of the cells was visible and no decrease in cell viability.

The transfected cells were trypsinised and seeded into new wells with cell culture medium mixed with Geneticin ($c = 0{,}3\,\mu g/\mu l$). The selective medium was removed two days after plating, to remove dead cells, and new selective medium was added. After one week the cells started to grow in isles and after another week only green fluorescent cells were left in the cell culture (Figure 5.2B).

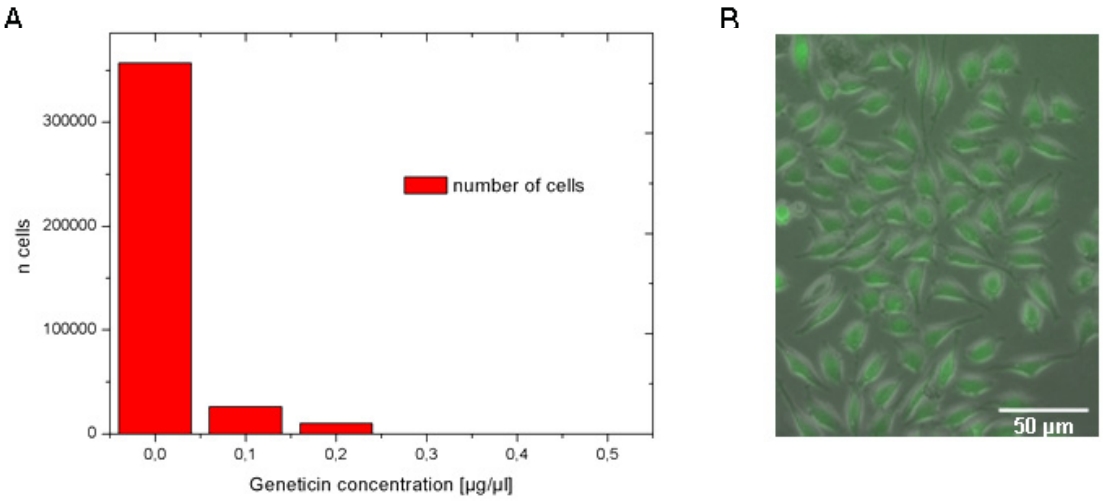

Figure 5.2: Graph A shows the histogram of the number of cells over increasing selective antibiotic (Geneticin) concentration. A Geneticin concentration of 0,3 µg/µl in cell culture medium is necessary for the selection of non-transfected L929 mouse fibroblasts. Image B shows the merged phase contrast and fluorescence microscopic images of a L929 mouse fibroblast cell line stable transfected with pEGFP plasmid.

5.1.2 Reculture of Living Cells

Recultivation experiments in the context of single cell tracking in irradiation experiments, revealed varying results. The use of DuplexDishs made the LMPC easier, however it was not always possible to catapult the isolated pieces into the capture device. Nevertheless, this method enabled the recultivation and tracking of single cells as indicated in Figure 5.3.

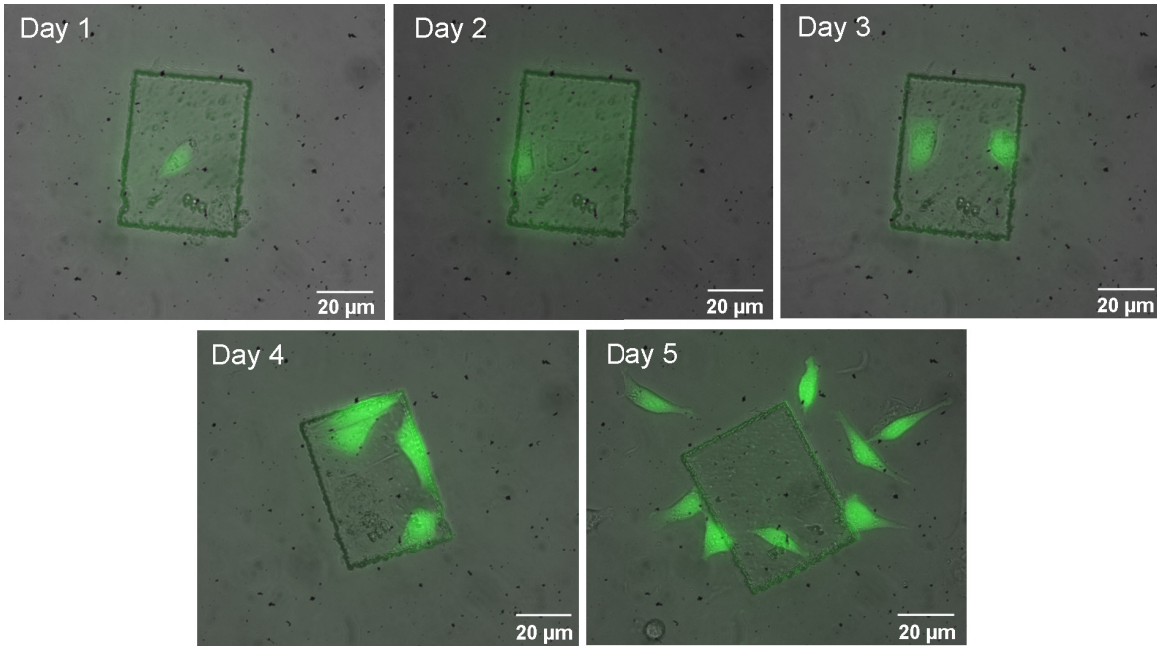

Figure 5.3: Merged fluorescence and phase contrast microscopic images of a single green fluorescent cell via LMPC. The isolated cell starts to divide and, thus, to proliferate again two days post LMPC. A new cell colony arose from the single cell.

A single green fluorescent L929 mouse fibroblast cultivated in a DuplexDish was isolated with the laser, catapulted in the collection device, and seeded into a new well filled with cell culture medium. On day three, thus two days after the LMPC, a cell division of the isolated cell was observed. The isolated single cell started to proliferate. Further cell divisions were visible the following days (Day 4 > 4 cells, Day 5 > 8 cells…). The success rate of cell survival of single isolated cells after LMPC was around 30%. Most cells, did not survive the recultivation process.

However also cell behaviour, which was out of character was observed. In several cases the isolated single cells did not divide after a couple of days and, thus, to proliferate. The cells enlarged their size without cell division, and the existence of more cell nuclei was observed in these cells (Figure 5.4).

This kind of cell is called ‘Syncytium’, which is a multinucleated cell. It can occur due to incomplete exhibited cell division. While nuclei undergo S-phase and the

sister chromatids are pulled apart, thus, forming two daughter nuclei, cytokinesis dose not occur. As a consequence, a Syncytium is a large cell-like structure consisting of cytoplasm and many nuclei (23).

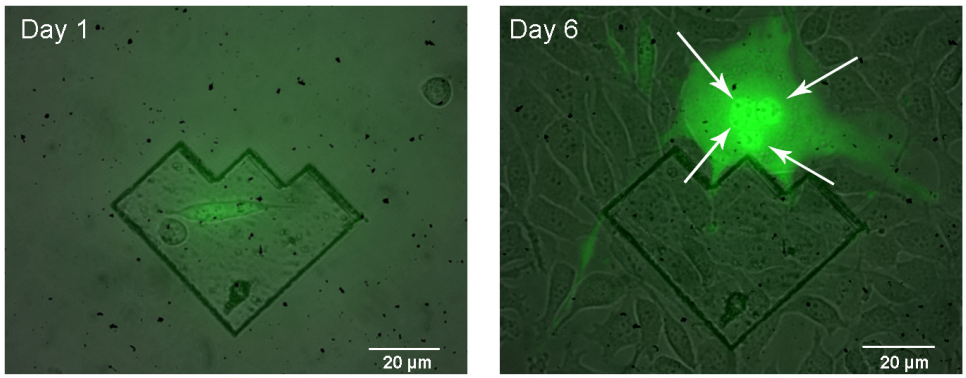

Figure 5.4: Merged phase contrast and fluorescence microscopic images of a single pEGFP transfected mouse fibroblast cell recultivated via LMPC. The pen foil piece with the single green fluorescent cell is brought into a cell culture of non-transfected cells and the cells are left to grow. In the further process of the cell growth, the cell nucleus did divide but not the cytoplasm. Thus, the recultivated cell became a Syncytium, a cell like structure filled with cytoplasm containing multiple nuclei (indicated by arrows).

Since it was not possible to catapult all isolated pieces with a laser impulse into the collection device, the use of the low pressure transfer system was included in the isolation and recultivation process. Thus, it was possible to obtain a higher success rate in the isolation process of single pieces. As soon as the isolated foil pieces with cells were adsorbed at the adsorption head, they were released into new wells filled with cell culture medium, by turning off the low pressure. Variations in the adsorption process like reducing the low pressure, isolating larger foil pieces, and increasing the speed during the process lead all to the same result: The cells did not survive this recultivation procedure. Figure 5.5 shows the recultivation process with the low-pressure transfer system of a foil piece with several mouse fibroblasts (indicated by black arrows).

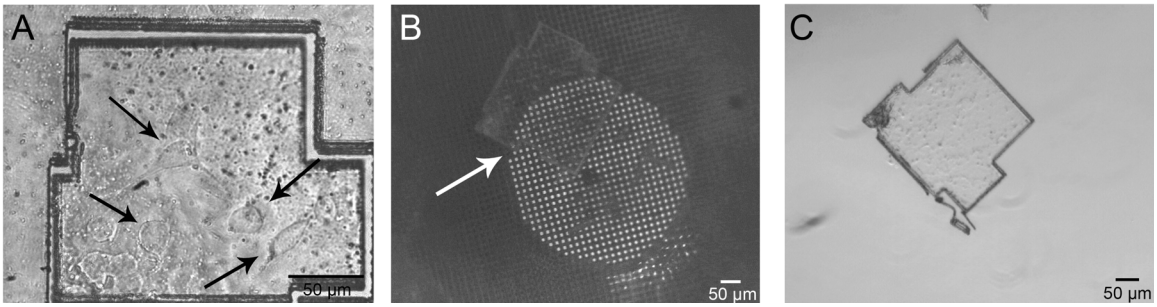

Figure 5.5: Phase contrast microscopic images of the recultivation workflow with the low-pressure transfer system. Before adsorption the cells were clearly visible on the isolated foil piece (A, black arrows), image B illustrates the absorbed foil piece with cells at the grid of the transfer system (white arrow). Image C is the microscopic image of the isolated foil piece in the new culture well without cells.

Before adsorption, the cells were clearly visible under the microscope. After the foil piece was released in the new well it was searched under the microscope to investigate the survival of the isolated cells. However, since the cells did not survive the isolation process they could not be found on or near the isolated foil piece.

5.1.3 Growth Statistic and Behaviour of Cellular Co-Cultures

Analysis of cell proliferation rates is often used to determine the response of cells to particular stimuli. A cell growth curve can be divided in three parts: the lag phase, the exponential growth phase (log phase), and the stationary phase (plateau phase) as indicated in Figure 5.6.

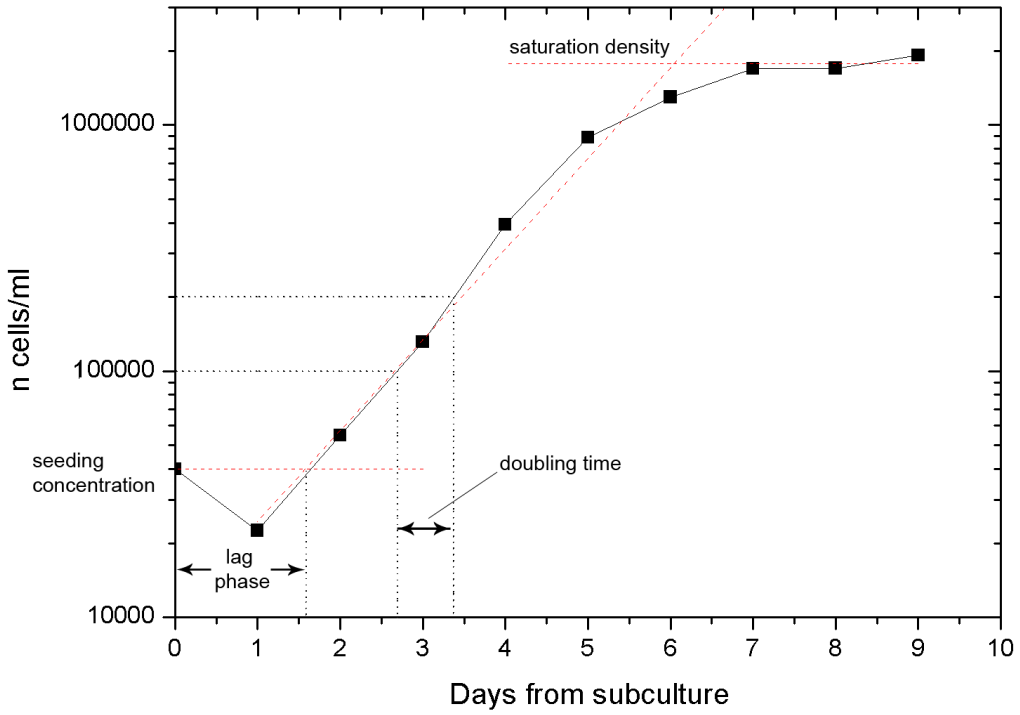

Figure 5.6: The graph shows an exemplary cell growth curve of L929 mouse fibroblasts over 9 days. It is possible to determine the trend lines for the three cell growth phases lag phase, log phase and plateau phase. From the slope of the log phase trend line it is possible to calculate the PDT of the cell culture as well as the duration of the lag phase. By determining the trend line of the plateau phase it is possible to calculate the average number of cells reached in the plateau phase.

The lag phase describes the time interval before the cells start to proliferate and enter the log phase. It gives information of a possible retarding effect in cell growth after stimuli induction. Log and plateau phase give vital information about the cell line used. It is also possible to calculate the population doubling time (PDT) during the exponential growth phase, which is used to quantify the influence of certain inhibitory and stimulatory

culture conditions. The PDT is not equal to the cell cycle time. Where the cell cycle time is measured from one point of the cell cycle until this point is reached again, the PDT is the average figure that applies to the whole population. This means, the PDT describes the result of a wide range of division rates and is influenced by nongrowing and dying cells as well. The cell cycle time reverse only to dividing cells (23, 98, 117).
Following parameters were analysed in the growth statistic experiments: the duration of the lag phase, the PDT, and the average cell number reached during the plateau phase.

5.1.3.1 Cytokinetic Experiments with L929 Mouse Fibroblasts

Growth Behaviour of Not-irradiated and Irradiated Non-transfected and Transfected Mouse Fibroblast Monocultures

The cell proliferation behaviour was analysed for L929 mouse fibroblasts in various experimental approaches over a threefold determination. The standard deviations are not shown in the graphs of all experiments due to the clarity of the curve progressions. In the first set of experiments, the growth of L929 mouse fibroblasts was analysed with and without irradiation. The same experiment was then performed with L929 mouse fibroblasts transfected with the pEGFP plasmid in order to investigate if the vector had an influence on the growth behaviour of the cells. The starting number of cells per well was kept constant at a value of 20.000 cells in all experiments. The arrow in the graphs shows the time-point of irradiation

By analysing the cell growth curves in Figure 5.7, it was possible to observe reduced cell numbers for all irradiated samples of the non-transfected L929 mouse fibroblasts on the first day from subculture and post-irradiation when compared to the plated cell numbers before irradiation. This could be due to the irradiation but could also be an effect of the plating efficiency, since not all cells survive the cell handling during the preparation of the experiments. The lowest cell number was reached for the 50 mGy sample, but the determined cell numbers for the 250 mGy sample was only slightly higher. This could also be seen in the calculated time spans of the lag phases for the different cell cultures (Table 5.2). The longest lag phase was confirmed for the 50 mGy sample followed by the 250 mGy sample, the shortest lag phase was calculated for the 0 mGy, the reference sample.

When analysing the log phase of the cell growth curves it was possible to see that the 50 mGy sample as well as the 250 mGy sample had also lower cell numbers during

the first days of the log phase. On day four from subculture and post-irradiation, a reduced cell number for the 1000 mGy sample was counted. This value was even lower than the analysed cell number of the 1000 mGy sample from the day before. Also on day five the 1000 mGy sample had still a lower cell number compared to the other samples. Cell numbers of all samples were again in the same range on day six, which remained constant until saturation was reached.

The growth behaviour of the 50 mGy sample was also reflected in the calculated PDT. It had the shortest time span for the doubling of the cell population. The longest PDT was determined for the 1000 mGy sample, which is in correlation to the reduced cell number on day four and five of the experiment. However, no exact dose dependence was observed for the PDT time spans. When comparing the average cell numbers in the plateau phase again no dose dependence was observed. The sample irradiated with 1000 mGy reached the highest average cell number and the 10 mGy sample the lowest.

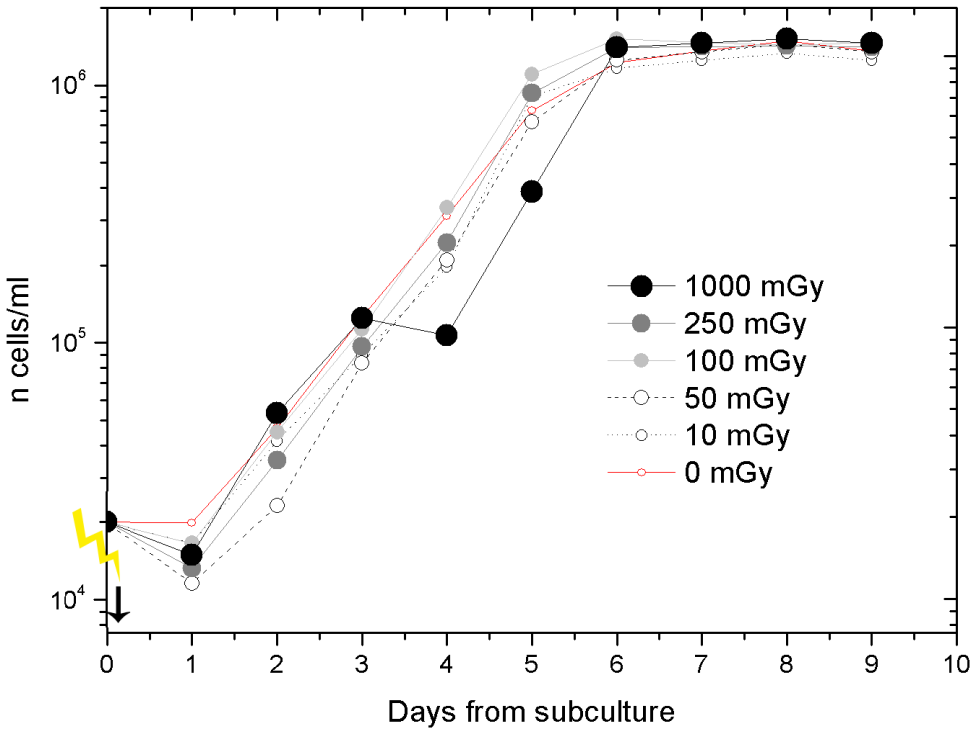

Figure 5.7: Cell growth curves of the irradiated L929 mouse fibroblasts as well as the reference sample (0 mGy red curve). A reduced cell number was observed for all samples on the first days from subculture and after irradiation. The lowest numbers were determined for the 50 mGy and 250 mGy samples from the first to third day from subculture. On day four a lower cell number was counted for the 1000 mGy sample, which was even lower than the value determined for this sample the day before. The analysed cell number of the 1000 mGy sample was also still lower than the cell numbers of the other samples on day five. The analysed cell numbers were again in the same range for all samples on day six of the experiment.

Since the cell numbers for each sample were determined over a threefold count, it could be that certain curve behaviours were induced due to errors in the analysis of one sample.

Figure 5.8 illustrates the cell growth curves of the three single samples of the non-transfected L929 monocultures, whose average is Figure 5.7.

It was possible to see from the three different graphs that the cell growth curves did not exactly look like each other, but that the overall trends were already visible in the single experiments. The undershooting of the cell numbers on the first day from subculture is predominating in the left graph. However, this extreme divergence from the originally plated cell number is antagonised by the cell growth behaviour of the other two samples (middle and right graph). The behaviour of the 1000 mGy sample, when reaching lower cell numbers than expected from the exponential growth, was visible in all three graphs on day four and five. Thus, the average from all three experiments gave a good idea about the general cell growth behaviour since extreme divergences were compensated by the other samples of the threefold determination.

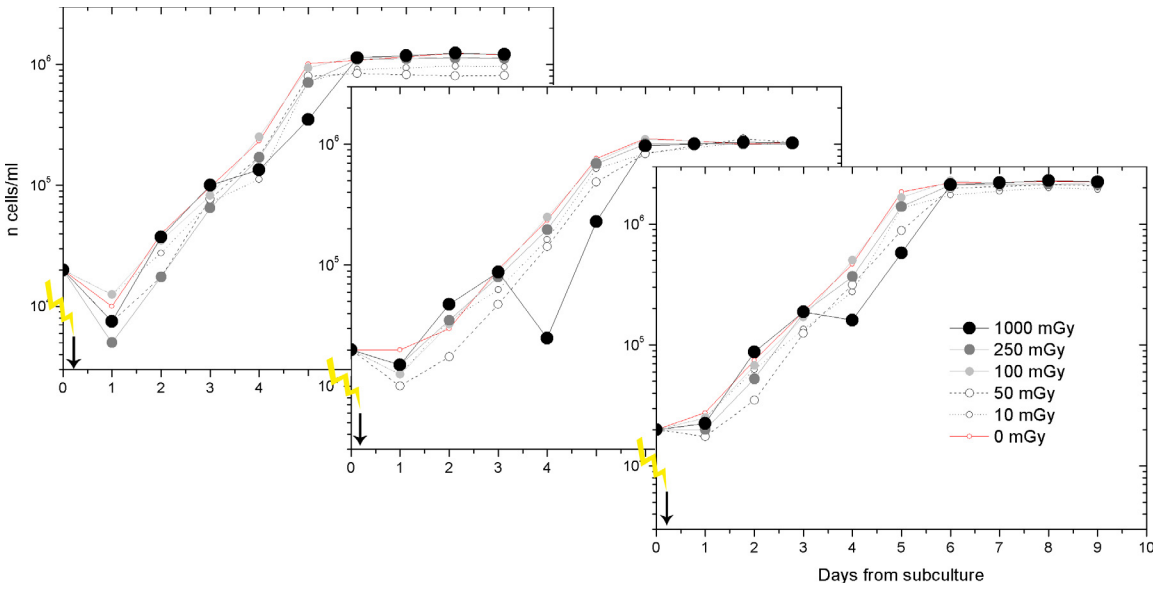

Figure 5.8: Cell growth curves of the three different examples for the threefold determination of the cell growth curves of non-transfected L929 mouse fibroblast monocultures. When comparing the three graphs the overall trends were visible in all of them like the undershooting in cell number of the 1000 mGy sample on day four and five from subculture. Other extreme divergences like the undershooting in cell number are antagonised by the corresponding samples of the other experiments of the threefold determination on day one.

Also for the EGFP transfected L929 mouse fibroblasts a lower cell number was observed on the first day from subculture and post irradiation for all irradiated samples as well as the reference sample when compared to the originally plated cell number (Figure 5.9).

The counted cell number of the 100 mGy sample reached the lowest value. When calculating the time spans of the lag phase for the different samples, the longest lag phase was determined for the 0 mGy sample. All irradiated samples had shorter lag phases

(Table 5.2). The difference between the lag phase of the 0 mGy sample and the 250 and 1000 mGy samples was only around one hour. But compared to the other samples a difference of three to five hours was analysed.

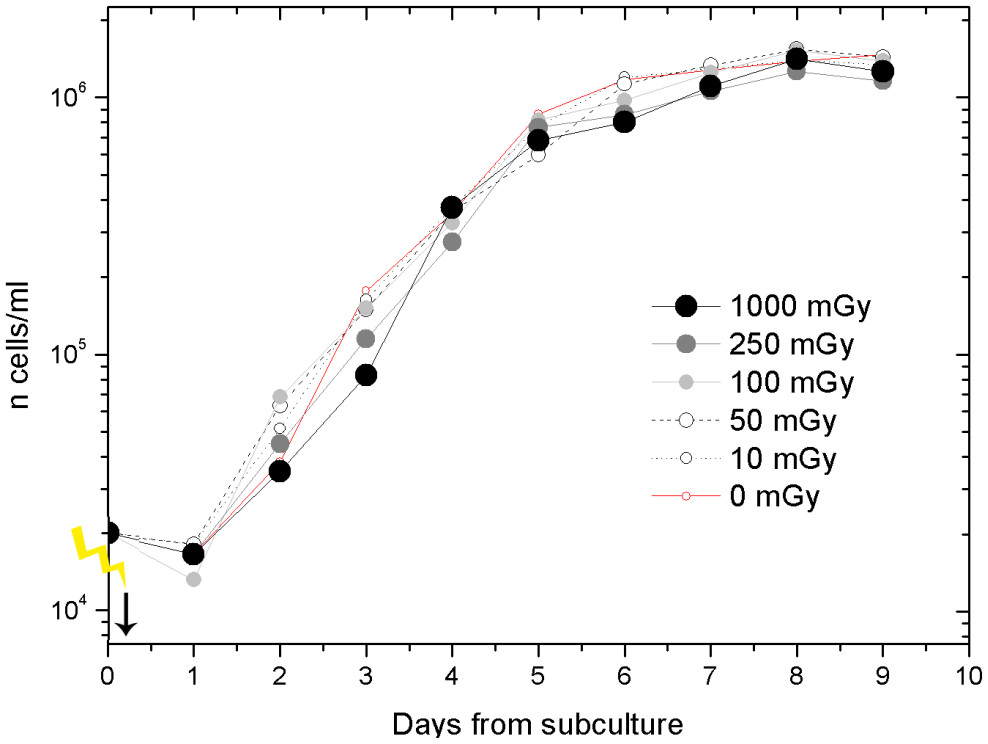

Figure 5.9: Cell growth curves of the irradiated and transfected L929 mouse fibroblasts as well as the reference sample (0 mGy red curve). The first day of the experiment revealed an undershooting in cell numbers for all samples, where the lowest cell number was counted for the 100 mGy sample. For the 1000 mGy samples lower cell numbers were counted in the log phase on day two and three from subculture. However, the number adjusted again to the numbers of the remaining samples on day four. The cell numbers of the 250 mGy sample were also lower than the numbers counted for the samples irradiated with 100 mGy and lower doses. On day five the cell numbers were in the same range for all samples, but before reaching the plateau phase again lower cell numbers were observed for the 250 mGy and 1000 mGy samples.

In the log phase an undershooting in the cell number was observed on day three of the experiment for the 1000 mGy sample. Also the number of the 250 mGy sample was slightly lower when compared to the remaining samples. A value in the range of the other samples was determined for the 1000 mGy sample on day four. Only the cell number of the 250 mGy sample was still lower than the rest on this day. But on day five all samples had cell numbers in the same range. Shortly before reaching the plateau phase, again lower cell numbers were observed for the 250 mGy and 1000 mGy samples. This growth behaviour was also reflected in the calculated PDTs. The 1000 mGy had the longest time span followed by the 250 mGy sample. The other samples followed this dose dependence, thus, the PDT decreased with dose. By calculating the average cell number of each sample in the plateau phase no exact dose dependence of the cell numbers was

observed. The highest cell number was determined for the 50 mGy sample and the lowest for the 1000 mGy sample.

Table 5.2: Calculated values for the length of the lag phase [h], the PDT [h] and the average cell number in the plateau phase for the cell growth experiment for non-transfected and transfected L929 mouse fibroblast monocultures.

	0 mGy	**10 mGy**	**50 mGy**	**100 mGy**	**250 mGy**	**1000 mGy**
Lag Phase L929 [h]	32,9	38,22	49,96	34,32	40,42	36,39
Lag Phase EGFP L929 [h]	33,46	30,57	28,28	29,7	32,61	32,1
PDT L929 [h]	17,8	17,56	14,82	17,51	17,9	20,44
PDT EGFP L929 [h]	17,25	17,42	19,1	19,62	20,03	22,23
Average cell number in plateau phase L929	1.404.444	1.277500	1.382.777	1.458.333	1.418.611	1.483.333
Average cell number in plateau phase EGFP L929	1.270.417	1.368750	1.490.000	1.453.750	1.212.500	1.337.083

When comparing both experiments with non-transfected and transfected L929 mouse fibroblasts with each other, some similarities as well as differences in the growth behaviour for both cell lines were observed. The lag phases lasted longer for the non-transfected cells. And the difference between the lag phases of the 0 mGy sample and the irradiated samples was bigger for them as well. The pEGFP transfected cells showed only small differences in the lag phases. The shortest and the longest lag phase were both observed for the 0 mGy samples for the non-transfected and transfected mouse fibroblasts respectively. However, the lag phases for both 0 mGy samples were almost in the same range, only the irradiated samples behaved differently. The 1000 mGy sample showed for both experiments the biggest dose response when compared to the other samples. When comparing the PDTs of the 0 mGy sample and the 1000 mGy sample an increase in time span was observed. However, the non-transfected cells did not show such a strong dose dependent behaviour in PDT as the transfected cells.

Growth Behaviour of Mouse Fibroblasts in Co-culture with Irradiated and Transfected Mouse Fibroblasts

In the next set of experiments, the influence of ionising radiation on cellular behaviour was investigated, when only one part of the cell culture was irradiated. Thus, non-transfected and transfected L929 mouse fibroblasts were cultivated in co-culture with the

transfected and irradiated L929 mouse fibroblasts. Again cell numbers were determined over a threefold approach and the standard deviations are not shown in the graphs due to clarity. These experiments should shed light in the cellular behaviour of not-directly irradiated cells (called indirectly in the following chapter) in co-culture with directly irradiated cells from the same cell type. The ratio was 20:100 between transfected and non-transfected cells. The cell number in sum for both cell types was 20.000 cells per well at the beginning of the experiment. Arrows in the graphs indicate the time-point of irradiation.

Figure 5.10 shows the cell growth curves of the non-transfected L929 mouse fibroblasts in co-culture with irradiated and transfected L929 mouse fibroblasts. The cell curve progressions of the L929 mouse fibroblasts in co-culture with irradiated and transfected L929 mouse fibroblasts looked slightly different when compared to the cell culture curves of the irradiated L929 mouse fibroblast monocultures.

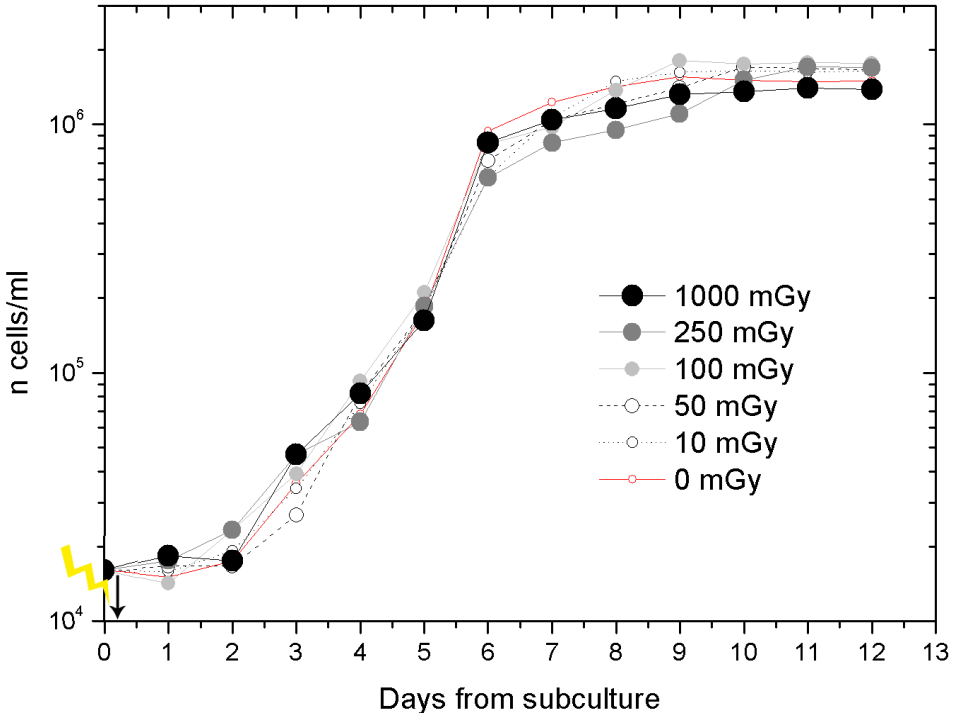

Figure 5.10: Cell growth curves of the non-transfected mouse fibroblasts, which were cultivated in co-culture with irradiated and transfected mouse fibroblasts. All curves show different curve progressions when compared to the non-transfected cells in monoculture. The exponential growth phase starts at a later time-point and lasts longer for the cells in co-culture. Lower cell numbers were observed for cells in co-culture with the 250 mGy irradiated and transfected cells when compared to the other samples in the last days before saturation was reached.

The calculated lag phases in the co-culture experiment lasted longer for all doses when compared to the monoculture experiment apart from the 100 mGy and 250 mGy samples (Table 5.3). Both curves enter the exponential growth phase earlier than the other curves. The lag phase also lasted longer for the non-transfected cells in co-culture with the

0 mGy transfected cells. It was even the longest lag phase compared to the other non-transfected cells in co-culture with irradiated and transfected cells. In the further curve progression, it was possible to see that the cell numbers of the non-transfected mouse fibroblasts approached each other and were almost in the same range on day five. On day six, a split-up between the counted cell numbers of the different non-transfected cell samples was observed. The lowest cell number was then determined for the 250 mGy sample, which carried on for the following three days until saturation was reached where an ascent in cell number was observed.

An increase in time was observed for the cells in co-culture when comparing the time-points saturation was reached for the non-transfected mouse fibroblasts. Furthermore, a split-up between the counted cell numbers of the different non-transfected cell samples was observed. The lowest cell number was then determined for the 250 mGy sample, which carried on the following three days until saturation was reached where an ascent in cell number was determined.

An increase in time was observed for the cells in co-culture when comparing the time-points when saturation was reached for the non-transfected mouse fibroblasts of the co-culture experiment with the monoculture experiment. However, the difference between the 0 mGy samples of the non-transfected cells of the mono- and co-culture is only small in comparison to the other samples. It seems for all samples that the exponential growth phase is retarded for the L929 mouse fibroblasts in co-culture. It starts later and ends later. By calculating the PDTs from the exponential trend lines of all cell growth curves no big difference between the 0 mGy samples was observed. The cells in co-culture with irradiated and transfected cells had longer PDT time spans when compared to the cells in monoculture. But the increase in the PDTs did not follow strict dose dependence. It was possible to see variations from the expected increase in time span with dose, which was also observed for the non-transfected mouse fibroblasts in monoculture. Comparing the average cell numbers in the plateau phase with each other again no exact dose dependence was observed. The highest value was reached for the 0 mGy sample and the lowest for the 1000 mGy sample.

Figure 5.11 shows the cell growth curves of transfected and irradiated mouse fibroblasts in co-culture with non-transfected and not-irradiated mouse fibroblasts. All samples did show an undershooting of the originally plated cell number before irradiation apart from the 1000 mGy sample. The lowest cell number was analysed for the 250 mGy

sample. Furthermore, it was possible to see that the lag phases lasted longer for the transfected cells in co-culture than for the cells in monoculture (Table 5.3).

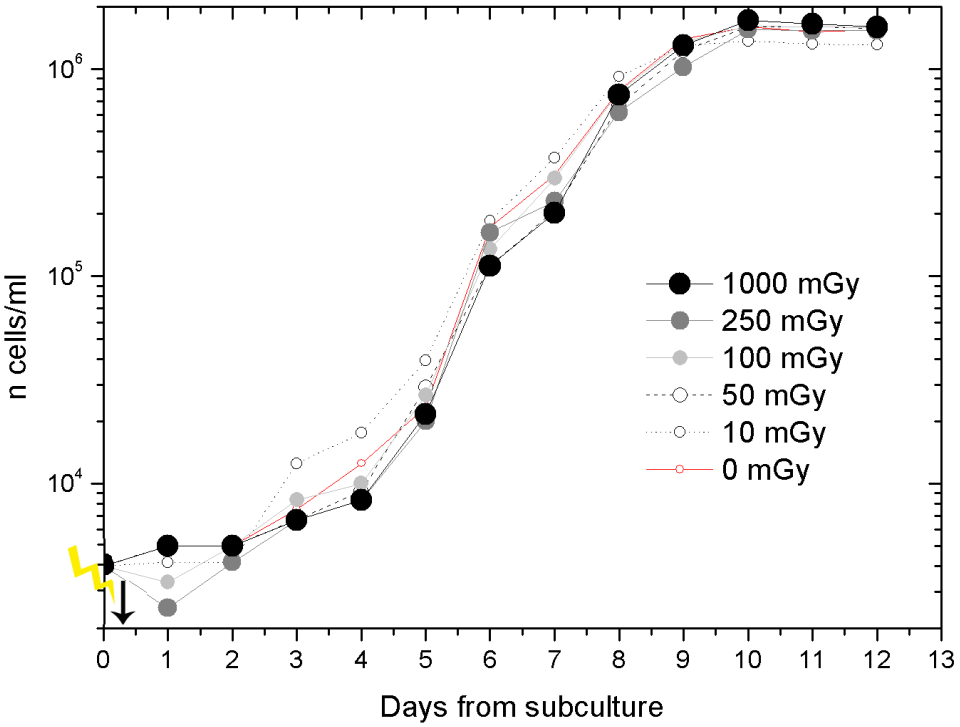

Figure 5.11: Cell growth curves of the transfected and irradiated mouse fibroblasts in co-culture with non-transfected and not-irradiated mouse fibroblasts. All curves showed lower values than plated originally in the wells apart from the 1000 mGy sample on day one from subculture. The lowest cell number was reached from the 250 mGy sample. During the exponential growth phase there was no significant difference observed between the different samples only the 10 mGy sample had always higher cell numbers compared to the remaining samples. From day six to day seven a kink was observed in the exponential growth phase of all samples. Saturation was also reached later for the cells in co-culture compared to the cells in monoculture.

By calculating the length of the lag phases from the trend lines, almost threefold longer time spans were calculated for the cells in co-culture. During the exponential growth phase, it was not possible to see any clear differences between the curve progressions of the different samples. Only the 10 mGy sample reached always higher cell numbers when compared to the other samples. From day six to seven a kink from the exponential curve progression was observed for all samples.

By analysing the trend lines of the exponential growth phase and by calculating the PDTs no big difference between the cells in co-culture and the cells in monoculture was observed. The time spans of the PDTs were in the same range and did not follow a dose dependence. For the transfected cells irradiated with 1000 mGy an even shorter time span was calculated than for 0 mGy sample. As for the non-transfected cells in co-culture also the transfected cells in co-culture reached their saturation phases at later time-points

when compared to the monocultures. A dose dependence was observed in the average cell numbers for the different co-culture samples.

Table 5.3: Calculated values for the length of the lag phase [h], the PDT [h] and average cell number reached in the plateau phase for the growth experiment of non-transfected and not-irradiated L929 mouse fibroblasts in co-culture with transfected and irradiated L929 mouse fibroblasts.

	0 mGy	**10 mGy**	**50 mGy**	**100 mGy**	**250 mGy**	**1000 mGy**
Lag Phase L929 [h]	60,19	51,95	58,17	36,29	36,24	52,06
Lag Phase EGFP L929 [h]	97,08	89,75	101,41	98,2	106,15	107,75,3
PDT L929 [h]	17,14	21,04	18,49	24,02	24,85	19,53
PDT EGFP L929 [h]	18,93	19,73	18,97	20,15	19,26	18,55
Average cell number in plateau phase L929	1.151.388	1.088.333	1.065.277	1.068.888	1.071.388	1.028.888
Average cell number in plateau phase EGFP L929	818.055	625.833	521.111	466.388	466.944	425.833

Since both cell kinds were assumed to be the same cell line in this experiment also the behaviour of the total cell number was analysed. The cell growth curves of the total number of cells (Figure 5.12) looked similar to the cell growth curve of the non-transfected L929 mouse fibroblasts (Figure 5.10).

The transfected and irradiated cells were added in a smaller quantity to the samples and, thus, had in the beginning not much influence on the curve progression. However, a clear difference between the single cell culture parts of the co-culture and the total co-culture could be observed when calculating the time spans of the lag phases. The lag phases of the total co-culture showed dose dependence in contrast to both parts of the co-culture, the non-irradiated and irradiated part (Table 5.4). The higher the dose the shorter the lag phase, only the 50 mGy sample had a longer lag phase than the 10 mGy sample. A clear difference was also observed in the lag phase durations between the monocultures and corresponding co-cultures. The monocultures did not show dose dependence in the lag phases. In the further curve progressions of the total cell number, the same observations were made as for the non-transfected cells in co-culture. Nevertheless, on day seven from subculture a divergence between the two graphs could be observed since the number of irradiated and transfected mouse fibroblasts in the co-culture had reached a higher number and, thus, had more influence on the total cell number in the experiment. The kink observed in the cell growth curves of the irradiated

cells recurs in the cell growth curves of the total co-culture, thus, retarding the incidence of the plateau phase.

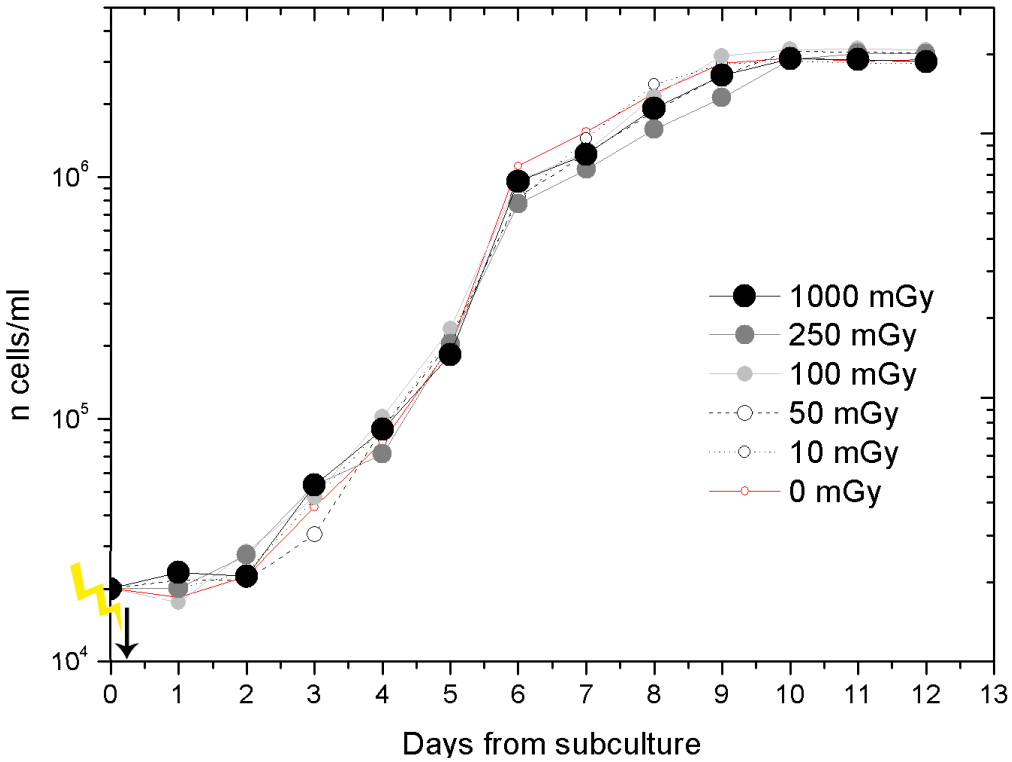

Figure 5.12: Cell growth curves of the total co-culture of non-transfected and not-irradiated L929 mouse fibroblasts with transfected and irradiated L929 mouse fibroblasts. Similar cell growth behaviours as for the non-transfected part were observed for the total cell culture. On day seven from subculture a divergence between the total cell culture and the non-transfected part could be seen. The kink, which occurred in the transfected cell culture parts, retarded the incidence of the plateau phase in the total co-culture.

Table 5.4: Calculated values for the length of the lag phase [h], the PDT [h] and average cell number reached in the plateau phase for both monocultures of non-transfected and transfected L929 mouse fibroblasts as well as the complete co-culture of both cell lines.

	0 mGy	**10 mGy**	**50 mGy**	**100 mGy**	**250 mGy**	**1000 mGy**
Lag Phase L929 [h]	32,9	38,22	49,96	34,32	40,42	36,39
Lag Phase EGFP L929 [h]	33,46	30,57	28,28	29,7	32,61	32,1
Lag Phase co-culture [h]	50,75	45,66	49,51	40,54	40,43	39,66
PDT L929 [h]	17,8	17,56	14,82	17,51	17,9	20,44
PDT EGFP L929 [h]	17,25	17,42	19,1	19,62	20,03	22,23
PDT co-culture [h]	19,43	20,38	20,33	21,39	22,8	23
Average cell number in plateau phase L929	1.404.444	1.277500	1.382.777	1.458.333	1.418.611	1.483.333
Average cell number in plateau phase EGFP L929	1.270.417	1.368750	1.490.000	1.453.750	1.212.500	1.337.083
Average cell number in plateau phase co-culture	1.969.444	1.714.166	1.586.389	1.535.277	1.538333	1.454.722

When calculating the PDTs from the exponential trend lines, a clear difference could be observed between the total co-culture and the different parts of it as well as the monocultures. The PDT time spans lasted longer for the total co-culture when compared to the corresponding PDTs of the monocultures. Furthermore, dose dependence between PDT and irradiation dose was observed for the total co-culture, an increase in dose resulted in longer PDTs. When comparing the average cell numbers reached in the plateau phase of the total co-culture with the monocultures, higher numbers were counted for all samples of the co-culture experiment apart from the 1000 mGy sample.

80% Confluent L929 Mouse Fibroblasts in Co-culture with EGFP L929 Mouse Fibroblasts

In the next set of experiments non-transfected L929 mouse fibroblasts were left to grow until they reached a confluence of around 80% before adding the transfected mouse fibroblasts. These experiments were performed to investigate whether the state of confluence, i.e. the intercellular contact has an influence on the cellular behaviour. Furthermore, the influence of radiation on the cellular growth was analysed by either irradiating the whole sample or by only irradiating the transfected cells before adding them to the non-transfected cells. Cell numbers were determined over a threefold approach and the standard deviations are not shown due to clarity reasons.

When comparing both graphs for the non-transfected (Figure 5.13 and Figure 5.14) of both experiments, it was possible to see some differences in the corresponding curve progressions. In both graphs of the non-transfected cells it was possible to see that the 1000 mGy samples reached the lowest values until saturation was reached. The other cell growth curves did not show clear dose dependences. It was determined that the 0 mGy sample in the experiment where the whole co-cultures were irradiated reached the highest cell numbers when compared to the other samples. This was also observed in the experiment where only the transfected cells were irradiated.

Dose dependence in the cell numbers was analysed by averaging the cell numbers in the plateau phase for all samples in both irradiation experiments, (Table 5.5). The higher the irradiation doses the lower the cell number reached in the plateau phase. Furthermore, when comparing the cell numbers reached in both experiments, bigger differences between the 0 mGy sample and most of the irradiated samples were observed for the experiment where only the transfected cells were irradiated.

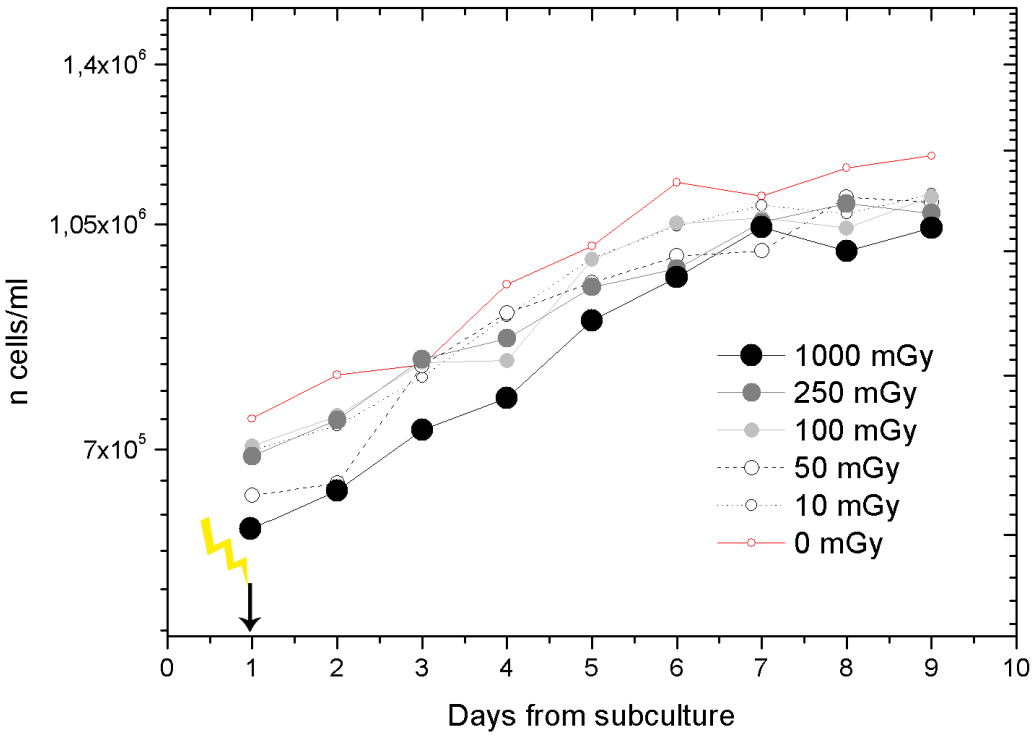

Figure 5.13: Cell growth curves of the non-transfected mouse fibroblasts in the 80% confluence experiment where the whole samples were irradiated. The lowest cell numbers were counted for the 1000 mGy sample and the highest for the 0 mGy sample. During the further curve progression until saturation was reached no clear dose dependence between the other samples could be analysed. When reaching saturation a dose dependence of the average cell numbers reached was observed.

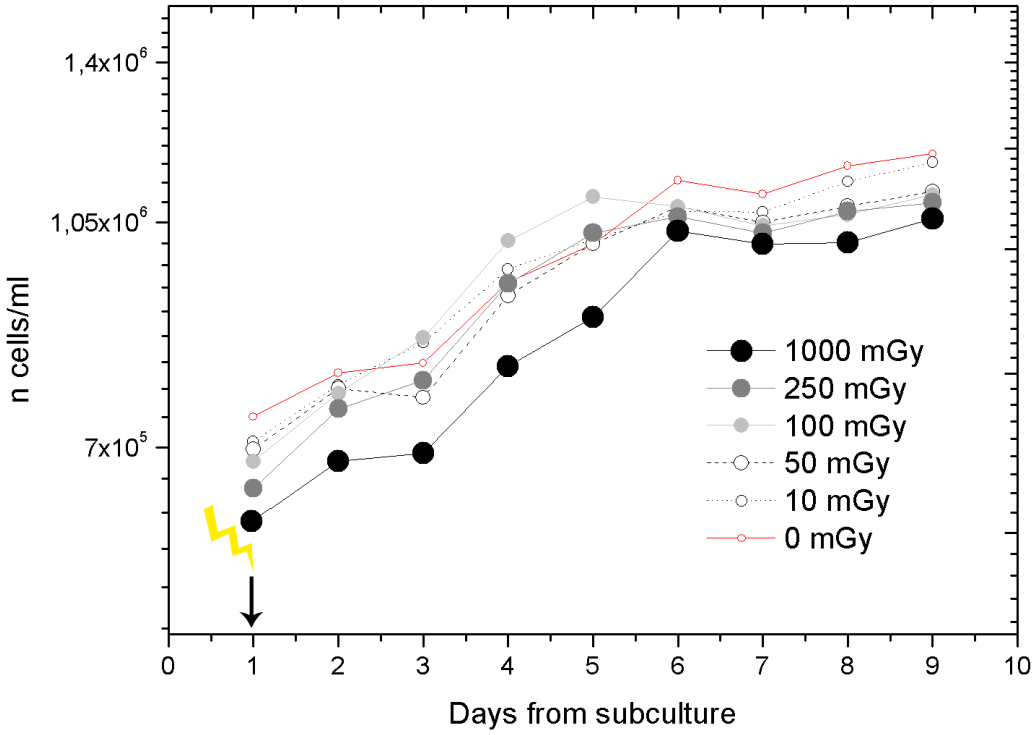

Figure 5.14: Cell growth curves of the non-transfected mouse fibroblasts in the 80% confluence experiment where only the transfected mouse fibroblasts were irradiated. The 1000 mGy sample reached also in this experiment the lowest cell numbers. The 0 mGy sample did not reach the highest value during curve progression in this experiment. Only in the beginning of the experiment and in the end the highest cell numbers were counted for this sample. Again a dose dependence was observed for the average cell numbers in the plateau phase.

Table 5.5: Average cell numbers in the plateau phase of the non-transfected L929 mouse fibroblasts for both 80% confluence experiments.

	0 mGy	10 mGy	50 mGy	100 mGy	250 mGy	1000 mGy
Average cell number in plateau phase , 80% all irradiated	1.151.388	1.122.777	1.080.277	1.070.277	1.062.777	1.026.111
Average cell number in plateau phase, 80% only EGFP irradiated	1.151.388	1.088.333	1.065.277	1.068.888	1.071.388	1.028.888

By looking at the cell growth curves of the transfected mouse fibroblasts for both experiments, more differences in the growth behaviour between the experiments were possible to see (Figure 5.15, Figure 5.16).

When all cells were irradiated, after adding the transfected cells to the existing cell culture a reduction in cell number was observed for the samples irradiated with doses exceeding 10 mGy. In this experiment, the 10 mGy curve reached almost the same values as the 0 mGy sample. This is in correlation with the longer lag phase but higher PDT for the 10 mGy sample (Table 5.6).

The 1000 mGy sample reached the lowest values throughout the whole experiment, followed by the 250 mGy and 100 mGy showing not much difference in their curve progressions. In the beginning, the 50 mGy sample had a curve development similar to the 10 mGy sample but approached then the cell growth curves of the higher irradiation doses. The lag phase duration of this sample was in the range of the 10 mGy sample and about 20 h shorter than the lag phases of the higher doses. But the PDT only reached a 4 -5 h shorter time span compared to the higher dose samples indicating a slower cell growth.

For the 1000 mGy samples of both experiments it was possible to see that the cells stayed the longest time span in the lag phase, which was also calculated from the trend lines. Furthermore, dose dependence of the lag phases in general was observed. The higher the irradiation dose the longer the lag phase. The lag phases lasted longer in the experiment where only the transfected cells were irradiated than in the experiment where the whole samples were irradiated. When compared to the corresponding samples of the whole irradiation experiment, lower cell numbers were counted for each irradiated sample where only the transfected cells were irradiated.

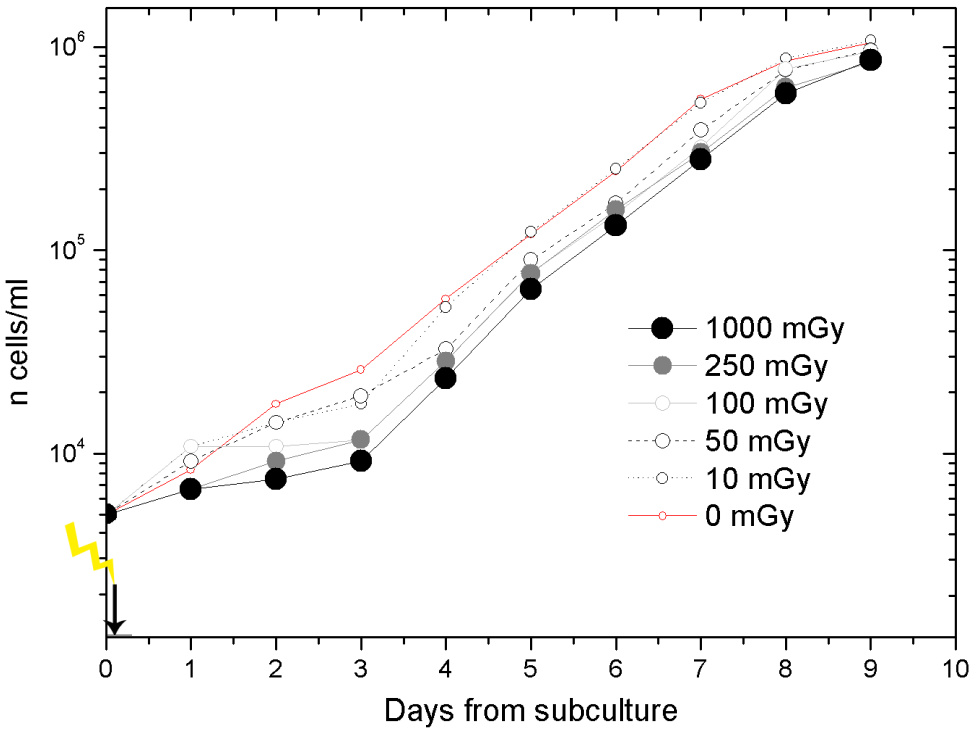

Figure 5.15: Cell growth curves of the transfected mouse fibroblasts in the 80% confluence experiment where the whole samples were irradiated. When comparing the different cell growth curves a reduction in cell numbers was observed for the samples irradiated with doses exceeding 10 mGy. The 10 mGy sample reached cell numbers in the range of the 0 mGy sample. Also a dose dependence of the lag phases and the cell numbers reached at the end of the experiment were observed. The higher the dose the longer was the lag phase and the lower the reached cell number.

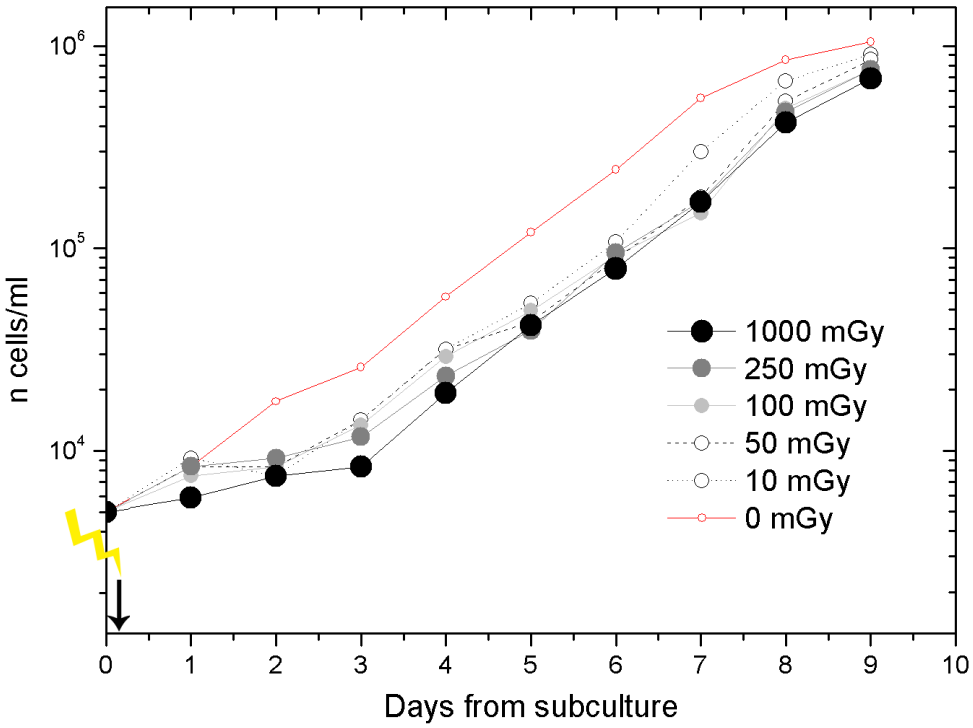

Figure 5.16: Cell growth curves of the transfected mouse fibroblasts in the 80% confluence experiment where only the transfected cells were irradiated. The counted cell numbers were in this experiment even lower than the corresponding cell numbers in the experiment where the whole samples were irradiated. The lowest numbers were analysed for the 1000 mGy sample. And again a dose dependence of the lag phases as well as the cell numbers reached at the end of the experiment was observed.

Table 5.6: Calculated values for the length of the lag phase [h], and the PDT [h] as well as the average cell numbers reached on the last day of the experiment for EGFP transfected L929 mouse fibroblasts in the 80 % co-cultures experiments.

	0 mGy	10 mGy	50 mGy	100 mGy	250 mGy	1000 mGy
80% All Lag phase	53,93	62,61	64,05	84,03	82,35	89,98
80% GFP Lag phase	53,93	83,16	84,57	84,35	91,93	99,14
80% All PDT	26,07	24,28	26,01	21,71	22,82	21,52
80% GFP PDT	26,07	23,03	24,64	25,43	23,34	22,17
Average cell number on the last day 80% all	1.050.000	1.070.833	962.500	950.000	840.000	860.833
Average cell number on the last day 80% EGFP	1.050.000	907.500	855.000	759.166	760.000	690.833

In addition dose dependence was observed for the average cell numbers reached at the end of both experiment. The cell numbers decreased with increasing dose. A stronger reduction in cell numbers was observed in the experiment where only the transfected cells were irradiated.

The comparison of the curve progression of the total co-culture for both experiments did not reveal new results. The graphs were very similar when compared to the graphs of the non-transfected cells.

5.1.3.2 Co-cultures of Human Fibroblasts and HeLa Cells

Cell Growth Experiments with BJ1-hTERT cells in Co-culture with HeLa H2B cells in different cellular ratios

Growth experiments with co-cultures of human fibroblasts, BJ1-hTERT, and human cancer cells transfected with EGFP, HeLa H2B, were performed in order to analyse eventual differences in growth behaviour of the two different cell lines by either cultivating the cells in different cellular ratios or by irradiating the cells. Again the cell numbers were determined over a threefold approach. Due to clarity reasons the standard deviations of each sample are not shown in the graphs.

These experiments can only be understood as models for the tumor development and therapy inside an organism. Thus, it is not possible to draw a one to one conclusion from the cellular behaviour. Nevertheless, these kinds of experiments could shed light on

the tumor development inside an organism as well as the cellular reaction to ionising radiation.

In the first set of experiments, the behaviour of both cell lines in co-culture were analysed for different ratios. Again a constant cell number of 20.000 cells/ml was used as starting concentration. Figure 5.17 shows the cell growth curves of BJ1-hTERT cells cultivated in co-culture with HeLa H2B cells in different cellular ratios.

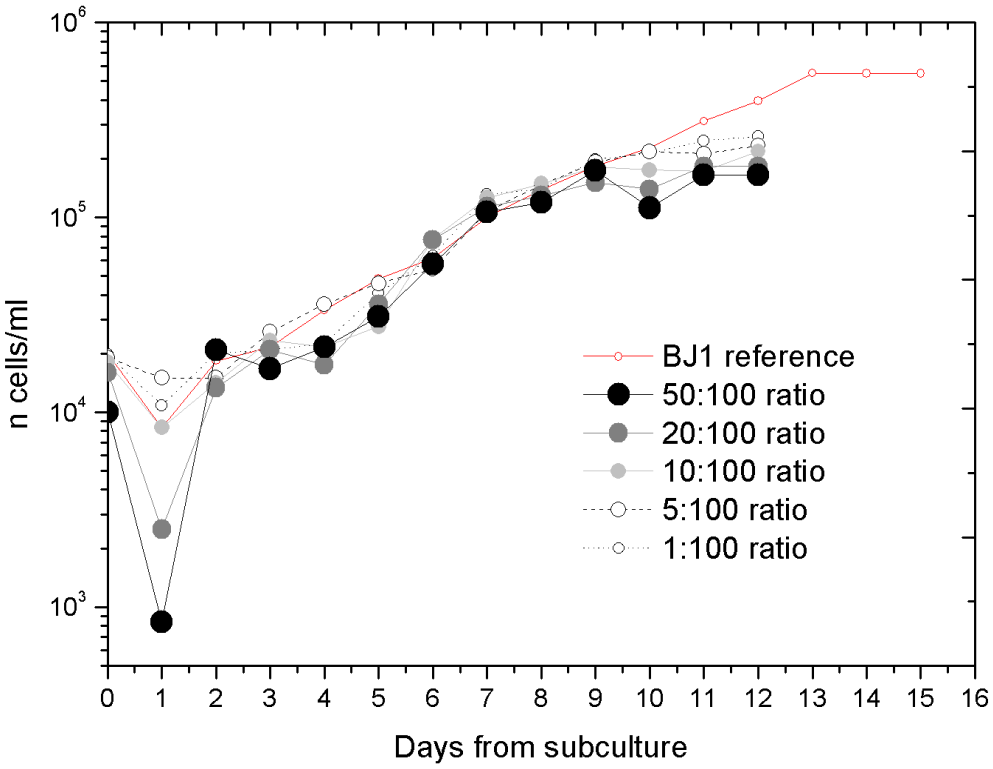

Figure 5.17: Cell growth curves of the BJ1-hTERT cells in co-culture with HeLa H2B cells in different cellular ratios. All growth curves show an undershooting in cell number possibly due to the plating efficiency on day one from subculture. The lowest number was counted for the 50:100 sample followed by the 20:100 sample. On day four from subculture, during the log phase, lower cell numbers were counted for all samples apart from the reference and 5:100 sample. The values did not follow the exponential growth. Saturation was reached for BJ1-hTERT cells in co-culture earlier and at lower cell numbers when compared to the BJ1-hTERT monoculture, the reference sample.

When comparing the different curve progressions it was possible to see, first, that BJ1-HTERT cells cultivated without HeLa H2B cells needed a longer time span to reach saturation. By analysing the first day from subculture an undershooting in cell number was seen for all samples where the lowest cell number was counted for the 50:100 sample followed by the 20:100 sample (number of HeLa H2B cells : total cell number). This could possibly be induced through the plating efficiency.

The calculated time spans of the lag phases revealed a dependence of the HeLa H2B cell concentration in the co-cultures for the 5:100, 10:100 and 20:100 samples

(Table 5.7). The higher the number of HeLa H2B cells in the co-culture in the beginning of the experiment, the longer were the lag phases. But the lag phases of the 5:100 and 50:100 samples did not follow this trend. They had a lag phase even shorter than calculated for the reference sample.

When analysing the log phase of the cell growth curves, a decrease in cell numbers was observed for all samples apart from the reference sample and the 5:100 sample on day four. The cell numbers did not follow the expected exponential cell growth. When calculating the PDTs, it was noticed that the PDTs were shorter for the BJ1-hTERT cells in co-culture with HeLa H2B cells when compared to the BJ1-hTERT monoculture, the reference sample. No exact cell ratio dependent trend was seen for the PDTs.

But cell ratio dependence was observed for the average cell numbers reached in the plateau phase for the different samples. The highest cell number in the plateau phase was counted for the BJ1-hTERT reference sample, the lowest for the 50:100 sample. This means that the BJ1-hTERT cell numbers reached in the plateau phase decreased with increasing ratio between BJ1-hTERT and HeLa H2B cells. Possibly, due to the increased number of HeLa H2B cells in the cell culture and their faster growth, less space was available for the BJ1-hTERT cells. Thus, only lower cell numbers could be reached.

A clear difference between the cell growth curves of the HeLa H2B cells cultivated in different co-culture ratios with BJ1-hTERT cells was observed (Figure 5.18). On day one, an undershooting of the originally plated cell numbers was observed for the 1:100 and the 10:100 sample. The other samples had cell numbers in the range of the originally plated cell numbers per ml on day one. By calculating the time spans of the lag phases, a ratio dependence was determined (Table 5.7). The higher the HeLa H2B cell number plated into the wells the shorter the lag phase. This dependence was only broken by the 10:100 sample, which had the shortest calculated lag phase duration.

In the log phase, all samples followed the exponential growth. Only the 5:100 sample had a higher counted cell number on day three, but on day four the cell number of this sample was back to the expected value from the exponential curve progression. During the whole growth phase, a clear difference in counted cell numbers was observed for all samples. No sample with a lower concentration of HeLa H2B cells, at the start of the experiment, reached higher cell numbers during the whole exponential growth phase. But the values did approximate each other when approaching saturation at the end of the experiment.

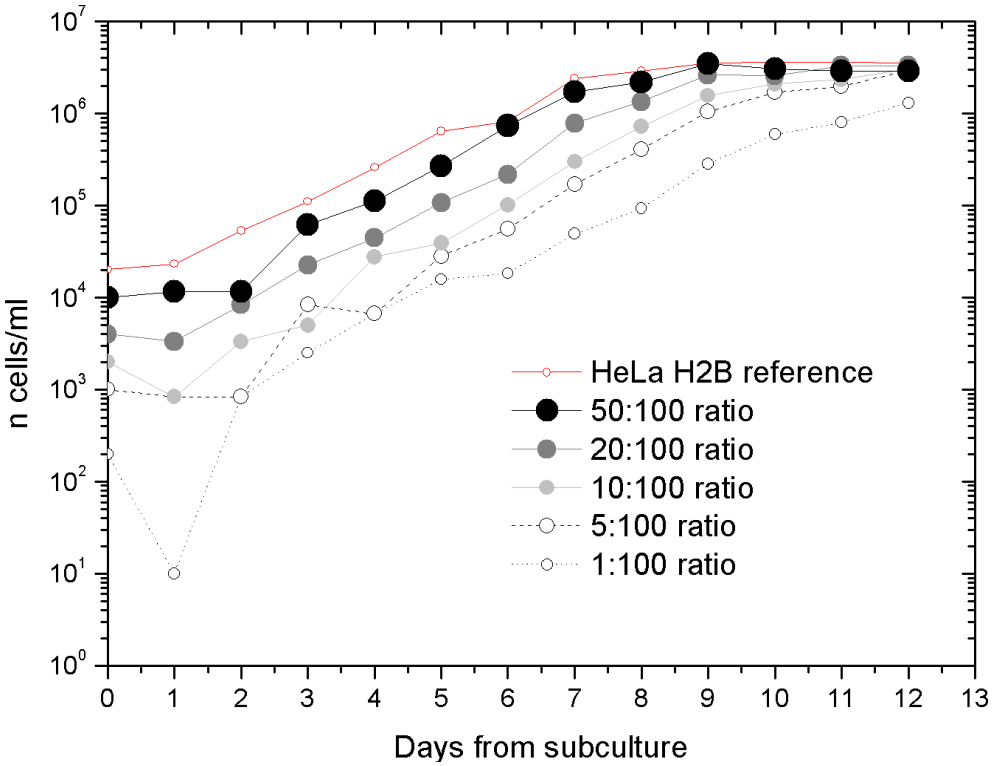

Figure 5.18: Cell growth curves of the HeLa H2B cells in co-culture with BJ1-hTERT cells in different cellular ratios. From the beginning of the experiment until the end a clear difference in the cell numbers reached could be observed for the different plating ratios. The highest cell numbers were obtained for the samples with the highest ratio for HeLa cells. The cell numbers of all samples were almost in the same range when reaching saturation. Only the counted cell number of the 1:100 sample was not in the range since this sample had not yet reached saturation at the end of the experiment. But still a ratio dependence of the cell numbers was observed.

Table 5.7: Calculated values for the length of the lag phase [h], and the PDT [h] as well as the average cell numbers reached in the plateau phase for the co-cultures of BJ1-hTERT and HeLa H2B cells in different cellular ratios.

	Reference	**1:100**	**5:100**	**10:100**	**20:100**	**50:100**
Lag phase BJ1-hTERT	55,23	33,32	58,7	69,74	66,87	24,74
Lag phase HeLa H2B	14,98	43,6	23,15	13,49	18,56	16,8
PDT BJ1-hTERT	52,59	38,04	46,65	39,45	37,99	47,75
PDT HeLa H2B	22,06	16,99	18,14	18,38	19,72	19,22
Average cell number in plateau phase BJ1	547.777	253.333	222.916	218.333	182.500	165.000
Average cell number in plateau phase HeLa H2B	3.580.000	1.051.666	2.449.583	2.694.166	3.293.333	2.893.333

It was also possible to see from the curve progressions that trend lines of the exponential growth phase had slightly different slopes, which were ratio dependent. The lower the HeLa H2B cell numbers were at the beginning of the experiment the steeper the trend line and, thus, shorter were the PDT time spans.

On the last day, all samples had cell numbers almost in the same range apart from the 1:100 sample, which had on the final day not yet reached the plateau phase. But the other samples showed in the average cell numbers a dependence on the HeLa H2B cell ratio. The higher the HeLa H2B cell numbers at the beginning of the experiment the higher were the cell numbers at the end of the experiment.

The Influence of Ionising Radiation on Cellular Co-cultures of BJ1-hTERT and HeLa H2B cells

After analysing the growth behaviour of BJ1-hTERT cells in co-culture with HeLa H2B cells cultivated in different ratios, the 20:100 ratio was used for further cell growth experiments. In the following experiments, the influence of X-ray radiation on cell proliferation was analysed when irradiating the whole co-culture.

Figure 5.19 shows the BJ1-hTERT cell growth curves of the irradiated samples as well as the reference, the 0 mGy sample, for the irradiation experiments where the whole co-cultures were irradiated.

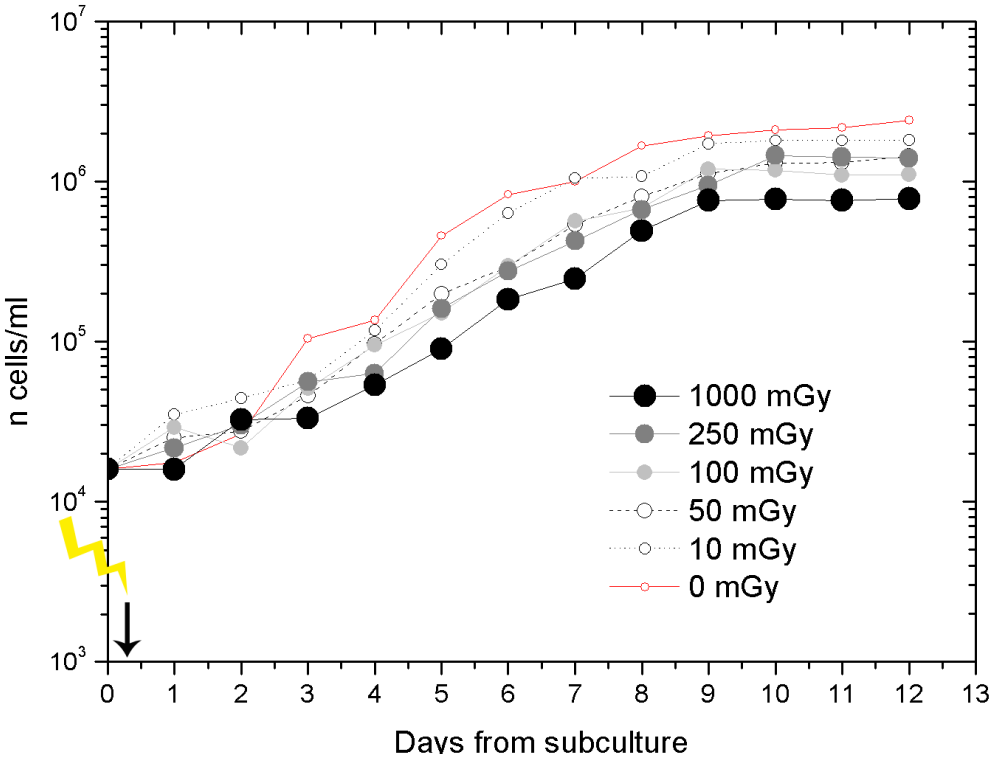

Figure 5.19: Cell growth curves of the BJ1-hTERT cells in co-culture with HeLa H2B cells in the ratio of 20:100. In this experiment the whole samples were irradiated. When only comparing the irradiated samples, a dose dependence in cell numbers could be observed during the exponential growth phase. The lowest cell numbers were counted for the 1000 mGy sample and the highest for the 10 mGy sample, which sometimes even had cell numbers higher than the reference sample. Also in the average cell numbers reached in the plateau phase a dose dependence was observed for the irradiated samples. The higher the dose, the lower were the cell numbers reached in saturation.

No sample showed an undershooting on the first day from subculture. All irradiated samples did respond to the irradiation and showed dose dependence in their cell numbers. Cell numbers were lower for higher irradiation doses.

When only comparing the irradiated samples it was possible to see that the 1000 mGy sample always reached the lowest cell numbers of the irradiated samples during the whole experiment and the 10 mGy sample the highest. Furthermore, the 10 mGy sample sometimes had cell numbers in the range of the 0 mGy sample. The difference in the cell growth curves was also reflected in the calculated lag phase time spans (Table 5.8).

The longest lag phase of the irradiated samples was determined for the 1000 mGy sample. No lag phase could be calculated for the 10 mGy sample, the graph started to rise immediately, indicating induced cell growth shortly after irradiation. No exact dose dependence was observed in the calculated PDTs. However, the average cell numbers reached in the plateau phase did show dose dependence. The higher the dose the lower were the reached numbers in saturation. Only the 250 mGy sample reached higher cell numbers in the plateau phase than the 100 mGy sample, thus, breaking the exact dose dependence of the samples.

The analysis of the HeLa H2B cells in co-culture with the BJ1-HTERT cells revealed different relations between irradiated and unirradiated samples (Figure 5.20). For the 1000 mGy sample an undershooting in cell number was observed on day one of the experiment. The 50 mGy sample showed an undershooting on day two from subculture.

This growth behaviour could also be seen in the calculated lag phases. The determined lag phases revealed that all irradiated samples apart from the 1000 mGy sample had shorter lag phases than the un-irradiated sample (Table 5.8). No real dose dependence could be observed for the lag phases since the time span for the 50 mGy lag phase was longer than the time span of the 100 mGy and 250 mGy samples. So, no steady increase with dose was determined.

During the exponential growth phase the highest cell numbers were counted for the 10 mGy sample until day eight when the 0 mGy sample reached higher cell numbers. When calculating the PDTs longer durations for the irradiated samples were determined, which is in correlation with the lower cell numbers reached at the end of the experiment. The time span increased with dose, only the 1000 mGy sample had a shorter PDT when

compared to the remaining irradiated samples. Again a dose dependence between cell number reached in the plateau phase and irradiation dose was observed.

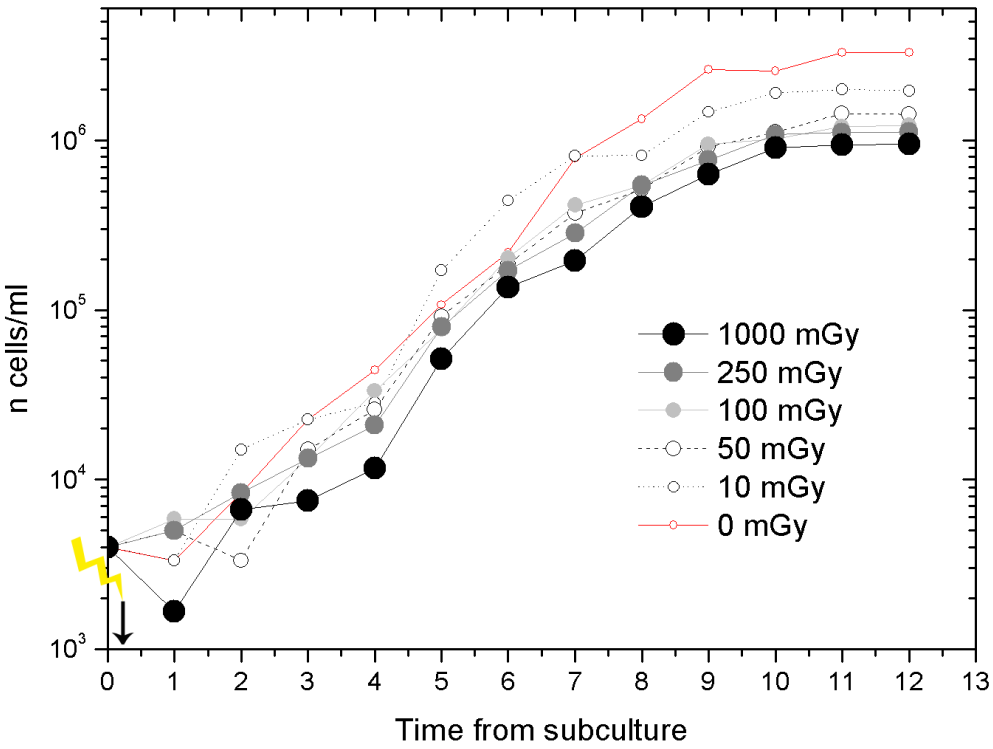

Figure 5.20: Cell growth curves of the HeLa H2B cells in co-culture with BJ1-hTERT cells in the ratio 20:100 after irradiation of the whole samples. For the HeLa cells all curves, thus, counted cell numbers were in the same range in contrast to the observance for the BJ1-hTERT cells. An undershooting in cell number was observed on day one for the 1000 mGy sample and on day two for the 50 mGy sample. During the exponential growth phase no dose dependence between all samples could be observed, only that the 1000 mGy sample reached throughout the whole experiment the lowest cell numbers. The average cell numbers reached in the plateau phase follow dose dependence, the higher the irradiation dose, the lower were the cell numbers reached.

Table 5.8: Calculated values for the length of the lag phase [h], and the PDT [h] as well as the average cell numbers reached in the plateau phase for the co-cultures of BJ1-hTERT and HeLa H2B cells when all cells were irradiated.

	0 mGy	**10 mGy**	**50 mGy**	**100 mGy**	**250 mGy**	**1000 mGy**
Lag phase BJ1-hTERT	14,46	--	13,15	9,14	12,68	26,81
Lag phase HeLa H2B	26,56	11,42	23,44	12,43	16,5	43,28
PDT BJ1-hTERT	24,84	33,04	31,82	34,15	34,03	34,56
PDT HeLa H2B	19,72	23,23	25,3	27,02	27,07	23,28
Average cell number in plateau phase BJ1	2.153.787	1.808.888	1.355.000	1.126.833	1.425.277	771.388
Average cell number in plateau phase HeLa H2B	3.293.333	1.949.444	1.321.944	1.145.833	1.103.888	929.444

Un-irradiated BJ1-hTERT cells in Co-culture with Irradiated HeLa H2B Cells

Another way to investigate the influence of ionising radiation was to irradiate only the HeLa H2B cells. Then, they were added to the BJ1-hTERT cells in the ratio 20:100. As a consequence, one can say that the BJ1-hTERT cells are only getting indirectly in contact with ionising radiation if at all. These samples will be called indirectly irradiated in the following chapters. This kind of experiment was performed in order to investigate the reaction of not-directly irradiated cells on the presence of directly irradiated cells, of another cell line, in context of a possible bystander effect. A threefold determination was performed to determine the cell numbers. No standard deviations are shown in the graphs due to clarity reasons.

When analysing the cell growth curves of BJ1-HTERT cells in co-culture with irradiated HeLa H2B cells, it was observed that the 50 mGy and 100 mGy samples showed an undershooting in cell number on day one from subculture (Figure 5.21).

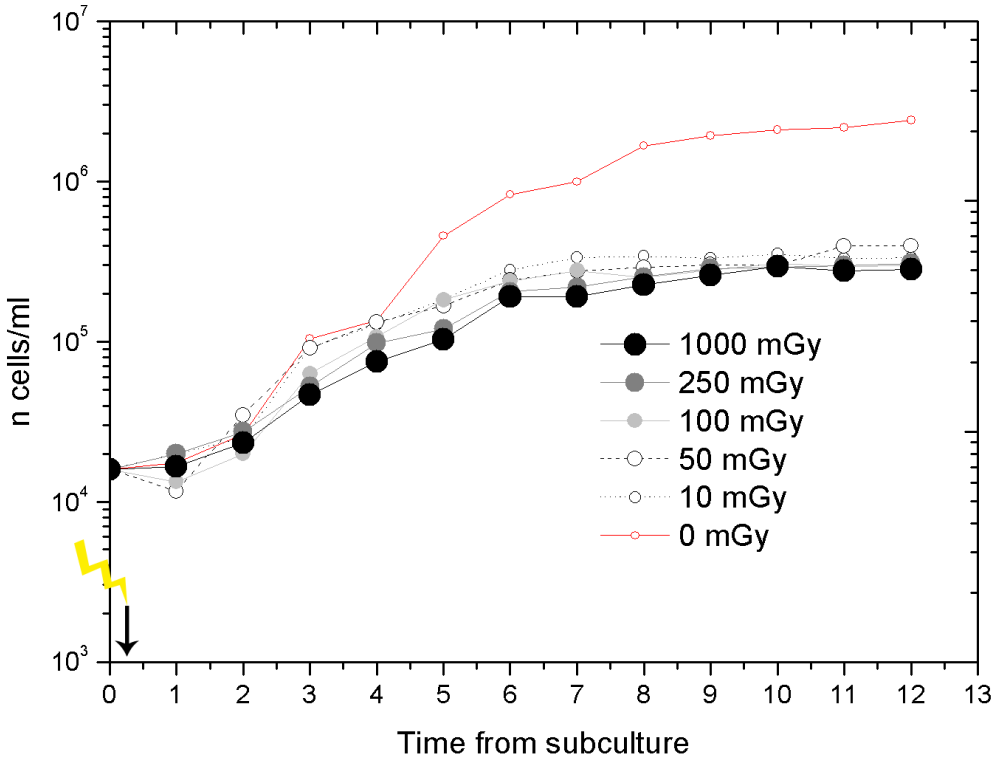

Figure 5.21: Cell growth curves of BJ1-hTERT cells in co-culture with irradiated HeLa H2B cells in the ratio of 20:100. On day one of the experiment the 50 mGy and 100 mGy samples reached lower values than originally plated on the day before. In contrast, the other indirectly irradiated samples showed no undershooting in cell numbers. The cell number counted for the 1000 mGy was in the range of the plated number, the cells of the 10 mGy and 250 mGy sample started to proliferate immediately after adding the irradiated HeLa cells. During the further curve progression of the indirectly irradiated samples a dose dependence of cell numbers was observed. This dose dependence was also observed in the average cell numbers reached in the plateau phase whereas the highest number was reached by the 0 mGy sample.

The 1000 mGy had a value in the same range as originally plated and the values of the 10 mGy and 250 mGy samples did already increase on day one. This growth behaviour is also reflected in the calculated lag phases (Table 5.9). It was not possible to calculate the duration of the lag phase for the 250 mGy sample since the cells started to proliferate immediately after adding the irradiated HeLa cells. In the log phase, a faster growth was analysed for the 50 mGy sample. The counted cell numbers were in the range of the 10 mGy sample and higher than the numbers counted for all other indirectly irradiated samples.

The fast increase in cell number of the 50 mGy sample can also be seen in the PDT. Its PDT had apart from the 250 mGy sample the shortest duration. The longest PDT time span was calculated for the 1000 mGy since the curve progression was flatter when compared to all other samples. Furthermore, dose dependence was observed for all samples in the average cell numbers counted in the plateau phase. For higher doses, lower cell numbers were determined, whereas the difference between the reference sample and the indirectly irradiated samples was much bigger in this experiment as for the direct irradiated cells.

It was possible to see that the growth curves of the indirectly irradiated BJ1-HTERT cells increased their cell numbers similar to the directly irradiated cells in the beginning of the experiment, but a flattening of the growth curves was observed starting from day six. This remained constant until saturation was reached at much lower cell numbers when compared to the directly irradiated BJ1-HTERT cells. The cell numbers of the indirectly irradiated cells reached numbers of only around ¼ of the directly irradiated samples. No huge differences in lag phase duration and PDT was observed between both experiments.

Figure 5.22 shows the cell growth curves of the irradiated HeLa H2B cells in co-culture with un-irradiated BJ1-hTERT cells. When comparing the graphs, it was possible to see that the irradiated HeLa H2B cells reached lower cell numbers than the 0 mGy sample throughout the whole experiment, which was not observed in the experiment where the whole samples were irradiated. On the first day, an almost dose dependent undershooting in cell numbers was observed for the irradiated samples. The lowest number was counted for the 1000 mGy sample followed by the 250 mGy sample. The number determined for the 100 mGy sample was slightly higher than the value of the 50 mGy sample but both samples still showed the undershooting. On the first day, in contrast a higher cell number as originally plated in the wells was detected for the

10 mGy sample. By calculating the lag phases from the trend lines the shortest was determined for the 0 mGy sample and the longest for the 1000 mGy sample (Table 5.9). All lag phases showed dose dependent increase in time span with increasing dose.

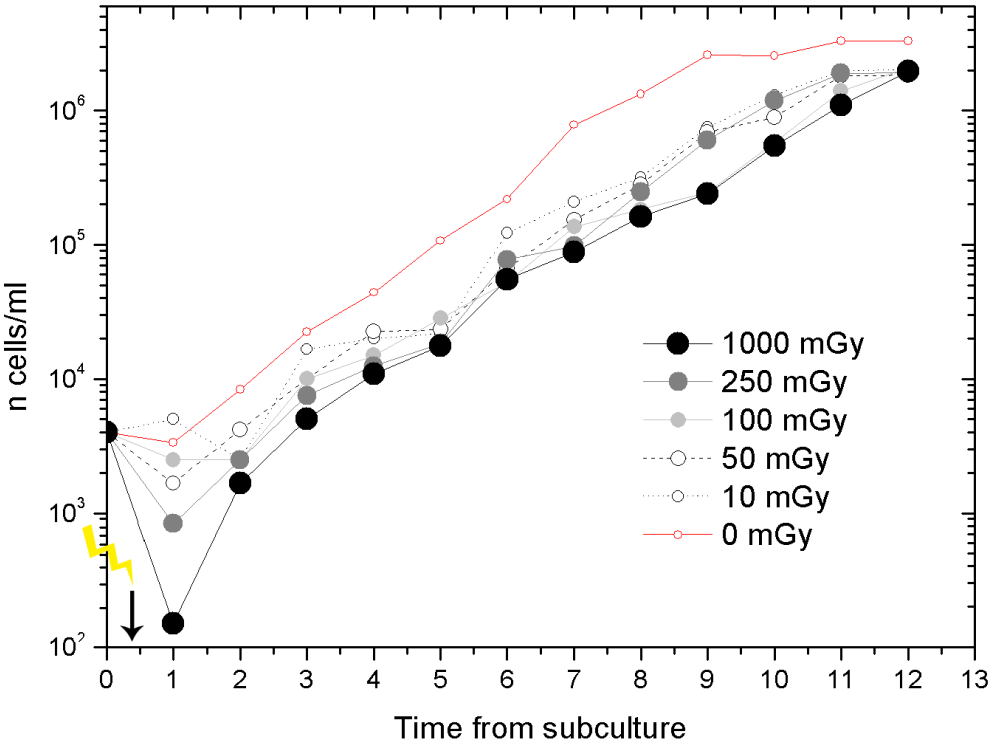

Figure 5.22: Cell growth curves of irradiated HeLa H2B cells in co-culture with un-irradiated BJ1-hTERT cells in the ratio of 20:100. An almost dose dependent behaviour was observed in the cell numbers counted on the first day from subculture. The lowest number was counted for the 1000 mGy sample followed by the 250 mGy sample. The determined value for the 100 mGy sample was slightly higher than the value of the 50 mGy sample. The 10 mGy sample did even show a higher cell number as originally plated. During the exponential growth phase also dose dependent behaviour could be observed in the cell numbers reached. Throughout the whole experiment the irradiated samples reached lower cell numbers when compared to the 0 mGy sample. At the end of the experiment saturation was not reached for all samples. The 100, 250 and 1000 mGy samples were still in the exponential growth phase.

During the exponential growth phase fluctuations in the cell numbers were observed for the 10 and 50 mGy samples. Small fluctuations were observed in the growth curve of the 250 mGy sample. Also during the whole growth process dose dependence in cell number was determined. Only the cell number of the 250 mGy exceeded the cell number of the 100 mGy sample, thus, breaking the dose dependence. The calculated PDTs were longer for all irradiated samples when compared to the un-irradiated sample. But no dose dependence in duration of the PDTs was observed. When analysing the graphs in their further curve progression, it was possible to see that no real saturation was reached on day 12 of the experiment. Apparently the data for 10 and 50 mGy samples reached

saturation, but the remaining three irradiated samples were still in the exponential growth.

Some differences in growth curves were observed when comparing the HeLa H2B cell growth curves of the direct and indirect irradiation experiments. Throughout the lag phase as well as the exponential growth, the cell numbers were lower in the indirect irradiation experiment. On the other hand, cell numbers reached in the plateau phase were higher for this experiment. Furthermore, the lag phases had longer durations for the indirect irradiation experiment, but the PDTs were in the same range for both experiments.

Table 5.9: Calculated values for the length of the lag phase [h], and the PDT [h] as well as the average cell numbers reached in the plateau phase for co-cultures of BJ1-hTERT and HeLa H2B cells when only the HeLa H2B cells were irradiated.

	0 mGy	**10 mGy**	**50 mGy**	**100 mGy**	**250 mGy**	**1000 mGy**
Lag phase BJ1-hTERT	14,46	7,9	17,12	23,55	--	22,84
Lag phase HeLa H2B	26,56	26,6	35,57	36,12	48,53	66,63
PDT BJ1-hTERT	24,84	33,29	18,43	30,98	16,64	50,64
PDT HeLa H2B	19,72	26,14	25,93	28,23	26,35	24,38
Average cell number in plateau phase BJ1	2.153.787	339.444	364.444	301.111	299.722	285.277
Average cell number in plateau phase HeLa H2B	3.293.333	2.024.166	1.840.833	2.103.333	1.930.833	1.963.333

80% Confluent BJ1-hTERT Cells in Co-culture with HeLa H2B cells

It was also investigated for the BJ1-hTERT and HeLa H2B co-cultures, if the state of confluence had an influence on the cellular behaviour with direct and indirect irradiation. The same experimental approach was performed here as for the L929 mouse fibroblasts. The BJ1-hTERT cells were left to reach a confluence of 80%. Then the HeLa H2B cells were added to the cell culture and either the whole samples were irradiated or only the HeLa H2B cells. Again the cell numbers were determined over a threefold approach and the standard deviations are not shown due to clarity reasons.

Figure 5.23 shows the cell growth curves of the directly irradiated BJ1-hTERT cells, Figure 5.24 the cell growth curves of the indirectly irradiated BJ1-hTERT cells for the 80% confluence experiments. When comparing both graphs clear differences in the curve progressions of the corresponding samples were analysed.

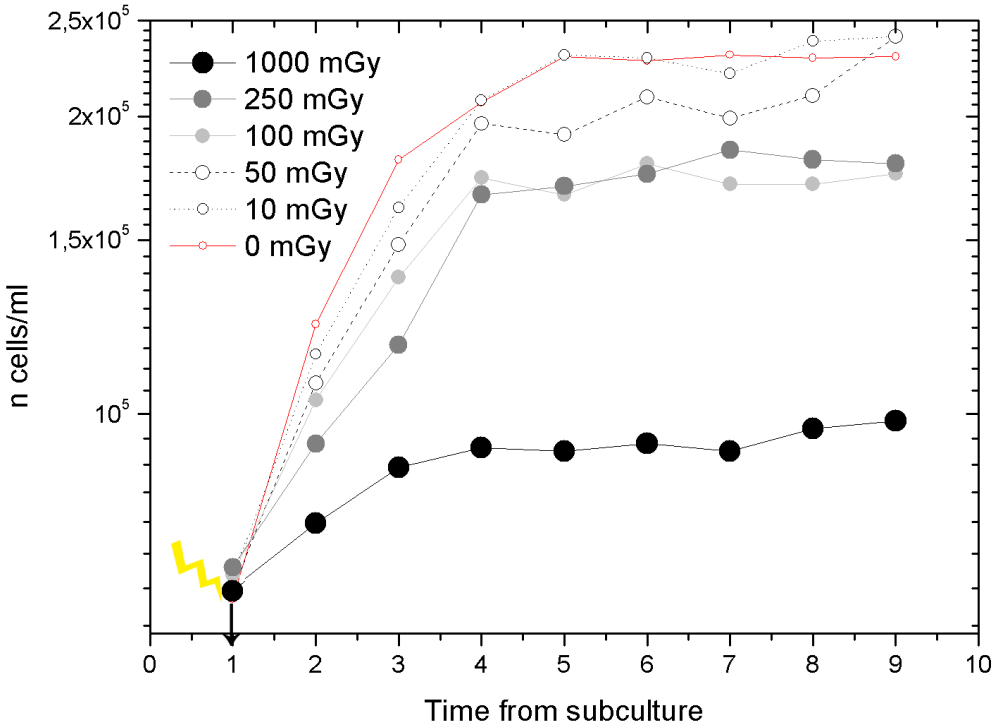

Figure 5.23: Cell growth curves of BJ1-hTERT cells in co-culture with HeLa H2B cells in the 80% confluence experiments when irradiating the whole samples. When comparing the curve progressions of the different samples a clear difference could be observed between the 1000 mGy sample and the remaining samples. The 1000 mGy reached saturation at a lower cell number already on the second day after adding the HeLa cells. All other samples reached saturation at higher cell numbers, but dose dependence could also be observed for them. The higher the dose the lower the cell number reached in the plateau phase.

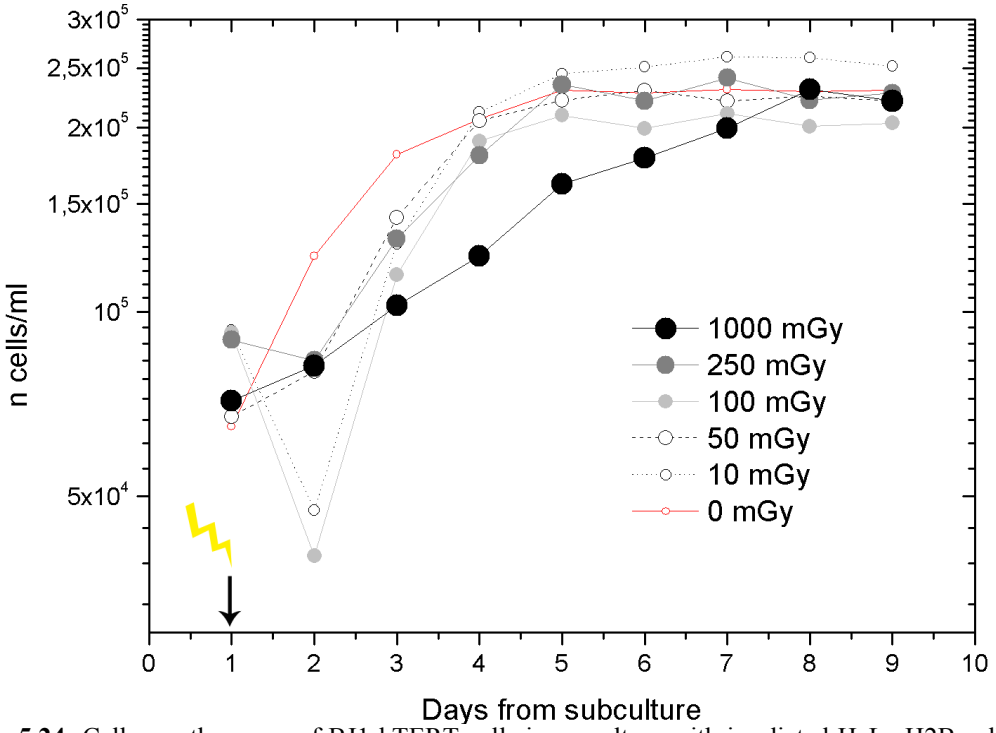

Figure 5.24: Cell growth curves of BJ1-hTERT cells in co-culture with irradiated HeLa H2B cells in the 80% confluence experiments. An undershooting in cell numbers was observed for the 10 mGy and the 100 mGy samples on the first day after adding the HeLa cells. But their cell numbers were on the following day again in the range of the remaining samples. The curve of the 1000 mGy sample showed a steady increase in cell number throughout the whole experiment and reached saturation around four days later than the other samples. No dose dependence in the cell numbers reached in the plateau phase was observed.

For the directly irradiated BJ1-hTERT cells it was observed that the 1000 mGy sample reached the plateau phase already two days after adding the HeLa cells. Also the other growth curves showed a negative influence of irradiation on the cell numbers reached in saturation. When averaging the cell numbers in the plateau phase dose dependence was observed (Table 5.10).

The cell growth curves of the indirectly irradiated BJ1-hTERT cells in contrast had completely different curve progressions. The 10 mGy and 100 mGy samples showed an undershooting in cell numbers two days after adding the irradiated HeLa cells to the cell culture. But the values reached again higher cell numbers the following day, and were in the same range as the cell numbers of the other indirectly irradiated samples apart from the 1000 mGy sample. This indicates a possible error in the cell number determination. The 1000 mGy sample had a steady increase in cell numbers over the whole experiment and reached saturation around four days later than the remaining samples.

When comparing the average BJ1-hTERT cell numbers reached in the plateau phase no dose dependence could be observed for the indirectly irradiated cells, but for the directly irradiated cells a clear decline in cell number with increasing irradiation dose was observed.

Table 5.10: Average cell numbers in the plateau phase of the BJ1-hTERT cell for both 80% confluence experiments.

	0 mGy	**10 mGy**	**50 mGy**	**100 mGy**	**250 mGy**	**1000 mGy**
Cell number in plateau phase, 80% all IR	229.375	232.291	214.791	173.958	180.000	95.000
Cell number in plateau phase, 80% HeLa IR	229.375	255.833	224.166	203.541	227.708	225.833

A comparison of the graphs of the HeLa H2B cells for both irradiation experiments with each other on the first observation no huge difference in the curve progressions could be determined (Figure 5.25 and Figure 5.26).

On the first day after adding the HeLa cells to the BJ1-hTERT cells, a dose dependence in cell numbers reached for the different samples was observed in both experiments. The lowest number was counted for the 1000 mGy samples. The calculated lag phase time spans were for all irradiated samples longer than for the un-irradiated samples (Table 5.11).

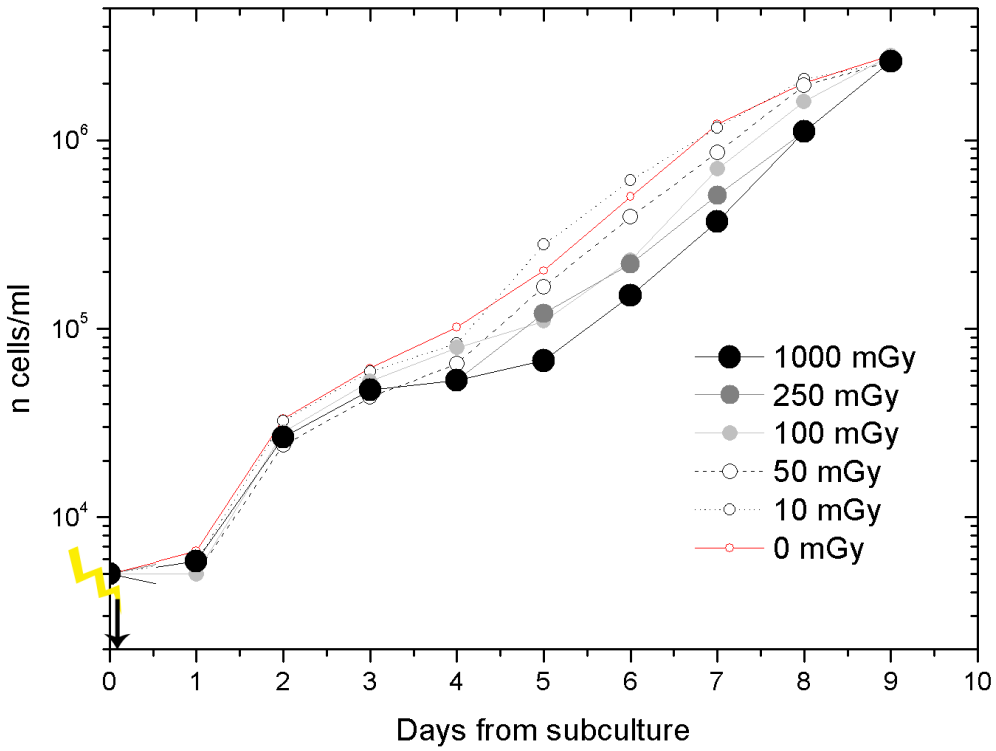

Figure 5.25: Cell growth curves of HeLa H2B cells in co-culture with BJ1-hTERT cells in the 80% confluence experiments when irradiating the whole co-culture. Dose dependent growth behaviour was observed in all growth curves throughout the experiment. The higher the dose, the lower was the counted cell number. At the end of the experiment no saturation was reached for all samples.

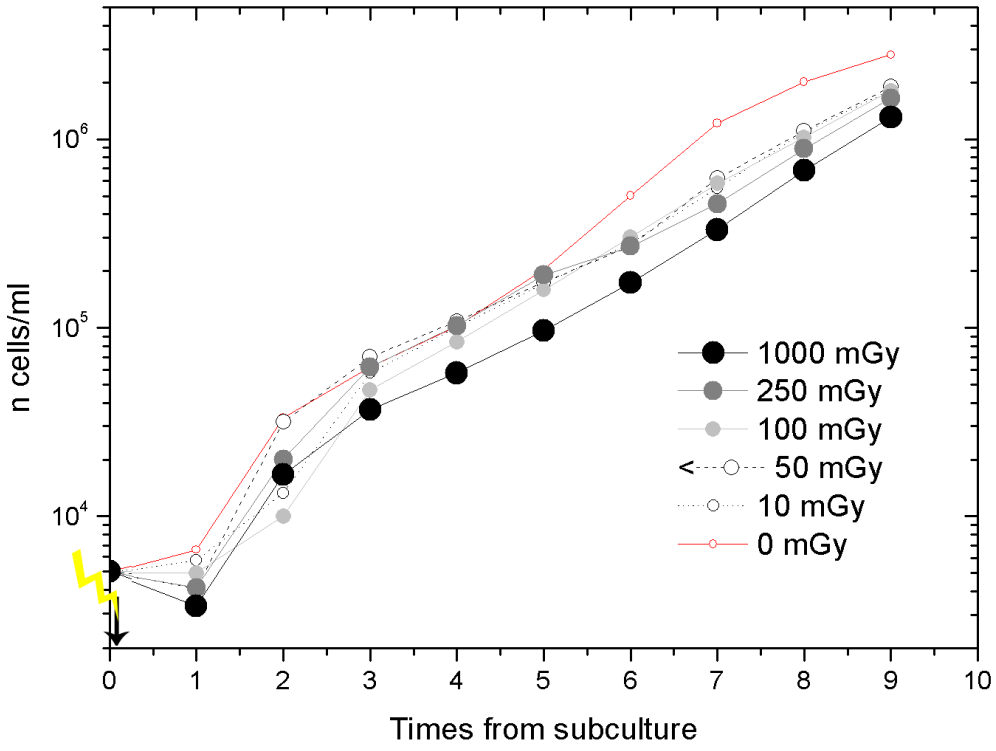

Figure 5.26: Cell growth curves of irradiated HeLa H2B cells in co-culture with un-irradiated BJ1-hTERT cells in the 80% confluence experiments. On the first day of the experiment a dose dependent behaviour of the counted cell numbers was observed for the different samples. The phenomenon, that the cell numbers were lower for higher irradiation doses, was also visible in the further curve progressions. The lowest cell numbers were counted for the 1000 mGy sample.

For both experiments time spans in the same range were determined. The longest lag phases were calculated for the 1000 mGy samples. The dose dependence of the cell numbers reached for the different samples was not constant during the whole experiment, but a dose dependent trend was visible.

Table 5.11: Calculated values for the length of the lag phase [h], and the PDT [h] as well as the average cell numbers reached in the end of the experiment for the HeLa H2B cells in both 80 % confluence experiments.

	0 mGy	**10 mGy**	**50 mGy**	**100 mGy**	**250 mGy**	**1000 mGy**
Lag phase BJ1-hTERT	42,15	43,35	53,54	52,74	53,17	65,42
Lag phase HeLa H2B	42,15	52,64	45,59	58,58	51,45	64,7
PDT BJ1-hTERT	22,87	22,31	21,74	22,88	24,09	23,35
PDT HeLa H2B	22,87	23,84	24,86	22,82	24,69	24,73
Cell number at the end of the experiment, 80% all IR	2.802.500	2.601.666	2.603.333	2.804.166	2.600.833	2.302.500
Cell number in the end of the experiment, 80%, only HeLa IR	2.802.500	1.820.000	1.900.833	1.802.500	1.644.166	1.300.833

When comparing the relation between the curves of the un-irradiated samples with the curves of the irradiated samples a difference was observed between both experiments. In the beginning, the curves of the irradiated samples were in the same range as for the un-irradiated samples. But from day six on lower cell numbers were counted for the HeLa H2B cells in the experiment where only the HeLa H2B cells were irradiated.

This was also reflected in the average cell numbers reached at the end of the experiment. It was difficult to compare the cell numbers with each other since not all were yet in the plateau phase but it was feasible to compare the two cell numbers reached of the corresponding samples from both experiments. Higher cell numbers were reached in the plateau phase for the experiment where the whole samples were irradiated. When comparing the PDTs with each other no huge difference in the time spans was observed.

5.1.3.3 Differences between the Cellular Co-cultures

A comparison of both co-cultures (mouse and human) used in the cytokinetic studies revealed some differences in behaviour for diverse cell cultures. In both experiments

where only the transfected cell lines were irradiated and plated with a ratio of 20:100 in a cell culture of either mouse or human fibroblasts, it was possible to see that both non-irradiated cell lines had shorter lag phases when they were in co-culture with irradiated cells. The difference in lag phases between the 0 mGy sample and the remaining samples was bigger for the human fibroblasts, BJ1-hTERT. They had a threefold and higher difference between the irradiated and the un-irradiated sample. The L929 mouse fibroblasts had maximal a twofold difference. However, both 0 mGy samples had lag phases in the same range.

The difference between the lag phases of the transfected cell lines was more obvious. Both showed a dose dependent increase in the lag phase time span with increasing dose. But whereas the lag phase for the 0 mGy sample lasted only around 26 h for the HeLa H2B cells it lasted around 97 h for the transfected L929 mouse fibroblasts.

Furthermore, it was observed for the calculated PDTs that the human fibroblasts needed a longer time span for doubling their number when compared to the non-transfected mouse fibroblasts. Both cell lines did not show dose dependence in the duration of their PDTs. Also no dose dependence in the PDTs was observed for the transfected and irradiated mouse fibroblasts. The irradiated HeLa cells showed an increase in the PDT duration when the cells were irradiated but no dose dependence. Longer PDTs for the irradiated samples were observed for the transfected mouse fibroblasts than for the HeLa cells when comparing the PDTs of both transfected and irradiated cell lines with each other. But the difference was not as big as for the non-transfected cell lines.

Independently from the calculated values of the different cell growth parameters, a big difference in the cell growth behaviour was also observed for both co-cultures when comparing acquired microscopic images. Figure 5.27 shows merged fluorescence microscopic images and phase contrast images of the same areas of both cellular co-cultures on different days from subculture. Both image sequences are images of co-cultures with the ratio 20:100 between transfected and non-transfected cells. The images were acquired from un-irradiated co-cultures, but the same observations were also made in co-cultures with irradiation as well as for the 80% confluence experiments.

The delay in the lag phase of the transfected mouse fibroblasts can clearly be seen in the number of green fluorescent cells on day four from subculture. Whereas the HeLa cells started to proliferate already after around one day, the transfected mouse fibroblasts needed around four days to overcome the lag phase, which can be seen in the difference

in cell number on day four from subculture. However the most striking difference in both co-cultures was observed when the co-cultures were reaching saturation. Whereas the transfected mouse fibroblasts were embedded in the non-transfected cell culture and only took the space they needed, HeLa cells started to overgrow the human fibroblasts and to replace them. This could be seen in the microscopic images acquired on day seven and eight from subculture.

The ability of HeLa cells to replace or crowd out the human fibroblasts was also observed in movies of living cells in co-culture over a certain time span. It was observed that the BJ1-hTERT cells started to move away from the HeLa cells during their cell division. Thus, the two daughter cells of the HeLa cells had more space and were able to attach easily to the bottom of the cell culture plate and to proliferate. The corresponding movie is attached in Appendix E.

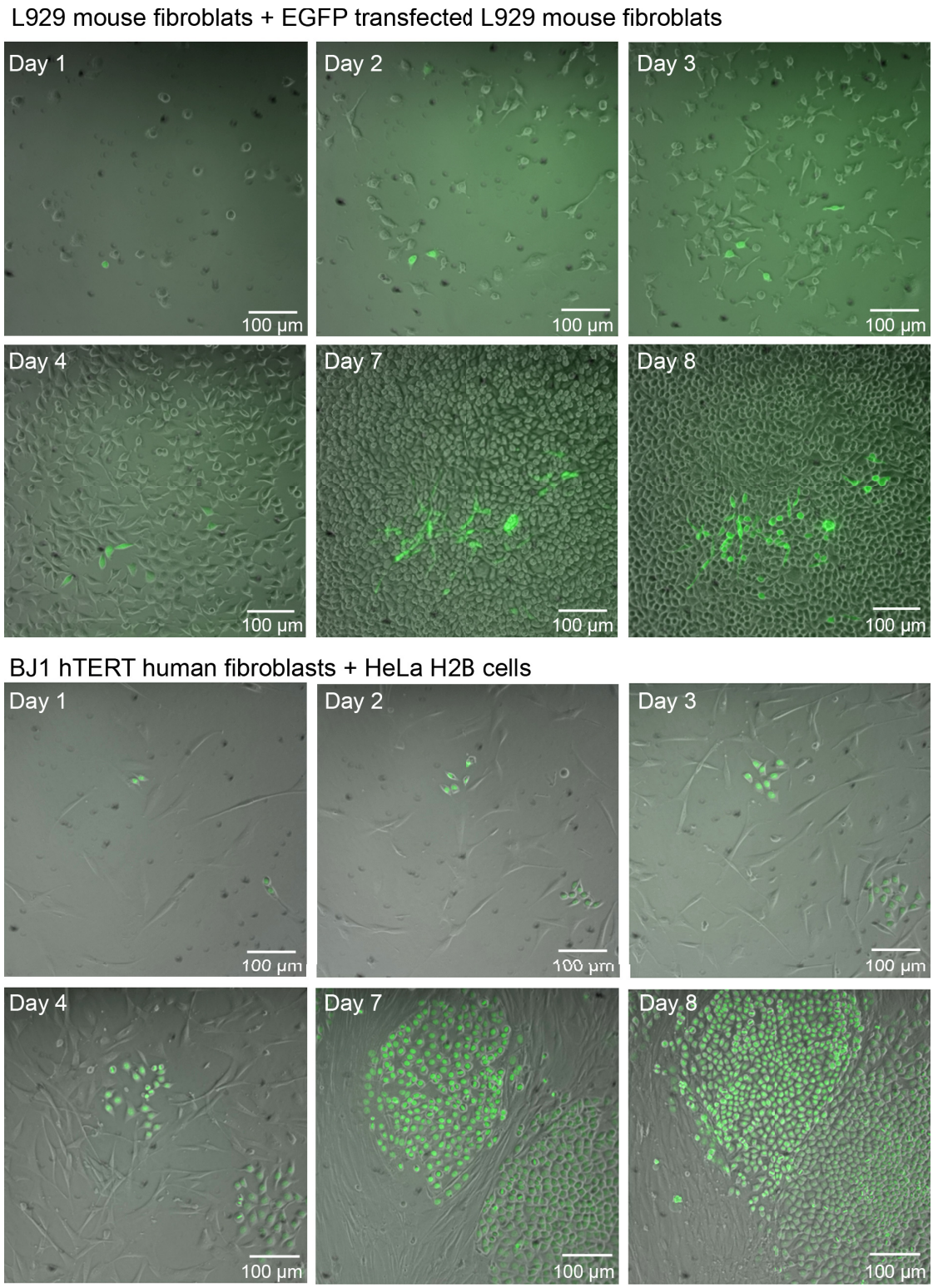

Figure 5.27: Merged fluorescence microscopic and phase contrast images of cellular co-cultures of either mouse cells or human cells. Both cell lines had in the beginning of the experiment a ratio of 20:100 between transfected and non-transfected cells. The samples in these images were not irradiated, but the same observations were also made for irradiated samples as well as for the 80% confluence experiments. On day four from subculture a clear difference in the number of green cells could be observed between both experiments, which was a result of the longer lag phase of the transfected mouse fibroblasts when compared to the transfected HeLa cells. Also different cellular behaviour was observed for both transfected cell lines. While the transfected mouse fibroblasts were embedded in the culture of the non-transfected cells the transfected HeLa cells started to overgrow and to crowd out the human fibroblasts (day 7 and day 8).

5.2 Discussion

5.2.1 Is GFP Plasmid Toxic for Cells?

Unsuccessful transfection of BJ1-hTERT cells leads to the conclusion that the EGFP plasmid used for transfection was either possibly toxic for these cells, since reduced cell vitality and survival was observed following transfection (before adding the selective antibiotic), or the plasmid was not build into the cellular genome, thus, the cells had no resistance against the selective antibiotic (Figure 5.1).

The use of EGFP as a live cell reporter is based on the assumption that cellular functions are not affected severely (118). However, GFP expression was linked to induction of apoptosis in a number of cell lines (119). It was also observed that GFP by itself can selectively induce the expression of certain genes in endothelial cells. Increasing concentration of GFP resulted in an up-regulation of HSP70[10] (120). Furthermore, EGFP was shown to affect actin-myosin interactions in heart muscle cells (121). And it was observed that GFP expression affects the p53 homeostasis (118). All these findings indicate that the GFP plasmid should not be used as live cell reporter without knowing the alterations it might evolve in the genome of living cells. Protein arrays of non-transfected and transfected cells would give an insight in the proteins up- or down-regulated in both cell lines and whether there is an change in the cellular behaviour induced by the GFP expression.

The transfection of L929 mouse fibroblast resulted in a stable cell line expressing pEGFP (Figure 5.2). No differences in the growth behaviour as well as in the morphology of non-transfected and transfected cells was observed. Thus, both cell lines were assumed to be directly comparable and of the same kind in the cell growth experiments. However, for experiments where the influence of irradiated and transfected cells on un-irradiated and non-transfected cells is analysed over the up- and down-regulation of certain proteins, it is essential to perform protein arrays of both cell lines before the experiment to ensure the comparability of both cell lines since only proteins, and hence the proteome, are able to reflect the physiological state of a cell (122).

[10] HSP70 belongs to the family of heat shock proteins, which are an important part of the cell ability for protein folding. Furthermore, it helps to protect cells from stress.

5.2.2 Recultviation of Single Cells - a possible Tool for the Analysis of Ionising Radiation Influences?

In recultivation experiments for the tracking of single cells, varying results were observed. In general, it was possible to recultivate single cells via the laser microdissection and catapulting principle. The cells survived the process and started to proliferate again after a certain time-span (Figure 5.3). Thus, it is possible to irradiate transfected cells, to isolate single cells of these cultures and to plate them in non-irradiated cell cultures in order to analyse their influence on the existing cell culture. So far, this is only possible over the analysis of induced apoptosis or changes in the growth behaviour. The analysis via a protein array over a minute amount of cells would give more insights in the cellular behaviour, and possible changes induced through both, the direct or indirect influence of ionising radiation.

Nevertheless, also not so promising results were observed. Some cells did not divide properly and became huge cells with multiple nuclei, so-called Syncytien (Figure 5.4). The occurrence of multinucleated cells in non-transfected L929 mouse fibroblasts was never observed during cell culture. This indicates that a syncytien-like state is not part of the maturation process as in for example myocytes[11] (123). Furthermore, multinucleated cells sometimes accompany inflammation (124) and can occur during tumor formation (125). The most likely explanation for the occurrence of syncytien in the recultivation process of single cells is the stress factor.

A transfection of cells with the plasmid DNA is stressful for the cells. The plasmid DNA has to be integrated in the cellular DNA for a stable transfection, which was the case for the L929 mouse fibroblasts. Furthermore, the recultivation process is also stressful for cells and might have an influence on the cellular behaviour and the ability to divide. More experiments have to be performed including the analysis of transfected cells via protein arrays in order to understand if the occurring multinucleated cells are generated due to the stress of the GFP expression, genomic plasmid integration site or due to the recultivation process. One could argue that most likely the multinucleated cells occurred due to the recultviation process since they were never observed in normal cell cultures. However, the possibility to find a single multinucleated cell in a cell culture of around 1.000.000 cells is very low.

The recultivation of single cells via the low pressure adsorbing transfer system is a promising experimental approach since it is more effective in transferring isolated

[11] Skeletal muscle cells in human.

pieces than the catapulting principle. However, the stress on the isolated cells through the low-pressure applied to the system was too much, and the cells did not survive the transfer with this system. By reducing the size of the glass tube connected to the adsorption head, the size of the grid pattern on the adsorption head and by further reducing the applied low-pressure, the stress on the cells could be reduced and they would possibly survive the transfer process.

However, it is necessary to bear in mind that the GFP plasmid transfection, as well as the recultivation process are stress for the cells. Thus, to analyse the influence of ionising radiation on neighbour cells of a single irradiated cell via this approach might not be as useful as first thought. Stress-factors expressed in the irradiated cell and signalled to the neighbour cells might result from the GFP plasmid transfection, the recultivation process as well as the irradiation. The stress induced through the GFP transfection could be excluded through the use of stable transfected cell line. Nevertheless, the recultivation process has to be performed in order to be able to investigate the influence of a single irradiated cell on its neighbours in this approach, which is stressful for the cell.

Hence, it is better to perform single cell irradiation experiments with a microbeam set-up, as for example the SNAKE set-up at the TU Munich (126). This approach would exclude stress factors resulting from for example the recultivation process after irradiation. Furthermore, the irradiated cell is already part of the cell culture and effects evoked by either soluble factors secreted from the directly irradiated cell in the media or via gap-junction communication right after the irradiation are not lost due to a further experimental step, the recultivation process.

5.2.3 The Informative Value of Cell Growth Curves

Cell growth curves are widely used in biology to investigate the growth behaviour of different cells. They play for example an important role in cancer research (127). Furthermore, the analysis of cell proliferation rates is often used to determine the response of cells to certain influences, here ionising radiation.

Cell numbers were determined in the cytokinetic experiments with a Neubauer cell counting chamber, which uses only a small volume for the determination. The cell number per ml was then acquired over an extrapolation. Hence, this approach included

some uncertainties. The use of a Coulter counter[12], which uses the total volume of $V = 1\,ml$, optimises the cell number determination but it cannot distinguish between non-fluorescent and fluorescent cells, which was necessary for the performed experiments. This differentiation can be achieved over fluorescence-activated cell sorting (FACS), which is a specialised type of flow cytometry and sorts a heterogeneous mixture of biological cells into different containers (128). The principle of a FACS device is the specific light scattering and fluorescent characteristic of each cell. Thus, a larger volume of cell suspension could be analysed easily, and the cell number could be determined more accurate. However, the cell number determination with a Neubauer cell counting chamber still gives a relatively good insight into the cellular behaviour in cytokinetic experiments. But one has to be careful with absoluteness in the declarations.

The undershooting in cell number on the first day from subculture observed in some experiments is, for example, most likely an artefact of inconsistent cell suspension dilution in order to obtain the desired cell number per ml in the beginning of the experiment (e.g. in Figure 5.7). However, the consideration arises in some experiments that the reduced cell number in the beginning of the experiment is not only induced by plating the wrong number of cells, but by the influence of the irradiation, since dose dependence was observed for some experiments (e.g. in Figure 5.19, Figure 5.22). On the other hand, changes in the growth behaviour during the log phase as well as the cell numbers reached in the plateau phase are most likely real effects induced by the different experimental approaches since the cell numbers were determined over a threefold determination and the actual cell number per ml was the average of all three. As shown in Figure 5.8 the three cell growth curves, which define the corresponding average growth curve did all have similar curve progressions. Thus, the observed trends were consistent over the whole threefold determination.

5.2.3.1 Mono- and Co-cultures of Non-transfected and Transfected L929 Mouse Fibroblasts

The monoculture experiments with L929 mouse fibroblasts either non-transfected or transfected with an EGFP expression plasmid revealed certain differences in behaviour during the growth experiment (Figure 5.7, Figure 5.9). This suggests that possibly the

[12] A Coulter counter detects changes in electrical conductance of a small aperture as a cell suspension is drawn through and, thus, counts and sizes particles and cells. The effective cross-section of the conductive channels is altered since cells are non-conducting particles.

alterations in the genome through the random integration of the EGFP expression plasmid had an influence on the overall cellular behaviour. But the difference between both cell kinds showed not extreme differences in cell growth and the cells were assumed to be the same cell line. For the reference samples almost analogue growth behaviour was observed. Furthermore, the biggest dose response was observed for the 1000 mGy samples in both cell lines as well as a dose dependence in the PDTs (Table 5.2), whereas the reaction to the irradiation was more reduced in the non-transfected cells. This could be a possible influence of the GFP expression in the transfected cells.

When plating both cell lines in co-culture longer lag phases were observed when analysing the cells individually, whereas the difference in the lag phases was small for the non-transfected cells in contrast to the transfected cells (Table 5.3). The divergence from the monocultures can be explained by the lower cell numbers plated for each cell line in this experiment, which is increasing the possibility of deviations in the cell suspension dilutions. However, a dose dependence of the lag phases was observed for the total co-culture in contrast to the observance in the monocultures. No dose dependence was observed for both parts of the cell culture individually, and the undershooting in cell numbers of the transfected cells had almost no influence on the total cell number since the number of these cells was too low in the beginning of the experiment (Figure 5.12). Furthermore, longer PDTs were calculated for the total co-culture when compared to the individual monocultures as well as a dose dependence of the time spans. Also a delay in the transition into the plateau phase and higher average cell numbers in the plateau phase were observed for the co-culture experiment apart from the 1000 mGy sample.

One could argue that these observations do indicate that the irradiation of only a small fraction of a cell culture has a stronger influence on the cell growth than a total irradiation. However, also the reference co-culture (0 mGy) did show the same behaviour, e.g. reaching higher cell numbers in the plateau phase (Table 5.3). Thus, the effects can not only be attributed to irradiation effects but also to effects induced by the co-culture of non-transfected and transfected cells.

When comparing the two irradiation experiments performed with 80% confluent and non-transfected L929 mouse fibroblasts in co-cultures with transfected L929 cells, a clear difference in the cell growth curves between both experiments was observed. The difference in the growth behaviours of the non-transfected cells can be led back to the different kinds of irradiation (Figure 5.13, Figure 5.14). The directly irradiated cells showed a clear difference in the cell numbers between the reference sample and the

irradiated samples. In contrast the reference sample for the indirectly irradiated cells had cell numbers in the range of the samples irradiated with doses under 1000 mGy. These findings clearly indicate that the difference in irradiation had an effect on the cell growth, which was also observed in the growth experiment with a lower cell density at the time of irradiation.

Directly irradiated cells were more affected by the ionising radiation than the cells, which were only exposed indirectly to the irradiation. Nevertheless dose dependence was observed in the cell numbers reached in plateau phase indicating that the effect of the ionising radiation was maybe not clearly visible in the indirectly irradiated samples in the beginning of the experiment but arose towards the end when saturation was reached. This implies that the indirectly irradiated cells were possibly affected by factors secreted in the medium by the irradiated cells. But not via gap function, since the L929 mouse fibroblast do not form gap-junctions for signal transmission. However, these effects were not as effective as the direct irradiation since the cells were not affected immediately but it took a certain time interval for the cells to respond to the effects.

The results presented, are in correlation with prior findings where the medium from irradiated cells affected not-irradiated cells (3, 129, 130). Similar behaviour was observed for the reference samples and irradiated samples of the transfected cell (Figure 5.15, Figure 5.16). However, the 10 mGy samples in the whole irradiation experiment reached cell numbers in the range of the 0 mGy sample indicating that no clear effect of the radiation was observable in this case. But all other samples showed a dose dependent behaviour demonstrating the negative influence of ionising radiation on the cellular growth behaviour. The effect was more predominating for the experiment where only the transfected cells were irradiated suggesting that possibly the stress of the trypsination in addition to the irradiation did influence the cells negatively.

5.2.3.2 Human Fibroblasts vs. Human Cancer Cells

Interesting growth behaviour was observed in the cellular co-cultures where different ratios of BJ1-hTERT and HeLa H2B cells were cultivated in co-culture. It was observed that the BJ1-hTERT monoculture needed a longer time span to reach saturation (Figure 5.17). The more HeLa H2B cells were in the cell culture the faster the saturation was reached by the BJ1-hTERT cells. This behaviour can be explained easily by the faster cell division of the HeLa H2B cells and, consequently, faster increasing cell number. Hence less free space was available in the cell culture wells, which had an influence on

both, the time-point when saturation was reached and the average cell number reached by the BJ1-hTERT cells in the plateau phase.

It was also interesting to see that HeLa H2B cells proliferated faster for lower cellular concentrations in the beginning of the experiment suggesting that the HeLa H2B cells wanted to faster increase their number in dependence on their concentration in the cell culture (Figure 5.18). In the end of the experiment no huge difference was observed for HeLa H2B cells in the average cell numbers reached in the plateau phase. This was also demonstrated by the corresponding images acquired each day of the cell culture. HeLa H2B cells started to overgrow the BJ1-hTERT cells when there was not enough space left in the cell culture wells. Hence, they were still able to increase their number and, thus, to reach cell numbers in the range of the reference HeLa H2B sample.

For BJ1-hTERT in co-culture with H2B, a dose dependent behaviour in the curve progression was observed for both irradiation experiments (Figure 5.19, Figure 5.21). The samples had decreasing numbers with increasing irradiation dose, which was also reflected in the average numbers reached in the plateau phase, whereas the difference in the counted cell numbers between the different irradiation doses was bigger for the directly irradiated cells. No dose dependence was observed for both, the lag phases as well as the PDTs. However, the lag phases were shorter for either the directly as well as the indirectly irradiated samples than for the reference sample and in the same range for both.

It was also not possible to determine the lag phases for all irradiated samples since some growth curves started to rise immediately at the beginning of the experiment. These findings reflect an induced cell proliferation and some kind of adaptive response in BJ1-hTERT cells through both irradiation kinds in the beginning of the experiment. However, this radiation-induced cell growth was not observed in the following days of the experiment since the 0 mGy sample reached then higher cell numbers. This suggests that the radiation-induced cell growth from the beginning of the experiment was not dominating the natural cell growth in the further development. Furthermore, it seemed as the indirectly irradiated cells were not as strongly stimulated as the irradiated BJ1-hTERT cells. They reached in the end of the experiment lower cell numbers.

The HeLa H2B cells also showed a dose dependent behaviour in the cell numbers, which were reached during and in the end of the experiment (Figure 5.20, Figure 5.22). Curiously, the HeLa H2B cells in the direct irradiation experiment showed stronger dose dependence in their cell numbers when comparing the irradiated samples with each other,

although the HeLa H2B cells in the indirect irradiation experiment were also irradiated directly. Possibly, the trypsination affected the effect induced by the ionising radiation in the indirect irradiation experiment, or the cell to cell contact between HeLa H2B cells and BJ1-hTERT cells during irradiation, had an influence on the cell growth. Nevertheless, when comparing the reference sample with the irradiated sample a huge difference for the HeLa H2B cells in the indirect irradiation experiment was observed. This finding is in correlation with the consideration that possibly the trypsination of the HeLa H2B cells had a further effect on the cells.

The growth behaviour of BJ1-hTERT cells after direct or indirect irradiation revealed that the cell density possibly had an influence on the reaction of the cells to different irradiation doses. A huge difference between the growth curves of BJ1-hTERT cells from both experiments could be seen (Figure 5.23, Figure 5.24). Both experiments showed a dose dependent proliferation of cells. This could also be seen in the cell numbers when saturation was reached, but only for the directly irradiated cells. The indirectly irradiated cells did not show any dose dependence. The biggest irradiation effect was evoked in the 1000 mGy samples, but while the directly irradiated cells reached saturation shortly after the beginning of the experiment the indirectly irradiated cells showed a steady increase during the whole experiment until saturation was reached.

These findings indicate that the cell density possibly had an influence on the cellular growth behaviour. In the exponential growth experiments the difference between the two graphs of the different irradiation experiments was not as huge as for the 80% confluence experiments. As mentioned above most effects of low LET radiation, i.e. X-rays, are induced in cells through the radicals generated through the hydrolysis of water. Thus, the probability of cells being either directly damaged by ionising radiation or indirectly through the radicals is higher for more confluent cell cultures, at least for lower irradiation doses.

The cells have more contact to each other and, hence signals secreted via gap junction from hit cells can easily be distributed to non-hit cells and affect them. Also factors secreted from the irradiated cells into the medium might have an influence on neighbouring cells and affect them negatively. If the cells are only sparsely distributed over the cell culture plate the probability of a hit is much lower and, thus, the distribution of a signal to the non-hit cells.

The analysis of the HeLa H2B cells from both irradiation experiments did not result in such huge differences in growth behaviour (Figure 5.25, Figure 5.26). Some dose dependent behaviour was observed for both experiments but it was not as obvious as for the BJ1-hTERT cells. Nevertheless, it is possible to derive from the growth behaviour as well as the cell numbers reached in the end of the experiment that again a negative effect of the trypsination in addition to the irradiation could be observed for the HeLa H2B cells in the indirect irradiation experiment. But the cell density of the BJ1-hTERT cells had no influence on the HeLa H2B cells since the cell numbers reached throughout the whole experiment were in the same range as in the exponential growth experiment.

5.2.3.3 What Difference makes a Cellular Co-Culture with Cancer Cells?

At first sight, it is difficult to compare the mouse fibroblast co-cultures with human fibroblast co-cultures. Both cell lines show completely different growth behaviour. However, it is still possible to draw conclusions from the cell growth of both co-cultures in which way a co-culture with the “same” cell kind and a cancer cell from the same species can affect the other cells.

Whereas the transfected L929 mouse fibroblasts seemed to embed into the cell culture of the non-transfected mouse fibroblasts the human fibroblasts seemed to move away from the HeLa cells. This observance is displayed in both, the acquired fluorescence microscopic images (Figure 5.27) as well as the in movie (Appendix E) from the cell cultures. The non-transfected and transfected mouse fibroblasts are from the same kind, independent from the genetic changes induced through the GFP expression. Thus, the cells do not secrete any cell type dependent factors and do not have a different extracellular matrix, which could affect the cell growth of the other cells. However, HeLa cells on the other hand are a complete different kind when compared to the BJ1-hTERT cells.

Thus, a lot of cytokines can affect the other cell line. As seen in the images (Figure 5.27) as well as the movie (Appendix E) the BJ1-hTERT cells are more affected by the HeLa cells than the other way round. Cytokines could regulate the signalling between both cell lines. One of these cytokines could be for example TGFβ, whereas the regulation might be due to the expression as well as the activation (131). Furthermore, the signalling could also be controlled over extracellular calcium as well as the epidermal growth factor (EGF) or fibroblast growth factor (FGF) and their related signalling

molecules. It is also most likely that the HeLa cells produce in the membrane extracellular superoxide anions over their nicotinamide adenine dinucleotide phosphate-oxidase (NADPH-oxidase), which react to hydrogen peroxidase. Like most tumor cells, HeLa might have a catalase expression on the membrane, which elmininates the hydrogen peroxide. Thus, the HeLa cells themselves can prevent the intercellular reactive oxygen species (ROS) signalling (132). ROS signalling can increase dramatically during times of environmental stress and, hence damage the cell structures significantly.

It is necessary to perform experiments with quantifiable measurement systems in order to understand, which secreted factor is eventually responsible for the back off of the BJ1-hTERT cells from the HeLa cells. In this context, neutralising antibodies against certain cytokines could influence the observed cell reaction in all experiments, in order to find the responsible signalling molecule. Thus, it would be also possible to observe the changes in cellular signalling induced by the ionising radiation, which influences the cellular behaviour of the other cells in the co-culture.

6 Conclusions and Outlook

A new imaging platform and mathematical tools to quantify the DNA damage response of cells imaged by immunofluorescence microscopy were introduced in this work. This advance enabled a fast and low cost analysis over a wide range of experiments in one experimental approach. After optimisation of the immunostaining process the responses of two normal human cell lines (MCF10A, HCA2) were characterised by irradiating one multiwell slide with two different doses. The analysis of these experiments revealed that as the number of DSB increases in a cell, the number of RIF does not increase proportionally and the RIF kinetic is altered. RIF appear faster but remain longer in the cells with increasing irradiation dose. Additional experiments with two other cell lines (BJ1-hTERT, HeLa) confirmed these findings.

Then, a further optimisation of the experiments was attempted by introducing step-filter absorption, thus, enabling the irradiation of one slide with six different doses in one go. Again the same kinetic behaviour and saturation in RIF yield was observed. However, the successive absorption of X-rays through the used Pb step-filter resulted in alterations in the X-ray emission spectra and, thus, changes in the response of the cells. With more experiments including the step-filter absorption it would be possible to determine the rate of the factor, which alters the response. By including this factor in the results it would be then possible to perform step-filter experiments without loss and compare them directly to experiments without filtration.

Apart from that, the results from all experiments contradict the assumption that one DSB always leads to one RIF. Furthermore, experiments with high energy ions (not presented here) did show that complete different RIF yields and kinetic can be measured simultaneously in the same cell (102). This suggests that the apparent saturation of the DNA damage response cannot be attributed entirely to an overall exhaustion of kinases or substrates in the cell. Instead, it may reflect a mechanical aspect of repair, where multiple DSB in close vicinity would rapidly cluster into one single RIF. With such hypothesis, as the X-ray dose increased, the probability of having two DSB close enough to cluster within one common RIF increases also. Thus, as the dose increases, RIF count per dose would be lower and DSB cluster would have a higher chance to be detected faster but would take longer to repair.

In agreement with this hypothesis, a recent theoretical study taking into account the track structure of high energy ions and the supercoiled topography of DNA, suggests

that multiple DSB can be contained within one single RIF (133). In fact, high-energy ions may shed some light on the range of interaction between DSB. The existence of repair centres has already been shown in yeast *saccharomyces cerevisiae* (134). However, for human cells it remains to be seen if the DSB clusters suggested by this work are the result of random coalescence of DNA damage sensor proteins or of active movement of DSB towards pre-existing repair centres.

Fractionated irradiation experiments did not lead to optimal results since no clear trend could be observed in the time responses. More experiments have to be performed in order to be able to declare absolute assertions. However, it was possible to derive from the experiments that the response of the cells was not altered by further stress factors due to for example the cultivation in only some µl of medium or multiple handling of the slide during the experiment. Nevertheless, it is also necessary to perform more experiments with the step-filter absorption to determine the factor, which alters the response of the cells due to the changes in the X-ray emission spectra. After determination of the factor it would be possible to easily perform fractionated irradiation experiments over a wide range of doses and time intervals between the multiple irradiations with this set-up.

Recultivation of single transfected cells showed that the processes of recultivation and transfection are of enormous stress for cells and might alter the response of the cells in addition to the irradiation-induced effects and, thus, hinder the analysis of the radiation effects. The analysed bystander effects could be hindered because of this alteration. Thus, in order to analyse bystander effects after single cell irradiation it would be better to revert to microbeam irradiation. Also the first signals transmitted from the irradiated cells to not irradiated neighbour cells, which get lost through the recultivation process, would then be included in the analysis.

Cytokinetic experiments presented here can only be understood as a model for cellular behaviour *in vivo* since the cells are not embedded in three-dimensional tissue in the *in vitro* experiments. Nevertheless, it is possible to draw conclusions about cellular behaviour with and without irradiation also from *in vitro* experiments. For both co-culture experiments with mouse and human fibroblasts, it was observed that the partial irradiation of cells in a cell culture resulted in stronger effects in the cell growth behaviour. Furthermore, it was observed that also the state of confluence affected the cellular reaction, while the effect for the cell cultures with human fibroblasts was more drastic than the effects evoked in the mouse fibroblast cell cultures. Thus, one can say

the possibility of radiation-induced bystander effects is higher in cell cultures with higher density and, hence, also in the tissue. To completely understand the cellular behaviour and which signals lead to the response of the surrounding cells more experiments have to be performed in this context. Nevertheless, the observed dose dependence in growth behaviours in the different experiments is in correlation with the higher number of DSB induced by the ionising radiation. Thus, the cells need a longer time for repair, which explains the delay in cell growth and the lower cell numbers reached throughout the experiment.

Regulatory agencies currently apply a linear scale extrapolating cancer risk from high doses to low doses of ionizing radiation. The findings in RIF experiments presented in this work question the current risk assessments and provide instead a mechanism that could address risk dose dependency.

7 Literature

1. BfS (2008) *Jahresbericht* (Bundesamt für Strahlenschutz, Salzgitter).
2. UNSCEAR (2006) Effects of Ionizing Radiation. II.
3. Lyng FM, Seymour CB, & Mothersill C (2002) Initiation of apoptosis in cells exposed to medium from the progeny of irradiated cells: a possible mechanism for bystander-induced genomic instability? (Translated from eng) *Radiat Res* 157(4):365-370 (in eng).
4. Morgan W (2003) Non-targeted and delayed effects of exposure to ionizing radiation: II. Radiation-induced genomic instability and bystander effects in vivo, clastogenic factors and transgenerational effects. *Radiation Research* 159(5):581-596.
5. Morgan WF (2003) Non-targeted and delayed effects of exposure to ionizing radiation: I. Radiation-induced genomic instability and bystander effects in vitro. (Translated from eng) *Radiat Res* 159(5):567-580 (in eng).
6. Huang L, Kim PM, Nickoloff JA, & Morgan WF (2007) Targeted and nontargeted effects of low-dose ionizing radiation on delayed genomic instability in human cells. (Translated from eng) *Cancer Res* 67(3):1099-1104 (in eng).
7. van Gent D, Hoeijmakers J, & Kanaar R (2001) Chromosomal stability and the DNA double-stranded break connection. *Nature Reviews Genetics* 2(3):196-206.
8. Haaf T, Golub E, Reddy G, Radding C, & Ward D (1995) Nuclear foci of mammalian Rad51 recombination protein in somatic cells after DNA damage and its localization in synaptonemal complexes. *Proceedings of the National Academy of Sciences* 92(6):2298.
9. Rothkamm K & Lobrich M (2003) Evidence for a lack of DNA double-strand break repair in human cells exposed to very low x-ray doses. *Proc Natl Acad Sci U S A* 100(9):5057-5062.
10. Costes SV*, et al.* (2006) Imaging features that discriminate between foci induced by high- and low-LET radiation in human fibroblasts. *Radiat Res* 165(5):505-515.
11. Ashley T*, et al.* (1995) Dynamic changes in Rad51 distribution on chromatin during meiosis in male and female vertebrates. *Chromosoma* 104(1):19-28.
12. Schultz L, Chehab N, Malikzay A, & Halazonetis T (2000) p53 binding protein 1 (53BP1) is an early participant in the cellular response to DNA double-strand breaks. *Journal of Cell Biology* 151(7):1381.
13. Rogakou E, Pilch D, Orr A, Ivanova V, & Bonner W (1998) DNA double-stranded breaks induce histone H2AX phosphorylation on serine 139. *Journal of Biological Chemistry* 273(10):5858.
14. Bakkenist C & Kastan M (2003) DNA damage activates ATM through intermolecular autophosphorylation and dimer dissociation. *Nature* 421(6922):499-506.
15. Asaithamby A & Chen D (2009) Cellular responses to DNA double-strand breaks after low-dose {gamma}-irradiation. *Nucleic Acids Research*.
16. Costes S, Chiolo I, Pluth J, Barcellos-Hoff M, & Jakob B (2010) Spatiotemporal characterization of ionizing radiation induced DNA damage foci and their relation to chromatin organization. *Mutation Research/Reviews in Mutation Research*.
17. Stenerlow B, Karlsson K, Cooper B, & Rydberg B (2003) Measurement of prompt DNA double-strand breaks in mammalian cells without including heat-labile sites: Results for cells deficient in nonhomologous end joining. *Radiation research* 159(4):502-510.

18. MacPhail S*, et al.* (2003) Expression of phosphorylated histone H2AX in cultured cell lines following exposure to X-rays. *International Journal of Radiation Biology* 79(5):351-359.
19. Wilson PF*, et al.* (2010) Inter-individual variation in DNA double-strand break repair in human fibroblasts before and after exposure to low doses of ionizing radiation. (Translated from eng) *Mutat Res* 683(1-2):91-97 (in eng).
20. Vogt A*, et al.* (2008) A green fluorescent protein with photoswitchable emission from the deep sea. (Translated from eng) *PLoS One* 3(11):e3766 (in eng).
21. Turner JE (2007) *Atoms, Radiation, and Radiation Protection* (Wiley-VCH, Weinheim) 3. Ed.
22. Hall E (2000) Radiobiology for the Radiobiologist. *Radiobiology for the Radiobiologist; Lippincott Williams & Wilkins: Philadelphia*:446ñ460.
23. Alberts B. JA, Lewis J., Raff M., Roberts K., Walter P. (2002) *Molecular Biology of the Cell* (Garland Science, New York) 4th Ed.
24. Ward J (1988) DNA damage produced by ionizing radiation in mammalian cells: identities, mechanisms of formation, and reparability. *Progress in nucleic acid research and molecular biology* 35:95.
25. Goodhead D (1994) Initial events in the cellular effects of ionizing radiations: clustered damage in DNA. *International Journal of Radiation Biology* 65(1):7-17.
26. Vispe S & Satoh M (2000) DNA repair patch-mediated double strand DNA break formation in human cells. *Journal of Biological Chemistry* 275(35):27386.
27. Bryant P (1985) Enzymatic restriction of mammalian cell DNA: evidence for double-strand breaks as potentially lethal lesions. *International Journal of Radiation Biology* 48(1):55-60.
28. Burma S, Chen B, & Chen D (2006) Role of non-homologous end joining (NHEJ) in maintaining genomic integrity. *DNA repair* 5(9-10):1042-1048.
29. Critchlow S & Jackson S (1998) DNA end-joining: from yeast to man. *Trends in biochemical sciences* 23(10):394-398.
30. Lieber M, Ma Y, Pannicke U, & Schwarz K (2003) Mechanism and regulation of human non-homologous DNA end-joining. *Immunogenetics* 500:89081.
31. Khanna K & Jackson S (2001) DNA double-strand breaks: signaling, repair and the cancer connection. *Nature genetics* 27(3):247-254.
32. Richardson C & Jasin M (2000) Coupled homologous and nonhomologous repair of a double-strand break preserves genomic integrity in mammalian cells. *Molecular and Cellular Biology* 20(23):9068.
33. Delacote F, Han M, Stamato T, Jasin M, & Lopez B (2002) An xrcc4 defect or Wortmannin stimulates homologous recombination specifically induced by double-strand breaks in mammalian cells. *Nucleic acids research* 30(15):3454.
34. Allen C, Halbrook J, & Nickoloff J (2003) Interactive competition between homologous recombination and non-homologous end joining. *Molecular Cancer Research* 1(12):913.
35. Hoeijmakers J (2001) Genome maintenance mechanisms for preventing cancer. *Nature* 411(6835):366-374.
36. Sonoda E, Hochegger H, Saberi A, Taniguchi Y, & Takeda S (2006) Differential usage of non-homologous end-joining and homologous recombination in double strand break repair. *DNA repair* 5(9-10):1021-1029.
37. Takata M*, et al.* (1998) Homologous recombination and non-homologous end-joining pathways of DNA double-strand break repair have overlapping roles in the maintenance of chromosomal integrity in vertebrate cells. *The EMBO journal* 17(18):5497.

38. Saleh-Gohari N & Helleday T (2004) Conservative homologous recombination preferentially repairs DNA double-strand breaks in the S phase of the cell cycle in human cells. *Nucleic acids research* 32(12):3683.
39. Bree R, Neary C, Samali A, & Lowndes N (2004) The switch from survival responses to apoptosis after chromosomal breaks. *DNA repair* 3(8-9):989-995.
40. Lukas J, Lukas C, & Bartek J (2004) Mammalian cell cycle checkpoints: signalling pathways and their organization in space and time. *DNA repair* 3(8-9):997-1007.
41. Stiff T*, et al.* (2004) ATM and DNA-PK function redundantly to phosphorylate H2AX after exposure to ionizing radiation. *Cancer Research* 64(7):2390.
42. Bassing C*, et al.* (2002) Increased ionizing radiation sensitivity and genomic instability in the absence of histone H2AX. *Proceedings of the National Academy of Sciences* 99(12):8173.
43. Celeste A*, et al.* (2002) Genomic instability in mice lacking histone H2AX. *Science* 296(5569):922.
44. Paull T*, et al.* (2000) A critical role for histone H2AX in recruitment of repair factors to nuclear foci after DNA damage. *Current Biology* 10(15):886-895.
45. Bekker-Jensen S*, et al.* (2006) Spatial organization of the mammalian genome surveillance machinery in response to DNA strand breaks. *Journal of Cell Biology* 173(2):195.
46. Wang B, Matsuoka S, Carpenter P, & Elledge S (2002) 53BP1, a mediator of the DNA damage checkpoint. *Science Signaling* 298(5597):1435.
47. Morgan W, Day J, Kaplan M, McGhee E, & Limoli C (1996) Genomic instability induced by ionizing radiation. *Radiation research*:247-258.
48. Little J (2000) Radiation carcinogenesis. *Carcinogenesis* 21(3):397.
49. Morgan WF (2006) Non-targeted and delayed effects of exposure to ionizing radiaton *UNSCEAR 2006 Report* II.
50. Kadhim M*, et al.* (1992) Transmission of chromosomal instability after plutonium -particle irradiation.
51. Lorimore S*, et al.* (1998) Chromosomal instability in the descendants of unirradiated surviving cells after -particle irradiation. *Proceedings of the National Academy of Sciences* 95(10):5730.
52. Johnson J & Fleshner M (2006) Releasing signals, secretory pathways, and immune function of endogenous extracellular heat shock protein 72. *Journal of leukocyte biology* 79(3):425.
53. Ingber D (2006) Cellular mechanotransduction: putting all the pieces together again. *The FASEB Journal* 20(7):811.
54. Lyng FM, Seymour CB, & Mothersill C (2000) Production of a signal by irradiated cells which leads to a response in unirradiated cells characteristic of initiation of apoptosis. (Translated from eng) *Br J Cancer* 83(9):1223-1230 (in eng).
55. Resat M & Morgan W (2004) Radiation-induced genomic instability: a role for secreted soluble factors in communicating the radiation response to non-irradiated cells. *Journal of cellular biochemistry* 92:1013-1019.
56. Azzam E, de Toledo S, Gooding T, & Little J (1998) Intercellular communication is involved in the bystander regulation of gene expression in human cells exposed to very low fluences of alpha particles. *Radiation Research* 150(5):497-504.
57. Azzam E, de Toledo S, & Little J (2001) Direct evidence for the participation of gap junction-mediated intercellular communication in the transmission of damage signals from -particle irradiated to nonirradiated cells. *Proceedings of the National Academy of Sciences of the United States of America* 98(2):473.

58. Belyakov OV, *et al.* (2005) Biological effects in unirradiated human tissue induced by radiation damage up to 1 mm away. (Translated from eng) *Proc Natl Acad Sci U S A* 102(40):14203-14208 (in eng).
59. Mothersill C, *et al.* (2005) Genetic factors influencing bystander signaling in murine bladder epithelium after low-dose irradiation in vivo. *Radiation research* 163(4):391-399.
60. Morgan W & Sowa M (2007) Non-targeted bystander effects induced by ionizing radiation. *Mutation Research-Fundamental and Molecular Mechanisms of Mutagenesis* 616(1-2):159-164.
61. Sokolov M, *et al.* (2005) Ionizing radiation induces DNA double-strand breaks in bystander primary human fibroblasts. *ONCOGENE-BASINGSTOKE-* 24(49):7257.
62. Yang H, Asaad N, & Held K (2005) Medium-mediated intercellular communication is involved in bystander responses of X-ray-irradiated normal human fibroblasts. *Oncogene* 24(12):2096-2103.
63. Mothersill C, Seymour R, & Seymour C (2004) Bystander effects in repair-deficient cell lines. *Radiation research* 161(3):256-263.
64. Iyer R & Lehnert B (2002) Low dose, low-LET ionizing radiation-induced radioadaptation and associated early responses in unirradiated cells. *Mutation Research-Fundamental and Molecular Mechanisms of Mutagenesis* 503(1-2):1-9.
65. Iyer R & Lehnert B (2002) Alpha-particle-induced increases in the radioresistance of normal human bystander cells. *Radiation Research*:3-7.
66. Brenner D, *et al.* (2003) Cancer risks attributable to low doses of ionizing radiation: assessing what we really know. *Proceedings of the National Academy of Sciences of the United States of America* 100(24):13761.
67. Prise M (2003) A review of the bystander effect and its implications for low-dose exposure. *Radiation protection dosimetry* 104(4):347.
68. NCRP (2001) Evaluation of the Linear Nonthreshold Dose-Response Model for Ionizing Radiation. *Report No. 136*.
69. ICRP (1999) Genetic Susceptibility to Cancer. *ICRP Publ No. 79*.
70. Joiner M, Marples B, Lambin P, Short S, & Turesson I (2001) Low-dose hypersensitivity: current status and possible mechanisms. *International Journal of Radiation Oncology* Biology* Physics* 49(2):379-389.
71. Nagasawa H & Little J (1999) Unexpected sensitivity to the induction of mutations by very low doses of alpha-particle radiation: evidence for a bystander effect. *Radiation research*:552-557.
72. White R, *et al.* (1993) Bone sarcoma characteristics and distribution in beagles fed strontium-90. *Radiation research* 136(2):178-189.
73. Upton A (2001) Radiation hormesis: data and interpretations. *CRC Critical Reviews in Toxicology* 31(4-5):681-695.
74. Xu Y, Greenstock C, Trivedi A, & Mitchel R (1996) Occupational levels of radiation exposure induce surface expression of interleukin-2 receptors in stimulated human peripheral blood lymphocytes. *Radiation and environmental biophysics* 35(2):89-93.
75. Pollycove M & Feinendegen L (1999) Molecular biology, epidemiology, and the demise of the linear no-threshold (LNT) hypothesis. *Comptes Rendus de l'Academie des Sciences Series III Sciences de la Vie* 322(2-3):197-204.
76. Preston D, Shimizu Y, Pierce D, Suyama A, & Mabuchi K (2003) Studies of mortality of atomic bomb survivors. Report 13: Solid cancer and noncancer disease mortality: 1950-1997. *Radiation Research* 160(4):381-407.

77. Cornforth M, Bailey S, & Goodwin E (2002) Dose responses for chromosome aberrations produced in noncycling primary human fibroblasts by alpha particles, and by gamma rays delivered at sublimiting low dose rates. *Radiation research* 158(1):43-53.
78. Sachs R, Hahnfeld P, & Brenner D (1997) Review The link between low-LET dose-response relations and the underlying kinetics of damage production/repair/misrepair. *International journal of radiation biology* 72(4):351-374.
79. Cucinotta F, Nikjoo H, & Goodhead D (2000) Model for radial dependence of frequency distributions for energy imparted in nanometer volumes from HZE particles. *Radiation research* 153(4):459-468.
80. BioFluidix (BioSpot Protocol.).
81. Evans P (2009) SpekCalc: a program to calculate photon spectra from tungsten anode x-ray tubes. *PHYSICS IN MEDICINE AND BIOLOGY* 54(19):N433-N438.
82. Demtröder W (2000) *Experimentalphysik 3* (Springer Verlag, Berlin, Heidelberg, New York).
83. Seltzer S (1993) Calculation of photon mass energy-transfer and mass energy-absorption coefficients. *Radiation research* 136(2):147-170.
84. Davidson M & Abramowitz M (2002) Optical microscopy. *Encyclopedia of Imaging Science and Technology, Wiley-Interscience, New York*:1106-1141.
85. Demtröder W (1999) *Experimentalphysik 2* (Springer, Berlin Heidelberg New York) 2 Ed p 463.
86. S. Wilhelm BG, M. Gluch, H. Heinz (Die konfokale Laser Scanning Mikroskopie. *Broschüre, Carl Zeiss Jena GmbH*.
87. Beyer H (1985) *Handbuch der Mikrsokopie* (VEB Verlag Technik Berlin) 2. Ed.
88. Thomas J. Feller MWD (Introduction to Confocal Microscopy. (Olympus GmbH), p http://www.olympusconfocal.com/theory/confocalintro.html.
89. Hauptner A (2006) Mikroskopisch genaue Zellbestrahlung mit hochenergetischen Ionen. Doktorarbeit (TU München, München).
90. Zeiss (ApoTome. ed Jena CZ).
91. Carrel A (1913) Artificial activation of the growth in vitro of connective tissue. *Journal of Experimental Medicine* 17(1):14.
92. Stich M*, et al.* (2003) Live cell catapulting and recultivation. (Translated from eng) *Pathol Res Pract* 199(6):405-409 (in eng).
93. Woide D*, et al.* (2009) Single particle adsorbing transfer system. *Biomedical Microdevices* 11(3):609-614.
94. Niwa H*, et al.* (1996) Chemical nature of the light emitter of the Aequorea green fluorescent protein. *Proceedings of the National Academy of Sciences of the United States of America* 93(24):13617.
95. Dirks W, Wirth M, & Hauser H (1993) Dicistronic transcription units for gene expression in mammalian cells. *Gene* 128(2):247-249.
96. Dirks W, Schaper F, Kirchhoff S, Morelle C, & Hauser H (1994) A multifunctional vector family for gene expression in mammalian cells. *Gene* 149(2):387-388.
97. Qiagen (Superfect Transfection Reagent. (Qiagen).
98. Freshney RI (2005) *Culture of Animal Cells: A Manual of Basic Technique* (John Wiley & Sons) 5 Ed p 960.
99. Olivo-Marin J (2002) Extraction of spots in biological images using multiscale products. *Pattern Recognition* 35(9):1989-1996.

100. Cucinotta FA, Pluth JM, Anderson JA, Harper JV, & O'Neill P (2008) Biochemical kinetics model of DSB repair and induction of gamma-H2AX foci by non-homologous end joining. (Translated from eng) *Radiat Res* 169(2):214-222 (in eng).
101. Bewersdorf J, Bennett BT, & Knight KL (2006) H2AX chromatin structures and their response to DNA damage revealed by 4Pi microscopy. *Proc Natl Acad Sci U S A* 103(48):18137-18142.
102. Neumaier T YB, Chen J, Polyzos A, Pham C, Thalhammer S, Costes S V (Non-linear DNA damage response to ionizing radiation suggests clustering of DNA breaks in normal human cells. *in preparation*.
103. Costes SV, Chiolo I, Pluth JM, Barcellos-Hoff MH, & Jakob B (2010) Spatiotemporal characterization of ionizing radiation induced DNA damage foci and their relation to chromatin organization. (Translated from Eng) *Mutat Res* (in Eng).
104. Stenerlow B, Karlsson KH, Cooper B, & Rydberg B (2003) Measurement of prompt DNA double-strand breaks in mammalian cells without including heat-labile sites: results for cells deficient in nonhomologous end joining. *Radiat Res* 159(4):502-510.
105. MacPhail SH*, et al.* (2003) Expression of phosphorylated histone H2AX in cultured cell lines following exposure to X-rays. *Int J Radiat Biol* 79(5):351-358.
106. Kato TA, Okayasu R, & Bedford JS (2008) Comparison of the induction and disappearance of DNA double strand breaks and gamma-H2AX foci after irradiation of chromosomes in G1-phase or in condensed metaphase cells. *Mutat Res* 639(1-2):108-112.
107. Leatherbarrow EL, Harper JV, Cucinotta FA, & O'Neill P (2006) Induction and quantification of gamma-H2AX foci following low and high LET-irradiation. *Int J Radiat Biol* 82(2):111-118.
108. Wang H*, et al.* (2001) Efficient rejoining of radiation-induced DNA double-strand breaks in vertebrate cells deficient in genes of the RAD52 epistasis group. *Oncogene* 20(18):2212-2224.
109. Nikjoo H, O'Neill P, Goodhead DT, & Terrissol M (1997) Computational modelling of low-energy electron-induced DNA damage by early physical and chemical events. *Int J Radiat Biol* 71(5):467-483.
110. Nikjoo H, O'Neill P, Wilson WE, & Goodhead DT (2001) Computational approach for determining the spectrum of DNA damage induced by ionizing radiation. (Translated from eng) *Radiat Res* 156(5 Pt 2):577-583 (in eng).
111. Löbrich M*, et al.* (gamma H2AX foci analysis for monitoring DNA double-strand break repair: Strengths, limitations and optimization. *Cell cycle (Georgetown, Tex.)* 9(4).
112. Wolff S (1996) Aspects of the adaptive response to very low doses of radiation and other agents. *Mutation Research/Fundamental and Molecular Mechanisms of Mutagenesis* 358(2):135-142.
113. Shadley J, Afzal V, & Wolff S (1987) Characterization of the adaptive response to ionizing radiation induced by low doses of X rays to human lymphocytes. *Radiation Research* 111(3):511-517.
114. Wolff S (1998) The adaptive response in radiobiology: evolving insights and implications. *Environmental Health Perspectives* 106(Suppl 1):277.
115. Pogribny I*, et al.* (2005) Fractionated low-dose radiation exposure leads to accumulation of DNA damage and profound alterations in DNA and histone methylation in the murine thymus. *Molecular Cancer Research* 3(10):553.

116. Yip S (2006) Applied Nuclear Physics. (MIT OpenCourseWare, Nuclear Science and Engineering).
117. Bruce Alberts AJ, Julian Lewis, Martin Raff, Keith Roberts, Peter Walter (2002) *Molecular Biology of the Cell* (Garland Science, New York) 4th Ed.
118. Baens M*, et al.* (2006) The dark side of EGFP: defective polyubiquitination. *PLoS One* 1(1).
119. Liu H, Jan M, Chou C, Chen P, & Ke N (1999) Is green fluorescent protein toxic to the living cells? *Biochemical and Biophysical Research Communications* 260(3):712-717.
120. Zhang F*, et al.* (2003) Green fluorescent protein selectively induces HSP70-mediated up-regulation of COX-2 expression in endothelial cells. *Blood* 102(6):2115.
121. Agbulut O*, et al.* (2006) GFP expression in muscle cells impairs actin-myosin interactions: implications for cell therapy. *Nature Methods* 3(5):331.
122. Hartmann M, Roeraade J, Stoll D, Templin M, & Joos T (2009) Protein microarrays for diagnostic assays. *Analytical and Bioanalytical Chemistry* 393(5):1407-1416.
123. Lodish HBA, Matsudaira P., Kaiser CA., Krieger M., Scott MP., Zipursky SL, Darnell J. (2004) *Molecular Cell Biology* (WH Freeman, New York) 5th Ed.
124. Goldring S, Roelke M, Petrison K, & Bhan A (1987) Human giant cell tumors of bone identification and characterization of cell types. *Journal of Clinical Investigation* 79(2):483.
125. Pennisi E (2004) Evolutionary biology: the birth of the nucleus. *Science* 305(5685):766.
126. Hauptner A*, et al.* (2006) Spatial Distribution of DNA Double-Strand Breaks from Ion Tracks. *Ion Beam Science: Solved and Unsolved Problems. Matematisk-fysiske Meddelelser* 52:59-85.
127. Laird A (1965) Dynamics of tumour growth: comparison of growth rates and extrapolation of growth curve to one cell. *British journal of cancer* 19(2):278.
128. Loken M & Herzenberg L (2006) ANALYSIS OF CELL POPULATIONS WITH A FLUORESCENCE-ACTIVATED CELL SORTER*. *Annals of the New York Academy of Sciences* 254(Fifth International Conference on Immunofluorescence and Related Staining Techniques):163-171.
129. Mothersill C & Seymour C (1997) Medium from irradiated human epithelial cells but not human fibroblasts reduces the clonogenic survival of unirradiated cells. (Translated from eng) *Int J Radiat Biol* 71(4):421-427 (in eng).
130. Maguire P, Mothersill C, McClean B, Seymour C, & Lyng FM (2007) Modulation of radiation responses by pre-exposure to irradiated cell conditioned medium. (Translated from eng) *Radiat Res* 167(4):485-492 (in eng).
131. Akhurst R & Derynck R (2001) TGF-[beta] signaling in cancer-a double-edged sword. *Trends in Cell Biology* 11(11):S44-S51.
132. BECHTEL W & BAUER G (2009) Catalase Protects Tumor Cells from Apoptosis Induction by Intercellular ROS Signaling. *Anticancer research* 29(11):4541.
133. Ponomarev AL, Costes SV, & Cucinotta FA (2008) Stochastic properties of radiation-induced DSB: DSB distributions in large scale chromatin loops, the HPRT gene and within the visible volumes of DNA repair foci. *Int J Radiat Biol* 84(11):916-929.
134. Lisby M, Mortensen UH, & Rothstein R (2003) Colocalization of multiple DNA double-strand breaks at a single Rad52 repair centre. *Nat Cell Biol* 5(6):572-577.

Appendix

A) Lab Intern Protocol – BioSpot Pipetting Device for Immunostaining

- Start computer, switch on hardware (piezo control unit & movement control), start software "BioSpot®" (drive C:\\Program Files/BioSpot/software/BioSpot.exe or via shortcut "BioSpot®" on desktop) → at first, automatically x-axis stage and PipeJets™ move to parking position at $x = 0, z = 0$ respectively (initial position).
- Adjust speed/velocity of x- and z-axis in control window "Axis Control": $x_{vel} = 500, z_{vel} = 500$, press "Set Axis Speed" to validate changed settings; adjust the trackbar below for "Step width (mm)" to smallest values as well (= 0.01 mm). By adjusting these settings the motor gets prohibited of slippage/wheelspin when movement settings for x-position are changed from 0 to increasing values. In case of wheelspin, recalibrate the system by "Search Reference".

Description of single active control windows (Figure 2)

- Window **"(1) Axis Control and Axis Movement"**: for movement of LOC-slide on x-axis and of PipeJets™ on z-axis. For manual handling just the following settings are needed:

  "Move to Pos" for moving the LOC-slide and PipeJets™ in desired positions on the x- or z-axis respectively. Simply set desired numbers and start application with "Move" (black arrow buttons can only be used for movement when window "Enable Keyboard Control" is activated, but are not needed necessarily. Buttons "Search Reference", "Stop Search" and "Move to Parking Position" (x = 0, z = 0) are not needed for normal application as well). All of the following values for the x- and z- position presented in Table 1 are valid for the 13 Eppendorf reaction tubes (T1-T14; 5 x 1,5 ml, 8 x 0,5 ml) used in the immunostaining set-up as well as the reaction centers on the two multiwell slides on the x-axis.
- Window **"(3) Valve Control and Pump Control"**: to open and close valves of single PipeJets™ and to connect pump with valves, or with air or valves with air (bypass). The valve, which is going to be used to "Aspirate", must be open and connected to the pump (button "Valves (2)"), the other valves must be closed. The speed „PSpeed" for „Aspirate" or „Dispense" respectively can remain

unchanged at $t = 20\ ms$. The volume „PVol“ can be adjusted: e.g. to a volume of $V = 15\ \mu l$. After „Aspirate“ valves can remain connected to the pump, avoiding a low-pressure to occur. The “Dispense” function is needed to release the immunostaining reagents on the reaction center, to totally empty the valves and to dispense remaining liquids back into the tubes.

Table 1: Functions and values for using the BioSpot® for immunostaining.
PipeJet x-positions [mm]

PipeJet	**left multiwell slide**				**right multiwell slide**			
PJ3 (A, B, C, D)	105,5	155	159	164	177,5	182	186,5	191
PJ2 (A, B, C, D)	100	104,5	109	113,5	127	131,5	136	140,5
PJ1 (A, B, C, D)	47,5	52	56,5	61	74,5	79	83,5	88

PJ	**T1**	**T2**	**T3**	**T4**	**T5**	**T6**	**T7**	**T8**	**T9**	**T10**	**T11**	**T12**	**T13**
PJ3	245,5	259	272	285	298								
PJ2					245,5	259	272	285	298				
PJ1									245,5	259	272	285	298

PipeJet z-positions [mm]

Action	**z-position**
Aspiration (PJ1, PJ2, PJ3) from multiwell slide	33
Dispension (PJ1, PJ2, PJ3) on multiwell slide	31
Aspiration (PJ1, PJ2, PJ3) from tubes	44
Dispension (PJ1, PJ2, PJ3) in tubes	35
Movement of the x-axis stage	25

- Window **“(2) PipeJet™ Control”**: various settings for automatic shooting of a definite volume using single PipeJets™. There are just slight changes to be validated as most parameters are set as standard values and remain unchanged. Standard settings: Istroke = 36 µm, vdown = 200 µm/ms, thold = 10 µs, vup = 2 µm/ms, n = 5, delay = 100 ms. Just the “Istroke“ is recommended to be changed to 20 µm instead of 36 µm, and the number “n“ from 5 to 20 repetitions, when 1 µl is going to be shot. Any changes in the settings need to be validated by “Set PJ“. A volume of about 1 µl is shot, when having aspirated a volume of about 30 µl with PJ1 or PJ2 and when starting the shoot-function by “Shoot PJ“. Buttons “Detect mode“ as well as „Dispense mode“ do not have a specific function defined by the software and can be neglected.

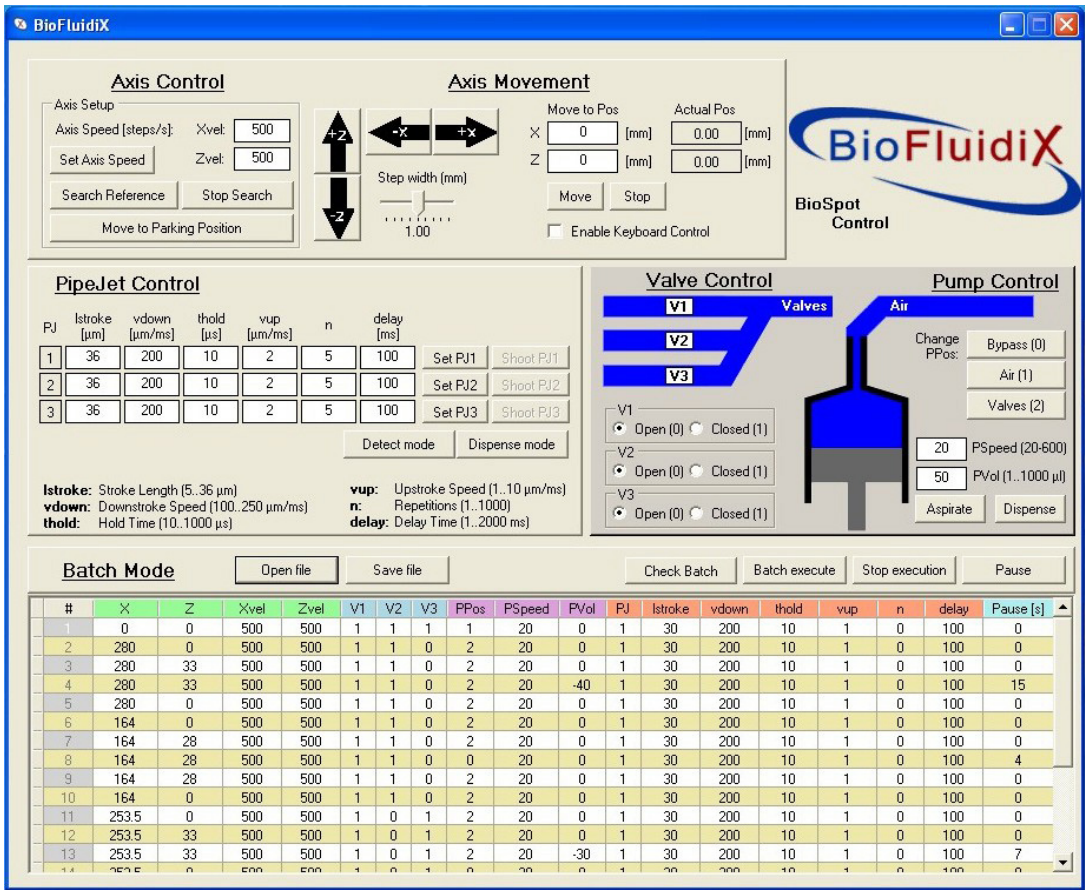

Figure 2: Screenshot of software "BioSpot®" (BioFluidix GmbH, Freiburg, Germany). The software is used for operating the automatic dispensing device BioSpot®. There are four single active control windows namely "(1) Axis Control and Axis Movement", "(2) PipeJet™ Control", "(3) Valve Control and Pump Control" for manually operated applications, as well as "(4) Batch Mode" for automatically operating protocols. (1) allows a regulation of speed and x-position of the slide rail and z-position of PipeJets™. (2) allows an adaption of depth of penetration, displacement speed, release speed and holding time of the piezostack driven piston, as well as number of repetitions and delay time. (3) allows opening and closing of PipeJet™ valves, connections to the syringe pump as well as setting speed and volumes for aspiration and dispension and to start these operations. (4) allows programming complete sequences, which can be run automatically.

- Window **"(4) Batch Mode"**: for programming and saving complex operations (in an excel-sheet). Thereby, a numerical code is applied. In the control window „(1) Axis Control and Movement" x-position values indicate a movement of the x-axis stage, z-position values indicate a movement of the PipeJets™. In the control window „(3) Valve and Pump Control" for valves V1, V2, V3 a "0" indicates open valves and a "1" means closed ones. For using the pump, at "PPos" a "0" stands for "Bypass", that is the connection of „Valve with Air", "1" indicates a connection "Pump with Air" and "2" means the connection "Pump with Valves". Volumes for "Aspirate" are indicated at "PVol" using a "-" for negative values, volumes for "Dispense" using a "+" for positive values. Errors during the operation can be checked and detected by "Check Batch". The operating process

can be started with “Batch execute“ and can be paused with “Pause” or aborted with “Stop execution”. When the “Stop execution” function is activated, the total batch process stops immediately and the execution is cancelled. When pressing “Batch execute” again, the system will try to get back to the initial starting positions of the actual batch file (the first line), and x-axis as well as z-axis will move simultaneously. Thus, to avoid PipeJets™ hitting the x-axis stage, use the “(1) Axis Control and Axis Movement” box to get the PipeJets™ (first) as well as the LOC-slide (second) manually back to the initial positions at z=0 and x=0, before starting “Batch execute” again. When “Pause” is pressed, a window “Batch Processing Paused” will appear. Now it is possible to change settings manually in window (1), (2) and (3), and to perform extra performances. However, the system will be back to the actual position in the batch mode and continue, after pressing “Ok”. So click “Ok” to continue.

Programming automatic pipetting operations using the “(4) Batch mode”

- Write a working procedure first: step-by-step, what to do.
- Final instructions can then be typed into an Excel-sheet in the software according to the “Batch mode”-code (Appendix B), or respectively, an already existing program can be loaded via “Open file” and then be changed (save changes via “Save file”).
- Via “Batch execute” the list of orders will be run line-by-line.
- The generated working sheet of the „Batch mode“ is saved with a .csv ending – this ending can simply be opened by Excel.

Working sheets generated in Excel can easily be saved as .xls as well as .csv ending files, and thus can easily be opened in the “Batch mode”.

B) Immunostaining Programm for the BioSpot

Attached on CD

C) Lab Intern Protocol – Cell Culture Workflow

- Warming of all cell culture reagents to a temperature of $T = 37°C$. Notice that Trypsin should not be kept longer than necessary at 37°C or room temperature since it starts to degrade after around 30 min and, thus, loosing its reactivity. Use Pb rings to weigh the reagent bottles down.
- Sterilise the cell culture hood by turning on the UV-light for at least 10 min.
- Open the cell culture hood.
- Sterilise the bench with 70% Ethanol by wiping from the back to the front.
- Open the gas.
- Before placing the reagents under the hood they have to be rinsed with 70% Ethanol. Furthermore, also the hands in latex gloves should be rinsed with 70% Ethanol.
- Remove the used cell culture medium from the cell culture flask with sterile single-use pipettes and discard it in the waste bottle.
- After opening the reagent bottles and before closing it, the bottleneck as well as the lid should be flamed off with the Bunsen burner!!! The screw threads of all lids should face upwards.
- Rinse the cell culture with sterile PBS (5 ml), remove and discard the supernatant.
- Add 2 ml Trypsin to the cell culture.
- Place the cell culture flask back into the cell incubator and incubate the cells with Trypsin for 5 min at 37°C.
- Remove the cell culture flask after 5 min from the cell incubator and check under the microscope. If the cells are detached from the bottom they are floating in the cell culture medium having a spherical shape.
- Put the cell culture flask back under the hood.
- Add 8 ml of fresh and warm cell culture medium to the detached cells to neutralise the Trypsin. The medium should be added without bubbles to the cell suspension with a new single-use pipette. Let the fresh medium rinse over the cells from the side of the cell culture flask.
- Add fresh medium into a new cell culture flask. Furthermore, add an appropriate volume of the cell suspension (depending on the cell culture) from the old cell culture flask into the new one.
- Label the cell culture flask with the important data, i.e. type of the cell culture, medium, passage, date, and name.

- Put the new cell culture flask back into the cell incubator and cultivate the cells at $T = 37°C$ with 5% CO_2.
- Take care that the heated glass door of the cell incubator is locked properly!!!
- After finishing the work with cells, turn of the gas and remove the rest gas from the pipe of the Bunsen burner by pressing the foot switch.
- Sterilise the bench with 70% Ethanol by wiping from the back to the front.
- Close the hood and turn on the UV-light for at least 10 min (maximal 20 min). The hood must be turned off completely after the final use of the UV-light. Otherwise the working hours carry on running!!!
- Turn off the water bath. Check for contamination in the water. Clean the water bath if the water is contaminated.
- Clean the microscope stage with 70% Ethanol and turn off the microscope and cover it. Check the optics for dirt. Clean the objective or ocular with a cotton swab soaked with 70% Ethanol and non-fuzzing fabrics for dirt in the optical path. Greasy dirt can be removed with fabrics soaked with aether.
- Remove all unnecessary equipment from the work area during the work.

D) Lab Intern Protocol – Laser Microdissection and Single Particle Adsorbing (Low-Pressure) Transfer System (SPATS)

- Switch on computer, microscope power supply box 231 and microscope button.
- Switch on laser control box → switch key to from "0" to "1", a green light appears (left side). Thus, the laser lamp is getting pre-warmed. Wait until the second green light turns on (right side). The laser can be turned on, by pressing the red button located between both green lights ("Laser On/Off"). When the right green light turns to red, the laser is ready to use.

Laser Microdissection

- Decontaminate adsorbing head by using a UVC light source.
- Make sure, that the arm of the transfer device is positioned out of the working area, on the right side of the XY-stage as

  a) this position favors an easy installation/fixation of the adsorbing head into the low-pressure supporting arm and

  b) the arm has enough space above to move up, as the software "Nanosauger" performs a calibration run of the XY-stage and the SPATS carrier arm when getting started.
- Either use the color firewire camera for colored images, or switch on the black & white CCD camera for black and white images.
- Run software "Nanosauger 2.5" (desktop) for fast working procedures (Figure 1) and "Nanosauger 2.6" (desktop) for slow working procedures, both without using autofocus unit, or "Nanosauger 2.7" for working with implemented autofocus function (desktop). Softwares "Nanosauger" serve the color firewire camera, while for utilizing the black & white CCD camera additionally the software "QCapture" or "QCapture Pro 6.0" needs to be started.
- Optionally the stage movement direction can be adjusted via clicking "Control Via Buttons" and then clicking "Inverted X-Direction" as well as "Inverted Y-Direction"; re-activate the box "Control Via Joystick".
- Speed of stage movement and up/down-direction of SPATS arm can be set by clicking "Control Via Buttons", then the speed can be adjusted by moving the mode controller in the box "Speed" (settings 1-7); re-activate the box "Control Via Joystick".

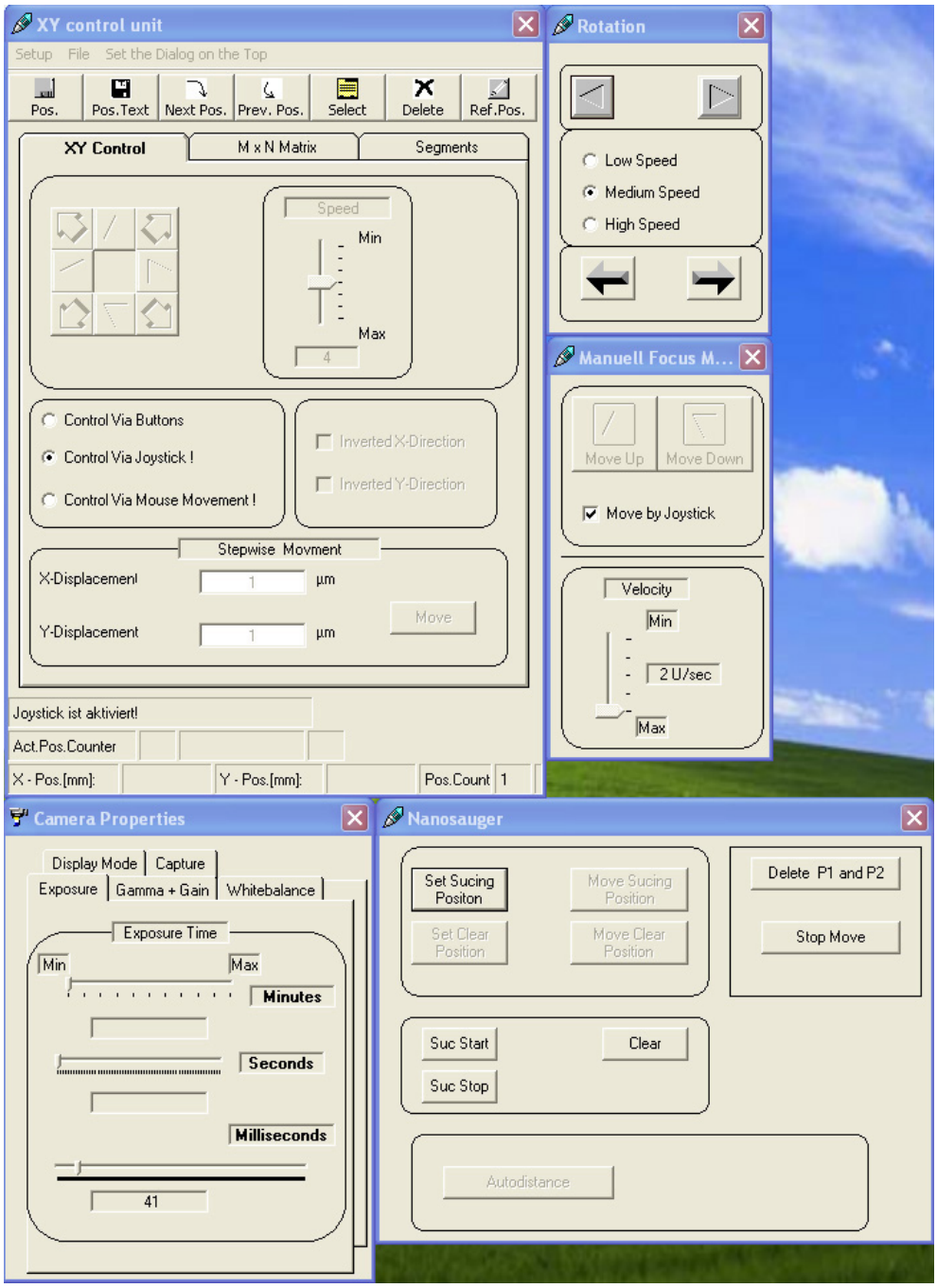

Figure 1: Screenshot of software "Nanosauger 2.5". Via the panel "XY Control unit" settings of the XY-stage can be changed. Activating the panel "Rotation" can move the SPATS device horizontally and various speed settings can be adjusted. The "Camera Properties" window allows taking pictures and provides several settings for optimized image taking. Via operating the "Nanosauger" panel, the low-pressure operation can be started (Suc Start/Suc Stop), stopped and a short impulse of high pressure can be applied by pressing "Clear".

- The SPATS arm can be move up/down by turning the joystick knob to the left and right; it can be moved left/right by pressing the arrow buttons in the box "Rotation", the speed of sideways movement can be adjusted by clicking "Low Speed", "Medium Speed" or "High Speed"; the length of the SPATS arm can be adjusted by turning the rotary knob located at the micrometer step motor.

- Test, if lattice is centered to the view field of the microscope by approaching the adsorbing head to the 10x objective; if not, center grid for easier sample take-up.
- For microdissection of single particles use the 40x objective; set microscope to "DL auf" (*Durchlicht* function is activated); laser can be switched on by operating the footswitch, or by activating the silver switch at the laser control box ("TRIGGER INT/EXT") to "INT" position; set microscope to "AL auf" (*Auflicht* function is activated) calibrate the laser beam by focusing it onto the level of the PEN-carrier membrane, adjust laser focus and cut energy. A thin focused cut line is desired.
- Isolate single areas by keeping laser running and moving the microscope's XY-stage.
- To switch off laser, either loosen footswitch or turn silver switch ("TRIGGER INT/EXT") to "EXT" position.

Single Particle Adsorbing Transfer System (SPATS)

- Use the 10x objective for controlled extraction/transfer via the SPATS device.
- Switch on pressure-supplying pneumatic picopump and turn on compressed air.
- Approach the grid/lattice of the adsorbing head to the surface of the isolated particle, start low-pressure process by clicking "Suck Start" (Figure 1); check if particle is fixed to the grid and that the area of PEN-membrane is empty where isolation happened.
- Move SPATS up and transfer particle to a tube, planar device or else; release particle by pressing "Suck Stop" and "Clear" for providing a short impulse of high-pressure.
- Check particle release by having a look at the grid; for doing so, move adsorbing head back to the 10x objective and approach grid to objective lens.
- To quit operations, move SPATS arm out of the working area, to the right side of the XY-stage; remove adsorbing head and store it accurately; switch off microscope, switch off microscope power supply box, turn off laser by pressing the red button at laser control box ("Laser On/Off"), switch off laser control box via moving the key from "1" to "0" position, quit software, turn off camera, shut down computer.

E) Movie of a cellular co-culture of BJ1-hTERT and HeLa H2B cells

Attached on CD

F) List of Reagents

Cell Culture

Cells

Name	Type	Company	Cat. No.
MCF10A	Human mammary epithelial cells	ATCC	CRL-10317
HCA2	Human foreskin diploid fibroblasts	Provided by Dr. Judith Campisi	-
BJ1-hTERT	Human foreskin fibroblasts	Provided by Dr. Guido Drexler	-
HeLa	Human cervial cancer cells	Provided by Dr. Guido Drexler	-
HeLa H2B	GFP transfected human cervial cancer cells	Provided by Dr. Kourosh Zolghadr	-
L929	Mouse connective tissue fibroblasts		

Cell Culture Reagents

Name	Company	Cat. No.	Conc. Stock Solution
MEBM	Invitrogen Inc	CC-3151	
MEM α	Invitrogen Inc	A10490-01	
Dulbecco's DMEM	Biochrom AG	FG 0445	
RPMI	Biochrom AG	FG 1385	
PBS	Biochrom AG	L 1815	
Trypsin/EDTA	Biochrom AG	L2163	
FBS superior	Biochrom AG	S 0613	
Bovine Pituitatry hormone	Invitrogen Inc.	CC-4136	13 mg/ml

Hydrocortisone	Invitrogen Inc.	CC-4136	0,5 mg/ml
hEGF	Invitrogen Inc.	CC-4136	10 µg/ml
Insulin	Invitrogen Inc.	CC-4136	5 mg/ml
Cholera toxin	Invitrogen Inc.	CC-4136	100 ng/ml

Cell Culture Material

Name	**Company**	**Cat. No.**
6-well Nunclon Δ surface	Nunc	140675
12-well Nunclon Δ surface	Nunc	150628
Petri dish 10 cm	Greiner Bio-One	633180
Petri dish 3,5 cm	Greiner Bio-One	627102
Cell culture flask T75	Greiner Bio-One	658175
Seriological pipettes 10 ml	Greiner Bio-One	607180
Seriological pipettes 5 ml	Greiner Bio-One	606180
Seriological pipettes 2 ml	Greiner Bio-One	710160
Falcon tubes 15 ml	Schubert und Weiß	352096
DuplexDish	Carl Zeiss Jena GmbH	415190-9121-000
µ-slide	Ibidi GmbH	80106

Chemcial Reagents

Name	**Company**	**Cat. No.**	**Conc. Stock Solution**
Paraformaldehyde	Sigma Aldrich GmbH	P6148	95%
Triton X 100	Merck KGaA	8603	
BSA	Sigma Aldrich GmbH	A4503	> 95%
Anti 53BP1 1 ry rabbit antibody	Acris GmbH	NB-100-305 LOT A4	0,2 mg/ml
Anti 53BP1 1ry rabbit antibody	Behyl Laboratories	A300-272A	1 mg/ml
Anti γH2AX 1ry mouse antibody	Millipore Corporation	16-193	1 mg/ml

AF488 2ry goat anti rabbit antibody	Invitrogen Inc.	A11008 LOT 57099A	2 mg/ml
FITC 2ry goat anti rabbit antibody	Invitrogen Inc.	65-6111	2 mg/ml
FITC 2ry goat anti mouse antibody	Invitrogen Inc.	626312	2 mg/ml
Cy3 2ry goat anti mouse antibody	Invitrogen Inc.	A10521 LOT 434574	2 mg/ml
T-Red 2ry goat anti mouse antibody	Invitrogen Inc.	T-862	2 mg/ml
SuperFect Transfection Reagent	Qiagen GmbH	301305	
Fibronectin	Sigma Aldrich GmbH	F1141	0,1%
Hepes	Gibco Inc.	15630130	1 M
Geneticin	Gibco Inc.	10131027	50 mg/ml
Puromycin	Sigma Aldrich	P9620	10 mg/ml
Vectashield mounting medium	Vector Laboratories Inc.	H-1000	

Laboratory Equipment

Name	**Company**
Cell culture hood Hera Safe	Kendro Laboratory Products
Cell incubator	Forma Scientific
Cell heating chamber	Ibidi GmbH
Water bath	Memmert
Rotina 35R centrifuge	Hettich Zentrifugen
5415D centrifuge	Eppendorf
Balance	Denver Instruments
BioSpot® pipetting robot	Microfluidix

Microscopes and Microscope Equipment

Name	Company
Axiovert 40C	Carl Zeiss Jena GmbH
10x CP-Acromat 0,25 PH1 objective	Carl Zeiss Jena GmbH
20x Plan-Neofluar 0,5 objective	Carl Zeiss Jena GmbH
Zeiss Observer Z1	Carl Zeiss Jena GmbH
10x CP-Achromat 0,25 PH1 objective	Carl Zeiss Jena GmbH
40x LD-Achroplan 0,6 Korr PH2 objective	Carl Zeiss Jena GmbH
63x LD-Achroplan 0,75 Korr PH2 objective	Carl Zeiss Jena GmbH
Mercury lamp HBO100	Carl Zeiss Jena GmbH
CCD camera Rolear XR fast 1394	QImaging
Adsorbing head (low pressure transfer system)	glass tube, hole ring, lattice/grid
PLI-100 pressure control unit	Harvard Apparatus
Nitrogen UVA laser	Palm (Carl Zeiss Jena GmbH)
Energy control system	Palm (Carl Zeiss Jena GmbH)
Laser control system CryLas FTSS 355-50	Palm (Carl Zeiss Jena GmbH)
ApoTome® Axiovert 200M	Carl Zeiss Jena GmbH
40x C-Apochromat 1,2W Korr objective	Carl Zeiss Jena GmbH
Mercury lamp ebq100	Carl Zeiss Jena GmbH
Axiocam HRM	Carl Zeiss Jena GmbH
Zeiss Axiovert 200M	Carl Zeiss Jena GmbH
CSU-10 spinning disk confocal scanner	Carl Zeiss Jena GmbH
Solid-state lasers (405, 491, 561, 638 nm)	Carl Zeiss Jena GmbH
EM-CCD camera	Hamamatsu

X-ray Irradiation

Name	Company
Stabiliplan TR 300f X-ray machine	Siemens AG
Dose area product meter Diamentor M4	PTW
Dosimentor II	PTW
CP160 X-ray machine	FAxitron
Ion chamber dosimeter	Victoreen

Software

Name	**Company**
Nanosauger Program (2.5, 2.6, 2.7)	XYZ High Precision
QCapture Pro 6.0	QImaging
AxioVision	Carl Zeiss Jena GmbH
ImageJ	National Institutes of Health
Metamorph Imaging Software	Molecular Devices
Matlab	MathWorks
DIPimage	Image processing toolbox for Matlab

G) List of Abbreviations

AOTF	Acousto-optical tunable filter
ATM	Ataxia telangiectasia mutated
BJ1-hTERT	Immortalised human foreskin fibroblast
53BP1	Tumor suppressor p53- binding protein 1
DNA	Deoxyribonucleic acid
DNA-PKcs	DNA-dependent protein kinase, catalytic subunit
DSB	Double strand break
dsDNA	Double stranded DNA
EGF	Epidermal growth factor
EGFP	Enhanced green fluorescent protein
FACS	Fluorescence-activated cell sorting
FGF	Fibroblast growth factor
GFP	Green fluorescent protein
γH2AX	Phosphorilated histone H2AX
Gy	Gray
h	Hour
HeLa	Cell line derived from cervical cancer (**He**nrietta **La**cks)
HR	Homologous recombination
HSP70	Heat shock protein 70
HT 1080 cells	Human fibrosarcoma cell line
hTERT	human Telomerase Reverse Transcriptase
ICRP	International Commission on Radiological Protection
ICRU	International Commission on Radiation Units and Measurements
IR	Ionising Radiation
kDa	Kilo Dalton
keV	Kilo electron volt
Ku-protein	Protein required for the non-homologous end joining
L929	Mouse fibroblast cell line
LET	Linear energy transfer
LIP	Laboratory intern protocol
LMPC	Laser microdissection and pressure catapulting
LMU	Ludwig Maximalian Universität

LNT model	Linear no-threshold model
MeV	Mega electron volt
µl	Microliter
NADPH	Nicotinamide adenine dinucleotide phosphate
NCRP	National Council on Radiation Protection and Measurements
NHEJ	Non-homologous end joining
nm	nanometer
p53	A tumor suppressor protein
Pb	Lead
PFGE	Pulsed field gel electrophoresis
Rad51	Protein assisting in repair of DNA double strand breaks
Rad52	Protein, wich is important for DNA double strand break repair
RIF	Radiation-induced foci
ROS	Reactive Oxygen Species
s	Second
SNAKE	**S**upraleitendes **N**anoskop für **A**ngewandte **K**ernphysikalische **E**xperimente
SPATS	**S**ingle **P**article **A**dsorbing **T**ransfer **S**ystem
SSB	Single strand break
ssDNA	Single stranded DNA
Sv	Sievert
TGFβ	Transforming growth factor beta
TU	Technical University

Curriculum Vitae

Persönliche Angaben

Name	Teresa Maria Neumaier
Geburtsdatum	19.05.1981
Geburtsort	Aichach

Wissenschaftliche Ausbildung

04/2007 - 05/2010	Promotion Physik Doktorarbeit: Possible Influences of Low Dose Ionising Radiation on living Cells – A static and a dynamic Approach
10/2004 - 03/2007	Diplom Physik (Nebenfach: Mathematik) Diplomarbeit: Mechanical Forces during Cell Adhesion – Physical Perspectives of Metastasis
10/2002 - 03/2007	Lehramt Gymnasium, Universität Augsburg Hauptfächer: Mathematik/Physik
10/2001 - 09/2002	Lehramt Grundschule, Universität Augsburg Hauptfach Sozialkunde, Nebenfächer: Mathematik/Deutsch/Kunst
1991 - 2001	Deutschherren Gymnasium Aichach Abitur

Forschungsaufenthalte

04/2008 - 07/2008	Forschungspraktikum am Lawrence Berkeley National Laboratory, Berkeley CA, USA (im Rahmen der Promotion)
07/2006 - 08/2006	Forschungspraktikum am Niels Bohr Institut, Kopenhagen, Dänemark (im Rahmen der Diplomarbeit)

Stipendien und Auszeichnungen

07/2009	2. Preis beim Young Scientist Poster Award, Heavy Ions in Therapy and Space Symposium, Köln
07/2007	Biochemcial Journal Young Investigator Award, 6th European Biophysics Congress, London
07/2006	Stipendiatin des Deutschen Akademischen Austauschdienstes für einen kurzfristigen Studienaufenthalt während Abschlussarbeiten (Kopenhagen)

Veröffentlichungen

2011	Quantification of Melanoma Cell Adhesion to VWF, Teresa Neumaier, Kumudesh Sritharan, Stefan.W. Schneider, Thomas Franke, Achim Wixforth, Matthias F. Schneider, Publikation in Vorbereitung
2011	Non-linear DNA damage response to ionizing radiation suggests clustering of DNA breaks in normal human cells, Teresa Neumaier, Brian Yang, James Chen, Aris Polyzos, Christopher Pham, Stefan Thalhammer, Sylvain V. Costes, Publikation in Vorbereitung

2010	Biocompatibility studies of solution-processable organic thin-film transistors for sensing applications, Giuseppe Scarpa, Anna-Lena Idzko, Stefan Götz, Teresa Neumaier, Stefan Thalhammer; Nano/Molecular Medicine and Engineering (NANOMED), 2009 IEEE International Conference on
2008	Programmable Cytogenetic Submicroliter Lab-on-a-Chip for Molecular Diagnostic Applications, Daniela Woide, Veronika Schlentner, Teresa Neumaier, Thorsten Wachtmeister, Herwig G. Paretzke, Zeno von Guttenberg, Achim Wixforth, Stefan Thalhammer; Biodevices 2008 – International Conference on Biomedical Electronics and Devices